Investigation of the water splitting reactions on multi-heteroatom doped cobalt-based carbon catalysts.

TECHNISCHE UNIVERSITÄT DARMSTADT

Graduate School of Energy Science and Engineering

Vom Fachbereich Chemie
der Technischen Universität Darmstadt

Zur Erlangung des Grades
Doktor-Ingenieurs
(Dr.-Ing.)

Dissertation

Von Ali Shahraei

Erstgutachter: Prof. Dr. Ulrike I. Kramm
Zweitgutachter: Prof. Dr. Jin Suntivich
Darmstadt 2018

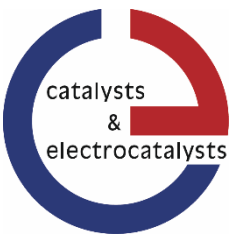

Investigation of the water splitting reactions on multi-heteroatom doped cobalt-based carbon catalysts

Tag der Einreichung: August 2018

Tag der mündlichen Prüfung: Oktober 2018

Shahraei, Ali
Investigation of the water splitting reactions on multi-heteroatom doped cobalt-based carbon catalysts
Darmstadt, Technische Universitäte Darmstadt
Jahr der Veröffentlichung der Dissertation auf TUprints: 2018
URN: urn:nbn:de:tuda-tuprints-81712
Tag der mündlichen Prüfung: 18.10.2018

This thesis is dedicated to my beloved parents, Nahid and Reza.

Thesis Statement pursuant

I hereby declare that the presented dissertation is based on original research and is the result of my own work. I certify that this dissertation contains no material which has been accepted for the award of any other degree in my name, in any university or other tertiary institution and, to the best of my knowledge and belief, contains no material previously published or written by another person, except where due reference has been made in the text.

Darmstadt, 27th August 2018

Abstract

In the context of energy transition, hydrogen is addressed as a clean future energy carrier that enables the emission-free production of energy to become independent of fossil fuels. The development of hydrogen production technologies like the electrolysis is strongly driven by the two main criteria: sustainability and economy. Over the past decades, various technological achievements resulted in a reduction of costs which has dramatically improved the economic potential of hydrogen produced by electrolysis. Especially in the field of material development, great effort was devoted to replace the precious state of the art catalyst materials with abundant cost-effective catalysts accelerating sluggish water splitting reactions.

This dissertation focuses on the investigation of carbon-based cobalt catalysts with multi-heteroatom doping for the oxygen evolution reaction (OER) and hydrogen evolution reactions (HER). Within this study, two major synthesis approaches, one with metal organic framework (MOF) and another with polyaniline (PANI), were investigated in terms of structural and electrochemical characterization. Moreover, the catalysts were analyzed in detail by active site identification and mechanistic understanding of the reactions within the scope of each project.

Within the MOF approach, the role of the metal species on HER activity was investigated using X-ray photoelectron spectroscopy (XPS). The discussion was further supported by density functional theory (DFT) calculations resulting in structure-activity correlations with emphasis on the importance of the nature of the metal. Besides, bimetallic catalysts with optimal hydrogen binding energies were suggested as a promising active catalyst toward HER .

The PANI approach was proposed to investigate multi heteroatom doping influence on the catalytic activity and material properties. Within this approach, cobalt catalysts with variation of cobalt loading and sulfur loading in the precursors were prepared. The catalysts were highly active toward both HER and OER, though the origin of activity might be different. Several physico-chemical characterization techniques combined with post mortem analysis were carried out in order to get insight into the origin of the activity. It was found that the high HER activity of PANI-based samples is attributed to MeN_4 sites, and the OER activity is originating from a hybrid cobalt complex depending on the synthesis route.

Table of contents

Acronyms

AC	Alternating current
ANI	Aniline
APS	Ammonium persulfate
CNT	Carbon nanotube
CoPc	Cobalt phthalocynine
CV	Cyclic voltammetry
CVD	Chemical vapor deposition
DFT	Density functional theory
DCDA	Dicyandimide
EC	Electrochemical conditioning
GHG	Greenhouse gases
GO	Graphene oxide
HBE	Hydrogen binding energy
HER	Hydrogen evolution reaction
IL	Ionic liquid
IL-TEM	Identical location Transmission electron microscopy
IPCC	Intergovernmental Panel on Climate Change
MLMN	Melamine
MOF	Metal organic framework
MWCNT	Multi-walled carbon nanotube
NPMC	Non-precious metal catalyst
OER	Oxygen evolution reaction
ORR	Oxygen reduction reaction
PABS	Polymerized aminobenzenesulfonic
PANI	Polymerized aniline
PEM	Proton exchange membrane
PES	Photo emission spectroscopy

Phen	Phenanthroline
RDE	Rotating disc electrode
RDS	Rate determining step
STM	Scanning tunneling microscopy
TEM	Transmission electron microscopy
TOF	Turn-over frequency
UHV	Ultra-high vacuum
VB 12	Vitamin V 12
XAS	X-ray absorption spectroscopy
XPS	X-ray photoelectron spectroscopy
XRD	X-ray diffraction
ZIF	Zeolitic imidazolate frameworks

1 Introduction

Total anthropogenic Greenhouse gas (GHG) emissions have continually increased over the last decades. The biggest share (~ 78%) of total GHG emissions is attributed to the CO_2 emission from fossil fuel combustion and industrial processes. Two main contributions to the increase of global CO_2 emissions are population and economic growth. Whereas the impact of population growth remained stable over the last three decades, the contribution of the economic sector to GHG emissions increased rapidly based on the IPPC report.[1] Figure 1.1 shows the total anthropogenic CO_2 emissions by economic sector, where the inner shell shows the direct emissions and the outer shell corresponds to the indirect share of CO_2 emissions from electricity and heat production. Therefore, a sustainable long-term scenario with a broad range of technological options and systematic assessment of local mitigation needs to be applied to achieve the ambitious target of 80-95% cuts in GHG emissions set within the European Union for 2050.[2] Among all proposed scenarios, hydrogen provides a long-standing solution to reduce GHG emissions in the economic sector, including energy production , industry, and transportation.

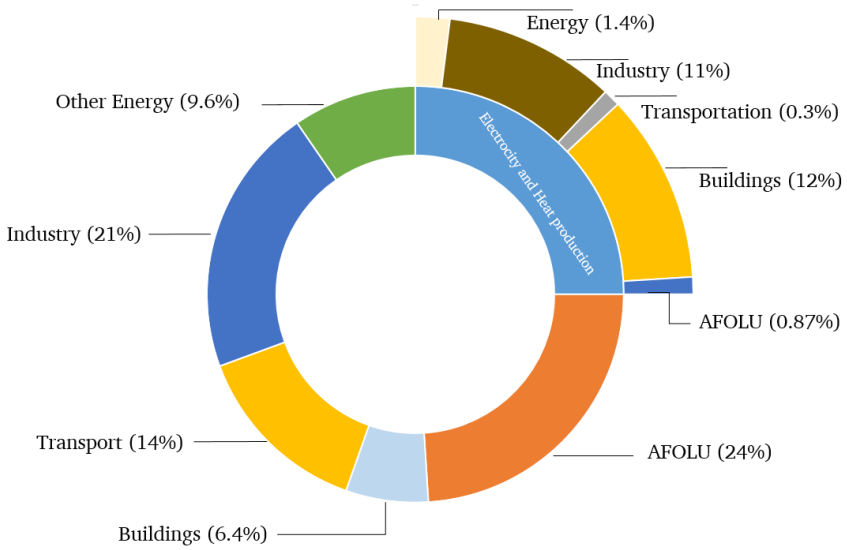

Figure 1.1 Greenhouse gas emissions by economic sector in 2010 adapted from IPCC[1],(AFOLU: Agriculture, Forestry and Other Land Use)

Hydrogen can be produced via various processes, for example, coal gasification, natural gas reforming processes, biomass pyrolysis, dark fermentation process, and water electrolysis. Although nowadays only 3.9% of total hydrogen is produced by water electrolyzers, it is the

only method of providing a CO_2-free fuel when it is produced with electricity from renewable sources.[3] Renewable energy production increased significantly (more than six folds) over the last 30 years in Germany. However, based upon the Eurostat report, gross renewable energy consumed (as primary energy) in Germany was only 15% of total energy consumption, on a path to the 2020 target of 18%. In the last few decades, several economic studies have been conducted to analyze hydrogen feasibility as the future energy carrier and its role in reducing GHG emissions in Germany.[2, 4] Indeed, based on simulated data, investment in hydrogen production is the most profitable in Germany (within the Europe) because of its highest share of renewables among European countries. Accordingly, it is possible to increase the share of renewable energy consumption up to 50% via coupling the electrolyzers to renewable power plants.[4]

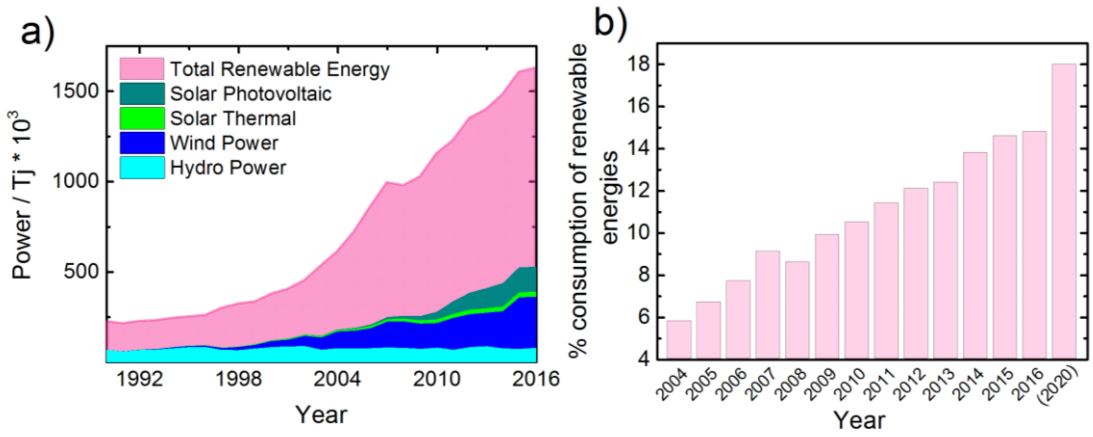

Figure 1.2 a) Primary production of energy and b) share of energy consumption from renewable sources in Germany

There is no doubt that hydrogen will play a key role in an environmentally sustainable energy cycle. However, there are several prerequisites for a successful energy transition via electrolysis: the availability of low-cost electricity generated by renewable energies, consideration of climate issues by "Market players" regardless of economic issues, and improvement of the technological efficiency. The availability of low-cost electricity is vital for the energy transition to hydrogen via a so-called "Maximum" scenario discussed by German Ministry for Environment.[4] This 'Maximum" scenario outlines the growth of the share of renewable energies in total energy mix and shows that it is technically feasible to build a world free of CO_2 emission earliest in 2070. Meanwhile, it is crucial to maintain a dedicated energy policy and to perform appropriate business models in order to attract the investors. It should be emphasized in the worldwide scale that climate change is a global issue that implies the need for individual cooperation. Last

but not least, it is necessary to use the time interval to determine technological weaknesses and strengths of electrolyzers in order to improve their performance.

For the transition of a fossil fuel based energy economy to a sustainable hydrogen based one, electrolyzers can be considered as key components. The catalysts developed in this work are applicable for low temperature applications as Alkaline and Proton Exchange Membrane (PEM) electrolyzers. Table 1 compares the two systems and summarizes their technological advantages and disadvantages

Table 1 Comparison of Alkaline and PEM electrolyzers [5, 6]

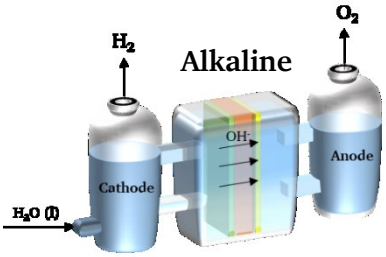	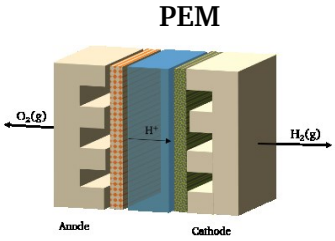
Advantages	
Sophisticated technology	Rapid system response
Relative low cost	Compact system design
Non-precious catalysts	Dynamic operation
Disadvantages	
Low dynamic	High capital cost
Corrosive electrolyte	Low durability
Crossover gases	Below MW range
Efficiency 50-80%	Efficiency 50-65%
Operation temperature	Operation temperature
65-100 °	below 80 °C

Besides the operational costs related to electricity procurement, the capital cost plays a key role on the hydrogen price in the near future. It is worthwhile to be noted that stack costs contribute 50 to 60 % to the overall system price. The stack cost breakdowns analyses are reported for the Alkaline and PEM electrolyzers as the most commercial systems.[6]

The capital cost reduction scenarios might be different based on the system configuration. The catalyst share in the total costs of the alkaline system is significantly higher than of the PEM system. Therefore, it is required to develop non-precious materials which remain stable under the corrosive environment of the alkaline electrolyzers. Regarding PEM electrolyzers, the design

of innovative new bipolar plates and the development of large area cells are major challenges beside the catalyst development in order to minimize the costs. However, reducing catalyst costs would be a long-term solution for manufacturers and investors of both systems.

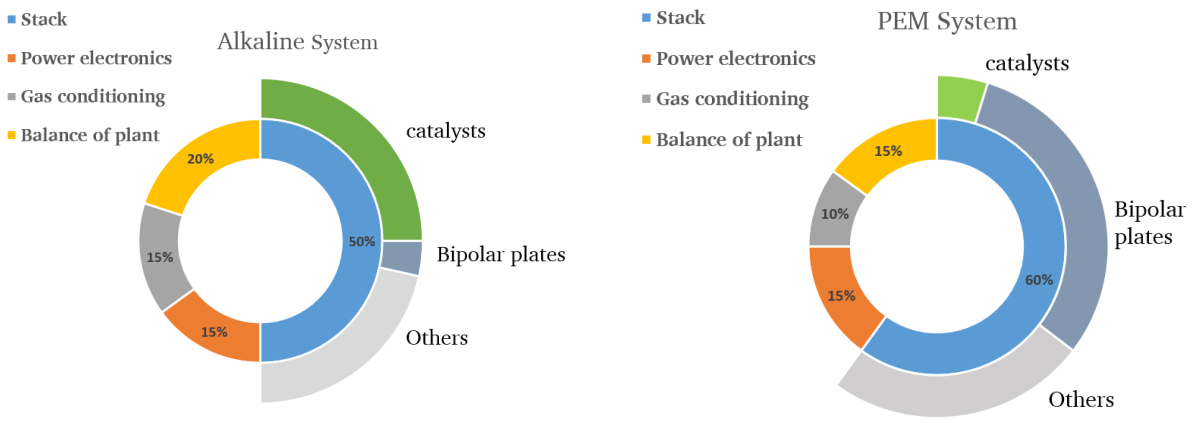

Figure 1.3 Capital cost break down for alkaline and PEM systems[6]

Starting from a bottom-up view of the hydrogen utilization as an energy career, the last step is the grid integration of the electrolyzers. Hydrogen produced by water splitting can be used for several uses (e.g. transportation, industry or energy storages), which significantly varies its price. Based on the statistics and simulations, the hydrogen price only for applications with on-site production would be comparable with other scenarios (fossil fuels, biomass fuels etc.) outlining the importance of grid integration.[2, 6] Therefore, the most profitable sector where renewable-generated hydrogen can be used is the transportation sector, which is reported as an economically feasible target by 2030.[6] In this scenario, the development of fuel cell powered vehicles will play an important role in the energy transition from fossil fuels to hydrogen.

1.1 Scope of the thesis

Despite the fact that Me-N-Cs have been heavily investigated regarding oxygen reduction reaction (ORR), only a small number of efforts has been made to optimize them for the electrocatalysis of the hydrogen evolution reaction (HER) and oxygen evolution reaction (OER). Therefore, it is necessary to get an insightful knowledge regarding the nature of activity for water splitting reactions activated by Me-N-Cs. The previous works focused on the model studies of non-pyrolyzed MeN_4-macrocyles to explore the origin of the activity. However, to proof the applicability of the concepts derived from these model catalysts, it is required to investigate the pyrolyzed Me-N-Cs as the real catalysts. In the scope if this thesis a new synthesis

approach was developed to prepare non-precious multi-heteroatom doped Me-N-C catalysts for the water splitting reactions. Beside physico-chemical characterization especially post mortem analysis provided significant insight into the nature of active sites. The comprehensively reported overview regarding co-doping effect, active site determination, structure-activity correlations and reaction mechanism can be used to further improve Me-N-Cs for other catalytic reactions.

2 Literature Review

The electrolysis process principally was introduced in 1789 AD by Van Troostwijk and Deiman in Europe.[7] It is an electrochemical process of water splitting to oxygen and hydrogen induced by a minimum thermodynamic potential (theoretically 1.23 V). Nevertheless, the required operating cell voltage is significantly higher than the theoretical thermodynamic potential due to excess energy that is required to overcome the electrolyte resistance and kinetic limitations in form of so called overpotentials.

Table 2 Water splitting reactions in acidic and alkaline media

	Alkaline electrolysis	**Acidic electrolysis**
Hydrogen Evolution Reaction **(HER) - Cathode**	$4H_2O + 4\ e^- \rightarrow 2H_2\uparrow + 4OH^-$	$4H^+ + 4\ e^- \rightarrow 2H_2\uparrow$
Oxygen Evolution Reaction **(OER) - Anode**	$4OH^- \rightarrow O_2\uparrow + 4\ e^- + 2H_2O$	$2H_2O \rightarrow 4H^+ + 4\ e^- + O_2\uparrow$

Table 2 shows the catalytic half-cell reactions occurring in alkaline and acidic media. The kinetic of both HER and OER, is strongly depending on the materials used as electrocatalysts. Generally, the state of the art catalysts are Pt-based and other precious metal-based oxides (Ir, Ru) for HER and OER, respectively. In this study, the Me-N-C catalysts were investigated for water splitting reactions with different approaches to replace the precious catalysts. In the following sections, the most important steps regarding preparation of Me-N-C catalysts, possible active site formation/determination and catalyst optimization considering both reactions (HER and OER) will be discussed in detail.

2.1 Hydrogen Evolution Reaction (HER)

2.1.1 Mechanistic understanding of HER

The HER is composed of elemental reaction steps and is fundamentally described in two ways based on electrolyte solution, water reduction (alkaline) and hydronium ion reduction (acidic).

Table 3 Elemental reaction steps for HER in Alkaline and Acid media

	Water reduction	**Hydronium ion reduction**	**Tafel slope($\alpha = 0.5$)**
Volmer reaction	$H_2O + e^- \rightarrow 2OH^- + H_{ad}$	$H_3O^+ + e^- \rightarrow H_{ad} + H_2O$	120 mV/dec
Heyrovsky reaction	$H_{ad} + H_2O + e^- \rightarrow H_2$	$H_{ad} + H^+ + e^- \rightarrow H_2$	40 mV/dec
Tafel reaction	$H_{ad} + H_{ad} \rightarrow H_2$	$H_{ad} + H_{ad} \rightarrow H_2$	30 mV/dec

The Volmer step represents the initial step for the hydrogen production and describes the adsorption of hydrogen on the electrodes surface (H_{ad} formation). Thereafter, the reaction path might involve the Heyrovsky or Tafel step for H_{ad} recombination and H_2 desorption. In order to investigate the reaction mechanism, several techniques have been applied such as Tafel analysis, AC impedance spectroscopy and potential step charging based on the literature.[8] In this work, Tafel analysis has been performed to study the reaction mechanism based on determination of the rate determining step (RDS) as an important activity descriptor, which governs the reaction rate. Tafel analysis results in two important parameters, namely exchange current density and Tafel slope based upon the equation below.

$$\eta = a + b \log(j)$$

The term η is the overpotential, which is the difference between the formal electrode potential of the reaction and the standard potential. The Tafel analysis can be derived from the well-known Bulter-Volmer equation, which relates current density with overpotential for reversible electrochemical reactions as stated below.[9]

$$j = j_0 \{\exp(-\alpha f \eta) - exp[(1-\alpha) f \eta]\}$$

The term j donates the current density, j_0 is the exchange current density, α is the transfer coefficient and $f = Fz/RT$ (*F:* Faraday's constant, z: number of transferred electrons, *R:* the universal gas constant and *T:* the absolute temperature). The equation above consists of the total current of both oxidation and reduction reactions. Therefore, the term overpotential (η) can be written as

$$\eta = \overbrace{\frac{1}{f\alpha}\ln(j_0)}^{a} - \overbrace{\frac{1}{f\alpha}}^{b}\ln(j)$$

Empirically the equation above is reported as Tafel relation, where the Tafel slope can be obtained by plotting overpotential (η) with $\log(j)$. The Tafel slopes used to evaluate the RDS in HER reaction are reported in Table 3. It should be noted that these slopes are obtained assuming the extreme coverage of the intermediates, even though the Tafel analysis is coverage dependent. For instance, Shinagawa et al. reported the slope of 120 mV/dec at higher coverage when Heyrovsky is considered as the rate determining step.[9] Therefore, the potential range where the Tafel slope is obtained significantly matters to evaluate the reaction mechanism.

The hydrogen evolution reaction includes adsorption and desorption of hydrogen atoms on the active site. Therefore, a suitable catalyst should bond to the reaction intermediates neither too strong nor too weak, following on the Sabatier's principle.[10] The free energy of hydrogen adsorption (ΔG_H) is defined as an appropriate descriptor for catalytic activities.[11] The influence of the adsorption energy on the reaction rate can be expressed with a volcano plot, as a function of the exchange current density (as an activity descriptor) obtained from Tafel slope extrapolation shown in Figure 2.1. It should be noted that these fundamental studies were reported for single crystal metals in the steady-state conditions.

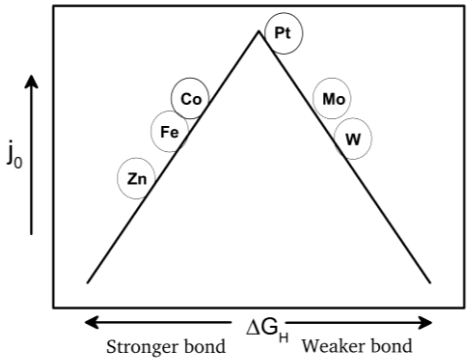

Figure 2.1 Activity volcano-shaped plot as a function of the ΔG_H for HER[10]

This volcano dependence is a clear demonstration of the relation between electrocatalysis and the nature of metals. Since the electrochemical reactions take place on the metal surface, their electrochemical properties, in the same way as the surface properties, are linked to the electronic structure.[12] Therefore, each metal with a unique electronic configuration has distinctive electrochemical properties, influenced by hydrogen adsorption/desorption energy. Platinum with an adsorption energy close to zero is placed on top of the volcano, which is known as the most active catalyst toward HER.[13-15]However, the economic feasibility of technological applications using Pt is hindered by the scarcity and high price of Pt.[16] Although

lowering the Pt loading or alloying with other transition metals have been suggested for reducing the catalyst price, it cannot be regarded as a long-term solution. More recently, considerable efforts have been made to find alternative materials composed of abundant transition metals known as Non-Precious Metal Catalysts (NPMC) to activate the hydrogen evolution reaction.

2.1.2 Me-N-C catalysts

Among all NPMCs, Me-N-C catalysts, heat-treated analogous to N_4-macrocycles, have attracted much more attention during the last decades as catalysts for oxygen reduction reaction (ORR) in fuel cell applications.[17, 18] Pioneer work in the field of developing Me-N-C catalysts were made by Jahnke, Jasinski and Yeager.[19-21] In fact, Jasinski was the first who successfully reported the activity of cobalt phtalocyanine, a non-pyrolyzed N_4-macrocycle, for the ORR. Later in 1976, Jahnke reported that the ORR activity and stability of N_4-compounds can be remarkably enhanced by performing a high temperature heat treatment.[21, 22] Another significant breakthrough in development of Me-N-Cs was achieved by replacement of the expensive macrocyclic N_4-complexes that was used as a precursors in the Me-N-C synthesis with independent metal, nitrogen and carbon sources.[23-25] The use of independent metal nitrogen and carbon sources opened up a broad range of new possibilities to specifically optimize the final composition and structure of the Me-N-C. In fact it was found, that the synthesis parameters like type of precursors, pyrolysis temperature, pyrolysis atmosphere and pyrolysis time have a strong impact on the resulting catalytic properties.[26, 27, 28] Despite huge debate in literature, it is widely believed that the most dominant ORR active motif in the structure is a metal atom coordinated with nitrogen embedded in carbon plane, named as MeN_X moieties (particularly MeN_4).[29, 30, 31]

In a work by Zagal et al., a volcano plot was experimentally obtained where the activity descriptor (kinetic current density, in this study) was plotted as a function of the number of electrons filled in d orbitals in various MeN_4 chelates related to ORR.[32-34] Interestingly, FeN_4 chelates were located on top of the volcano while Fe chelates have a partially filled orbital. Fe-based catalysts are known as the most promising catalyst for ORR since they contain the maximum density of MeN_x moieties formed during pyrolysis compared with other Me-N-C (Me: Co, Mn, Cu.[34] Beside the mass-based density (number of active sites), the turn-over frequency (TOF) contributes significantly to the catalytic activity as an intrinsic property.[35, 36]

Due to the interaction of d electrons of metal with nitrogen and π electrons of carbon plane, the local electronic structure will change by metal variation and influence the intermediate

adsorption.[37] Karweik and Winograd studied the charge distribution of nitrogen in different metalloporphyrins (Mg, Zn, Co, Cu, Ni and Ag-based) using X-ray Photoelectron Spectroscopy (XPS). They found a correlation between N 1s binding energy associated to MeN_4 and the corresponding metal electronegativity.[38] It was later reported that based on the N 1s spectra one could discriminate between the Me-N bonds attributed to MeN_4 from other nitrogen species.[39] Inspired by the findings of Karweik, Kramm et al. studied the change in electronic structure of Fe-N-C in relation to their turn-over frequency (TOF) for the ORR activity.[40] The outstanding performance and flexibility of Me-N-C catalysts for the ORR as well as the important role of the analog MeN_4 macrocycles in various bio-catalytic processes motivated the researcher to study these class of catalyst for other electrochemical reactions. Therefore, many efforts have been made to prepare nitrogen and metal-doped carbon-based catalysts to activate hydrogen evolution reaction. So far, the majority of the achieved approaches to synthesize Me-N-C catalysts for HER were adapted from those that were found to be the most active in ORR.[41] Also in the case of HER catalysts, metallic nanoparticles encapsulated in nanotubes (Me @ carbon) and metal-composites supported by carbon (Metal-composite @ carbon) gained more attraction because of their supreme stability under harsh electrochemical conditions.[42-46] The metal composites can typically contain metal nanoparticles, metal carbides, metal sulfides or/ and metal oxides as residuals which might be formed during the synthesis process. We here report that especially the type of dopant used in the synthesis process determines the type of inorganic species that is formed during the pyrolysis. In the following section, three types of structure related to heteroatom doped carbon-based catalysts are discussed.

I. Porphyrin-like macrocyclic complexes (central active sites)
II. Core-shell structure with metal nanoparticle/nanocomposite encapsulated in carbon
III. Metal nanoparticle/nanocomposite bounded with a carbon substrate

2.1.3 Active site determination controversy

Intensive theoretical and experimental studies have been carried out in order to explore the origin of activity of heteroatom-doped carbon-based catalysts for HER due to their complex structure. Traditionally, the synthesis of Me-N-C catalysts involves a high-temperature annealing of different metal, nitrogen and carbon sources. As mentioned above, the choice of precursors and pyrolysis temperature for carbon-based material synthesis could lead to different catalytic and structure characteristics. Therefore, several possible active sites could be formed through the synthesis procedure, where each solely can contribute to the catalytic activity. In the following, the identified sites which were mainly reported in literature are discussed.

Therefore, Table 4 provides a summary of the preparation of heteroatom doped carbon-based catalysts reported for HER (based on I - III).

Table 4 Summary of the preparation of heteroatom doped carbon-based catalysts reported for HER

Precursors	***U_{over} / mV**		**Condition**	**Formed Species**	**Ref.**
	PH1	**PH13**			
CoPc, KB (Me loading), (T)	370		HT1[700,1h,Ar] HT2[(800-1000),5m,Ar] AL	Co-np, **CoN_x**	[47]
CoTMPP/Co0PD, VB 12 (Me type), (T)	133	180	HT1[(600-1000),2h,N_2] AL HT2[(600-1000),2h,N_2]	Co-np, **CoN_x**	[48]
$CoCl_2$/$Fe(NO_3)_3$, Go (Me type), (D)	185	270	HT1[750,1h,Ar/NH_3]	**CoN_x-C-N**	[49]
$Co(NO_3)_2$/$Fe(NO_3)_2$, Pyridine (Me type)	290		CVD (H_2/Air: 20%)	Fe-np,Co-np,**FeCo-np**	[50]
Co Ac./Fe Ac., Imidazole (Me type)	200	210	HT1[900,2h,Ar] AL HT2[900,2h,Ar]	**Co-np**, **Fe-np**	[42]
ZIF-67, Phosphor, Sulphur (D)	80	148	HT1[600,2h/3days, N_2]	**CoPS**, C-N	[51]
$CoCl_2$, DCDA (T)	260	400	HT1[500, 2h,N_2 + 700-1200,2h,N_2]	Co-np, **C-N**	[52]
Co Ac., Go, cyanimide (T)	180		HT1(450,2h,N_2+ 600-900,2h,N_2], AL	Co-np, **C-N,** Co_3O_4	[43]
Co Ac, Glucose, Melamine (Me loading)	250	232	HT1[800,2h,Ar]	CoN_x, Co-np, **C-N**, Co-O	[53]
Me acetate, Phen, ZIF-8 (Me type)	180	270	HT1[1050,1h,Ar]	Me-np, Me-C, MeN_x	[54]
$Co(NO_3)_2$/$Fe(NO_3)_2$/$Ni(NO_3)_2$, PANI (Me type), (T)	138	178	HT[(550-950), - ,N_2] AL	Co-np,CoC_x, CoN_x,	[45]
$Co(NO_3)_2$/$Ni(NO_3)_2$, PANI, KB (Me type)	275	310	HT[900,1h,Ar] AL HT2[900,1h,Ar]	Co_9S_8, CoN_x	[55]
$Fe_3[Co(CN)_6]_2$ (T)	262		HT1[600-800,4h,N_2]	Co_4N	[56]
ZIF-67		298	HT1[600,5h,Ar]	Co-np, CoN_x	[57]
MoO_3, PANI	147	257	HT1[700,3h,Ar]	**Mo_2C**,MoO_2, C-N	[58]
NeNU-5	142	151	HT[800,6h,N_2]	**MoC_x**	[59]
$Co(NO_3)_2$, Aniline/ABS, $(NH_4)_2S_2O_8$ (D)	180	251	HT1[200,1h-900,5h] HF	**CoS_x, CoN_x**	[60]

*Overpotentials are reported @ 10 mA cm^{-2} for cobalt-based synthesis (T): temperature variation, (D): Heteroatom doping variation

- **Carbon in compound particles (Me @ carbon)**

Due to the instability of pure transition metals under acidic condition, metal encapsulation with thin carbon layers was suggested in order to protect the direct metal contact with the electrolyte. Up to now, a limited number of transition metals encapsulated in carbon has been investigated, such as Co, Fe and Ni.[41, 62]

Zhou et al. reported that N-doped carbon-wrapped cobalt nanoparticles on N-doped graphene have excellent activity and stability toward HER in acidic medium.[43] The synthesis included the adsorption of Co^{2+} and cyanimide onto graphene oxide, followed by decomposition of cyanamid and reduction of Co^{2+} through heat treatment at temperatures between 600 to 900 °C. Zou et al. synthesized cobalt-, nickel-, iron-embedded nitrogen-rich CNT catalysts via a heat treatment of the metal source and dicyandiamide at 700° C.[52] The authors claimed the formation of cobalt nanoparticles wrapped in nitrogen doped carbon layers/tubes. The HER activity was attributed to the carbon atoms with optimized work function tuned by cobalt particles. Wang et al. reported a Co-based catalyst prepared by cobalt acetate, glucose and melamine at a temperature of 800 °C. The catalyst contained hybrid sites composed of CoN_x complexes and cobalt nanoparticles with superior activity toward ORR and HER. In this work the HER activity was attributed to the carbon atoms adjacent to cobalt nanoparticles.[53]

Beside the development of various solid state synthesis methods, Deng et al. and Tavaloli et al. established the chemical vapor deposition of Fe-based materials (Fe@CNT) as new synthesis route. The resulting Fe@CNT catalysts are characterized by ultrathin core shell showed a high performance and were able to compete with commercial Pt-based catalysts for activation of HER.[44, 50] Heretofore, it is suggested by both experiment and theory that the HER active sites are located on the carbon shell where the metal core facilitates the charge transfer process in these studies. The presence of the nitrogen and metal core is considered vital for electrochemical activity. Therefore, the synergistic effect between carbon shell, metal particle and doped nitrogen plays an important role in the enhanced HER activity compared with non-metal carbon-based catalysts or pure metals.

- **Metal Nanoparticles/Nanocomposites (Me / MeC_x @ carbon)**

Metal Organic Frameworks (MOF) are porous crystalline materials including a metal ion coordinated with organic ligands within a 3D structure. Through annealing process, metal nanoparticles or metal carbides embedded in heteroatom-doped (mostly nitrogen) carbon network can be composed of MOF material. Li et al. reported active CoPS nanoparticles supported on N-doped carbon matrix via pyrolysis of ZIF-67 at a temperature of 600 °C for three days (carbonization and subsequent phosphosulfurization).[51] The uniform distribution of

nanoparticles as the active sites on carbon matrix was attributed to the origin of HER activity in this work. More recently, the formation of cobalt-based (CoFe, CoSe and CoPd) alloy nanoparticles as active centers embedded in carbon using MOF materials was reported as a rational way to prepare an active HER catalyst.[63, 64]

Based on the synthesis environment and annealing temperature, MeC_x nanocomposites (most reported, molybdenum carbide) can be derived from MOF materials with different morphology (nanoparticles, nanorods, nanobelts) embedded in N-doped carbon nanotubes.[54, 58, 59, 65] In a work by Wu et al. the formation of MoC_x nanocrystals by the pyrolysis of the MOF (NENU 5) at a temperature of 800 °C with excellent activity toward HER was reported. Within another approach, Zhang et al. prepared a catalyst with dominant active Mo_2C nanocrystals embedded in N-doped carbon via heat treatment of MoO_3/PANI hydride at a temperature of 700 °C.

- **MeS_x in hybrid carbon structures (MeS_x @ carbon)**

Metal-sulfur clusters are counted as active sites for HER learned from hydrogenase systems in nature.[66] Thus, numerous studies have been made to synthesize metal-sulfur complexes analogous to these natural active centers.[67-69] Recently, it was observed that MeS_x in a hybrid structure including carbon as a support shows better catalytic activity than pure MeS_x clusters toward HER.[41] Mo-based catalysts are reported as the most active and stable among MeS_x hybrid catalysts.[61] Li et al. reported an active HER hybrid catalyst with a molybdenum-sulfur complex supported by nitrogen-doped CNT (MoS_x/NCNT) prepared at a temperature of 600 °C. In this study, the important role of nitrogen and carbon were addressed adequately. It was claimed that carbon interacts as a promoter of electronic conductivity and nitrogen is a promotor for generation of dense nano-scale amorphous layers in lower pyrolysis temperature.[61] Other studies reported Co, Sn, Fe-based hybrid catalysts and investigated the individual effect of metal/carbon/nitrogen on the catalytic activity. [45, 68, 70]

Up to now, it is widely believed that MeS_x complexes are the dominant active center in hybrid carbon systems. Nevertheless, the controversy in assignment of the active center to the S on the edge or metal on the center of MeS_x clusters remains.[71, 72]

- **MeN_x in nitrogen-doped carbon-based material (Me-N-C)**

Due to the complex structure of Me-N-C catalysts, the aforementioned sites might be formed during the synthesis procedure and possibly participate in the catalytic activity. Between the 1970s-1990s, MeN_4 macrocycles gained a lot of attention due to their capability in catalyzing different electrochemical reactions as ORR, CO_2 reduction, formation of hydrogen peroxide, nitric oxide reduction and hydrocarbon oxidation and HER.[26] Inspired by N4-macrocycles,

MeN_x moieties were the focus of active center identification related to ORR activated by Me-N-C catalysts. Later, it was widely confirmed that MeN_x moieties mainly participate in ORR activity using in-situ measurement and DFT calculations.[30]

Recently, Liang et al. studied a pyrolyzed cobalt-N_4 macrocycle (CoTMPP) with VB12 at temperatures of 600 to 1000 °C for HER. They attributed the supreme activity to the molecular CoN_x active centers after acid leaching based upon structural analysis and SCN poisoning experiments. They excluded the effect of nanoparticles and nanocomposites on the HER activity.[48] Later, Wang et al. reported the preparation of a PANI-based cobalt catalyst at temperatures between 550 to 950 °C. The authors hypothesized a hybrid active site as the mixture of Co-4C and Co-4N optimizing the hydrogen adsorption energy for a PANI-based Co- N-C catalyst. Their proposition was based on calculated density of states of possible active sites (N-C, Co-4C and Co-4N) and profound X-ray Adsorption Spectroscopy (XAS) as a function of preparation temperature.[45] Maruyama et al. investigated the pyrolysis (800 to 1000 °C) of CoPc supported on Ketjenblack (KB). Based on their results derived from ex-situ XAS experiments, they found the correlation between HER activity and the density of CoN_4.[47]

In a work by Fei et al., the graphene oxide and cobalt salt was mixed and subjected to the heat treatment at 750 °C under NH_3 atmosphere. In this work, the stability and activity of the Co- NG catalyst for HER was attributed to the high temperature-induced strong coordination between cobalt and nitrogen. Their claim was made by insightful characterization and variation study of Co- and N-doping level onto graphene with a controlled synthesis procedure.[49] Zhang et al. prepared a Co-N-C catalyst using cobalt salt, PANI and Ketjenblack which were subjected to a heat treatment at a temperature of 900 °C. Based on the DFT calculation, Zhang et al. investigated the role of transition metal and nitrogen in Co-N-C catalyst for HER. Thus, CoN_x moieties were reported as the main active sites regarding the enhanced hydrogen adsorption energy.[55] Also, Deng et al. studied an active N- and S-doped Co-based catalyst toward HER prepared at 900 °C using cobalt salt and PABS. In this work, the cobalt complexes (Co in a combined coordination with N and S) were identified as the active centers based on structural characterizations in comparison with samples prepared with controlled synthesis.[60]

Up to now, there are not many deep investigations concerning active site identification of Me- N-C catalysts for HER, unlike those for ORR. Therefore, more systematic studies combined with theoretical calculations seemed to be required to propose and confirm the active center more adequately.

2.1.4 Preparation and structural changes

- **The role of the metal**

In Me-N-C preparation, variation of the precursors and preparation conditions might help to rationally design an electrocatalyst with various catalytic active centers, tuned structure and morphology. Several studies have been carried out regarding the precursors choice for ORR in the last decade. For instance, Kramm et al., studied Fe-N-C catalysts synthesized with a different nitrogen sources, such as phenanthroline, polyaniline and iron porphyrin and studied the formation of active sites and their correlation with ORR activity. [24] Gupta et al., studied the Fe-N-C morphology changes by variation of nitrogen and carbon sources (MLMN, DCDA and PANI). They claimed that using a combination of DCDA and PANI would favor the higher active site formation, higher active surface area and improve carbonization process.[73] However, a small number of comprehensive studies has been made in order to elucidate the role of precursors and pyrolysis conditions on HER, although it could be adapted from the structure-correlation reported in ORR studies.

Morozan et al. investigated the role of transition metals prepared with Zeolitic Imidazolate Framework (ZIF-8), 10-phenanthroline and metal salt imposed to heat treatment at 1050 °C.[54] The hydrogen evolution was observed more facile in acidic than alkaline media (which is known also for Pt), although transition metals are known to be less stable under acidic condition. The HER activity was investigated and reported in the following order Co > Cr > Zn > W > Ni > Cu, Mo, Mn, Fe for H_2SO_4 solution (PH 1) and Co, Ni, Fe > W > Mo > Cr > Mn, Zn, Cu for KOH solution (PH 13). The relatively high pyrolysis temperature resulted in the formation of metal carbides and metal nanoparticles in these types of catalysts. Indeed, similar activity trends were observed for the reported Me-N-C catalysts in different studies.[48, 60] Although the effect of metal species on the surface area and carbon morphology was discussed in these works, no systematic correlation of structure and activity as a function of metal nature was reported. Furthermore, several other studies reported the Co-based catalyst as the most active and stable electrocatalyst among nitrogen- and metal-doped carbon-based catalysts for hydrogen evolution.[52, 55] Besides, the metal loading in the precursor mixture is a key parameter to optimize the catalysts structure. In a work by Maruyama et al., the variation of CoPc loading supported on KB was investigated. The weight ratios of 0.25, 0.5, 1, 2 and 4 was chosen for CoPc:KB at a pyrolysis temperature of 800 °C. It was found that an increase in CoPc loading resulted in an increase in nitrogen and metal content in the final catalyst and a decrease in the BET surface area. Therefore, lower HER activity was found for extreme low and high cobalt loadings.[47]

Indeed, it was formerly shown that combination of transition metals (most reported, combination of cobalt with other metals) provides noteworthy enhancement for the HER activity considering the synergistic effect between two metals and the substrate.[68, 74, 75]. Jirkovsky et al. investigated a bimetallic Co-Mo-S_X chalcogel with excellent activity and stability toward HER in alkaline and acidic media, where the CoS_x was reported as the active site and MoS_x as the stabilization agent in the structure.[68] Deng et al, synthesized a FeCo@NCNT catalyst through the CVD method showing a promoted HER activity compared to monometallic Fe@NCNT and Co@NCNT samples.[50] Chen et al. presented the NiMo nitride nanosheets supported on carbon, where the presence of nickel tunes the Mo-H binding strength facilitating the hydrogen production confirmed by XAS measurements and DFT calculation.[76]

- **The role of heteroatoms**

The doping of heteroatoms into carbon matrix was found to be an effective way to promote the catalytic activity of NPMC materials. Nonmetal atoms, such as N, B, S, P or multiple doping (N/S and N/P) are the most reported effective optimization techniques to control the structure and improve catalytic activity.[60, 77-79] Non-metal heteroatom dopants can enhance the π bonding of the carbon matrix because of its single pair of electrons and different electronegativity in comparison to carbon. In addition, the metal particles can interact with dopants (N, S) and form new types of active sites (MeS_x, MeN_x).[79, 80]

Reported by Li et al., doping CNT with nitrogen improved the MoS_X nanoparticles formation resulting in a higher HER activity. It was shown that N-dopant at the carbon surface interacted with anionic precursors enhancing the structure of the active sites by the formation of dense nanoscale MoS_x layers.[61] Later, Ito et al. showed that co-doping of graphene with nitrogen and sulfur provides a synergistic effect by tuning the hydrogen adsorption on the carbon lattice.[78] In a work by Deng et al, the role of heteroatom doping (N, S) on HER activity was investigated using controlled synthesis routes.[60] The authors used combination of polymerized aniline (PANI) and polymerized aminobenzenesulfonic (PABS) to maintain the dual nitrogen and sulfur doping. They claimed that the obtained catalyst containing a new active site (S-Co-N complex) which is more active than catalysts prepared with individual PANI (containing Co-N complex) and PABS (containing Co-S complex) toward HER. Li et al. prepared Co, CoP, CoS and CoPS nanoparticles embedded in N-doped carbon matrix by heat treatment (600 °C) of ZIF-67 with none, P, S and combination of P and S doping, respectively.[81] It was shown that the electrochemical activity is improved once P and/or S are incorporated with cobalt.

Furthermore, introducing new active sites has been recommended via changing the precursors. MeS_4 sites (analogous to MeN_4) embedded in carbon matrix are reported to be an active electrocatalyst.[55, 82] Therefore, design and introduction of MeS_x complexes by choosing appropriate precursors provide enough active and stable centers to facilitate the catalytic reaction. Gu et al. replaced the N_4– with S_4-chelate complex and used graphene oxide as a carbon support to synthesize a cobalt-based catalyst.[83] Thus, it was shown that CoS_x complexes can be formed with traditional synthesis route and varying the precursors in the case of Me-N/S-C.

2.2 Oxygen Evolution Reaction (OER)

2.2.1 Mechanistic understanding of OER

The electrolyzer performance is determined by the anodic exchange production via oxygen evolution reaction (OER) as the main contributor to the overall overpotential. OER is a four proton-electron transfer process, which is much more complicated than HER. The possible elemental reaction steps for the OER (alkaline) on a single metal active site are shown in steps 1-4.

$$M + OH^- \overset{\Delta G_1}{\longleftrightarrow} M - OH_{ads} + e^- \quad (1)$$

$$M - OH_{ads} + OH^- \overset{\Delta G_2}{\longleftrightarrow} M - O_{ads} + H_2O + e^- \quad (2)$$

$$M - O_{ads} + OH^- \overset{\Delta G_3}{\longleftrightarrow} M - OOH_{ads} + e^- \quad (3)$$

$$M - OOH_{ads} + OH^- \overset{\Delta G_4}{\longleftrightarrow} M + H_2O + O_2 \uparrow + e^- \quad (4)$$

Each step involves one electron transfer with a different surface intermediate, where ΔG_i is the Gibbs free reaction energy of the step *i*. The overall reaction rate is described as a function of Gibbs free energy of reaction steps involving the adsorption of different intermediates. Hence, this relation is depending on the nature of the material used as catalyst. It is important to fundamentally study the reaction mechanism occurring on different materials. Beside noble metal state-of-the-art catalysts based on noble metals (Ru, Ir oxides), non-precious metal oxides, perovskites and carbon-based materials received a considerable amount of attention during the last decades for the application in alkaline media.[84-88]

Recently, numerous investigations have been performed studying the OER mechanism based on the link between thermodynamic and DFT calculations.[11] Rossmeisl et al. calculated the Gibbs free adsorption energies of each intermediate as a function of the electrode potential using density functional theory.[89, 90] Therefore, the reaction energy for each individual step (1-4) was determined by subtraction of the respective adsorption energies. Depicted in Figure 2.2, the blue line shows the so-called ideal catalyst situation in which $\Delta G_1 = \Delta G_2 = \Delta G_3 = \Delta G_4 = 1.23$ eV.[11] In contrast to the ideal case, the trace in a real catalyst is $\Delta G_4 < \Delta G_1 = \Delta G_2 < \Delta G_3$ and the overall thermodynamic of the reaction would be governed by the most unfavorable step (maximum Gibbs free energy).

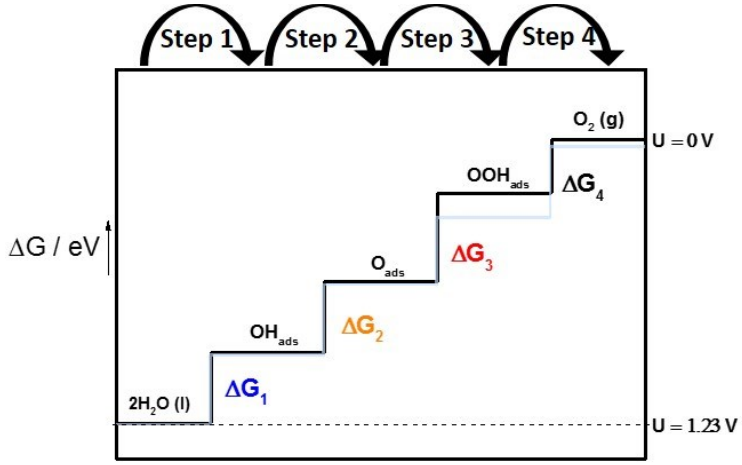

Figure 2.2 Schematic representation of the Gibbs free energy of the reactive species and intermediates in OER versus reaction coordinate

2.2.2 Scaling relation

It was described in section 2.1 that if j_0 is plotted as an activity descriptor versus the intermediate adsorption energy (H^+) in the corresponding catalytic reaction, a volcano-shaped plot appears for HER. Similar plots can be obtained for OER considering different intermediates and their binding energies, in the reaction steps 1-4. Calculation of binding energies is feasible via density functional theory (DFT) and was used as a descriptor in numerous studies related to metal- and metal oxide-based materials.[89-91] Therefore, OER activity was plotted versus the oxygen adsorption free energy ΔG_{O^*} or (ΔG_{OOH^*} - ΔG_{OH^*}), appearing as a volcano-shaped plot.[85,87]

In a thermochemical description of OER, it is required to modify the adsorption energy of intermediates in order to optimize the overall reaction thermodynamic. However, Rossmeisl et al. presented that the independent change of a single step intermediate is not feasible since the chemisorption energy of the individual intermediates are linearly related.[89, 90] The so-called scaling relations were reported independent of the investigated catalyst type, for the binding energies of HO^* and HOO^* (about 3.2 eV instead of 2.46 V) for metal oxides and oxide surfaces regardless of binding sites.[92]

However, Man et al. reported that the OER activity could not be improved simply by tuning the binding energy of intermediates using theoretical calculations due to fundamental limitations imposed by this scaling relation. The author suggested the stabilization of intermediates to improve the OER catalytic performance. [92]

In agreement with previous reports considering oxide surfaces, it was reported by Calle-Vallejo et al. that the similar scaling relations (ΔG_{OOH^*} - ΔG_{OH^*} = 3.1 eV) can be applied for Me-N-C catalysts.[93]

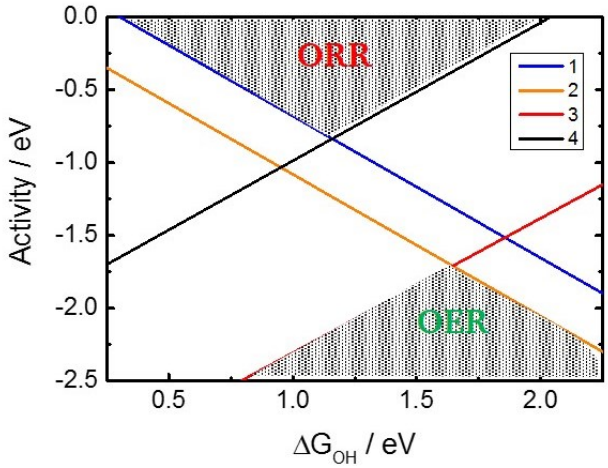

Figure 2.3 Combined volcano plot for ORR and OER.[93] (1-4) are corresponded to Gibbs free energy of each step in Figure 2.2

Generally speaking, OER and ORR can be regarded as two inverted sequences of the same four electron transfer steps with the same intermediates. In the work by Calle-Vallejo et al., the limitation imposed by the scaling relation for different Me-N-C type catalysts (metals belonged on the group 6 to 11 within periodic table) were explored in order to design active ORR and OER catalysts. The catalyst with transition metals belonging to group 7 to 9 were reported as active material toward ORR and OER, however, the scaling relation between HO* and HOO* imposed a limitation leading to a double volcano with a forbidden region separating the two tops of the volcano (Figure 2.3). This double volcano confirmed Fe as the best metal for ORR catalysis and found an optimal situation for Co with respect to OER.

More recently, Busch et al. investigated the scaling limitation using DFT calculation for Me-N-C catalysts (Me: Co, Fe, Mn) to design bifunctional catalysts. The author suggested introducing a hydrogen acceptor/donor ligand in the vicinity of the active site in order to design a catalyst falling into the forbidden region. It was claimed that MnN_4 embedded in graphene is the most promising catalyst toward ORR based on the theoretical calculations.[94] However, the volcano plots and scaling relations do not provide enough clarifications to rationally design new catalysts with improved activity, although they present qualitative information regarding the relation between catalytic activity and reaction intermediate bond strength.

2.2.3 Active site determination controversy

The carbon-based materials are known to be more stable in alkaline media considering the harsh conditions in which OER takes place. Therefore, this study is restricted to alkaline media for OER applications. Nonmetal- and metal-heteroatom doping enhances the OER activity of carbon-based materials, as it was described in the case of HER.[41] Recently, several studies have reported Me-N-C (Me: Fe, Co) materials as promising bifunctional catalysts toward ORR and OER in alkaline media.[95-98] Despite some profound investigations of the active site on Me-N-C related to ORR, the role of transition metals and nonmetal-doping on OER activity is still not well-known. In the following, the identified sites which were mainly reported in literature are discussed based on Table 5.

Table 5 summary of the preparation of heteroatom doped carbon-based catalysts reported for OER

Precursors	***U_{over} / mV**	**Condition**	**Formed Species**	**Ref.**
	PH13			
$FeCl_3$,KSCN,CNT, Bipyridine (D)	370	HT1[900,2h,Ar]	**FeN_x**, FeC_x, FeS_x	[99]
CoPc/$CoCl_2$, CNT (Me loading), (D)	310	HT1[900,2h,Ar] AL	Co-np,**CoN_x**	[100]
$MeCl_2$(**Co**,Fe,Ni), Cyanamid (Me type), (T)	390	HT1[(700-900),2h,Ar] AL	**Co-np**,CoN_x, C-N	[101]
ZIF-67@ZIF-8 (T)	312	HT1[(900-1100),6h,Ar]	**Co-np**	[102]
$Co(NO_3)_2$, MLMN	260	HT1[600,1h,N_2 + 800,1h,N_2]	**CoO_x**, Co-np	[64]
$CoCl_2$, Bacterial cellulose, Urea, Thiourea (D)	320	HT1[600,1h,N_2+900,1h,N_2]	**CoO**, Co_3O_4	[103]
ZIF-67	370	HT1[600,5h,Ar]	Co-np,CoN_x	[57]
$Co(NO_3)_2$/CoS_2, GO /CNT, Thiourea (D)	390	HT1[400,2h,Ar]	CoS_2	[104]
$Co(NO_3)_2$, Na_2S, (GO,C_3N_4)/(Go,PANI) (Carbon source)	350	HT1[550,3h,N_2]	Co_9S_8, C-N,C-S	[105]
Co Ac., Phen, GO, S (D)	371	HT[750, 30min, Ar] ±AL	CoS_x, CoN_x, C-N, C-S	[106]
ZIF-67 (pyrolysis environment)	410	HT1[800,2h,He:H2(10%)] HT2[250,(2h,6h),He:O2(15%)]	Co-np, Co_3O_4, CoN_x	[107]
Fe/**$Co(NO_3)$**, MLMN, KB (Me type)	460	HT1[700,1.5h,NH_3]	CoN_x, C-N	[95]

*Overpotentials are reported @ 10 mA cm^{-2} for cobalt-based synthesis (T): temperature variation, (D): Heteroatom doping variation

Can MeN_x satisfy OER?

MeN_x moieties are known to be catalytically active toward ORR and HER as it was discussed in the previous chapter. However, there are not enough available studies investigating the MeN_x moieties as a possible active center for OER. In fact, it is under strong debate whether metal complexes (MeN_4) are participating in the reaction directly, or they are unstable in the OER potential window and transformed into metal oxides.[108, 109] However, because of limitation in characterization techniques, there are not enough reliable reports considering identification of active sites and the role of metal complexes. Recently, Daniel et al. reported the decomposition of (non-pyrolyzed) cobalt porphyrin deposited on FTO into CoO_x species under OER conditions. The author attributed the activity to the formed CoO_x species deposited on FTO as the real catalyst, confirmed with soft-X-ray photoelectron spectroscopy. [109]

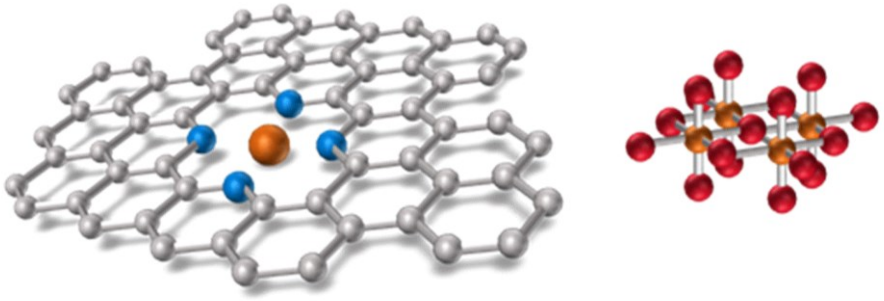

Figure 2.4 MeN4 sites Vs. MeOx

In contradiction with this work, Wang et al. studied cationic cobalt porphyrin catalyzing water oxidation and excluded the cobalt oxide film formation under OER condition as active site. The authors demonstrated formation of Co^{4+}-porphyrin cation radical as the active site for oxygen evolution reaction.[110] Later, Wunster et al. prepared monolayers of various metalloporphyrins on clean Au (1 1 1) surface and investigated these under OER conditions. The author claimed that the Co^{2+} species attributed to MeN_4 species remained intact during OER as the main active sites, confirmed by post-mortem analysis (XPS, STM).[111]

Indeed, Me-N-Cs were studied mostly as bifunctional catalysts with dual active sites for OER and ORR in alkaline media. Repeatedly, Co-N-C and Fe-N-C catalysts are reported as active bifunctional catalysts. In these works, the OER activity was mainly attributed to the nitrogen-containing species (N-C) while the ORR activity was credited to the MeN_X moieties.[31, 97, 112] More Recently, Chen et al. presented an active bifunctional Fe-N-C catalyst by doping CNT with pyridine and Fe salt, followed by pyrolysis at 900 °C for alkaline media. The authors claimed that high-density FeN_x moieties are dispersed in hierarchical carbon layers which are responsible for the high OER activity.[99]

Because of the complex structure of Me-N-C catalysts consisting of different possible active sites, often a combination of synergistic effect and hybrid active sites has been proposed responsible for OER activity.[53, 106, 107] For instance, Qiao et al. pyrolyzed graphene oxide with cobalt acetate, phenanthroline and sulfur in order to embed CoS_x nanoparticles in N-, S-doped graphene sheet. In this work, CoS_x particles, nitrogen and sulfur dopant, and CoN_x sites are nominated as possible active sites for the bifunctional activity of CoS_x/N-S-G catalyst.[106] Nevertheless, a more detailed intensive investigation is required exploring the real OER active sites using in-situ experiments and post-mortem analysis in order to drive structure-activity correlations for Me-N-C catalysts with dominant MeN_x moieties.

- **Metal Nanoparticles/Nanocomposites (Me / MeO_x/$MeO_x(OH)_y$ @ carbon)**

As explained in the HER section, encapsulation of metallic nanoparticles or metal compounds (specifically metal oxides) into carbon plane/tube offers several advantages. It enhances the mechanical and chemical stability, electronic conductivity and graphitization degree of the material.[41] Liu et al. prepared a Co-N-C catalyst using metal salt and cyanimide subjected to a heat treatment at temperatures of 700 to 900 °C as bifunctional catalysts activating ORR and OER. The catalyst contained encapsulated cobalt nanoparticles in carbon nanotubes and MeN_x species. The author suggested the cobalt nanoparticles as a promotor for the formation of CNTs where the stable catalytic reaction proceeds.[101]

Li et al. reported the formation of cobalt nanoparticles embedded on carbon skelton with pyrolysis of core-shell MOF (ZIF-67) at a temperature of 600 °C for 5 hours. The authors identified the in-situ transformation of cobalt particles to CoO_x species during OER using profound post-mortem analysis (TEM, XPS and XRD). Indeed, the author claimed that the oxidized cobalt centers can be active sites implemented in carbon plane.[57] Later, Zhao et al. synthesized encapsulated cobalt nanoparticles in carbon nanotube derived from ZIF-67 at 1000° C active toward OER. The authors confirmed the established CoO_x particles from cobalt nanoparticles during the OER as the real active sites for OER.[102]

In the work by Jin et al., a highly active Co-CoO_x/N-doped carbon-based catalyst was prepared composed of a hybrid structure including cobalt nanoparticles, CoO and Co_3O_4 nanocomposites. By post-mortem XPS analysis of the catalysts, it was claimed that the Co^{2+} species corresponded to CoO are the main contributor to the OER activity.[64]

Moreover, it has been reported that metal oxy/hydroxide materials exhibit remarkable activity toward OER in alkaline media.[86] Among all, Ni/Co-based composites are reported as the most active OER catalysts. Weidler et al. studied various cobalt oxide films under OER condition and reported the in-situ transition of oxides to oxy/hydroxide materials as the origin of activity.

The authors claimed that the deposition of a hydroxide like $MeO_x(OH)_2$ presents an optimum initial state for the aforementioned transition.[113, 114] Recently, more efforts have been made to implement the oxy/hydroxide particles (active sites) into nitrogen-doped carbon in order to enhance the catalytic performance.[115, 116]

- **MeS_x in hybrid carbon structures (MeS_x @ carbon)**

Cobalt sulfides (CoS_x) are known to be active toward oxygen evolution reaction based on theoretical and experimental reports.[117, 118]However, their application is restricted due to the poor electronic conductivity.[106] Therefore, implementation of the MeS_x compounds on a carbon support was suggested as a solution. [119]Ganesan et al. presented an approach to synthesize cobalt sulfide nanoparticles on the N-doped graphene oxide using cobalt thiourea at temperatures between 400 to 600 °C. Depending on the pyrolysis temperature, CoS_2 or Co_9S_8 were reported as the major phase existing in the composite.[120] Later, Tang et al. reported a simple ionic assembly to fabricate Co_9S_8 embedded in N/S-doped graphene sheet at a temperature of 550 °C.[105] Wang et al. presented a novel Co_3S_4/NCNT active catalyst by the first formation of $Co(OH)_2$/NCNT and subsequent anion exchange of S^{2-} and OH^-. [121]
Heretofore, the metal sulfide compounds were reported as the main contributor to the OER activity, though the synergistic effect between nitrogen, sulfur and carbon is not negligible.

2.2.4 Preparation and structural changes

In order to rationally design Me-N-C catalysts applicable for oxygen evolution reaction, it is required to understand the parameters affecting the structure, morphology and stability of the materials as-prepared and under OER conditions. In the next step, newly suggested methods must be applied to optimize further the present catalysts inspired by the achieved knowledge.

- **Carbon properties**

It is well known that carbon corrosion starts thermodynamically above the potential of 0.207 V and increases to a significant level at 1.23 V where OER takes place. As it was reported by Choi et al. the destruction of MeN_x is inevitable at potentials over 0.9 V because of carbon oxidation in Me-N-C catalysts. [122] The importance of contribution of carbon oxidation during OER is often neglected in the case of carbon-based materials. [123] Therefore, using highly graphitized nanocarbons and encapsulation of MeN_x sites in carbon nanotubes are strongly recommended in order to improve the catalyst stability under harsh OER condition.[124] Polymerized aniline (PANI) with a unique π −conjugated configuration was used firstly for deposition on carbon support to protect commercial Pt/C catalyst against corrosion for fuel cell application.[125]

Later, Zhang et al. demonstrated a highly porous PANI-based nanocarbon co-doped with nitrogen and phosphorous as a promising active catalyst toward OER. Thereof, the carbon structure made by pyrolysis of doped-PANI provides a high surface area, strong accommodation of active sites and high resistivity against carbon corrosion.[112] Indeed, combining PANI with another carbon source as a multi-precursors synthesis route can further tune the catalyst morphology promoting the carbon stability under OER condition.[73] However, Tang et al. prepared Co_9S_8 nanoparticles supported on (GO, C_3N_4) and (GO, PANI) at a temperature of 550 °C. It was claimed that the smaller number of active nanoparticles were accommodated on carbon substrate in the case of (GO,PANI) compared with (GO, C_3N_4).[105]

Carbon Nanotubes (CNT) have been widely used as catalysts of energy-relevant electrochemical reactions due to their high electronic conductivity and oxidative corrosion resistance.[126] Therefore, encapsulation of MeN_x moieties inside the CNTs can prohibit the active site destruction because of high resistive carbon structure and simultaneously provide facile charge transfer. In the work of Byon et al., formation of this type of active site (FeN_x) by nitrogen functionalizing of MWCNT was presented using heat treatment of precursor in a N-rich atmosphere. The author later showed that the catalyst prepared with MWCNTs is more active and stable than the PANI-based one toward ORR.[127] Therefore, fundamental understanding of the role of carbon in an atomic level is important to design an optimal and robust Me-N-C catalyst activating OER.

- **Multiple-heteroatom doping**

It is often reported that multiple-heteroatom doping is likely to create more active sites, enhance charge transfer and consequently improve OER activity.[105, 124] Among non-metal heteroatoms, dual N/S doping into carbon have been employed most. Although metal-free N/S-doped carbon-based materials were reported as active OER catalysts, embedding transition metals into co-doped carbon seems vital improving the catalytic performance.

For instance, in a work by Sahraie et al., it has been shown that multi-heteroatom doping (N/S/Fe) significantly enhances the stability of Ketjenblack considering carbon corrosion and CO_2 formation. The conclusion was drawn mainly by differential electrochemical mass spectrometry.[96] Qiao et al. studied systematically the multiple-doping effect by characterization of pure, (N/S)- and (N/S/Co) graphene as a bifunctional catalyst (ORR and OER) in alkaline media.[106] It was shown that nitrogen and sulfur were successfully doped into graphene sheets in interaction with both metal and carbon. The main conclusion was that a high density of active sites was introduced and enabled to contribute to catalytic activity, and

the dual doping of N and S onto graphene enhanced the graphitization and porosity of the carbon. In a work by Chen et al., KSCN was added to the synthesis to dope sulfur into N- and Fe-doped CNT. it was shown that sulfur doping can improve the surface area, increase the active site density (FeN_x moieties) and facilitate charge transfer capacity for Fe-N-C catalysts.[99]

Furthermore, it has been reported that the catalytic activity of transition metal-based catalysts is tunable via introducing the second metal through the synthesis by overcoming the limitation imposed by scaling relation. Oxide/hydroxide of Ni-based alloys and encapsulated Co-based alloys in carbon nanotube exhibits remarkable activity toward OER with improved stability compared to their monometallic counterparts.[128-130] Nevertheless, double heterobimetallic doping has not been widely investigated in Me-N-C catalysts for OER, unlike ORR and HER. In a work reported by Wunster et al., the dual combination of Fe-based and Co-based metal sources (metalloporphyrins) was investigated, when the catalyst was deposited on a gold substrate prepared in UHV.[111] After spectroscopic and microscopic characterizations, it was reported that the first metal was coordinated at porphyrin-like center of the molecule and the second metal was positioned by four pyridyl groups between the molecules, both with an oxidation state of Me^{2+}. Despite demonstrating successful implementation of the second metal in the complex and boosted activity, no structural-activity correlation was found out to explain the effect of second metal on the promoted activity. Therefore, a comprehensive investigation of dual- doping of transition metal in traditional preparation of Me-N-C catalysts is required in order to elucidate the role of the second metal on the structure and OER activity.

3 Experimental

This chapter addresses the experimental methods used in this thesis. It includes the preparation of the catalysts, material characterization and post-mortem techniques.

3.1 Catalyst preparation

In this thesis, two main approaches were applied to synthesize Me-N-C catalysts. One is the MOF-based which will be discussed first, followed by the PANI-based approach.

3.1.1 MOF approach

Metal Organic Frameworks (MOF) include a metal ion coordinated with organic ligands that can be decomposed to a carbon network through pyrolysis. MOF-based preparation route has been adapted by the work of Proietti et al. who reported one of the most active Fe-N-C catalyst toward ORR prepared with MOF.[131] Our study aimed to investigate the role of transition metal in the structure and catalytic activity of Me-N-Cs. Accordingly, MOF (Z1200, 2.0 mmol), Phenanthroline (Phen, 1.5 mmol) and various metal acetates (0.25 mmol) were used to synthesize Me-N-C catalysts. The prepared monometallic catalysts were based upon Fe, Co, Ni, Mn, Mo, Cu metals. Also, a combination of cobalt with iron, manganese and molybdenum with the molar ratio of 1:1 was probed in order to prepare the bimetallic catalysts. The given precursors contained 2 wt% of the corresponding metal(s) and about 16 wt% Zn from ZIF-8 (Z1200). The temperature of 950 °C was chosen because zinc should evaporate at this temperature and should result in a pure carbon network.

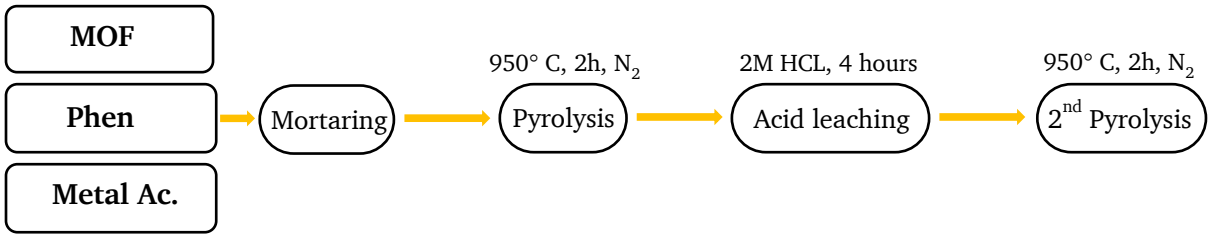

Figure 3.1 Preparation procedure of MOF-based catalysts

The final mixed powder of the precursors was subjected to a heat treatment at 950 °C with a heating rate of 450 °C/h under nitrogen atmosphere for 2 hours. The remaining powder was cooled down to room temperature and transferred to the solution of 2 M HCl and kept 4 hours for the acid leaching step. The catalysts were obtained and grounded for further characterization after second heat treatment (similar to first heat treatment).

3.1.2 PANI approach

Polymerized aniline (PANI) is well-known template compound in which aromatic benzene rings are connected through NH_2 groups. PANI provides remarkable stability, mechanical flexibility and great accommodation of active sites if it is used for the preparation of Me-N-Cs.[73] In this work, we used two different methods to synthesize PANI based on the choice of APS:ANI ratio and post-treatment method.

- **$PANI_{ref}$ synthesis**

Aniline (20mmol) was blended with ammonium peroxidisulfate (APS, 20mmol) in 0.5M HCl for polymerization at the temperature below 4 °C. The polymerization proceeded for 24 hours. Then, the suspension was filtered and washed with distilled water to remove APS residuals. This PANI was prepared in order to synthesize the catalysts with absence of sulfur in the precursors. This preparation is known to be the standard method for polymerization of aniline which is often reported in literature related to Me-N-Cs.[132] Therefore the label $PANI_{ref}$ was assigned to address the reference PANI for the sake of comparison.

- **$PANI_{evap}$ synthesis**

Aniline (20mmol) was blended with ammonium peroxidisulfate (APS, 60mmol) in 0.5M HCl for polymerization at the temperature below 4 °C. The polymerization proceeded for 24 hours. Then, the suspension was evaporated by heating at 100 °C to remove the HCl solution and keep the APS residuals (not reacted during polymerization because of high APS to ANI ratio 3:1) inside the PANI. The $PANI_{evap}$ was synthesized to achieve co-doping of nitrogen and sulfur in Co-N-C catalyst. The combination PANI and dicyandiamide (DCDA) was suggested by Gupta

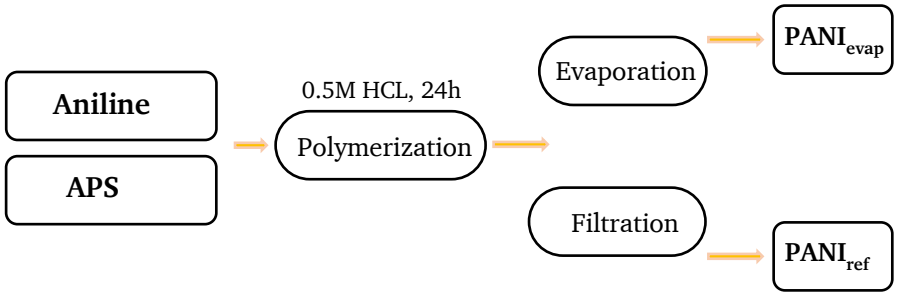

Figure 3.2 Illustration of Aniline Polymerization

et al. who showed that the combination offers a tuned morphology and higher active site density. [73] The Co-N-C catalysts were synthesized using cobalt acetate (variable), PANI ($PANI_{evap}$/$PANI_{ref}$, 680 mg), DCDA (27 mmol) and elemental sulfur (variable).

In the first project (Chapter 4.1.2), the cobalt catalysts were prepared with different metal loadings (0-20 wt%). The label Co_x-N-$C_{evap/ref}$ was used for naming the catalysts where x is the cobalt wt% in the precursors and evap/ref index has attributed the type of PANI used in the

synthesis. Beside this, a bimetallic catalyst of $(Co,Mn)_2$-N-C_{evap} was prepared with Co/Mn molar ration of 2:1. The second project (Chapter 4.2.1) was related to the effect of elemental sulfur addition to the PANI-based Co-N-C_{evap} catalysts. Therefore, the elemental sulfur was introduced to Co_3-N-C_{evap} with variation of (additional of elemental sulfur, 0 to 11 mmol). The catalysts were investigated for OER. Finally, the third project (Chapter 4.2.2) was related to $PANI_{evap}$-based catalysts with focus on the influence of the species on OER activity and stability. Therefore the most active Co-N-C was compared to its (Co,Mn) analogy. The molar ratio of Co/Mn ~ 2:1 was maintained to synthesize the bimetallic catalyst used in this project.

Figure 3.3 demonstrates the synthesis route applied in these projects. The corresponding

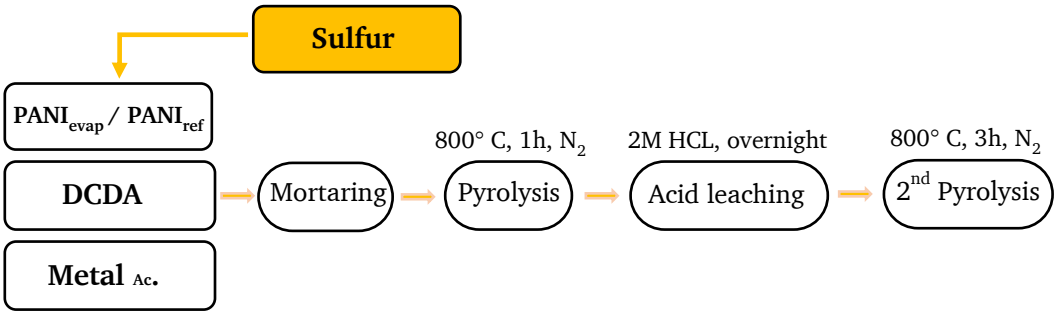

Figure 3.3 The PANI approach illustration

mixture was first subjected to heat treatment step at 800 °C with a heating ramp of 300 °C/h. This heat treatment involved 30 min dwelling at 300 °C and 500 °C followed with 60 min dwelling at 800 °C. After cooling down to room temperature, the powder was transferred to 2M HCl solution and kept overnight for acid leaching process. The obtained catalyst was filtered, dried and transferred to the oven for the second pyrolysis. The second heat treatment included a fast ramp (~38 °C/min) to 600 °C and a slower ramp of 300 °C/h to the final temperature of 800 °C where it was held for 3 hours. Table 6 provides information regarding the chemical compounds used for preparation methods in this project.

The contribution of Ioanna Martinaiou, K. Alexander Creutz and Simon T. Ranecky is gratefully acknowledged.

Table 6 List of chemical compounds used for MOF and PANI approach

Material	Chemical formula	Provider
Manganese acetate, 98%	$Mn(CH_3COO)_2$	Alfa Aesar
Molybdenum acetate dimer	$Mo_2(CH_3COO)_4$	Alfa Aesar
Copper acetate, 99%	$Cu(CH_3COO)_2$	Alfa Aesar
Iron acetate	$Fe(CH_3COO)_2$	Alfa Aesar
Nickle acetate tetrahydrate, 99%	$Ni(CH_3COO)_2 . 4H_2O$	Alfa Aesar
Cobalt acetate tetrahydrate, 99%	$Co(CH_3COO)_2 . 4H_2O$	Alfa Aesar
Basolite Z1200 (MOF)	$C_8H_{10}N_4Zn$	Sigma Aldrich
1.10 Phenanthroline (Phen)	$C_{12}H_8N_2$	Sigma Aldrich
Aniline	$C_6H_5NH_2$	Alfa Aesar
Ammonium peroxydisulfate (APS), 98%	$(NH_4)_2S_2O_8$	Alfa Aesar
Sulfur, 99%	S_8	Carl Roth
Dicyandiamide (DCDA)	$C_2H_4N_4$	Alfa Aesar

3.2 Characterization techniques

The catalysts were characterized electrochemically and with respect to their structural composition. For electrochemical characterization, mainly Cyclic Voltammetry (CV) and Rotating Disc Electrode (RDE) methods were applied. Surface and bulk techniques such as N_2-sorption, X-ray Photoelectron Spectroscopy (XPS), Raman Spectroscopy, Transmission Electron Microscopy (TEM) and X-ray Diffraction (XRD) were applied to study the structure and morphology of the catalysts. The detailed description of these techniques is reported in this chapter.

3.2.1 Electrochemical characterization

- **Electrode preparation**

In order to carry out the electrochemical characterization in this work, the drop-casting method was applied. Therefore, it was required to provide an optimized ink formulation to prepare an appropriate working electrode for RDE measurements. In this thesis, a fixed ink formulation was applied to all projects related to HER and OER. Thereof, 5 mg of well-grinned catalyst powder was mixed with 25 μl of Nafion (5wt%), 83 μl of distilled water and 142 μl of ethanol. The ink solution was sonicated for 15 minutes for homogenization. The homogenized

ink was vibrated in the vortex for 1 minute, then transferred for another 15 minutes sonication. The ultrasonic needle was used for 30 seconds for final dispersion of the catalyst in the ink. Depending on the project, the desired catalyst loading was maintained by dropping a corresponding amount of the ink on glassy carbon (GC, 0.1963 cm^2). The Ag/AgCl (3 M KCL) and Hg/HgO (1 M NaOH) were used as reference electrodes in acid and alkaline media, respectively. The glassy carbon was used as the counter electrode for all measurements.

- **Rotation Disc Electrode (RDE) setup**

The electrochemical measurement of the working electrode prepared with catalyst were performed using a three-electrode configuration shown in Figure 3.4. The working electrode a (glassy carbon disk coated with catalyst ink), reference electrode (Ag/AgCl or Hg/HgO) and counter electrode (glassy carbon rod) were connected to the potentiostat device (Nordic FC 200i). The potentiostat applies the potential between Working electrode (WE) and the reference electrode (Ref), while it measures the current between WE and counter electrode, simultaneously. The freshly made 0.1M H_2SO_4 and 0.1M KOH electrolyte solutions were used as acid and alkaline medias, respectively. Before running any measurement, the electrolyte was saturated with nitrogen for 5 minutes. During the measurement, the nitrogen gas flow was kept on the surface of the electrolyte. All the measurements were carried out at room temperature and ambient pressure.

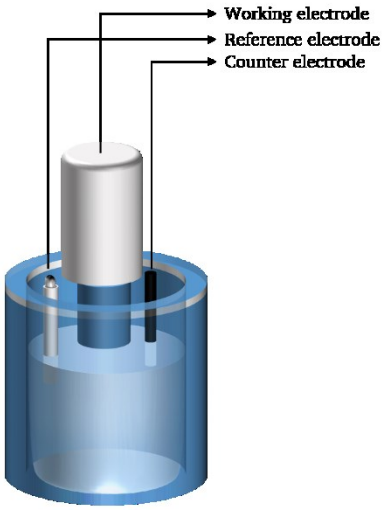

Figure 3.4 Schematic of standdard three elecrode configuration cell

A typical HER and OER measurement in this project involved a cyclic voltammetry (CV) with a sweep rate of 100 mV s^{-1} between 0 – 1 V vs. SHE. The initial activity was evaluated by performing a CV with a sweep rate of 5 mV s^{-1} in the corresponding potential window depending on the catalytic reaction (HER, OER). The short stability tests were performed by taking CVs

with a sweep rate of 300 mV s^{-1} for 90 and 30 cycles for HER and OER, respectively. The final activity was evaluated by a CV with a sweep rate of 5 mV s^{-1} in the corresponding potential window. The rotation rate was kept at 1500 rpm during the measurements to enable removal of the gas bubbles formed in the reaction. Long-term Galvano-static stability tests were performed at a constant current of 10 mA cm^{-2} for 6 hours.

- **Sequential correction for data analysis**

In this thesis, all the results are reported after corrections for ohmic losses (iR correction) and potential (U Vs. SHE) for the sake of comparison. During the measurement, the ohmic resistance was measured by EC4 software (Nordic application) which recorded the impedance spectra at 5 kHZ. Accordingly, the electrolyte resistivity was calculated and applied for iR correction. For reference potential correction, the reference electrode potential versus standard hydrogen electrode was measured before each experiment. The reported activity data are corresponded to the measured CV after short cycling. For CVs, the average of forward and backward scans was reported to normalize for the possible capacity effect.

The contribution of K. Alexander Creutz (RDE measurements) and Simon T. Ranecky (RDE measurements) is gratefully acknowledged.

3.2.2 Morphology and structure characterization

To investigate the morphology, surface and bulk properties of the materials several techniques were applied and reported in this work. Following, a short description of the methods and related experimental conditions are reported.

- **N_2-sorption**

Surface area and porosity are important parameters for heterogeneous catalysis. Gas adsorption (particularly nitrogen) is one the most common method used for investigation of surface area and porosity of carbon-based materials.

To carry out the N_2-sorption measurements a Quantachrome autosorb 3-B instrument was used. Before the sorption analysis, it is necessary to remove any gas and vapor that may have been adsorbed on the surface in contact with air. Therefore, the sample (known mass, *m*) was fed into a tube and heated to 200° C where it was held in vacuum of ca. 0.15 mbar for 12 hours for degassing process. Then, the tube was filled with a controlled flow of nitrogen. The nitrogen

adsorption on the surface leads to pressure reduction lower than the pressure of the reference cell connected to the setup.

The contribution of Ioanna Martinaiou, Stephen Paul and W. David Z. Wallace is gratefully acknowledged. [Measurement and data analysis]

Transmission Electron Microscopy (TEM)

This technique involves a high voltage electron beam emitted by a cathode through an ultra-thin specimen. The electron interacts with this specimen when it passes through. The transmitted electrons form an image containing information about the structure of the specimen. Then, the formed image is magnified by a series of lenses and can be recorded by focusing on a fluorescence or CCD camera (light sensitive camera, transferable to a computer).

In order to perform TEM experiments, a small amount of the sample was dispersed in ethanol by placing the solution in the sonication bath for 30 seconds. Then, the suspension was kept for settlement of the particles using a magnet, to remove the large magnetic particles. A drop was cast on holey carbon grid (Plano) and allowed to dry. The grid was coated with carbon (Baltec MED010) to avoid charging under the incident electron beam.

Transmission electron microscopy (TEM) characterization was performed with a FEI CM20STEM (Eindhoven, The Netherlands) microscope equipped with a LaB_6 cathode and a Gatan double tilt holder at a nominal acceleration voltage of 200 kV. EDS were recorded using an Oxford X-MAX 80 silicon drift detector (Oxford Instruments Nanoanalysis, High Wycombe, United Kingdom) attached to the CM20. Spectra were quantified using the internal Cliff-Lorime sensitivity factors from Oxford Instruments INCA Ver. 4.15.
The contribution of Markus Kübler and Stefan Lauterbach is gratefully acknowledged. [Measurement and data analysis]

- **X-ray Diffraction (XRD)**

XRD is widely used to study the crystal structures and atomic spacing. The X-rays are generated by a cathode ray tube and directed to bombard the sample. Due to the interaction of the incident beam with the sample, a diffracted ray is produced. Then, this diffracted beam is detected for analysis based on Bragg's law. For the MOF project, measurements were done in transmission with a STADIP (STOE & Cie GmbH, Darmstadt) diffractometer in Debye−Scherrer geometry with a position-sensitive detector using either Mo Kα1 radiation (λ = 0.70930 Å) [Ge(111)

monochromatic] or Cu Kα1 radiation (λ = 1.54056 Å). Samples were prepared on an acetate foil tape that gives low background intensity in the diffractograms. Patterns were collected three times with a step size of 0.5° and a collection time of 30 s step^{-1} and then overlaid three times with a step size of 0.5° and a collection time of 30 s step^{-1} and then overlaid.

For the PANI project, XRD measurements were performed using a Bruker D8 Advance in Bragg−Brentano geometry with Cu K_α radiation and a VANTEC detector. Data were recorded in an angular range between 5° and 50° (2θ) for a total measurement time of 1h using a step size of ~0.007°, a step time of 0.5 step s^{-1} and a fixed divergence slit of 0.3°.

The contribution of Stebastian klemenz, Stephanie Dolique and Mohammad Ali Nowroozi is gratefully acknowledged. [Measurement and data analysis]

- **Raman Spectroscopy**

Raman spectroscopy is a nondestructive technique which involves scattering of electromagnetic radiation by atoms or molecules. Thereof, vibrational, rotational and other low frequency modes of molecules are examined by interaction of the exposed light. During the experiment, the sample is illuminated by a monochromatic light source (e.g. laser). The electric field of the incident light can interact with the sample through the polarization of the molecule and results in molecular vibrations. Therefore, in the case of in elastic scattering, the energy lost or gained after interaction with the molecule can be detected from scattered light. The Raman spectra demonstrates the intensity of the light versus for each energy of incident light.

Raman spectroscopy has become a key technology particularly for the characterization of carbon-based materials. This technique offers detailed information regarding, carbon structural disorder, state of dispersion and orientation.[133] Moreover, the low-wave length analysis of the Raman spectra would provide useful information regarding the existence of transition metals composites (metal oxides/sulfides). Hence, this technique provides crucial information about multi-heteroatom doped carbon-based catalysts (Me-N-C) structure.

In this thesis, an alpha 300R confical Raman microscope from WiTec with a grid of 600 lines mm^{-1} was used. A laser with the power of 1 mW with excitation of 532.2 nm was applied to obtain the Raman spectra. The measurement range of spectra was from 0 to 4000 cm^{-1}. The spectra were obtained by overlapping 10 scans, and with an integration time of 10 seconds per scan. The measurements were repeated for at least 3 positions for each sample and an average of the spectra was reported.

The contribution of Ioanna Martinaiou [measurement and data analysis] and Ling mei Ni [measurement] is gratefully acknowledged.

- **X-ray Photoelectron Spectroscopy (XPS)**

Photoelectron spectroscopy (PES) is a surface-sensitive technique that irradiates a solid with photons and analyzes the energy of emitted electrons, based on the photoelectric effect. With respect to the photon energy range provided by the source, different experiments and analyses could be performed. Figure 3.5 illustrates different types of experiments involved in PES. In order to study the core level electron, the X-ray regime of 100 eV to > 1000 eV is required. Irradiation by an X-ray beam energy larger than the core level electron binding energy, results in escaping of the electron and emitting out of the surface.

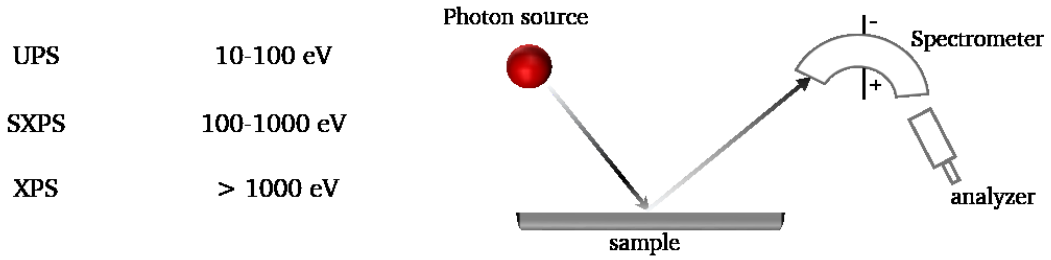

Figure 3.5 Sketch of PES experiments

Therefore, the emitted electrons have measured kinetic energy (E_k) given by:

$$E_k = hv - BE - \emptyset_s$$

Where hv is the incident photon energy, BE is the binding energy of the electrons (generally in solids referred to the Fermi level) and $\emptyset_s$ is the spectrometer work function. Figure 3.6 shows the energy-level diagram in a metal, where the Fermi level is higher than the valence band. This means that the photoelectron can be detected with kinetic energy (E_K) in the vacuum if the absorption is happening in the core level with binding energy of BE. It should be noted that the term $\emptyset_s$ related to the work function can be determined experimentally. In this way, the Fermi level of a clean metal surface would be measured and applied for future calibration. The emitted electrons are detected by an electron spectrometer, based upon their kinetic energy and sent to the analyzer. Thereof, scanning for different energies is obtained by applying a retardation potential (0 to > hv) before the analyzer. Then, the number of electrons for a given detection time and energy is counted and displayed as a function of the binding energy.

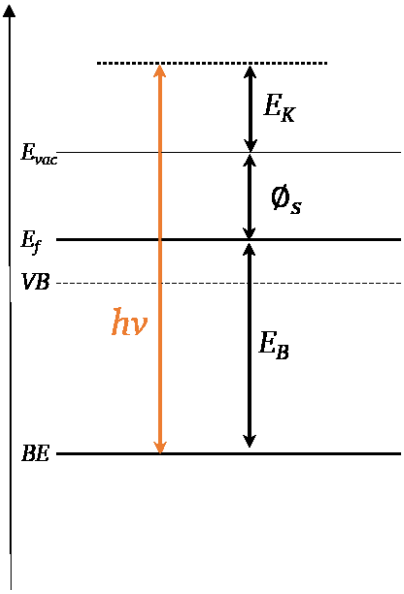

Figure 3.6 Schematic illustration of energy levels in a solid (metal) in the presence of incident photon

XPS is a popular technique to study the chemical and physical changes applied for heterogeneous catalysts in which the active sites are located on the surface. Particularly for Me-N-Cs with a complex structure, the surface analysis is remarkably informative in order to understand the elemental compositions, local environmental changes of an atom.

Me-N-Cs are the heat treated analogous to MeN_4 macrocycles in which it was reported that the N 1s region analysis provides more useful information regarding charge distribution than Me 2p region. In the previous studies, no change in the metal ion binding energy with small change in the charge distribution between the metal orbitals and macrocycle was detected. Hence N 1s binding energies are more sensitive to the local changes, since nitrogen is the link between ∂-bonding orbitals of metal-nitrogen and π-bonding orbitals of carbon-nitrogen.[38] Therefore, the N 1s analysis were used to study the local changes on metal atoms via Me-N binding energies in this thesis. The schematic illustration of suggested nitrogen coordination for Me-N-C catalysts are reported in Table 7. Moreover, an exemplary N 1s spectrum of Co-N-C (Cat. A chapter 4.2.1) is depicted in Figure 3.7.

Figure 3.7. It demonstrates different proposed nitrogen species present in Me-N-C catalysts.

Table 7 the model constrains for N 1s analysis used in this work adapted from Jaouen et al. [39]

N 1s	Pyridinic	Me-N	Pyrrolic	Graphitic	oxidized
No.	I	II	III	IV, V	VI
Binding energy	398 – 399.5	399 – 400.5	400.2 – 400.9	401 - 403	402 - 405
FWHM	1.1-1.3	1-1.1	1-1.1	G2 (1-1.1) G3 (1-2.5)	1-4

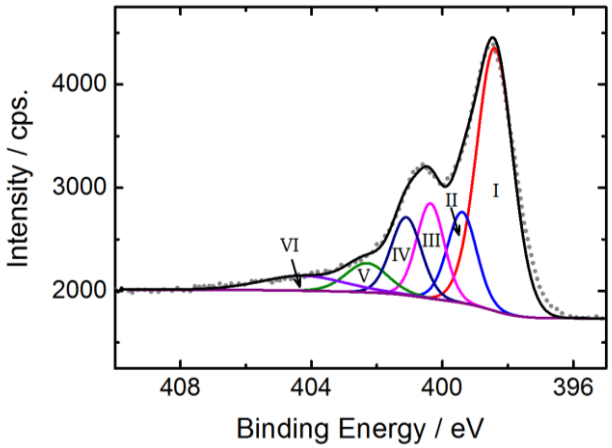

Figure 3.7 Examplary deconvolution of N 1s spectrum of Co-N-C catalyst with the suggested model

Moreover, the model constrains used for the analysis of O 1s and S 2p spectra with an exemplary plot (Cat. A chapter 4.2.1) are depicted in this part.

Table 8 The model constrains for O 1s analysis used in this work based on Lindberg et al. [134]

O 1s	Me-O	Me-OH	C-O	C=O / S=O
No.	I	II	III	IV
Binding energy	529.5-530.1	531-532	532-533	533-534
FWHM	1-1.2	1-1.2	1-1.2	1-2

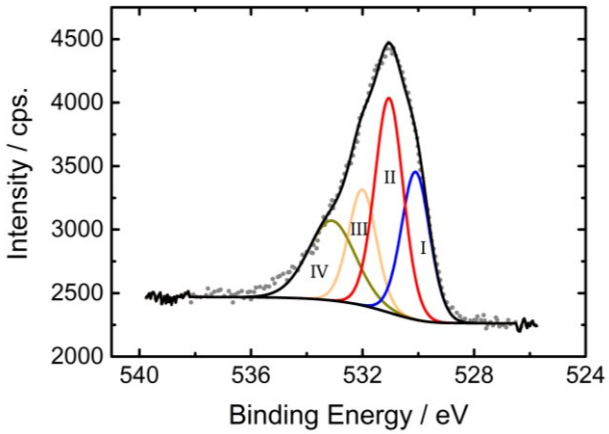

Figure 3.8 Examplary deconvolution of O 1s spectrum of Co-N-C catalyst with the suggested model

Table 9 The model constrains for O 1s analysis used in this work based on Biesinger and Alstrup et al. [135, 136]

S 2p Δ =1.18 eV	**MeS_x**	**S-C**	**S-O-C**	**S-O**
No.	**I**	**II**	**III**	**IV**
Binding energy	161.9-162.7	163.6-163.7	165.7-165.8	168.2-168.3
FWHM	1-1.2	1-1.2	1-1.2	1-2

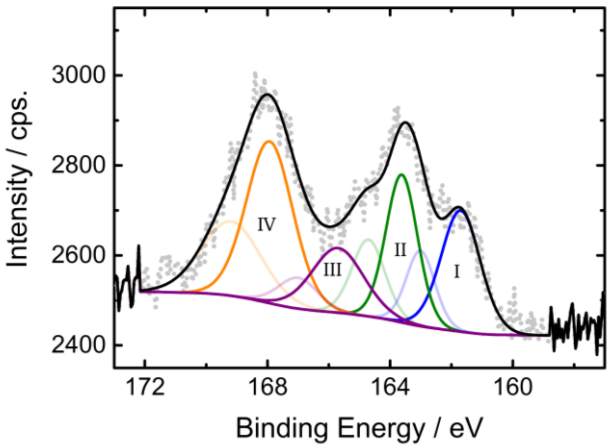

Figure 3.9 Examplary deconvolution of S 2p spectrum of Co-N-C catalyst with the suggested model

In this work, the measurements were performed with a Specs Phoibos 150 hemispherical analyzer and a Specs XR50M Al K_α X-ray source (E = 1486.7 eV) at Daisy Fun belonged to Prof. Jeagermann's group. For sample preparation, the catalyst powder was squeezed on an indium foil and mounted on the sample holder. For all the survey scans and the high-resolution scans, the energy step of 1 eV and 0.05 eV were applied, respectively. The software CasaXPS was used

in order to analyze the data. A Shirley background was used, and fits were made allowing for both Gaussian and Lorentzian (GL30) contributions to the peaks.

Table 10 XPS experimental parameters for MOF-project

region	Survey	C 1s	N 1s	O 1s	Me 2p	Zn 2p
No. scans	2	10	100	10	5	5

Table 11 XPS experimental parameters for PANI-project

region	Survey	C 1s	N 1s	O 1s	Me 2p	S 2p
No. scans	2	15	50	15	15	20

The partial contribution of Natascha Weidler [Data analysis] is gratefully acknowledged. The possibility to do X-ray-induced photoelectron spectroscopy at the DAISY-FUN system of Wolfram Jaegermann's group at TU Darmstadt is gratefully acknowledged.

3.3 DFT calculation

Computational surface science by means of density functional theory (DFT) coupled with experimental achievement enabled the development of new concepts of heterogeneous catalysis. Particularly, numerous effort have been made to study the surface phenomena for the transition metals investigating bond formation and trends in reactivity (volcano plots).[137] Accordingly, density functional theory was applied for Me-N-C catalysts in collaboration with FU Berlin in this project. In order to investigate the role of metal on HER activity more detailed information are given in the related article.

The contribution of Ashkan Moradabadi is gratefully acknowledged. [Theoretical calculation]

3.4 Post-mortem methods

In the case of Me-N-C catalysts, there are noticeable limitations in identification of active sites and structural changes during catalytic reactions. Most importantly, in-situ characterization methods suitable for electrochemical reactions are restricted to the specific adsorption, emission or scattering of the photons or other fundamental particles not accessible for in-house laboratories. Therefore, inspired by the in-situ measurements, post-mortem studies can be carried out when the electrochemical process has been terminated. In this project, XPS and TEM techniques were used for post-mortem analysis in order to evaluate the surface and bulk properties of Me-N-C catalysts after electrochemical conditioning (RDE experiments).

- **XPS coupled with RDE**

The first step to carry out the experiments is designing an appropriate sample holders that is suitable for both electrochemical and XPS characterization based on their instrumental specifications. To design the sample holder suitable for XPS setup (Figure 3.10), a male screw thread was built on top of a standard sample holder for mounting the electrode. To maintain the electronic conduction, a gold pin was installed in order to connect the glassy carbon to the sample holder. The height of the electrode was adjusted to maintain suitable optimization of beam radiation. For each experiment, a corresponding amount of the catalyst ink was dropped on the glassy carbon.

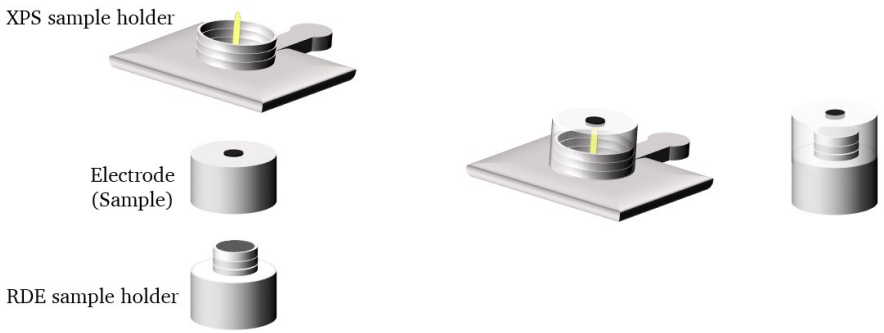

Figure 3.10 Designed apparatuses for XPS measurement coupled with RDE

After drying of the ink, the electrode was mounted on the XPS sample holder and introduced to the XPS setup. After XPS, the electrode was mounted on RDE sample holder for electrochemical conditioning (EC). After EC, the electrode was washed with distilled water and remounted on the XPS sample holder for spectroscopy measurement. This procedure was repeated for more EC steps depending on the project and the catalytic reaction.

With this method, remarkable information regarding the structural changes in relation with electrochemical conditioning can be obtained by XPS post-mortem analysis. For instance, oxidation state changes in metal region, changes in nitrogen species and their effect on the stability and activity of the catalysts. It should be noted that because of electrochemical conditioning, X-ray beam damage and sample transfer, the particle loss on the electrode was unavoidable. Thus, the RDE measurements were repeated without transferring the sample out of electrolyte as a complete measurement repeating with the protocol identical to post mortem experiment. The electrochemical conditioning protocol is shown in the Table 12.

Table 12 Electrochemical conditioning protocol for post mortem analysis

Galvanostatic	@ 10 $mAcm^{-2}$	5, 10, 60 minutes
Potentiostatic	@ 1.85 V vs. SHE	5,10, 60 minutes
Cycling	1.2 – 1.8 V vs. SHE	2000 cycles, 300 mV sec^{-1}

- **TEM coupled with RDE**

Identical location TEM (IL-TEM) coupled with RDE enables us to study localized changes exposed on the Me-N-C catalyst after electrochemical conditioning. To perform the experiment, a drop of catalyst suspension was placed on a gold mesh (perforated carbon layer on gold finder grid F1/200) suitable for identical location TEM measurement.

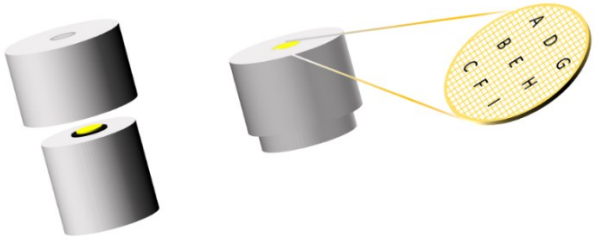

Figure 3.11 Designed apparatus for Identical location TEM measurement coupled with RDE

The mesh was transferred to the TEM setup to perform the initial microscopy. Then, the gold mesh was placed on the glassy carbon and mounted on the RDE shaft for the electrical connection. A cap was designed to be mounted on the electrode to fix the position of gold mesh in contact between the glassy carbon and electrolyte. This method was adapted from [138]. After EC, the gold mesh was transferred to the TEM setup for further characterization. Thus, it is possible to study the effect of EC on the carbon morphology, surface structure and nanoparticles including corrosion processes, particle agglomeration or particle disappearance with use of IL-TEM post-mortem analysis. The protocol applied for this method was identical to the XPS post-mortem experiments. However, it should be noted that, in the case of IL-TEM, it was only possible to obtain reliable results with potentiostatic EC method because of the ultrathin gold mesh used in this experiment. Galvanostatic and cycling methods (in the corresponding protocol) resulted in to destruction of catalysts or redepositing of the gold particles on the mesh, which interferes the obtained results. For each sample, two different positions were selected in order to obtain consistent TEM images after electrochemical conditioning. For instance, the failed experiment with Galvanostatic conditioning of Mn-doped Co-N-C catalyst is depicted in Table 13. It was observed that only spot (B) remained intact after

conditioning the catalyst for 5 minutes at constant current of 10 $mAcm^{-2}$. Indeed, the spot B was disappeared after 10 minutes conditioning which resulted in a failure in the experiment.

Table 13 Failed IL-TEM experiment after galvanostatic conditioning

	A (100nm)	B (100nm)
initial	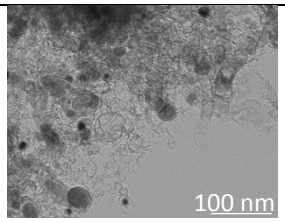	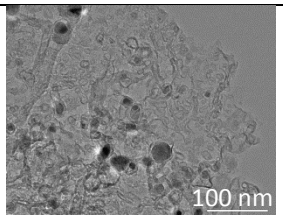
5 minutes	✖	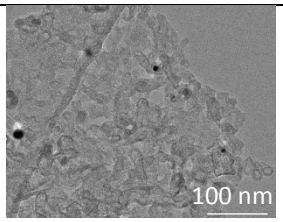
10 minutes	✖	✖

4 Results and discussion

This chapter includes the "results and discussion" in the form of publications regarding the investigation of Non-PGM catalysts for water splitting reactions, which are listed below. Moreover, a conclusive summery of the multi-heteroatom doing approaches, applied in this thesis, is reported. For each subchapter, the project targets and individual contribution are briefly described.

Elucidating the Origin of Hydrogen Evolution Reaction Activity in Mono- and Bimetallic Metal- and Nitrogen-Doped Carbon Catalysts (Me-N-C),

Shahraei, Ali; Moradabadi, Ashkan; Martinaiou, Ioanna; Lauterbach, Stefan; Klemenz, Sebastian; Dolique, Stephanie; Kleebe, Hans-Joachim; Kaghazchi, Payam; Kramm, Ulrike I.

2017-ACS Applied Material and Interfaces, DOI: 10.1021/acsami.7b01647

Exploring Active Sites in Multi-Heteroatom-Doped Co-Based Catalysts for Hydrogen Evolution Reactions

Shahraei, Ali; Martinaiou, Ioanna; Creutz, K. Alexander; Kübler, Markus; Weidler, Natascha; Ranecky, Simon T.; Wallace, W. David Z.; Nowroozi, Mohammad Ali; Clemens, Oliver; Stark, Robert W.; Kramm, Ulrike I.

2018-Chemistry-A European Journal, DOI: 10.1002/chem.201802684
Placed on the Hot Topic collections: Carbon, Graphite, and Graphene – water splitting
invited for the frontiespiece image

On the role of hydroxide species in sulphur- and nitrogen-doped cobalt-based carbon catalysts for the oxygen evolution reaction

Shahraei, Ali; Kübler, Markus; Martinaiou, Ioanna; Creutz, K. Alexander; Wallace, W. David Z.; Nowroozi, Mohammad Ali; Paul Stephen; Weidler, Natascha; Stark, Robert W.; Clemens, Oliver; and Kramm, Ulrike I.

2018-Journal of Material Chemistry A, DOI: 10.1039/C8TA05769A

Post mortem evaluation of sulfur- and manganese-doped cobalt-based catalyst under water oxidation

Shahraei, Ali; *Weidler, Natascha*; *Kübler, Markus; Ni, Lingmei; Martinaiou, Ioanna*; *Kaiser, Bernhard; Stark, Robert W.; Jeagermann Wolfram, and Kramm, Ulrike I.*

2018-Prepared manuscript, Submission Timeline: November 2018

4.1 Investigation of HER on Non-PGM catalysts

4.1.1 Variation of metal species on HER in alkaline

In this project, MOF-based mono- and bimetallic Me-N-C catalysts were investigated for HER in alkaline media. The main target was to explore the role of the metal in Me-N-Cs regarding the catalytic activity and structural changes. Therefore, several characterization techniques beside DFT calculations were performed to identify the origin of the activity regarding various metal sources.

Contribution to the project: Catalyst preparation, X-ray photoelectron spectroscopy (XPS) characterization, Electrochemical characterizations, Establishing the collaboration with Freie Universität Berlin (DFT calculation), Data analysis and writing

ACS APPLIED MATERIALS & INTERFACES

Research Article

www.acsami.org

Elucidating the Origin of Hydrogen Evolution Reaction Activity in Mono- and Bimetallic Metal- and Nitrogen-Doped Carbon Catalysts (Me−N−C)

Ali Shahraei,[†,‡] Ashkan Moradabadi,[§,⊥] Ioanna Martinaiou,[†,§] Stefan Lauterbach,[#] Sebastian Klemenz,[∥,△] Stephanie Dolique,[∥] Hans-Joachim Kleebe,[#] Payam Kaghazchi,[⊥] and Ulrike I. Kramm*[,†,‡,§]

[†]Graduate School of Excellence Energy Science and Engineering, [‡]Department of Chemistry, and [§]Department of Materials and Earth Science, TU Darmstadt, Jovanka-Bontschits-Straße 2, 64287 Darmstadt, Germany

[∥]Eduard-Zintl-Institute for Physical and Inorganic Chemistry, TU Darmstadt, Alarich-Weiss-Straße 12, 64287 Darmstadt, Germany

[⊥]Department of Chemistry and Biochemistry, Freie Universität Berlin, Taku Straße 3, 14195 Berlin, Germany

[#]Department of Materials and Earth Science, Institute of Applied Geosciences, Department of Geometrical Science, TU Darmstadt, Schnittspahn Straße 9, 64287 Darmstadt, Germany

S *Supporting Information*

ABSTRACT: In this work, we present a comprehensive study on the role of metal species in MOF-based Me−N−C (mono- and bimetallic) catalysts for the hydrogen evolution reaction (HER). The catalysts are investigated with respect to HER activity and stability in alkaline electrolyte. On the basis of the structural analysis by X-ray diffraction, X-ray-induced photoelectron spectroscopy, and transmission electron microscopy, it is concluded that MeN_4 sites seem to dominate the HER activity of these catalysts. There is a strong relation between the amount of MeN_4 sites that are formed and the energy of formation related to these sites integrated at the edge of a graphene layer, as obtained from density functional theory (DFT) calculations. Our results show, for the first time, that the combination of two metals (Co and Mo) in a bimetallic (Co,Mo)−N−C catalyst allows hydrogen production with a significantly improved overpotential in comparison to its monometallic counterparts and other Me−N−C catalysts. By the combination of experimental results with DFT calculations, we show that the origin of the enhanced performance of our (Co,Mo)−N−C catalyst seems to be provided by an improved hydrogen binding energy on one MeN_4 site because of the presence of a second MeN_4 site in its close vicinity, as investigated in detail for our most active (Co,Mo)−N−C catalyst. The outstanding stability and good activity make especially the bimetallic Me−N−C catalysts interesting candidates for solar fuel applications.

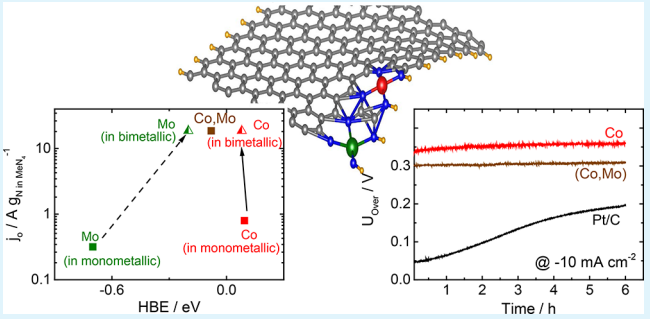

KEYWORDS: *hydrogen evolution reaction, Me−N−C catalysts, nonprecious metal catalyst, DFT calculation, alkaline electrolyte, structure−activity correlation*

1. INTRODUCTION

Climate change due to greenhouse gases is one of the important issues of 21st century. Renewable energy resources contribute to the diminution of greenhouse gases and dust emissions and hence improve the quality of air in densely populated areas. Hydrogen plays a crucial role as an energy carrier for proton exchange membrane fuel cells and alkaline fuel cells, as well as for the fabrication of chemical compounds, for example, via Fischer−Tropsch or Haber−Bosch synthesis. Nowadays, hydrogen production is achieved by either steam reforming or electrolysis with the drawbacks of formation of undesired byproducts (CO and H_2S—both are poisons for common precious metal catalysts) or high costs due to the utilization of expensive catalysts.

Unlike the reforming process, the electrolysis of water to molecular hydrogen and oxygen offers a significant promise for supplying CO_2- and CO-free hydrogen as stated by the intergovernmental panel on climate change (IPCC).[1] In particular, electrolysis is also considered for the storage of excess energy produced by solar power devices that are ideally coupled with cheap and earth-abundant catalysts. The achievable current density in such devices is defined by the ratio of photo to current efficiency of the photoabsorber, which is usually about 10 mA cm^{-2}.[2] Solar fuel devices can be realized by different combinations of photoabsorbers, photocatalysts,

Received: February 9, 2017
Accepted: June 27, 2017
Published: June 27, 2017

DOI: 10.1021/acsami.7b01647
ACS Appl. Mater. Interfaces 2017, 9, 25184−25193

and dark catalysts.[3] Considering a combination of a photoanode for the oxygen evolution reaction and a dark catalyst for hydrogen evolution reaction (HER), typical stable semiconductors, for example, WO_3, α-Fe_2O_3, and $MeVO_4$ (Me = In, Bi, and W), have band gaps of >2.3 eV.[4,5] As the main energy losses on the anode are about 0.8 eV, there is a possible overvoltage on the cathode of 0.3 V that can be used to reach the aforementioned 10 mA cm^{-2}.

Because of excellent kinetics for the HER on platinum, this current density is reached for low overvoltage.[6,7] However, high cost, scarcity, and relatively poor performance of Pt in alkaline electrolyte prevent its commercial use.[8] Numerous efforts have been made to find suitable alternatives to replace Pt for the HER.

For instance, third transition-metal alloys of Co, Fe, Ni, and Mo;[9−13] sulfides;[14−16] and phosphides[17,18] catalyze the HER. An interesting effect regarding metal sulfides has been recently found by Staszak-Jirkovský and co-authors.[15] It was shown that the combination of cobalt and molybdenum compared with the monometallic catalysts exhibited a significant improved onset potential and stability for the HER.

In addition, recently, Liang et al. have presented a Co−N−C catalyst prepared at 800 °C with a very promising HER activity that was attributed to CoN_4 sites. It should be noted that Me−N−C catalysts can be considered as the pyrolyzed analogues to MeN_4 macrocycles and were investigated in detail for the oxygen reduction reaction (ORR).[19−21] Today, it is known that Me−N−C catalysts can be prepared from independent metal, nitrogen, and carbon sources as demonstrated by the authors and others.[22−26] However, depending on the precursor composition, heat-treatment temperature, and the type of pyrolysis gas that are applied, the catalysts reveal a heterogeneous composition of MeN_4 sites, metal nitrides, carbides, and/or other metal species (e.g., sulfides if the precursor contains sulfur).[27,28]

For instance, Wang et al. synthesized PANI-based Co−N−C catalysts in a temperature range of 550−950 °C to investigate the effect of heat-treatment temperature and related composition on the HER activity.[29] They proposed a hybrid CoC_3N site as the active center after investigation of several possible CoC_xN_y coordinations using density functional theory (DFT) calculations. Although Wang et al. assigned the HER activity to monometallic dispersed cobalt coordinated by nitrogen and carbon, Morozan et al. assigned the HER activity of their investigated Me−N−C catalysts to carbides and nitrides.[30] In their approach, catalysts were prepared from a metal organic framework (MOF), phenanthroline, and various metal acetates to obtain Me−N−C catalysts (Me = Fe, Co, Mn, Ni, Cu, Zn, W, Mo, and Cr) at 1050 °C, that is, at a significant higher temperature compared with the most active catalyst in Wang et al.[29] This might explain why the catalysts in Morozan's study were dominated by nitride and carbide species. Nevertheless, also regarding the ORR, it was shown that the presence of inorganic metal species in Me−N−C catalysts might be of importance, as it was suggested that a high ORR activity of Me−N−C catalysts can only be reached by the interaction of two MeN_4 sites with each other or with other metal-containing species.[31,32] In addition, recent reports have showed that graphitic shells surrounding metal carbide particles can work independently as ORR active sites without participation of MeN_4 sites.[33−35]

To the best of our knowledge, a comprehensive study on the role of metal centers in catalyzing the HER by Me−N−C catalysts with predominant presence of MeN_4 sites is missing. Therefore, we synthesized self-supported X-ray amorphous Me−N−C catalysts in this work. On the basis of our previous experiences in catalyst preparation[23,36−38] and as confirmed by our structural analysis, the chosen preparation conditions enable a predominate formation of MeN_4 sites, whereas excess metal is removed by acid leaching. For these catalysts, we demonstrate a very good stability and a volcano-type behavior correlating the HER activity with hydrogen binding energies (HBEs) obtained from DFT calculations and with experimentally obtained charge densities from XPS. Moreover, similar to the conclusions made for metal sulfides, a synergetic effect of metals is observed if cobalt is combined with other transition metals such as iron, manganese, or molybdenum. Such bimetallic catalysts exhibit the best performance and an outstanding stability under galvanostatic conditions (−10 mA cm^2) without any significant change in overpotential.

2. EXPERIMENTAL PART

2.1. Catalyst Preparation. Me−N−C catalysts were prepared by mixing 1.5 mM 1,10-phenanthroline (phen) and 2.0 mM Basolite framework (Z1200) with 0.25 mM metal acetate in a mortar. Therefore, the given precursor contained about 2 wt % metal (from metal acetate) and about 16 wt % Zn from Z1200. The mixture was filled in a quartz boat and heated up to 950 °C where the temperature was kept for 2 h before cooling down to room temperature. The overall pyrolysis was performed under a nitrogen flow, with a heating rate of 450 °C/h. The obtained powder was acid-leached in 2 M HCl to remove any undesired metal residuals (e.g., from decomposition of MeN_4 sites). The filter cake was washed with deionized water and dried. After drying, a second heat treatment identical to the first pyrolysis was performed.

The obtained catalyst powder is labeled as Me−N−C (where Me corresponds to the intended metal, i.e., from the metal acetate).

2.2. Electrochemical Testing. The HER activity and stability were investigated in a standard three-electrode arrangement with a glassy carbon (GC) disc with our catalysts as the working electrode, Ag/AgCl/3 M as the reference electrode, and a GC rod as the counter electrode. To prepare the working electrode, first an ink with the catalyst was prepared: 5 mg of the catalyst was mixed with 142 μL of ethanol, 83.2 μL of water, and 25 μL of Nafion. This mixture was kept in an ultrasonic bath for 30 min to obtain a homogeneous ink. To maintain a catalyst loading of 2 mg cm^{-2}, 20 μL of ink was dropped on the precleaned GC disc (A = 0.1963 cm^2). Electrochemical experiments were conducted in 0.1 M KOH (pH 13) that was always purged with nitrogen gas for 15 min before any measurement. All results presented in the paper refer to the standard hydrogen electrode and potentials are iR-corrected. For all experiments, the electrode was rotated with a speed of 1500 rpm to enhance the removal of hydrogen gas bubbles on the electrode.

To determine the HER activity, cyclic voltammograms are usually obtained in a potential window of 0.2 to −0.8 V with a sweep rate of 5 mV s^{-1} to keep the capacity contributions low. However, as still some catalysts showed significant capacity contributions, the averaged scan from the cathodic and anodic sweeps was plotted as polarization curves in Figures 1a and 3a. In Figure S1, the overall cyclic voltammetry and the averaged scan were compared for Co−N−C. It becomes clear that this procedure helped to eliminate the capacity contribution.

The short-term durability tests refer to cycling of the electrode in a potential range of −0.8 to 0.2 V for 100 scans with a sweep rate of 100 mV s^{-1}. The HER activity test was repeated afterward to assign changes in overpotential induced by this durability test. The obtained changes in overpotential were calculated for a given current density as given by eq 1

$$\Delta U_{over}(j) = U_{over,start}(j) - U_{over,end}(j) \quad (1)$$

DOI: 10.1021/acsami.7b01647
ACS Appl. Mater. Interfaces 2017, 9, 25184−25193

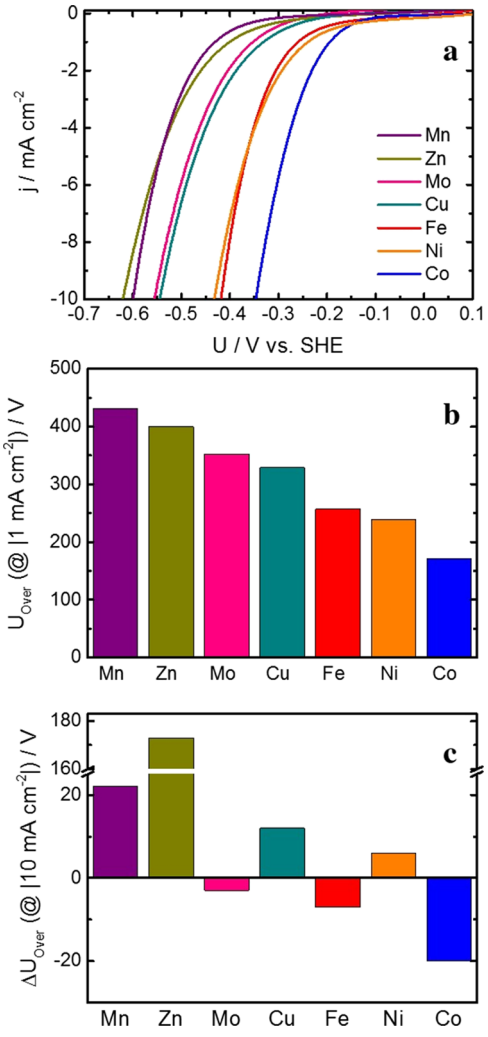

Figure 1. (a) Average cyclic voltammograms of various Me−N−C catalysts in 0.1 M KOH (2 mg cm^{-2}, 5 mV s^{-1}), (b) comparison of overpotentials U_{over} for $j = -1$ mA cm^{-2}, and (c) changes in overpotentials (ΔU_{over}) at −10 mA cm^{-2} induced by a short-term durability test (100 cycles, $U = -0.8$ to 0.2 V, 100 mV s^{-1}, 2 mg cm^{-2}).

That is, a negative ΔU_{over} value indicates an improved performance of the catalyst.

A long-term stability test was performed for Co−N−C and the most active bimetallic catalysts [(Co,Mo)−N−C and (Co,Mn)−N−C] by applying a current density of −10 mA cm^{-2} for 6 h.

2.3. X-ray-Induced Photoelectron Spectroscopy (XPS). X-ray-induced photoelectron spectra (XPS) were measured with a SPECS PHOIBOS 150 hemispherical analyzer and a SPECS XR50M Al Kα X-ray source (E = 1486.7 eV). Before the measurements, the catalyst powder was pressed on an indium foil and sealed on the sample holder. For the survey scans, an energy step of 1 eV has been applied and two scans were overlaid. For the N 1s region 100 scans, O 1s 10 scans, C 1s 10 scans, and all Me 2p regions 5 scans were overlaid. For these fine scans, an energy step of 0.05 eV has been used. Spectra were analyzed using CasaXPS, and peaks were fitted using a Shirley background and a mixed Gauss/Lorentz peak. All reported elemental compositions were determined considering relative sensitivity and transmission factors.

2.4. X-ray Diffraction. X-ray diffraction (XRD) was used as an additional measure of possible inorganic metal residuals. Measurements were done in transmission with a STADIP (STOE & Cie GmbH, Darmstadt) diffractometer in Debye−Scherrer geometry with a position-sensitive detector using either Mo $K_{\alpha 1}$ radiation (λ = 0.70930 Å) [Ge(111) monochromatic] or Cu $K_{\alpha 1}$ radiation (λ = 1.54056 Å). Samples were prepared on an acetate foil tape that gives low background intensity in the diffractograms. Patterns were collected three times with a step size of 0.5° and a collection time of 30 s step^{-1} and then overlayed.

2.5. Transmission Electron Microscopy. The two most active catalysts (Co,Mn)−N−C and (Co,Mo)−N−C were analyzed by transmission electron microscopy (TEM). Samples were prepared by dispersing a small amount of the powders in ethanol using an ultrasound bath (Bandelin) for approximately 30 s. The dispersion was allowed to settle for a short time to reduce the amount of large particles/agglomerates in the dispersion. A droplet of the dispersion was placed on a holey carbon grid (Plano) and allowed to dry. The grid was coated with carbon (Bal-Tec MED010) to avoid charging under the incident electron beam.

TEM characterization was performed with a FEI CM20STEM (Eindhoven, the Netherlands) microscope equipped with a LaB_6 cathode and a Gatan double tilt holder at a nominal acceleration voltage of 200 kV.

Energy-dispersive spectrometry (EDS) were recorded using an Oxford X-Max 80 silicon drift detector (Oxford Instruments Nanoanalysis, High Wycombe, United Kingdom) attached to the CM20. Spectra were quantified using the internal Cliff−Lorimer sensitivity factors from Oxford Instruments INCA ver. 4.15.

2.6. DFT Calculation. The DFT calculations were performed using the projector-augmented plane-wave code VASP[39] with PBE[40] exchange-correlation functional. The graphene layer was modeled by a 6 × 6 super cell with 66 carbon atoms in real space projection. Energy cutoff for all calculations was 440 eV, and all calculations were spin-polarized. At first, all possible configurations of N atoms doping on the graphene layer together with pure graphene, namely, C_4, C_3N, C_2N_2, CN_3, and N_4, were considered. At this step, total free energy of formation was calculated for all mentioned MeX_4 structures (X: carbon or nitrogen or mixtures thereof) and as summarized in Table 1 for cobalt and molybdenum. For all configurations at 0 K, the calculations were made according to eq 2

$$E_{tot}^{formation} = E_{tot}^{MeN_4} - nE_{tot}^{C} - mE_{tot}^{N} - pE_{tot}^{Me} - qE_{tot}^{H} \quad (2)$$

In this equation, $E_{tot}^{MeN_4}$ is the total energy of the doped structure, E_{tot}^{C} is the total energy per carbon atom with respect to graphite carbon, E_{tot}^{N} is the total energy per nitrogen atom from N_2 gas, E_{tot}^{H} is the total energy per hydrogen atom from H_2 gas, and E_{tot}^{Me} is the total energy of metal atoms derived from bulk metals. n, m, p, and q are the number of corresponding atom species in each structure. The large values of energies of formation are due to the H−C bonds in our model systems where the dangling bonds of the carbon atoms on edges were saturated by H atoms.

It becomes clear that the most stable configuration is the integration of MeN_4 sites at the edges of the graphene layers. Therefore, all further calculations were made for this site structure, as its formation seems to be the most favorable from a thermodynamic point of view.

Afterwards, the energy of formation for all monometallic catalysts using the MeN_4 at edges configuration was determined (Me = Co, Mo, Cu, Fe, Mn, Ni, and Zn).

Table 1. Energy of Formation of Various Possible Co−N−C and Mo−N−C Structures (Calculated by Eq 2, per Metal Atom in eV)

E/eV	MeC_4	MeC_3N	MeC_2N_2	$MeCN_3$	MeN_4	MeN_4 at edges
Co−N−C	6.986	0.112	−6.369	−13.047	−19.528	−19.739
Mo−N−C	8.448	2.347	−3.754	−9.855	−15.756	−15.993

DOI: 10.1021/acsami.7b01647
ACS Appl. Mater. Interfaces 2017, 9, 25184−25193

In the second part of our work, for better understanding of the origin of improved HER activity of bimetallic catalysts, the HBE was determined for bimetallic catalysts and their related monometallic catalysts using eq 3 without considering the zero-point energies

$$\mathrm{HBE} = E_{\mathrm{tot}}^{\mathrm{H+MeN_4}} - E_{\mathrm{tot}}^{\mathrm{MeN_4}} - \frac{1}{2}(E_{\mathrm{tot}}^{\mathrm{H_2}}) \quad (3)$$

For better assessment of possible configurations between cobalt and the second metal, various arrangements of possible configurations between cobalt and two MeN_4 sites in bimetallic catalysts were evaluated. Therefore, different separations of Mo in MoN_4 and Co in CoN_4 were considered. The corresponding energies of formations are reported in Table 2.

Table 2. Energy of Formation (per Metal Atom in eV) for the Assumption of MoN_4 + CoN_4 with Different Mo−Co Separations in Å

separation Mo−Co/Å	5.32	7.58	9.92
$E_{\mathrm{formation}}$/eV	−16.88	−16.75	−16.62

As the energy of formation is most negative for the closest configuration of MoN_4 and CoN_4 sites, the HBEs for bimetallic catalysts were calculated for this configuration and are compared with their monometallic counterparts in Table 3.

3. RESULTS

3.1. Investigation of Monometallic Catalysts. As described in the experimental part, the Me−N−C catalysts were prepared at 950 °C with relatively low intended metal loadings (2 wt %) and the use of an acid-leaching step previous to the second heat treatment. Higher temperatures and reactive gases such as ammonia were avoided to prevent our catalysts from carbide and nitride formation.[22,38,41] As confirmed by XRD in Figures S2 and S3, our most active catalysts showed X-ray amorphous behavior and did not contain any carbide or nitride particles in contrast to reports by other groups on the activity of nitride and/or carbide species.[30,33,34]

In Figure 1, the performance of the monometallic catalysts for the HER was illustrated. Cobalt gave the highest activity followed by iron and nickel and then followed by the other Me−N−C catalysts. The short-term stability test (Figure 1c) illustrated a stable performance with even improved overpotentials for Me−N−C catalysts with Me = Co, Fe, and Mo.

There are two intrinsic catalyst properties that contribute to the observed current densities, namely, the mass-based site density (MSD) and the turn-over frequency (TOF). Hence, to elucidate the role of the superior performance of our catalysts, structural analysis was performed to estimate MSD and TOF of our catalysts. To evaluate the elemental and electronic composition, X-ray-induced photoelectron spectroscopy (XPS) was used. As an example, the survey and N 1s fine scans of the Co−N−C catalyst are shown in Figure 2a,b. The N 1s fine scan is convoluted into six peaks, adopted from Jaouen et al.[42] As it is depicted in Table S2, three different graphitic nitrogen species might be integrated in the graphene layers, labeled as G1, G2, and G3. With the increasing number of benzene rings where the N_{graph} is integrated, the energetic position is shifted to higher E_{bind} value. Although the G1 type has about the same energetic position as N_{pyrrol}, two graphitic nitrogen peaks were used in our fitting model to consider the G2 and G3 types of graphitic nitrogen. In Figure S4, the C 1s, O 1s, Co 2p, and Zn 2p fine scans for the same catalyst were given.

The surface near elemental composition was determined from the survey scans for all catalysts. The catalysts contained mainly carbon together with 5−10 wt % nitrogen, 6−15 wt % oxygen, and up to 8.5 wt % metal (sum of desired metal species plus zinc). A summary of the elemental compositions derived from XPS is available in Table S2. It should be noted that even though not intended, most catalysts contain zinc as a residual from the Z1200 that was used as a structure forming agent. Based on the literature, it was expected that for the chosen pyrolysis conditions (950 °C, 2 × 2 h, acid leaching), zinc should be evaporated or leached out.[43]

The overall nitrogen and metal contents (sum of the metal contents plus zinc, Table S2a) are plotted in Figure 2b,c. In addition to this, the nitrogen content assigned to MeN_4 species (Figure 2b) and the content of the intended metal species (the one from the acetate) (Figure 2c) were indicated with dashed bars in the N and Me regions, respectively. The samples were ordered with increasing HER activity (compare Figure 1a,b from left to right).

There was obviously no correlation between N_{MeN} or the total N contents (independent from the type of metal) and HER activity. Also, neither the overall metal content nor the content of the intended metal determined the HER activity. Such a direct correlation can only be expected for groups of catalysts with about the same TOFs. However, as the type of metal center strongly affects the interaction with the reactants, we would also assume variations of the TOF values for our catalysts.

As described in the Supporting Information, the TOF values and mass-based site densities (MSDs) were calculated for all monometallic catalysts and are summarized in Table 4.

It is visible that the MSD values of Cu, Fe, and Co are almost identical, whereas the formation of MeN_4 sites seems favorable for Mn and Ni. On the other hand, Mo seems to form the least stable configuration. As shown in Figure S7, there was a good correlation between the energy of formation obtained for the different monometallic MeN_4 sites (integrated at the edges of a graphene layer) and the mass-based site density (MSD). This indicated a good agreement between our experimental data and theoretical calculations.

On the basis of the TOF values, the order of intrinsic activity was Co ≫ Fe > Ni ≈ Mo ≈ Cu > Zn > Mn.

Although the trend was not obvious from Table 4, we have included a graph in Figure 2e that gives the TOF values as a function of the 3d-orbital occupation of our Me−N−C. Mo−N−C as 4d-transition metal was added, for reasons of completeness. The result indicates a distinct volcano-type correlation following Sabatier's principle between the intrinsic activity (i.e., TOF) of MeN_4 sites and the d-orbital occupation. Such correlations were developed not only for various catalytic

Table 3. Calculated HBEs for Bimetallic Catalysts and Their Monometallic Counterparts[a]

	Co	Fe	Mn	Mo	(Co,Fe)	(Co,Mn)	(Co,Mo)
HBE/eV	0.094	0.061	0.221	−0.708	0.099	0.202	−0.082

[a]In the case of bimetallic catalysts, the given values represent the average for both metals.

DOI: 10.1021/acsami.7b01647
ACS Appl. Mater. Interfaces 2017, 9, 25184−25193

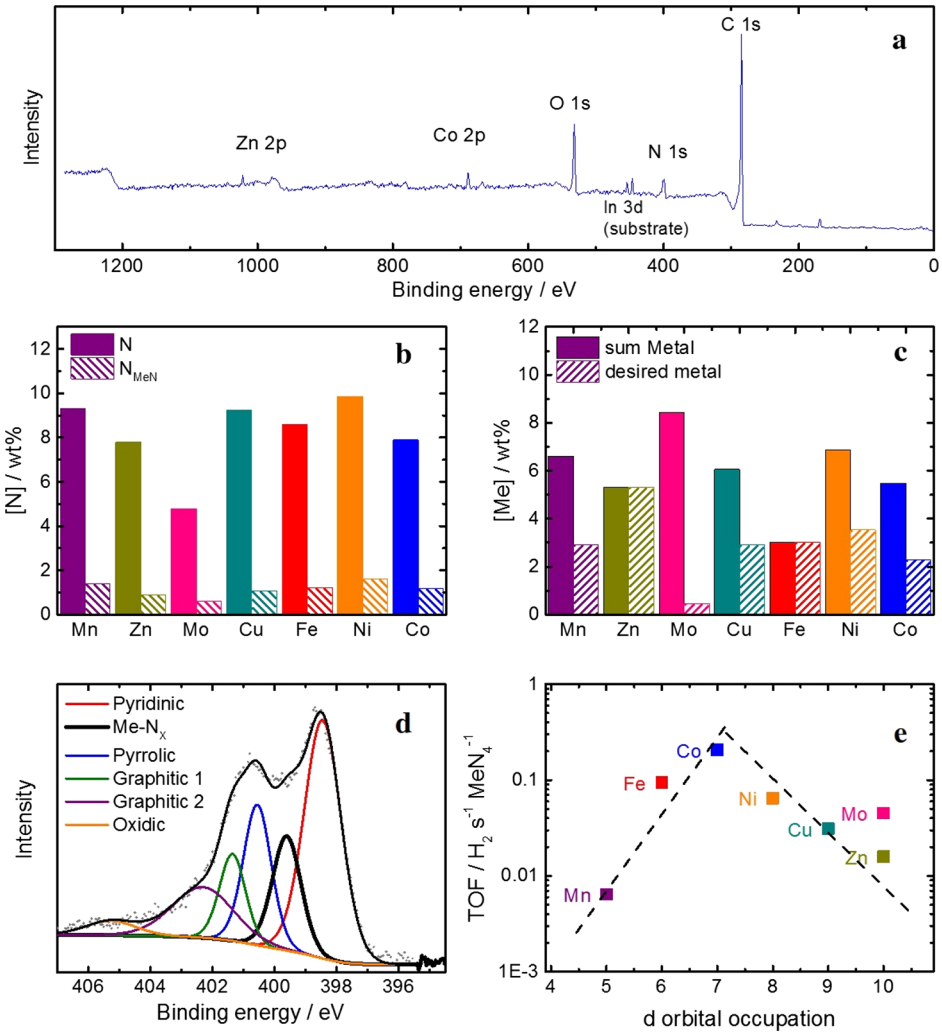

Figure 2. (a) Exemplary survey scan of the Co−N−C catalyst, (b) total content of nitrogen [N] and specifically nitrogen assigned to MeN_4 sites [N_{MeN}], and (c) overall content of metal species [Me] as well as the one assigned to the desired metal (from the metal acetate precursor) are shown. (d) N 1s fine scan region of Co−N−C and (e) correlation between TOF and the d-orbital occupation. Note: Mo should be considered with care, as Mo is the only investigated transition metal from the 4d group.

Table 4. Comparison of Mass-Based Site Densities (MSDs) and TOFs for All Monometallic Catalysts[a]

	Mn	Zn	Mo	Cu	Fe	Ni	Co
MSD/$\times 10^{19}$ MeN_4 sites g_{cat}^{-1}	15.2	9.8	6.6	11.6	13.1	17.3	12.6
TOF (−0.4 V)/$\times 10^{-2}$ H_2 MeN_4^{-1} s^{-1}	0.6	1.6	4.5	3.1	9.4	6.5	20.7

[a]TOF values were determined for −0.4 V as the number of hydrogen atoms formed per MeN_4 site and per second. Values were ordered with increasing HER activity of the catalysts from left to right.

reactions on metal or metal oxides but also for MeN_4 macrocycles.[44]

A typical approach to improve the performance of, for example, a metal catalyst that is located on the one slope of the volcano is to alloy this material with a second metal from the other slope of the volcano. Such improved metal alloys were for instance investigated by Jakšić for the HER.[45,46]

3.2. On the Possibility of an Synergetic Effect in Bimetallic Catalysts. Hence, motivated by the works of Staszak-Jirkovský et al. and Jakšić,[15,46] and studies of bimetallic Me−N−C catalysts for the ORR,[32,47−49] the possibility of a synergetic effect was investigated for cobalt—as the most active catalyst for the HER in combination with iron and manganese on the left slope and molybdenum on the right slope (compare Figure 2e).

As illustrated in Figure 3a, indeed a favorable onset potential in comparison with the monometallic catalysts was found. For comparison, the related monometallic catalysts were also given in Figure 3a and the significant improvement of performance is illustrated with arrows.

TEM images of the two most active catalysts (Co,Mo)−N−C and (Co,Mn)−N−C are shown in Figure 4. Although (Co,Mo)−N−C contained turbostratic carbon with nanoparticles encapsulated by graphene layers, there was no indication of cobalt or manganese particles in (Co,Mn)−N−C. By contrast, the TEM images showed only turbostratic carbon. EDS analysis of different regions of the (Co,Mo)−N−C catalyst indicated that the nanoparticles were composed of cobalt and small amounts of molybdenum.

How can the activity improvement for the bimetallic catalysts be described?

DOI: 10.1021/acsami.7b01647
ACS Appl. Mater. Interfaces 2017, 9, 25184−25193

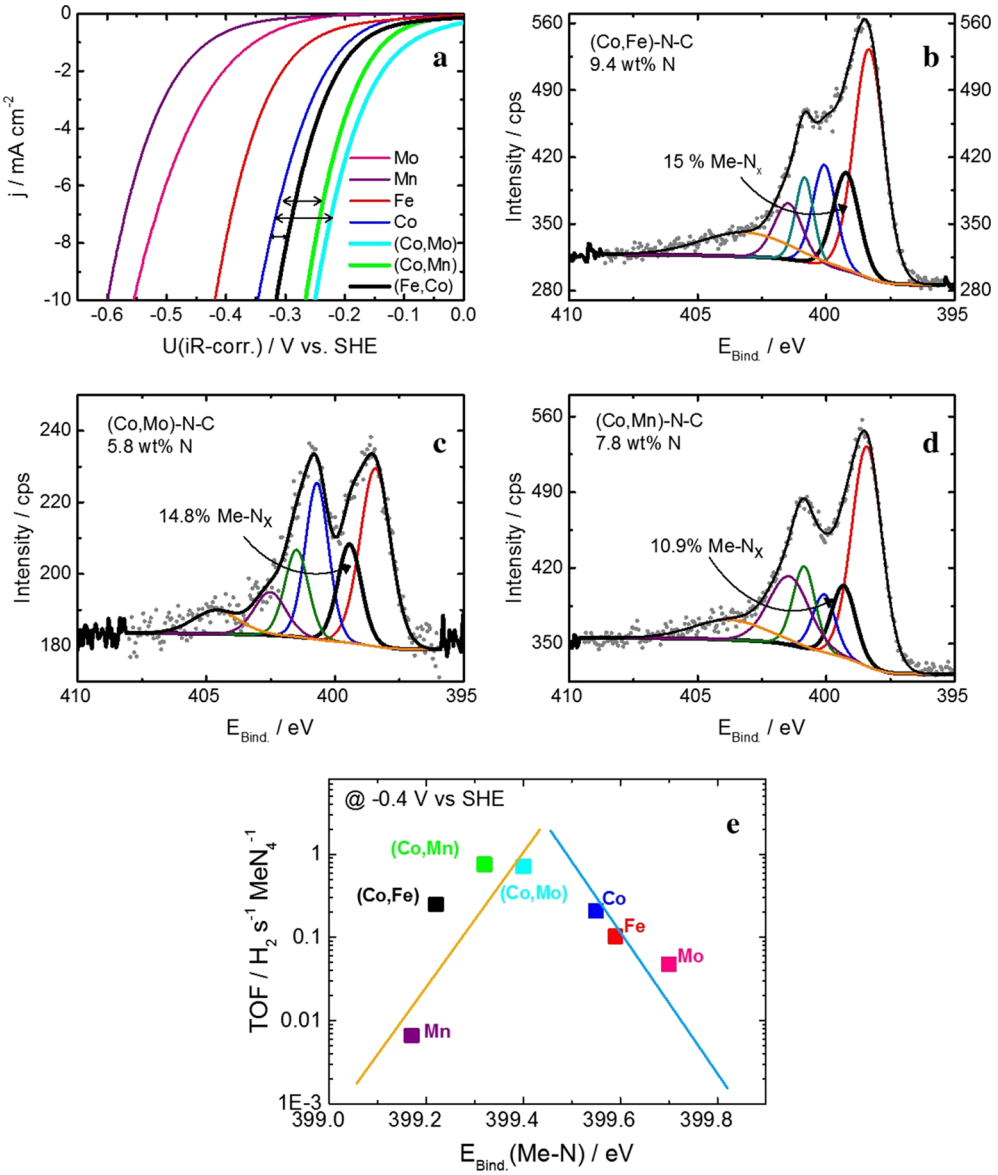

Figure 3. (a) Average cyclic voltammograms of bimetallic catalysts in 0.1 M KOH (2 mg cm^{-2}, 5 mV s^{-1}) and their corresponding monometallic polarization curves for comparison, N 1s fine scans of (b) (Co,Fe)−N−C, (c) (Co,Mo)−N−C, and (d) (Co,Mn)−N−C. (e) Correlation between TOF and binding energy E_{bind}(Me−N).

For our (Co,Mn)−N−C catalyst, all analyses pointed to the monoatomic dispersion of the metal species within the catalyst. Consequently, only N−C-sites (graphitic or pyridinic nitrogen species) or CoN_4 and MnN_4 sites could have contributed to the HER activity. If N−C sites were contributing significantly, the effect of metal species should not be as pronounced as observed for our catalysts. Instead of this, the HER activity would correlate with the content of the desired nitrogen species. The values are summarized in Table S2b in the order of decreasing overvoltage and indicated no defined trend. Therefore, the presence of CoN_4 sites and MnN_4 in this catalyst seemed to dominate its performance.

By contrast, (Co,Mo)−N−C contained CoN_4 sites, very small Co nanoparticles and molybdenum in a zero valent state. In relation to Morozan's work,[30] we attributed only a minor contribution of the HER activity to the cobalt nanoparticles as the overpotential required for 1 mA cm^{-2} was 260 mV in Morozan et al. (and assigned to cobalt nanoparticles) in contrast to 170 and 100 mV for our Co−N−C and (Co,Mo)−N−C catalysts, respectively.

Hence, because (Co,Mn)−N−C and (Co,Mo)−N−C were similarly active toward HER and behave similarly with respect to stability (compare Figures 5c and S12), we assumed that any cobalt nanoparticles present in (Co,Mo)−N−C could have only a minor contribution to the overall HER activity, although it was reported in other studies that carbon shells surrounding encapsulated nanoparticles might be electrochemically active.[33−35]

For better interpretation of the origin of the improved performance, series of DFT calculations were performed to understand the structural and electronic changes with the presence of a second metal. Despite the study by Wang et al. in which they exclusively investigated various possible coordination of CoN_xC_y hybrids based on the energetics of a variety of possible structures,[29] our DFT calculations systematically examined the energies of formation corresponding to each

DOI: 10.1021/acsami.7b01647
ACS Appl. Mater. Interfaces 2017, 9, 25184−25193

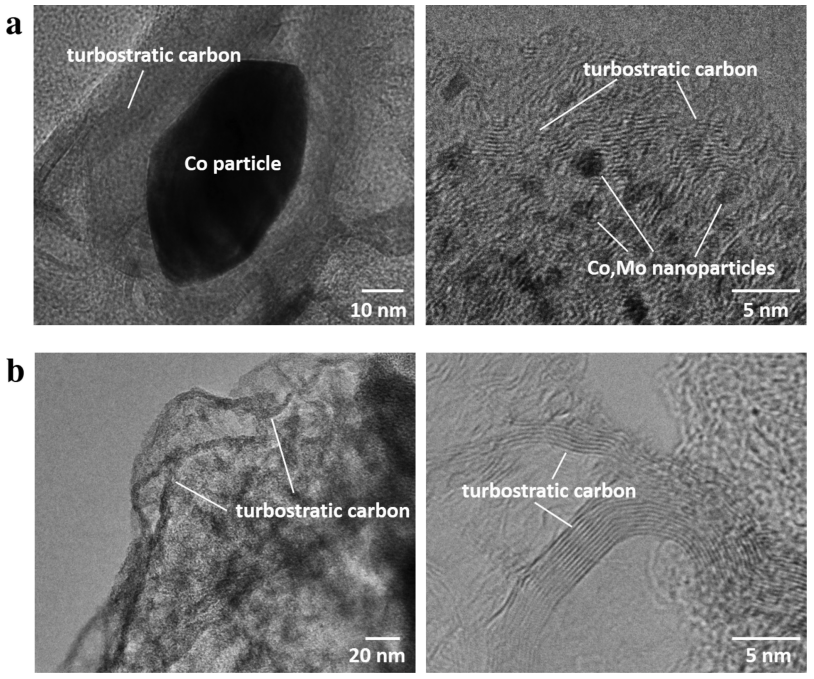

Figure 4. Representative TEM images of (a) (Co,Mo)−N−C and (b) (Co,Mn)−N−C catalysts.

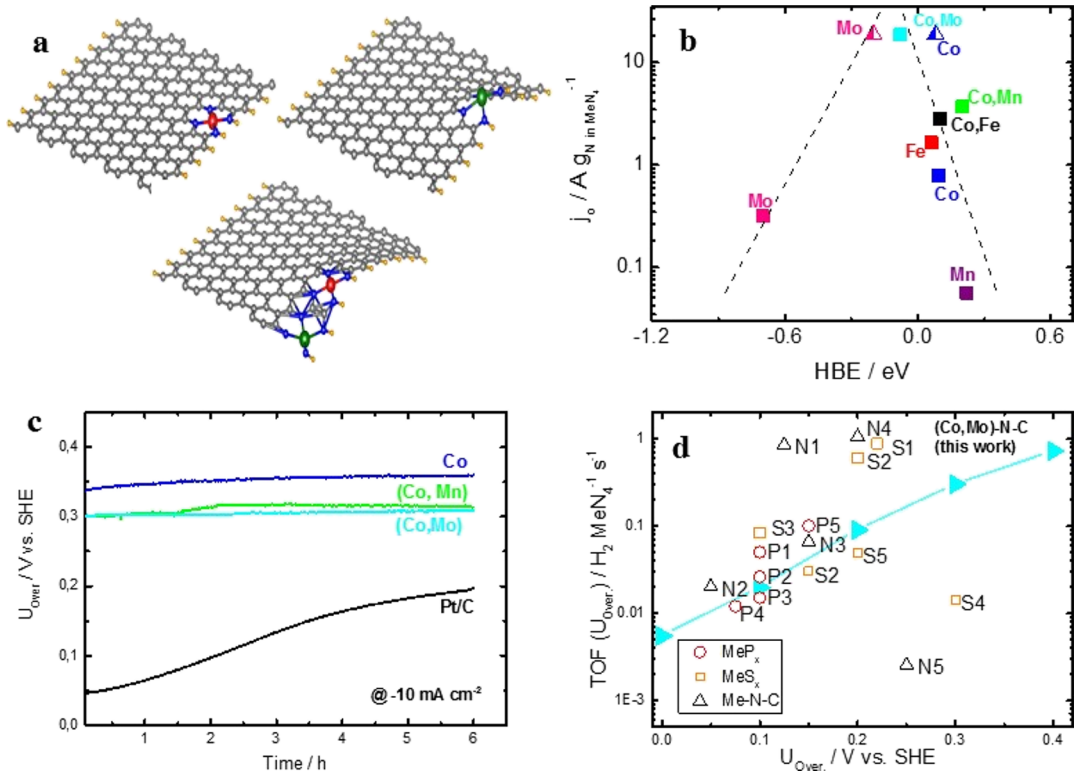

Figure 5. (a) Calculated most stable structures of Co−, Fe−, and MnN_4−graphene (top left) and MoN_4−graphene (top right) as well as (CoN_4 + MeN_4)−graphene with Me = Fe, Mn, and Mo. (b) Volcano plot of HBE vs exchange current density, for bimetallic catalysts the average values of HBE were plotted. However, for (Co,Mo) also the individual HBE on CoN_4 and MoN_4 were given as half-filled triangles. These values differ to the one of monometallic CoN_4 and MoN_4 sites because of the electronic interaction with the second metal. (c) Galvanostatic stability test for 6 h in 0.1 M KOH and (d) comparison of TOF of our most active catalyst (Co,Mo)−N−C with various nonprecious metal catalysts.

active site, as summarized in Table 1 for Co−N−C and Mo−N−C. We have also investigated the distance effect on the energy of formation in the case of MoN_4 + CoN_4 configurations on the edge of the graphene sheet and found MoN_4 and CoN_4 sites tend to be formed as close as possible to each other (separated by only two carbon atoms). Therefore, the energy of formation depended on the position of sites either in the graphene layer or at the edges as well as their relative distance from each other. These results were in agreement with the previous calculations by Holby et al., where

DOI: 10.1021/acsami.7b01647
ACS Appl. Mater. Interfaces 2017, 9, 25184−25193

it was also found that the most favorable structure is the case where two metal sites (same metals) share the coordinating nitrogen atoms in the form of a bimetallic Me_2N_5 site (separated by only two carbon atoms), rather than being well-separated.[50] In addition, both monometallic MeN_4 and bimetallic MeN_4 + MeN_4 configurations were found to be more favorable at the edges rather than in the middle of a graphene layer, which is also in agreement with the work by Holby and co-workers.[50] Our most favorable monometallic and bimetallic structures were given in Figure 5a. For the bimetallic catalyst, side and top views were included in Figure S8.

If the combination of two metals is beneficial, one has to assume that the electronic structure of (at least) one of the both metals was enhanced, so that one of the electron transfer steps (Volmer or Heyrovsky, compare eqs 4 and 5) or the combination of two adsorbed hydrogen atoms to H_2 (Tafel slopes)

$$\text{Volmer: } H_2O + e^- \rightarrow OH^- + H_{ads} \quad (\sim 120 \text{ mV dec}^{-1}) \tag{4}$$

$$\text{Heyrovsky: } H_2O + H_{ads} + e^- \rightarrow OH^- + H_2 \quad (\sim 40 \text{ mV dec}^{-1}) \tag{5}$$

$$\text{Tafel: } H_{ads} + H_{ads} \rightarrow H_2 \quad (\sim 30 \text{ mV dec}^{-1}) \tag{6}$$

In parentheses, the Tafel slopes for a transfer coefficient of α = 0.5 were added to the equations. If, for example, the Heyrovsky step was rate-determining, the investigated catalyst should have given a Tafel slope of about 40 mV dec^{-1}. Table S3 summarizes the Tafel slopes and exchange current densities of the investigated Me−N−C catalyst (the plots and procedures that were used to determine the exchange current density are given in Figures S9 and S10 and related text). For all catalysts, the Tafel slope is about 120 mV dec^{-1} or even higher. This indicates that the adsorption of the first hydrogen atom on the active site (Volmer step) is rate-determining. However, it was not possible to make conclusions whether the catalysts form hydrogen by a Volmer−Heyrovsky or Volmer−Tafel mechanism.

How fast the HER occurs on a specific MeN_4 site depends on the electronic properties of the metal ions. As shown by Karweik and Winograd,[51] the limited resolution of Me 2p regions in XPS hinders the identification of fine changes in energy density. However, it was shown that the N 1s region is highly sensitive to the changes in the electronegativity of the corresponding metal ion. A similar plot of N 1s binding energy assigned to N in MeN_4 versus electronegativity of our metals (for bimetallic catalysts, the average of both metals was calculated) is given in Figure S11. The metals were divided into two groups as indicated by the two correlation lines.

Therefore, the N 1s binding energy assigned to MeN_4 sites [E_{bind}(Me−N)] was evaluated as activity descriptor for the bimetallic catalysts and their monometallic counterparts. The N 1s fine scans of all bimetallic catalysts are given in Figure 3b−d for (Co,Fe)−N−C, (Co,Mo)−N−C, and (Co,Mn)−N−C. In a previous work, we have shown for ORR catalysts that Me−N-binding energies correlated with the TOF.[36] On the basis of the aforementioned considerations and this correlation, the TOF values (for U = −0.4 V) are plotted as a function of the Me−N binding energy in Figure 3e.

The results showed that the binding energy E_{bind}(Me−N) and the TOF values of the bimetallic catalysts were different compared with their monometallic counterparts. The obtained plot gave a volcano-type relation between TOF and E_{bind}(Me−N). Therefore, the interaction of two different MeN_4 sites seemed to positively affect the HER activity. For further confirmation of this statement, we performed DFT calculations for the analysis of HBE. Focusing on the most favorable structures for monometallic and bimetallic catalysts as given in Figure 5a, we have calculated the HBE as a complementary parameter for the interaction of hydrogen with the different MeN_4 sites for all bimetallic catalysts and their monometallic counterparts. At first, we tested different coordinates for H_{ads} on MeN_4 sites, such as on top of metals, on Me−N and N−N bridges, and on hollow sites, and found that the most stable structure was obtained when hydrogen was adsorbed on top of metal atoms as an axial ligand. As mentioned before, in the case of bimetallic catalysts, the reported values for HBE were averaged and compared with those in Table 3. In the case of the most active catalyst, it was also investigated whether the presence of the second metal near the first metal affects the adsorption energy (namely, correlated sites, separated with only two carbon atoms). The related data points were added in the correlation graph of exchange current density j_0 and HBE in Figure 5b as half-filled triangles. Figure 5b indicates that the HBE for CoN_4 + FeN_4 was almost equal to the average value of HBE for their corresponding isolated monometallic MeN_4 sites. However, the HBE for interacting CoN_4 + MoN_4 sites was found at the optimum of catalytic activity (TOF).

On the basis of these calculations, it is suggested that the HBE on MoN_4 sites was weakened by the additional presence of CoN_4 sites. Hence, this more favorable HBE might be at the origin of the improved HER activity of (Co,Mo)−N−C versus the monometallic counterparts. This important result was also in agreement with the larger Bader charge (by 0.05 |e|) for H_{ads} on MoN_4 sites in bimetallic (Co,Mo)−N−C than that in monometallic Mo−N−C catalysts. The Bader charge for H_{ads} on MnN_4 in (Co,Mn)−N−C was also slightly (by 0.01 |e|) larger than that in Mn−N−C, whereas the Bader charge for H_{ads} on FeN_4 was the same in (Co,Fe)−N−C and Fe−N−C. To compare the activity of different mono- and bimetallic catalysts, a detailed study on H diffusion as well as H_2 association and desorption would be required, but this is beyond the scope of this work. This will be the subject of our future work.

Beside an improved activity, our bimetallic catalysts also exhibited an outstanding stability in galvanostatic tests for 6 h of operation, as illustrated in Figure 5c (further short-term durability tests can be found in Figure S12).

In Figure 5d, the TOF of our best performing catalyst, (Co,Mo)−N−C, was compared with the literature data of other Me−N−C catalysts (N-labels), metal sulfides (S-labels), and metal phosphides (P-labels). In Table S4, the exact composition of these short labels and the related references are listed. Finally, Table S5 compares the overpotential, mass-based site density (MSD), and stability of our catalyst to the literature data for other Me−N−C catalysts. It can be seen from Figure 5d and Table S5 that (Co,Mo)−N−C was among the best performing Me−N−C catalysts with an exceptional good stability.

DOI: 10.1021/acsami.7b01647
ACS Appl. Mater. Interfaces 2017, 9, 25184−25193

4. CONCLUSIONS

In this work, the effect of metal species in Me−N−C catalysts was investigated. The synthesis of these catalysts included two heat treatment steps with an acid leaching step in between. The results from structural analysis showed that the catalysts contained up to 17 × 10^{19} MeN_4 sites per gram catalyst and that the amount of MeN_4 species correlated with the energy of formation derived from theoretical calculations. Besides MeN_4 sites, some catalysts also contained inorganic metal species. Based on strong similarities in the HER activity of catalysts with and without inorganic metal species, however, a strong contribution of such inorganic metal species to the HER activity was excluded in our discussion. For monometallic catalysts, a volcano-type relation between d-orbital occupation and the TOF was obtained. A significant improvement was found with respect to the HER activity of bimetallic (Co,Me)−N−C catalysts, with (Co,Mo)−N−C being the most active catalyst in this study. For this particular catalyst, the improved constitution of the catalyst was confirmed by DFT calculations that indicated a positive effect of a second MeN_4 site in the same graphene layer on the HBE of some MeN_4 sites. This improved HBE is supposed to be at the origin of the improved activity of the (Co,Mo)−N−C catalyst. In addition to this, our (Co,Mo)−N−C catalyst also demonstrated a very good stability in the investigated time frame, which could be of great interest for its implementation in solar fuel devices.

■ ASSOCIATED CONTENT

Supporting Information

The Supporting Information is available free of charge on the ACS Publications website at DOI: 10.1021/acsami.7b01647.

Comparison of as-measured cyclic voltammogram and the averaged sweep, XRD, additional data on X-ray-induced photoelectron spectroscopy, description of TOF determination for U = −0.4 V and calculation of mass-based site densities, (Co,Mo)−N−C structure scheme from side view and top view, determination of exchange current density and Tafel slopes and related figures, summary of exchange current densities and Tafel slopes, summary of various TOF data published in literature on other nonprecious metal catalysts applied in alkaline electrolyte, comparison of our Co−N−C and (Co,Mo)−N−C to other Me−N−C catalysts, and investigation of short-term durability of (Co,Me)−N−C catalysts (PDF)

■ AUTHOR INFORMATION

Corresponding Author

*E-mail: kramm@ese.tu-darmstadt.de.

ORCID

Ulrike I. Kramm: 0000-0002-0884-1459

Present Address

△Max-Planck-Institute for Chemical Physics of Solids, Nöthnitzer Straße 40, 01187 Dresden, Germany

Notes

The authors declare no competing financial interest.

■ ACKNOWLEDGMENTS

The possibility to do X-ray-induced photoelectron spectroscopy at the DAISY-FUN system of Wolfram Jaegermann's group at TU Darmstadt is gratefully acknowledged. The authors gratefully acknowledge the computing time granted on the Hessian high-performance computer cluster "Lichtenberg". Financial support by the German Research Foundation (DFG) via the Excellence initiative TU Darmstadt Graduate School of Excellence Energy Science and Engineering (ESE) (GSC1070) is acknowledged.

■ REFERENCES

(1) Edenhofer, O.; Pichs-Madruga, R.; Sokona, Y.; Minx, J.; Farahani, E.; Kadner, S.; Seyboth, K.; Eickemeier, P.; Kriemann, B.; Savolainen, J.; Schlömer, S.; Stechow, C.; Zwickel, T. *Climate Change 2014*; Cambridge University Press: New York, NY, 2014.

(2) Walter, M. G.; Warren, E. L.; McKone, J. R.; Boettcher, S. W.; Mi, Q.; Santori, E. A.; Lewis, N. S. Solar Water Splitting Cells. *Chem. Rev.* **2010**, *110*, 6446−6473.

(3) Fiechter, S.; Bogdanoff, P.; Bak, T.; Nowotny, J. Basic Concepts of Photoelectrochemical Solar Energy Conversion Systems. *Adv. Appl. Ceram.* **2012**, *111*, 39−43.

(4) van de Krol, R.; Liang, Y.; Schoonman, J. Solar Hydrogen Production with Nanostructured Metal Oxides. *J. Mater. Chem.* **2008**, *18*, 2311−2320.

(5) Abdi, F. F.; Han, L.; Smets, A. H. M.; Zeman, M.; Dam, B.; van de Krol, R. Efficient Solar Water Splitting by Enhanced Charge Separation in a Bismuth Vanadate-Silicon Tandem Photoelectrode. *Nat. Commun.* **2013**, *4*, 2195.

(6) Conway, B. E.; Tilak, B. V. Interfacial Processes Involving Electrocatalytic Evolution and Oxidation of H2, and the Role of Chemisorbed H. *Electrochim. Acta* **2002**, *47*, 3571−3594.

(7) Tymoczko, J.; Calle-Vallejo, F.; Schuhmann, W.; Bandarenka, A. S. Making the Hydrogen Evolution Reaction in Polymer Electrolyte Membrane Electrolysers Even Faster. *Nat. Commun.* **2016**, *7*, 10990.

(8) Durst, J.; Siebel, A.; Simon, C.; Hasché, F.; Herranz, J.; Gasteiger, H. A. New Insights Into the Electrochemical Hydrogen Oxidation and Evolution Reaction Mechanism. *Energy Environ. Sci.* **2014**, *7*, 2255−2260.

(9) Badawy, W. A.; Feky, H. E.; Helal, N. H.; Mohammed, H. H. Cathodic Hydrogen Evolution on Molybdenum in NaOH Solutions. *Int. J. Hydrogen Energy* **2013**, *38*, 9625−9632.

(10) Elezović, N. R.; Jović, V. D.; Krstajić, N. V. Kinetics of the Hydrogen Evolution Reaction on Fe−Mo Film Deposited on Mild Steel Support in Alkaline Solution. *Electrochim. Acta* **2005**, *50*, 5594−5601.

(11) Lasia, A.; Rami, A. Kinetics of Hydrogen Evolution on Nickel Electrodes. *J. Electroanal. Chem.* **1990**, *294*, 123−141.

(12) Müller, C. I.; Rauscher, T.; Schmidt, A.; Schubert, T.; Weißgärber, T.; Kieback, B.; Röntzsch, L. Electrochemical Investigations on Amorphous Fe-base Alloys for Alkaline Water electrolysis. *Int. J. Hydrogen Energy* **2014**, *39*, 8926−8937.

(13) McEnaney, J. M.; Soucy, T. L.; Hodges, J. M.; Callejas, J. F.; Mondschein, J. S.; Schaak, R. E. Colloidally-Synthesized Cobalt Molybdenum Nanoparticles as Active and stable Electrocatalysts for the Hydrogen Evolution Reaction under Alkaline Conditions. *J. Mater. Chem. A* **2016**, *4*, 3077−3081.

(14) Gonzalez, E. R.; Avaca, L. A.; Tremiliosi-Filho, G.; Machado, S. A. S.; Ferreira, M. Hydrogen Evolution Reaction on Ni−S Electrodes in Alkaline Solutions. *Int. J. Hydrogen Energy* **1994**, *19*, 17−21.

(15) Staszak-Jirkovský, J.; Malliakas, C. D.; Lopes, P. P.; Danilovic, N.; Kota, S. S.; Chang, K.-C.; Genorio, B.; Strmcnik, D.; Stamenkovic, V. R.; Kanatzidis, M. G.; Markovic, N. M. Design of Active and Stable Co−Mo−Sx Chalcogels as pH-Universal Catalysts for the Hydrogen Evolution Reaction. *Nat. Mater.* **2015**, *15*, 197−203.

(16) Faber, M. S.; Lukowski, M. A.; Ding, Q.; Kaiser, N. S.; Jin, S. Earth-Abundant Metal Pyrites (FeS2, CoS2, NiS2, and Their Alloys) for Highly Efficient Hydrogen Evolution and Polysulfide Reduction Electrocatalysis. *J. Phys. Chem. C* **2014**, *118*, 21347−21356.

(17) Madrama, A. R.; Zonouz, A. F.; Pouretedal, H. R. Kinetic Investigation of Quaternary Ni Fe P C Composite Coating as a New Catalyst for Hydrogen Evolution Reaction. *Port. Electrochim. Acta* **2015**, *33*, 153−163.

DOI: 10.1021/acsami.7b01647
ACS Appl. Mater. Interfaces 2017, 9, 25184−25193

(18) Popczun, E. J.; McKone, J. R.; Read, C. G.; Biacchi, A. J.; Wiltrout, A. M.; Lewis, N. S.; Schaak, R. E. Nanostructured Nickel Phosphide as an Electrocatalyst for the Hydrogen Evolution Reaction. *J. Am. Chem. Soc.* **2013**, *135*, 9267−9270.
(19) Jahnke, H.; Schönborn, M.; Zimmermann, G. Organic Dyestuffs as Catalysts for Fuel Cells. In *Topics in Current Chemistry*; Springer, 1976; Vol. *61*, pp 133−138.
(20) Kramm, U. I.; Bogdanoff, P.; Fiechter, S. Polymer Electrolyte Membrane Fuel Cells (PEM-FC) and Non-noble Metal Catalysts for Oxygen Reduction. In *Encyclopedia of Sustainability Science and Technology*; Meyers, R. A., Ed.; Springer New York: New York, NY, 2012; pp 8265−8307.
(21) Liang, H.-W.; Brüller, S.; Dong, R.; Zhang, J.; Feng, X.; Müllen, K. Molecular Metal−Nx Centres in Porous Carbon for Electrocatalytic Hydrogen Evolution. *Nat. Commun.* **2015**, *6*, 7992.
(22) Kramm, U. I.; Herranz, J.; Larouche, N.; Arruda, T. M.; Lefèvre, M.; Jaouen, F.; Bogdanoff, P.; Fiechter, S.; Abs-Wurmbach, I.; Mukerjee, S.; Dodelet, J.-P. Structure of the Catalytic Sites in Fe/N/C-Catalysts for O2-Reduction in PEM Fuel Cells. *Phys. Chem. Chem. Phys.* **2012**, *14*, 11673−11688.
(23) Kramm, U. I.; Lefèvre, M.; Larouche, N.; Schmeisser, D.; Dodelet, J.-P. Correlations Between mass Activity and Physicochemical Properties of Fe/N/C Catalysts for the ORR in PEM Fuel Cell via ^{57}Fe Mössbauer Spectroscopy and other Techniques. *J. Am. Chem. Soc.* **2014**, *136*, 978−985.
(24) Gupta, S.; Tryk, D.; Bae, I.; Aldred, W.; Yeager, E. Heat-Treated Polyacrylonitrile-based Catalysts for Oxygen Electroreduction. *J. Appl. Electrochem.* **1989**, *19*, 19−27.
(25) Jaouen, F.; Proietti, E.; Lefèvre, M.; Chenitz, R.; Dodelet, J.-P.; Wu, G.; Chung, H. T.; Johnston, C. M.; Zelenay, P. Recent Advances in Non-precious Metal Catalysis for Oxygen-Reduction Reaction in Polymer Electrolyte FuelCells. *Energy Environ. Sci.* **2011**, *4*, 114−130.
(26) Dodelet, J.-P. Oxygen Reduction in PEM Fuel Cell Conditions: Heat-treated Non-precious Metal-N4 Macrocycles and Beyond. In *N4-Macrocyclic Metal Complexes*; Zagal, J. H., Bedioui, F., Dodelet, J.-P., Eds.; Springer New York: New York, NY, 2006; pp 83−147.
(27) Ferrandon, M.; Kropf, A. J.; Myers, D. J.; Artyushkova, K.; Kramm, U.; Bogdanoff, P.; Wu, G.; Johnston, C. M.; Zelenay, P. Multitechnique Characterization of a Polyaniline−Iron−Carbon Oxygen Reduction Catalyst. *J. Phys. Chem. C* **2012**, *116*, 16001−16013.
(28) Kramm, U. I.; Zana, A.; Vosch, T.; Fiechter, S.; Arenz, M.; Schmeißer, D. On the Structural Composition and Stability of Fe−N−C Catalysts Prepared by an Intermediate Acid Leaching. *J. Solid State Electrochem.* **2016**, *20*, 969−981.
(29) Wang, Z.-L.; Hao, X.-F.; Jiang, Z.; Sun, X.-P.; Xu, D.; Wang, J.; Zhong, H.-X.; Meng, F.-L.; Zhang, X.-B. C and N Hybrid Coordination Derived Co−C−N Complex as a Highly Efficient Electrocatalyst for Hydrogen Evolution Reaction. *J. Am. Chem. Soc.* **2015**, *137*, 15070−15073.
(30) Morozan, A.; Goellner, V.; Nedellec, Y.; Hannauer, J.; Jaouen, F. Effect of the Transition Metal on Metal−Nitrogen−Carbon Catalysts for the Hydrogen Evolution Reaction. *J. Electrochem. Soc.* **2015**, *162*, H719−H726.
(31) Jaouen, F.; Marcotte, S.; Dodelet, J.-P.; Lindbergh, G. Oxygen Reduction Catalysts for Polymer Electrolyte Fuel Cells from the Pyrolysis of Iron Acetate Adsorbed on Various Carbon Supports. *J. Phys. Chem. B* **2003**, *107*, 1376−1386.
(32) Tributsch, H.; Koslowski, U. I.; Dorbandt, I. Experimental and Theoretical Modeling of Fe-, Co-, Cu-, Mn-Based Electrocatalysts for Oxygen Reduction. *Electrochim. Acta* **2008**, *53*, 2198−2209.
(33) Varnell, J. A.; Tse, E. C. M.; Schulz, C. E.; Fister, T. T.; Haasch, R. T.; Timoshenko, J.; Frenkel, A. I.; Gewirth, A. A. Identification of Carbon-Encapsulated Iron Nanoparticles as Active Species in Non-Precious Metal Oxygen Reduction catalysts. *Nat. Commun.* **2016**, *7*, 12582.
(34) Strickland, K.; Miner, E.; Jia, Q.; Tylus, U.; Ramaswamy, N.; Liang, W.; Sougrati, M.-T.; Jaouen, F.; Mukerjee, S. Highly Active Oxygen Reduction Non-Platinum Group Metal Electrocatalyst Without Direct Metal−Nitrogen Coordination. *Nat. Commun.* **2015**, *6*, 7343.
(35) Hu, P.; Huang, Z.; Amghouz, Z.; Makkee, M.; Xu, F.; Kapteijn, F.; Dikhtiarenko, A.; Chen, Y.; Gu, X.; Tang, X. Electronic Metal-Support Interactions in Single-Atom Catalysts. *Angew. Chem., Int. Ed.* **2014**, *53*, 3418−3421.
(36) Kramm, U. I.; Abs-Wurmbach, I.; Herrmann-Geppert, I.; Radnik, J.; Fiechter, S.; Bogdanoff, P. Influence of the Electron-Density of FeN_4-Centers Towards the Catalytic Activity of Pyrolyzed FeTMPPCl-based ORR-Electrocatalysts. *J. Electrochem. Soc.* **2011**, *158*, B69−B78.
(37) Kramm, U. I.; Herrmann-Geppert, I.; Behrends, J.; Lips, K.; Fiechter, S.; Bogdanoff, P. On an Easy Way To Prepare Metal−Nitrogen Doped Carbon with Exclusive Presence of MeN4-type Sites Active for the ORR. *J. Am. Chem. Soc.* **2016**, *138*, 635−640.
(38) Kramm, U. I.; Herrmann-Geppert, I.; Fiechter, S.; Zehl, G.; Zizak, I.; Dorbandt, I.; Schmeißer, D.; Bogdanoff, P. Effect of Iron-Carbide Formation on the Number of Active Sites in Fe-N-C Catalysts for the Oxygen Reduction Reaction in Acidic Media. *J. Mater. Chem. A* **2014**, *2*, 2663−2670.
(39) Kresse, G.; Furthmüller, J. Efficient Iterative Schemes for Ab Initio Total-Energy Calculations Using a Plane-Wave Basis Set. *Phys. Rev.* **1966**, *54*, 11169−11186.
(40) Perdew, P.; Burke, K.; Ernzerhof, M. Generalized Gradient Approximation Made Simple. *Phys. Rev. Lett.* **1996**, *77*, 3865−3868.
(41) Kramm, U. I.; Herrmann-Geppert, I.; Bogdanoff, P.; Fiechter, S. Effect of an Ammonia Treatment on Structure, Composition, and Oxygen Reduction Reaction Activity of Fe−N−C Catalysts. *J. Phys. Chem. C* **2011**, *115*, 23417−23427.
(42) Jaouen, F.; Herranz, J.; Lefèvre, M.; Dodelet, J.-P.; Kramm, U. I.; Herrmann, I.; Bogdanoff, P.; Maruyama, J.; Nagaoka, T.; Garsuch, A.; Dahn, J. R.; Olson, T.; Pylypenko, S.; Atanassov, P.; Ustinov, E. A. Cross-Laboratory Experimental Study of Non-Noble-Metal Electrocatalysts for the Oxygen Reduction Reaction. *ACS Appl. Mater. Interfaces* **2009**, *1*, 1623−1639.
(43) Proietti, E.; Jaouen, F.; Lefèvre, M.; Larouche, N.; Tian, J.; Herranz, J.; Dodelet, J.-P. Iron-based Cathode Catalyst with Enhanced Power Density in Polymer Electrolyte Membrane Fuel Cells. *Nat. Commun.* **2011**, *2*, 416.
(44) Zagal, J. H.; Koper, M. T. M. Reactivity Descriptors for the Activity of Molecular MN4 Catalysts for the Oxygen Reduction Reaction. *Angew. Chem., Int. Ed.* **2016**, *55*, 14510−14521.
(45) Calle-Vallejo, F.; Martínez, J. I.; Rossmeisl, J. Density Functional Studies of Functionalized Graphitic Materials with Late Transition Metals for Oxygen Reduction Reactions. *Phys. Chem. Chem. Phys.* **2011**, *13*, 15639−15643.
(46) Jakšić, M. M. Electrocatalysis of Hydrogen Evolution in the Light of the Brewer—Engel theory for Bonding in Metals and Intermetallic Phases. *Electrochim. Acta* **1984**, *29*, 1539−1550.
(47) Sahraie, N. R.; Kramm, U. I.; Steinberg, J.; Zhang, Y.; Thomas, A.; Reier, T.; Paraknowitsch, J.-P.; Strasser, P. Quantifying the Density and Utilization of Active Sites in Non-Precious Metal Oxygen Electroreduction Catalysts. *Nat. Commun.* **2015**, *6*, 8618.
(48) Herrmann, I.; Kramm, U. I.; Fiechter, S.; Bogdanoff, P. Oxalate Supported Pyrolysis of CoTMPP as Electrocatalysts for the Oxygen Reduction Reaction. *Electrochim. Acta* **2009**, *54*, 4275−4287.
(49) Wu, G.; More, K. L.; Johnston, C. M.; Zelenay, P. High-Performance Electrocatalysts for Oxygen Reduction Derived from Polyaniline, Iron, and Cobalt. *Science* **2011**, *332*, 443−447.
(50) Holby, E. F.; Wu, G.; Zelenay, P.; Taylor, C. D. Structure of Fe−Nx−C Defects in Oxygen Reduction Reaction Catalysts from First-Principles Modeling. *J. Phys. Chem. C* **2014**, *118*, 14388−14393.
(51) Karweik, D. H.; Winograd, N. Nitrogen Charge Distributions in Free-Base Porphyrins, Metalloporphyrins, and Their Reduced Analogs Observed by X-ray Photoelectron Spectroscopy. *Inorg. Chem.* **1976**, *15*, 2336−2342.

DOI: 10.1021/acsami.7b01647
ACS Appl. Mater. Interfaces 2017, 9, 25184−25193

Supporting Information

Elucidating the origin of HER activity in mono- and bimetallic metal- and nitrogen-doped carbon catalysts (Me-N-C)

*Ali Shahraei,[†§] Ashkan Moradabadi, [#,||] Ioanna Martinaiou[†||], Stefan Lauterbach[+], Sebastian Klemenz[§§], Stephanie Dolique[§§], Hans-Joachim Kleebe[+], Payam Kaghazchi[#], and Ulrike I. Kramm[†||§] **

kramm@ese.tu-darmstadt.de

[†] TU Darmstadt, Graduate School of Excellence Energy Science and Engineering, Jovanka-Bontschits-Str. 2, 64287 Darmstadt, Germany

[§]TU Darmstadt, Department of Chemistry, Jovanka-Bontschits-Str. 2, 64287 Darmstadt, Germany

[||]TU Darmstadt, Department of Materials- and Earth Science, Jovanka-Bontschits-Str. 2, 64287 Darmstadt, Germany

[§§]TU Darmstadt, Eduard-Zintl-Institute for Physical and Inorganic Chemistry, Alarich-Weiss-Str. 12, 64287 Darmstadt, Germany

[#] Freie Universität Berlin, Department of Chemistry and Biochemistry, Taku Str. 3, 14195 Berlin, Germany

[+] TU Darmstadt, Department of Materials- and Earth Science, Institute of Applied Geosciences, Department of Geometrical Science, Schnittspahn Str.9 64287 Darmstadt

SI contains:

- Figure S1: Comparison of as-measured cyclic voltammogram and the averaged sweep as shown in e.g. Figures 1a and 3a
- Figures S2 and S3: X-ray diffraction of the monometallic and bimetallic Me-N-C catalysts
- Supporting information for X-ray induced photoelectron spectroscopy:
- Table S1: Model for the deconvolution of the N 1s region,
- Figure S4: Exemplary visualization of XPS fine scan regions of the Co-N-C catalyst not implemented in the main manuscript (C 1s, O 1s, Zn 2p and Co 2p),
- Table S2: Summary of elemental composition derived from XPS (a: overall in wt%, b: specific for N 1s region in wt% and c: overall in at%)
- Figure S5, S6: High resolution Me 2p spectra of the Me-N-C catalysts
- Description of TOF determination for U = -0.4V and calculation of mass-based site densities
- Figure S7: Correlation between MSD as derived from XPS [N_{MeN}] contents and the energy of formation of the MeN_4 sites integrated at the edges of the graphene plane
- Figure S8: (Co,Mo)-N-C structure scheme from side view and top view
- Determination of exchange current density and Tafel slopes
- Figures S9 and S10: Tafel-plots after iR-correction (Figure S9) and for as-measured data (Figure S10)
- Table S3: Summary of exchange current densities and Tafel slopes for all investigated catalysts, obtained after iR-correction of the data.
- Figure S11: Correlation of the electronegativity of the metals with the N1s E(Me-N) binding energies in Me-N-C catalysts
- Table S4: Summary of various TOF data published in literature on other non-precious metal catalysts applied in alkaline electrolyte (compare Figure 5d of main manuscript)
- Table S5: Comparison of our Co-N-C and (Co,Mo)-N-C to other Me-N-C catalysts with respect to overpotential, number of active sites per gram catalyst and stability
- Figure S12: Investigation of short-term durability of (Co,Me)-N-C catalysts

Cyclic voltammetry

The average of the forward and backward scans of cyclic voltammetry is reported in the present work to avoid possible capacity effects.

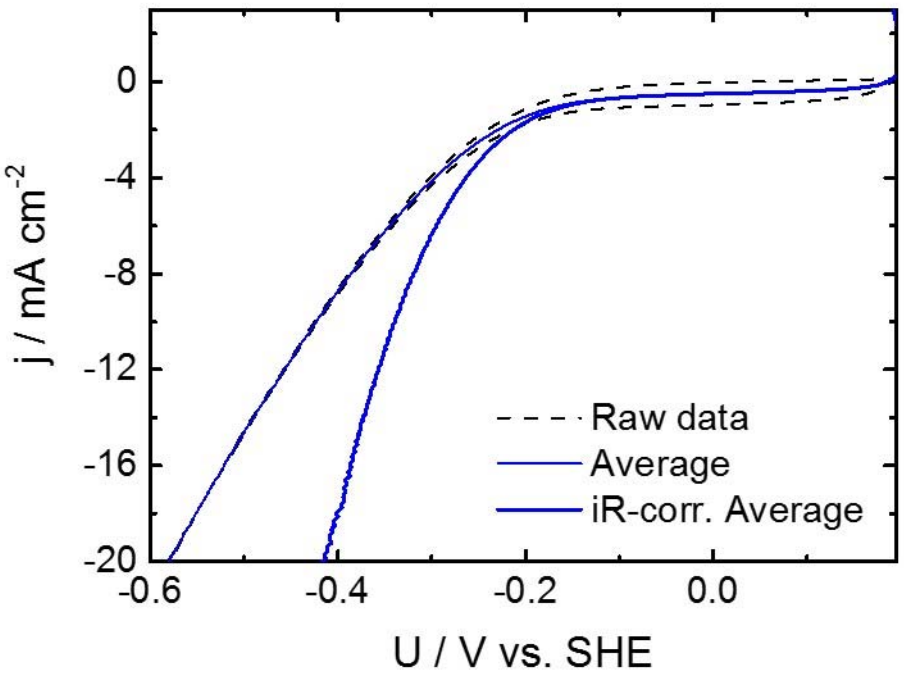

Figure S1. Comparison of as measured cyclic voltammogram of Co-N-C (5 mV s^{-1}) in 0.1M KOH, the average polarization curve – from anodic and cathodic sweep – and after iR correction.

X-ray diffraction images of the monometallic and bimetallic Me-N-C catalysts

Figure S2 and S3 give the X-ray diffractograms of all catalysts. Under such conditions, e.g. the typical diffraction patterns of metal carbides and nitrides would show-up in a 2θ-region of 16 to 24 ° (when measured with Mo-$K_{\alpha 1}$) and at about 40 – 46 ° (when measured with Cu $K_{\alpha 1}$). Only for Co-N-C, Zn-N-C weak indications of diffraction pattern assigned to nitrides/carbides were found, whereas the other catalysts exhibit a predominantly x-ray amorphous behavior. In the case of Cu-N-C intense reflexes assigned to the copper crystalline phase were found.

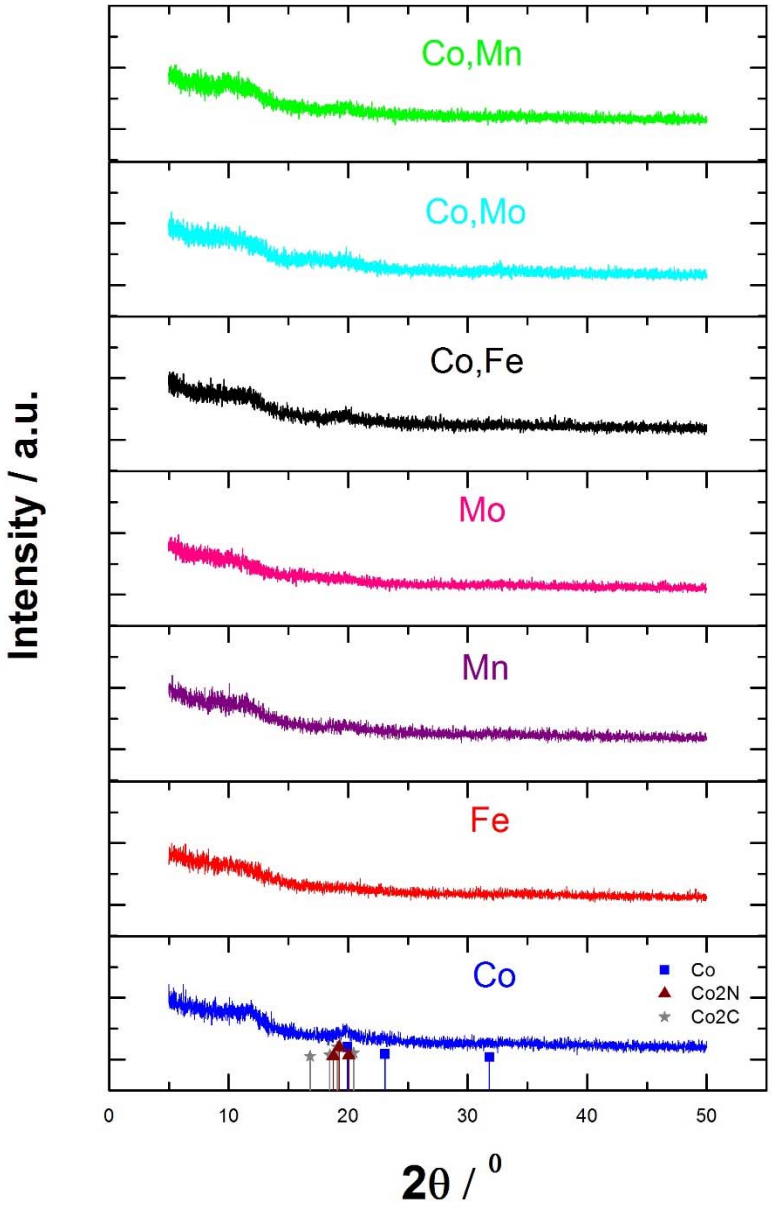

Figure S2. X-ray diffractograms of the Me-N-C catalysts. Measurements were performed with Mo-$K_{\alpha 1}$ radiation.

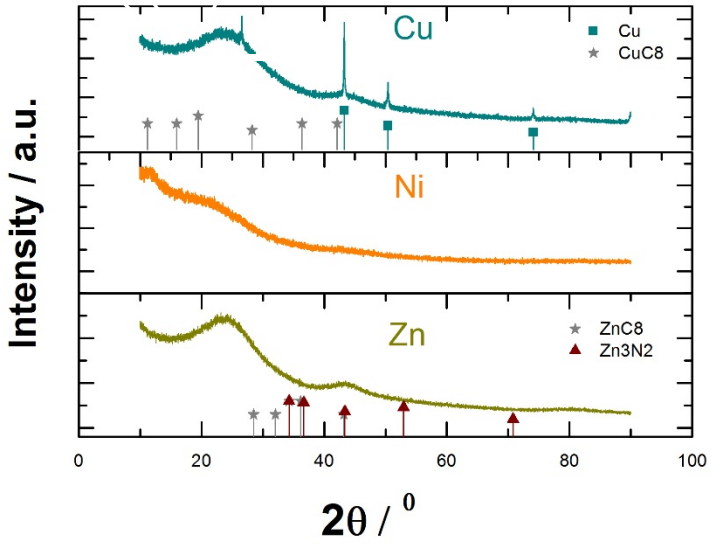

Figure S3. X-ray diffractograms of the Me-N-C catalysts. Measurements were performed with Cu-$K_{\alpha 1}$ radiation.

Exemplary visualization of XPS fine scan regions of the Co-N-C catalyst.

Table S1. Summary of N1s energies assigned to the related chemical species found in Me-N-C catalyst. The G1 $N_{graphitic}$ peak might overlay with the $N_{pyrrolic}$ configuration within the N 1s spectrum.

	Pyridinic	**Me-N**	**Pyrrolic**	**Graphitic**	**Oxidized**
Binding energy	397 – 399.5	399 – 400.5	400.2 – 400.9	401 - 403	402 - 405
Me C N H		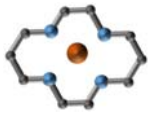		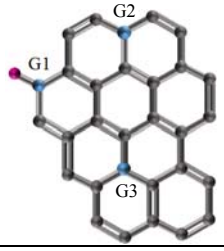	

For Co-N-C the different fine scan regions beside N1s (see main manuscript for it) are given that were used for the evaluation of elemental composition of each catalyst.

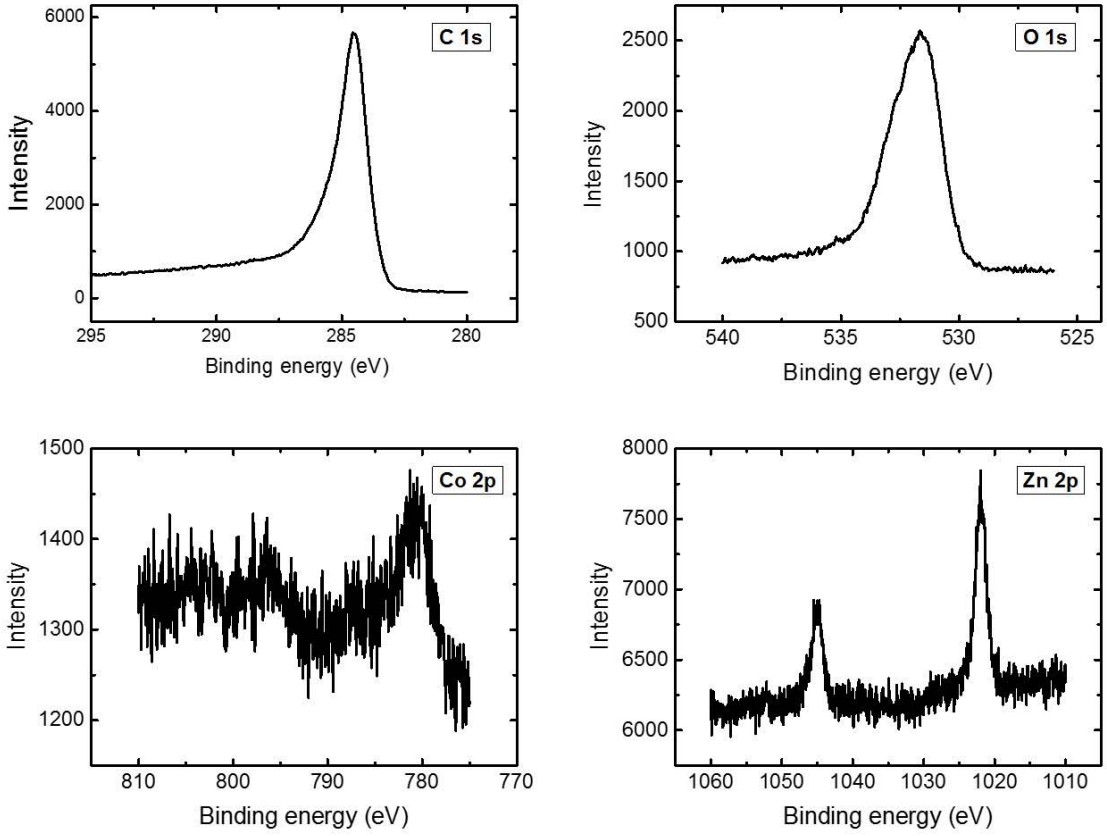

Figure S4. XPS C 1s, O 1s, Co 2p and Zn 2p spectra of the Co-N-C catalyst (N1s is shown in the main text).

Table S2. Elemental compositions derived from XPS for all Me-N-C catalysts (a) and specifically for the nitrogen species (b) in wt%. In (c) the elemental composition in at% is given for all Me-N-C catalysts for the sake of comparison to other publications. In all Tables values are ordered with decreasing overpotential. That means Mn-N-C had the largest overpotential and (Co,Mo)-N-C the smallest.

Table S2a.

(a)	Corres. Metal	Co in bimetallic	Zn *	C	O	N	thereof Me-N-coord. / %
Mn	2.9		3.7	76.2	7.9	9.3	15.2
Zn	5.3		0.0	79.6	7.3	7.8	11.7
Mo	0.5		8.0	78.9	7.8	4.8	12.7
Cu	2.9		3.2	75.3	9.5	9.2	11.7
Fe	3.0		n.d.	75.2	13.2	8.6	14.2
Ni	3.5		3.3	77.2	6.1	9.9	16.3
Co	2.3		3.2	71.7	15.0	7.9	14.9
Co,Fe	1.3	1.5	3.2	75.5	9.1	9.4	15.0
Co,Mn	0.2	4.1	3.4	75.6	8.8	7.9	10.9
Co,Mo	0.2	0.4	1.1	83.5	9.0	5.8	14.8

Table S2b.

(b)	$N_{pyrid.}$	N_{MeN}	$N_{pyrrol.}$	N_{ox}	Sum $N_{graphitic}$	N_{graph1}	N_{graph2}
Mn	3.7	1.4	1.9	0.54	1.8	1.0	0.73
Zn	3.1	0.91	1.6	1.2	1.0	0.67	0.37
Mo	1.7	0.61	1.3	0.65	0.51	0.26	0.25
Cu	4.1	1.1	0.83	1.2	2.0	1.4	0.63
Fe	3.7	1.2	1.1	0.58	2.0	0.87	1.1
Ni	4.1	1.6	1.5	0.56	2.1	0.96	1.1
Co	3.1	1.2	1.4	0.25	1.9	0.81	1.1
Co,Fe	3.8	1.4	1.3	1.2	1.7	0.85	0.88
Co,Mn	3.3	0.86	0.66	0.71	1.8	0.91	0.91
Co,Mo	2.0	0.86	1.3	0.39	1.2	0.75	0.50

Table S2c.

(c)	Corres. Metal	Co in bimetallic	Zn *	C	O	N
Mn	0.7		0.7	83.3	6.5	8.7
Zn	1.1		0.0	85.9	5.9	7.2
Mo	0.5		1.6	56.9	6.5	4.5
Cu	0.6		0.6	82.3	7.8	8.6
Fe	0.7		n.d	80.6	10.7	7.9
Ni	0.8		0.7	84	5	9.3
Co	0.5		0.7	79.0	12.4	7.4
Co,Fe	0.3	0.3	0.7	82.3	7.4	8.8
Co,Mn	0.2	0.9	0.8	83.3	7.3	7.4
Co,Mo	0.2	0.4	1.1	86.2	6.9	5.1

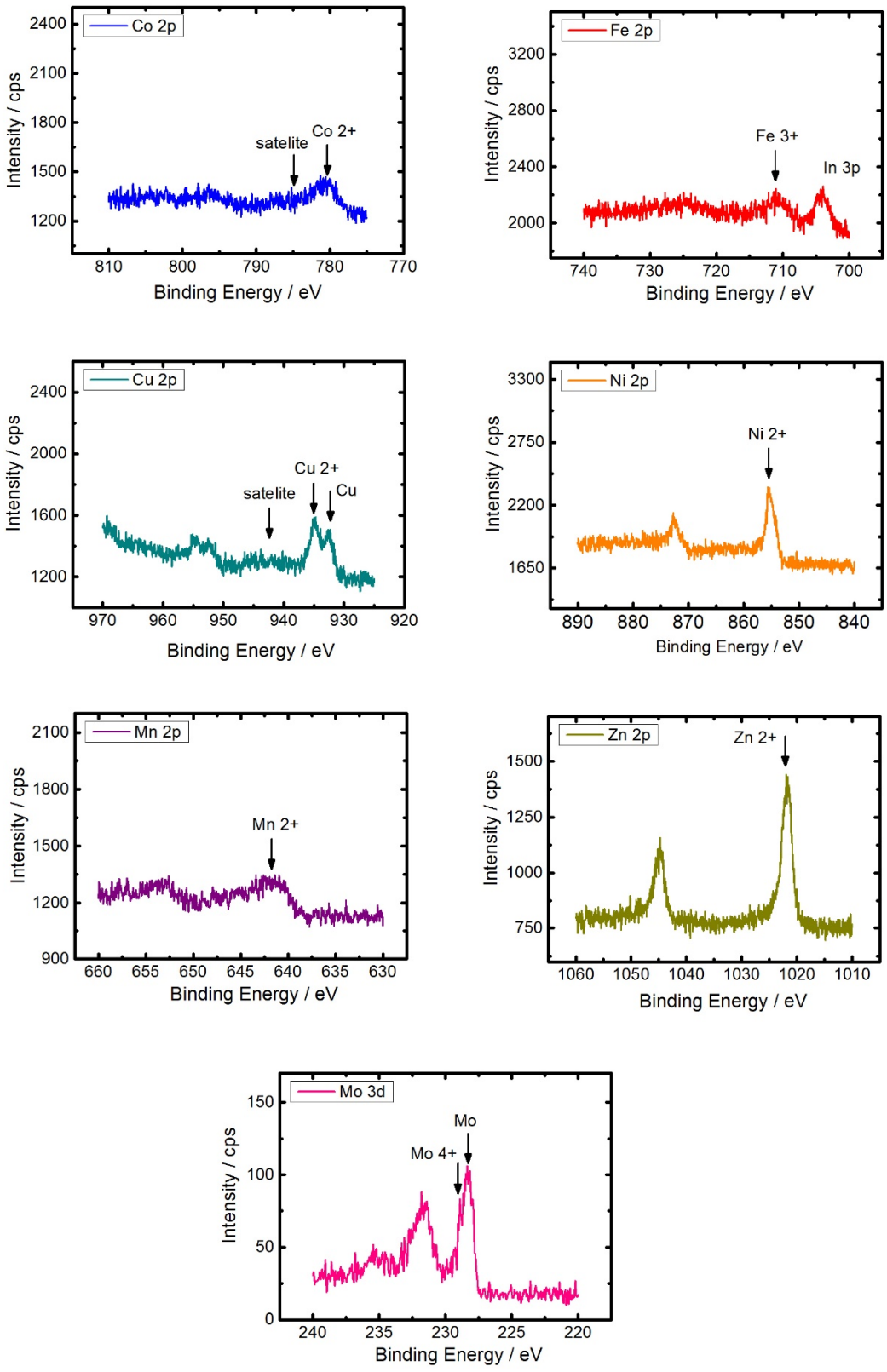

Figure S5. High resolution Me 2p spectra of the monometallic Me-N-C catalysts, metal species are indicated in the 2p 3/2 part of the spectra.

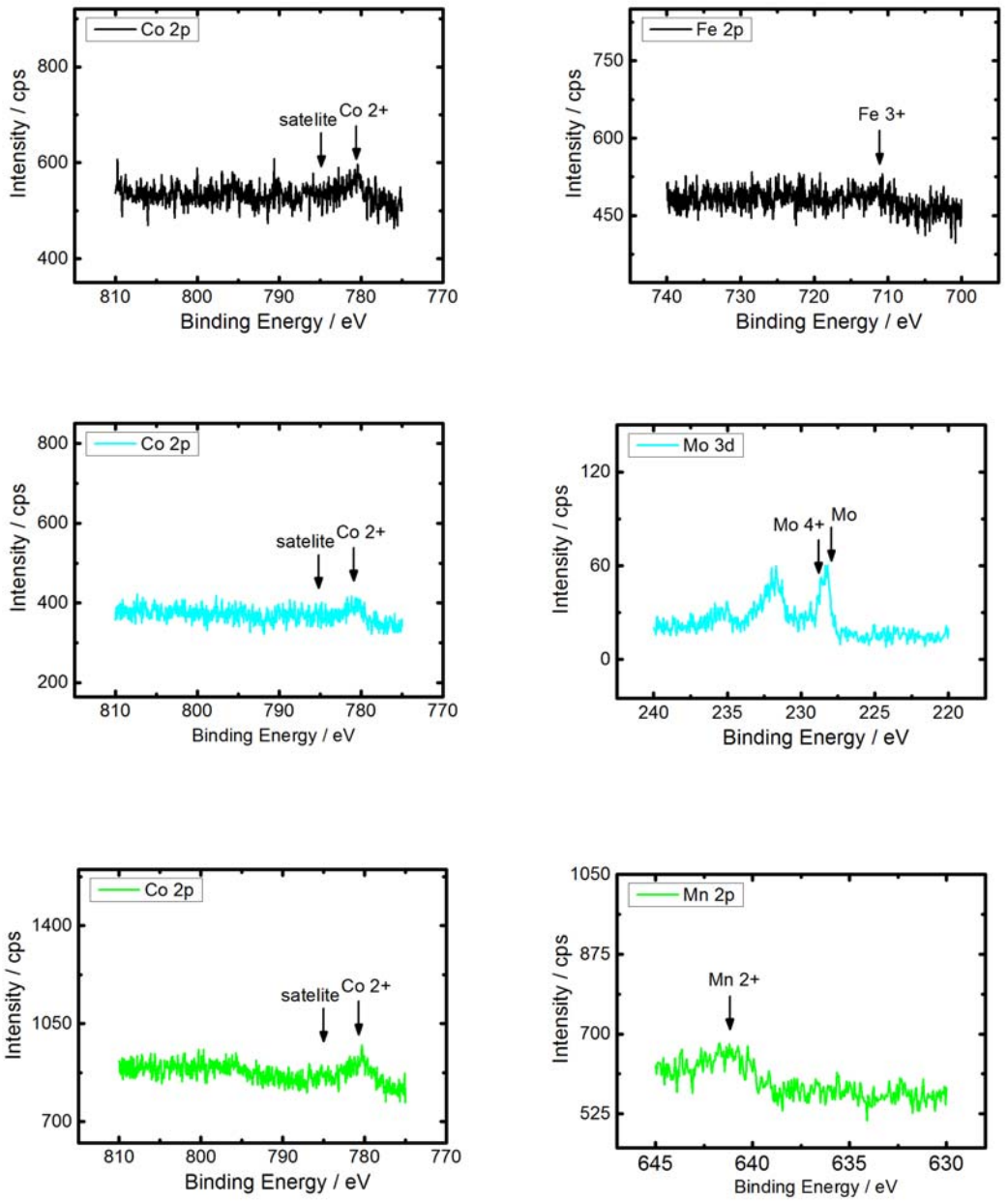

Figure S6. High resolution Me 2p spectra of the Me-N-C catalysts (bimetallic), metal species are indicated in the 2p 3/2 part of the spectra.

Calculation of the turn-over frequency (TOF) and mass-based site density (MSD)

The turn-over frequency is estimated assuming that the main part of the current density is attributed to MeN_4 sites and that the overall number of MeN_4 sites in a catalyst is participating in the reaction.

The mass-based site density of MeN_4 sites (MSD) can be estimated from the XPS N 1s fine scan. Based on the results of this work, it is assumed that MeN_4 sites are exclusively formed by coordination of the metal ions with nitrogen assigned to N_{MeN}. The content of nitrogen assigned to this peak is labelled as $[N_{MeN}]$ and is given in wt%. It is related to mesomerically coordinated MeN_4 sites that were found as active sites for a group of FeN_4 sites investigated for the ORR.[1] Therefore, the weight percentage of metal assigned to MeN_4 sites $[Me_{MeN4}]$ can be calculated if in addition to $[N_{MeN}]$ the atomic ratio of Me:N = 1:4 and the ratio of molar masses of M_{Me}:M_N are considered:

$$[Me_{MeN4}] = A_{MeN} \times [N_{total}]_{wt\%} \times ¼ \times M_{Me}/M_N \quad \textbf{(S.Eq. 1)}$$

A_{MeN} is the area in the N 1s region that is assigned to the N_{MeN} peak, $[N_{total}]_{wt\%}$ is the overall weight percentage of nitrogen, ¼ is related to the ratio Me:N and M_{Me}/M_N is the ratio of molar masses of the metal vs. nitrogen. Hence, MSD has a unit of "mass of metal assigned to MeN_4 sites per mass of catalyst" in weight percentage.

E.g. for cobalt: $[Co_{CoN4}] = 14.9\ \% \times 7.89\ wt\% \times ¼ \times 58.93/14 = 1.24\ wt\% = 0.0124\ g_{Co\ in\ CoN4}\ g_{cat}^{-1}$

The current densities j(-0.4V) can be converted to mass-based current densities J(-0.4V) when they are divided by the catalyst loading of 2 mg_{cat} cm^{-2}. The current density can be converted to the number of transferred electrons per second if it is divided by the Faraday constant, F = 96485 A s mol^{-1}. As the ratio H_2:e- is 1:2 the obtained value has to be multiplied by ½.

$$\dot{n}_{H2} = j(-0.4V) / (W \times F) \times ½ \quad \textbf{(S.Eq. 2)}$$

$\dot{n}_{H2}\ (Co) = 16.78\ mA\ cm^{-2} / (2\ mg_{cat}\ cm^{-2} \times 96485\ A\ s\ mol^{-1}) \times ½ = 4.35\ 10^{-5}\ mol\ H_2\ s^{-1}\ g_{cat}^{-1}$.

If this hydrogen molar flux $\dot{n}_{H2}$ is divided by $[Me_{MeN4}]$ one gets a turn over number as given below:

$$N_{TO} = \dot{n}_{H2} \times [Me_{MeN4}]^{-1} \quad \textbf{(S.Eq. 3)}$$

$N_{TO}\ (Co) = \dot{n}_{H2}\ (Co) / [Me_{MeN4}]\ (Co) = 0.0035\ mol\ H_2\ s^{-1}\ g_{Co\ in\ CoN4}^{-1}$.

In order to obtain the turn-over frequency N_{TO} needs to be multiplied by the molar mass of the metal:

$$\textbf{TOF} = N_{TO} \times M_{Me} \quad \textbf{(S.Eq. 4)}$$

$\textbf{TOF (Co)} = 0.0035\ mol\ H_2\ s^{-1}\ g_{Co\ in\ CoN4}^{-1} \times 58.93\ g_{Co}\ mol^{-1} = \textbf{0.21 } \mathbf{H_2\ s^{-1}\ CoN_4^{-1}}$

If one follows up the calculation (S.Eqs. 1-4), it becomes clear that the molar mass of the metal can be cancelled out in the overall TOF calculation by this approach, as basically the nitrogen content assigned to active sites is considered.

For the calculation of the mass-based site density MSD, the value $[Me_{MeN4}]$ is divided by the molar mass of the metal M_{Me} and multiplied by Avogardo's constant N_A.

$$\textbf{MSD} = [Me_{MeN4}] \times M_{Me}^{-1} \times N_A \qquad \textbf{(S.Eq. 5)}$$

$$\textbf{\textit{MSD (Co)}} = 0.0124\ g_{Co\ in\ CoN4}\ g_{cat}^{-1} \times (58.93\ g_{Co}\ mol^{-1})^{-1} \times 6.022 \cdot 10^{23}\ mol^{-1} = 12.6 \cdot 10^{19}\ sites\ g_{cat}^{-1}$$

Combining S.Eq. 1 and S.Eq. 5, it becomes apparent that also for MSD determination, the molar mass of the metal is cancelled out and MSD is directly related to the nitrogen content assigned to MeN_4 species $[N_{MeN}]$.

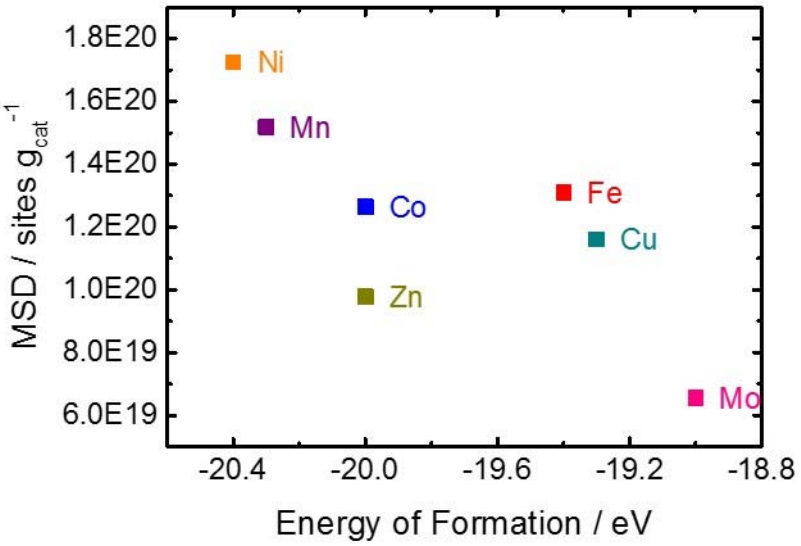

Figure S7. Correlation between MSD as derived from XPS [N_{MeN}] contents and the energy of formation of the MeN_4 sites integrated at the edges of graphene layers.

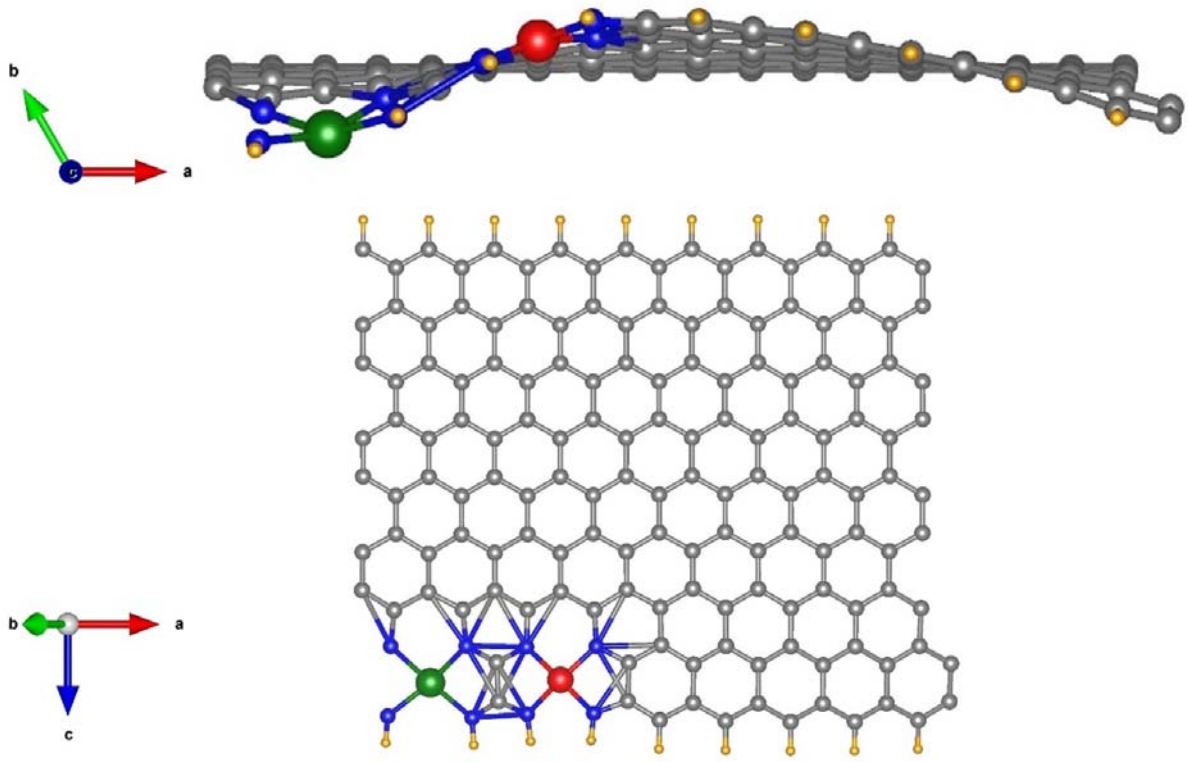

Figure S8. The favorable proposed structure of (Co,Mo)-N-C from side and top view (green: Mo site, red: Co site, blue: coordination by nitrogen).

Determination of exchange current density and Tafel slopes

In order to evaluate the intrinsic activity Tafel plot has been applied, which is shown for some of the catalysts in Figures S6 and S7. Owing Tafel equation $\eta = b\ log|j/j_0| + E_0$, the exchange current density corresponds to zero overpotential (each value has been estimated by extrapolating the Tafel plots). In order to account for the variation in the number of active MeN_4 sites, the obtained geometric current density was first related to the catalyst mass (by utilizing the electrode loading (mg cm^{-2})) and then the weight percentage of nitrogen assigned to Me-N-coordination.

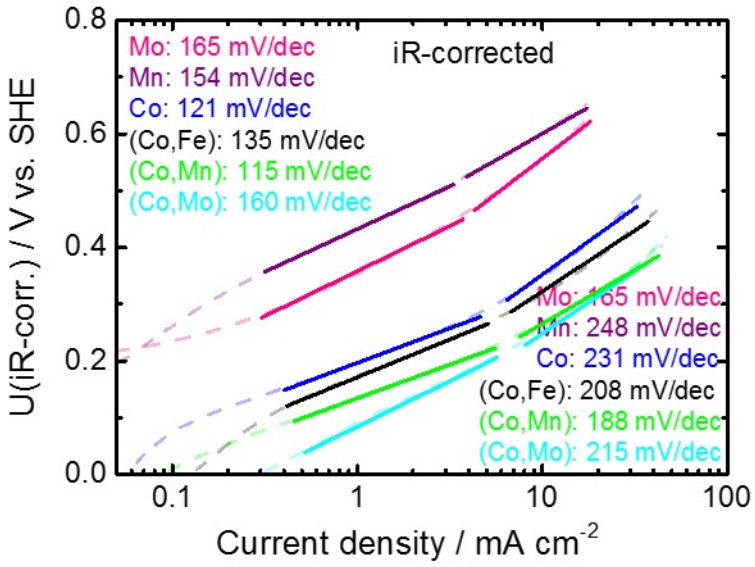

Figure S9. Tafel plots obtained from HER polarization curves related to high and low overpotential **after** iR correction.

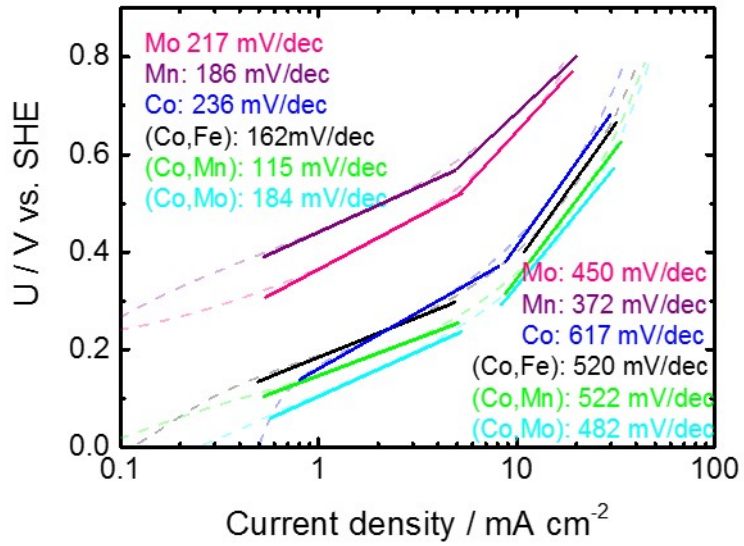

Figure S10. Tafel plots obtained from HER polarization curves related to high and low overpotential **without** iR correction.

Table S3. Tafel slope and exchange current density values driven from Tafel plot

Me in Me-N-C	**- log i_0 (A cm^{-2})**	**iR corrected-Tafel slope (mV/dec) (low-current density range)**
Mn	-5.8	154
Zn	-5.0	200
Mo	-5.4	165
Cu	-5.0	176
Fe	-4.4	164
Ni	-4.2	195
Co	-4.7	121
(Co,Fe)	-4.1	135
(Co,Mn)	-4.2	115
(Co,Mo)	**-3.5**	**160**

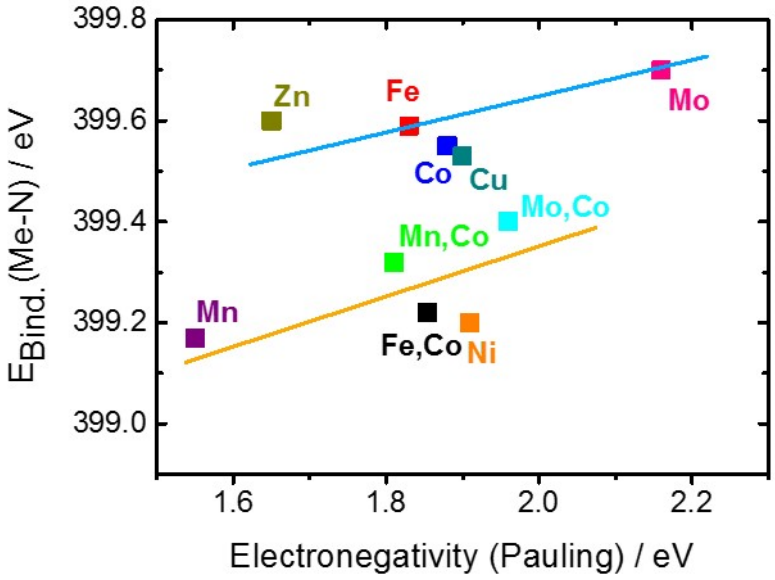

Figure S11. Correlation of metals electronegativity with corresponding Me-N binding energy analyzed with XPS.

Comparison of TOF data to literature

Table S4. Report of TOF value for active catalysts in alkaline medium

Type of catalyst	Label (Fig. 4d)	Ref.	Information on TOF data
Ni_2P	P1	2	Provided
MoP	P2	3	Provided
CoP	P3	4	Provided
MoS_3	S1	5	Provided
$[Mo_3S_{13}]^{2-}$	S2	6	Provided
CoN_xC	N1	7	Provided
CoNG	N2	8	Provided
Co@N-C	N3	9	Calculated*
Co-N-C	N4	10	Calculated*
Co-N-C	N5	11	Calculated*
CoS_x	S3	12	Calculated*
MoS_x	S4	12	Calculated*
$MoCoS_x$	S5	12	Calculated*

*Calculations are based on data (over-potential and metal contents as active sites) provided by the authors in the related works and might therefore be considered as approximate TOF values.

Table S5. Comparison of Co-N-C catalysts published in literature to our Co-N-C and (Co, Mo)-N-C.

Catalyst (temperature °C)	Overpotential (@ -1 mA cm^{-2}) / V	Mass-based site density / 10^{19} Sites g^{-1}_{cat}	Stability	Reference
Co-N-C (CoTMPP) (750)	140	No information	No information	7
Co-N-C (Co-*o*PD) (750)	70	1.4	~No loss After 2000 cycles	7
Co-N-C (MOF-based)(1050)	257	153	No information	11
Co-N-C(PANI-based) (750)	81	10.2	3% overpotential loss @ -10 mA cm^{-2} after 5000 cycles between 0.20 and −0.2 V	10
Co-N-C (950)	**171**	**12.6**	**5%** overpotential loss @ -10 mA cm^{-2} after 6 hr @ -10 mA cm^{-2}	**This work**
(Co,Mo)-N-C (950)	**88**	**9.2**	**< 1%** overpotential loss @ -10 mA cm^{-2} after 6 hr @ -10 mA cm	**This work**

Investigation of short-term durability of (Co,Me)-N-C catalysts

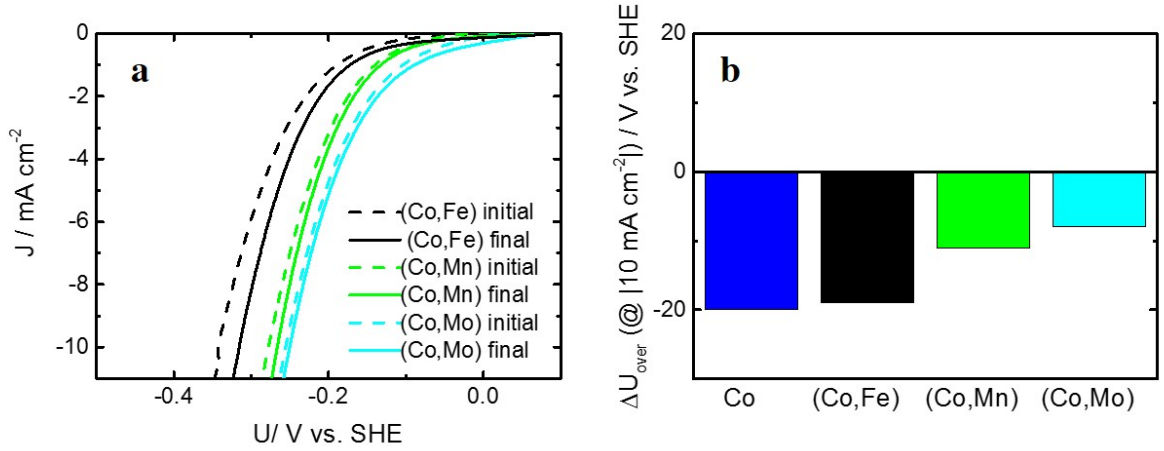

Figure S12. a) Average cyclic voltammograms of initial and final polarization curves during short durability test for bimetallic catalysts, b) activity improvement after short durability test (100 cycles, 100 mV s^{-1}) of bimetallic catalysts.

REFERENCES

(1) Kramm, U. I.; Abs-Wurmbach, I.; Herrmann-Geppert, I.; Radnik, J.; Fiechter, S.; and Bogdanoff, P. Influence of the Electron-Density of FeN4-Centers Towards the Catalytic Activity of Pyrolyzed FeTMPPCl-based ORR-Electrocatalysts. *J. Electrochem. Soc.* **2011**, *158*, B69-B78, DOI: 10.1149/1.3499621.

(2) Popczun, E. J.; McKone, J. R.; Read, C. G.; Biacchi, A. J.; Wiltrout, A. M.; Lewis, N. S.; Schaak, R. E. Nanostructured Nickel Phosphide as an Electrocatalyst for the Hydrogen Evolution Reaction. *J. Am. Chem. Soc.* **2013**, *135*, 9267–9270, DOI: 10.1021/ja403440e.

(3) Kibsgaard, J.; Jaramillo, T. F. Molybdenum Phosphosulfide: An Active, Acid-Stable, Earth-Abundant Catalyst for the Hydrogen Evolution Reaction. *Angew. Chem., Int. Ed. Engl.* **2014**, *53*, 14433–14437, DOI: 10.1002/anie.201408222.

(4) Popczun, E. J.; Read, C. G.; Roske, C. W.; Lewis, N. S.; Schaak, R. E. Highly Active Electrocatalysis of the Hydrogen Evolution Reaction by Cobalt Phosphide Nanoparticles. *Angew. Chem., Int. Ed. Engl.* **2014**, *53*, 5427–5430, DOI: 10.1002/anie.201402646.

(5) Merki, D.; Fierro, S.; Vrubel, H.; Hu, X. Amorphous Molybdenum Sulfide Films as Catalysts for Electrochemical Hydrogen Production in Water. *Chem. Sci.* **2011**, *2*, 1262–1267, DOI: 10.1039/C1SC00117E.

(6) Kibsgaard, J.; Jaramillo, T. F.; Besenbacher, F. Building An Appropriate Active-Site Motif into a Hydrogen-Evolution Catalyst with Thiomolybdate [Mo3S13]2− Clusters. *Nat. Chem.* **2014**, *6*, 248–253.

(7) Liang, H.-W.; Brüller, S.; Dong, R.; Zhang, J.; Feng, X.; Müllen, K. Molecular Metal-Nx Centers in Porous Carbon for Electrocatalytic Hydrogen Evolution. *Nat. Commun.* **2015**, *6, 7992*. DOI: 10.1038/ncomms8992.

(8) Fei, H.; Dong, J.; Arellano-Jiménez, M. J.; Ye, G.; Dong Kim, N.; Samuel, E. L. G.; Peng, Z.; Zhu, Z.; Qin, F.; Bao, J. ; Yacaman, M. J.; Ajayan, P. M.; Chen, D.; Tour, J. Atomic Cobalt on Nitrogen-Doped Graphene for Hydrogen Generation. *Nat. Commun.* **2015**, *6*, 8668, DOI: 10.1038/ncomms9668.

(9) Wang, J.; Gao, D.; Wang, G.; Miao, S.; Wu, H.; Li, J.; Bao, X. Cobalt Nanoparticles Encapsulated in Nitrogen-Doped Carbon as a Bifunctional Catalyst for Water Electrolysis. *J. Mater. Chem. A* **2014**, *2*, 20067–20074, DOI: 10.1039/C4TA04337E.

(10) Wang, Z.-L.; Hao, X.-F.; Jiang, Z.; Sun, X.-P.; Xu, D.; Wang, J.; Zhong, H.-X.; Meng, F.-L.; Zhang, X.-B. C and N Hybrid Coordination Derived Co–C–N Complex as a Highly Efficient Electrocatalyst for Hydrogen Evolution Reaction. *J. Am. Chem. Soc.* **2015**, *137*, 15070–15073, DOI: 10.1021/jacs.5b09021.

(11) Morozan, A.; Goellner, V.; Nedellec, Y.; Hannauer J. Effect of the Transition Metal on Metal–Nitrogen–Carbon Catalysts for the Hydrogen Evolution Reaction. *J. Electrochem. Soc.* **2015**, *162*, H719-H726.

(12) Staszak-Jirkovský, J.; Malliakas, C. D.; Lopes, P. P.; Danilovic, N.; Kota, S. S.; Chang, K.-C.; Genorio, B.; Strmcnik, D.; Stamenkovic, V. R.; Kanatzidis, M. G.; Markovic, N. M. Design of Active and Stable Co–Mo–Sx Chalcogels as pH-Universal Catalysts for the Hydrogen Evolution Reaction. *Nat. Mater.* **2015**, *15*, 197–203, DOI: 10.1038/nmat4481.

4.1.2 Variation of Co-content for HER in acid

In the scope of this project, a new multi-heteroatom doping approach was introduced using polymerized aniline (PANI). The sulfur- and nitrogen-rich PANI provides a hybrid structure with different possible active sites for HER. In order to elucidate the main active site for HER, a variation of the cobalt loading (wt%) in the precursor was performed. Several surface and bulk characterization techniques beside post-mortem XPS analysis support the discussion reported in this publication.

Contribution to the project: Project supervision (Two master's advance research projects related to this article), XPS characterization, Post-mortem XPS, Data analysis and writing

ChemPubSoc Europe

DOI: 10.1002/chem.201802684

CHEMISTRY
A European Journal
Communication

Hydrogen Evolution

Exploring Active Sites in Multi-Heteroatom-Doped Co-Based Catalysts for Hydrogen Evolution Reactions

Ali Shahraei,[a, b] Ioanna Martinaiou,[a, c] K. Alexander Creutz,[c] Markus Kübler,[b] Natascha Weidler,[c] Simon T. Ranecky,[c] W. David Z. Wallace,[b] Mohammad Ali Nowroozi,[c] Oliver Clemens,[c] Robert W. Stark,[c] and Ulrike I. Kramm*[a, b, c]

Abstract: Today, metal–N- as well as metal–S-doped carbon materials are known to catalyze the hydrogen evolution reaction (HER). However, especially N- and S-co-doped catalysts reach highest activity, but it remains unclear if the activity is related to MN_x or MS_y (M = metal) sites. In this work we apply a simple method for multi-heteroatom doping and investigate the effect of cobalt content on the HER in acidic medium. The CoN_x and CoS_y sites were evidenced on the basis of structural characterization by Raman, X-ray induced photoelectron spectroscopy, and TEM. The presence of sulfur enables the formation of a larger number of CoN_x sites. Structure–performance relationship proves that the HER activity is dominated by CoN_x rather than CoS_y sites. The most active catalysts also exhibit an excellent stability under galvanostatic conditions making them of interest for electrolyser application.

In view of the energy transition to meet CO_2-reduction targets, renewable energies have to be used extensively. However, their volatility and fluctuation encourage the search for possibilities to store the produced electric energy. Since hydrogen is multifunctional and enables sector coupling, it is considered the most promising solution.[1] Even though water electrolysis is recognized as the key technology to produce hydrogen, there are several technical and financial issues hindering the application in combination with renewable energy setups that might be operated in isolation. For such isolated operation, the use of cheap and earth-abundant catalysts for the hydrogen evolution reaction (HER) and oxygen evolution reaction (OER) is anticipated to replace Pt- and Ir-based catalysts.[2–4] In this way, the final price might be reduced down to 10% in the large scale.[5] In the last decades, third row transition-metal phosphides, sulfides, selenides, and oxides received considerable attention for the HER.[6,7]

Also, M–N–C (M = metal) catalysts have been a recent focus for catalysis of the HER.[8,9] Better known from the oxygen reduction reaction (ORR) fuel cell and metal air battery applications, experimental and theoretical approaches have shown that the ORR activity comes from MN_4 moieties embedded in the graphene layers.[10,11] Hence, M–N–C catalysts are the heat-treated analogues of MN_4 macrocycles. Consequently, they became of interest for several other electrochemical reactions.[8,12] Various approaches have been reported to improve the performance of these non-precious catalysts; for example, encapsulation of the metal within carbon nanotubes (CNT),[3,13] additional thermal treatment,[11,14–16] modification with ionic liquids,[17] or integration of a secondary nitrogen precursor.[18] Also a modification with sulfur has been intensely investigated.[19,20] Kramm et al. showed that sulfur can hinder iron carbide formation, leading to the destruction of MN_4 sites.[21] However, there are only few reports on the impact of sulfur modification on the HER on M–N–C catalysts. Deng et al. synthesized a CoNS-C catalyst with cobalt complexes as active centers in alkaline and neutral medium.[19] The integration of sulfur becomes even more of interest as MS_y sites were found to catalyze the HER.[22,7,23]

There is no systematic study that elucidates the role of sulfur in multi-heteroatom doped M–N–C catalysts for the HER. Therefore, we synthesized a series of catalysts from polyaniline (PANI), dicyandiamide (DCDA) in combination with different quantities of cobalt acetate. The change in cobalt content enabled the optimization of HER activity, while a comprehensive structural characterization helped to elucidate structure–activity relationships. In our previous work, we showed that MN_4 sites are responsible for the HER in alkaline medium and that the activity can even be improved by integrating a second metal such as manganese or molybdenum. Therefore, the concept of a bimetallic (Co,Mn)–N–C_{evap} catalyst was also tested in this work.

For the preparation of multi-heteroatom doped Co-based catalysts, $PANI_{evap}$ was used as a carbon, nitrogen and sulfur precursor. Sulfur is present as after oxidative polymerization of aniline by ammonium peroxidisulfate (APS), the solvent is just evaporated. The near-surface composition was determined

[a] A. Shahraei, I. Martinaiou, Prof. Dr. U. I. Kramm
TU Darmstadt,
Graduate School of Excellence Energy Science and Engineering
Otto-Berndt-Str. 3, 64287 Darmstadt (Germany)
E-mail: kramm@ese.tu-darmstadt.de

[b] A. Shahraei, M. Kübler, W. D. Z. Wallace, Prof. Dr. U. I. Kramm
TU Darmstadt, Department of Chemistry
Otto-Berndt-Str. 3, 64287 Darmstadt (Germany)

[c] I. Martinaiou, K. A. Creutz, Dr. N. Weidler, S. T. Ranecky, M. A. Nowroozi, Prof. Dr. O. Clemens, Prof. Dr. R. W. Stark, Prof. Dr. U. I. Kramm
TU Darmstadt, Department of Material and Earth Sciences
Otto-Berndt-Str. 3, 64287 Darmstadt (Germany)

Supporting information and the ORCID identification number(s) for the author(s) of this article can be found under:
https://doi.org/10.1002/chem.201802684.

from XPS and compared to our reference $PANI_{ref}$ (as prepared by filtration of the PANI product). The elemental composition is given in Table 1. Figure 1a shows the survey XP scans of $PANI_{evap}$ and $PANI_{ref}$; these results indicate that $PANI_{evap}$ contains 14 at% S, while $PANI_{ref}$ is almost free of sulfur and that the nitrogen content is also higher for $PANI_{evap}$. Both, the increase of sulfur and nitrogen are related to the presence of APS residuals after solvent evaporation. For a better evaluation of the change in HER activity as a function of the preparation steps, the cyclic voltammetry data of Co_2–N–C were evaluated after a first heat treatment (HT1), HT1 + acid leaching (HT1 + AL), and after a second heat treatment (HT2) see Figure 1b. The acid leaching step (AL) was applied to remove undesired inorganic by-products that might have been formed during preparation, but which are unstable in an acidic environment. As expected, activity can be observed already for the HT1 sample. Induced by AL, the HER activity was found to decrease, which indicates that some HER active species were formed during HT1 that do not withstand acidic conditions. Such species would have hindered structure–performance correlations. The best activity is achieved after HT2. This effect is commonly known for M–N–C catalysts.[15,24] When performed in an inert gas atmosphere, the increase in activity was basically correlated with an increase in BET surface area.[25]

In Figure 1b, also the HER activities of reference catalysts—all prepared as HT1-AL-HT2—and Pt/C are reported. It becomes clear, that cobalt is needed for the formation of highly active catalysts, as evidenced from the comparison to the badly performing metal-free N–C_{evap} catalyst. Also, the presence of considerable S-fractions in the precursor is beneficial, as the catalyst Co_2–N–C_{ref} prepared with $PANI_{ref}$ displays a low activity. An almost identical performance is given for Co_2–N–C HT2 and $(Co,Mn)_2$–N–C HT2. This bi-metallic catalyst was prepared in relation to our previous finding of improved activity and stability by integration of a second metal.[26] The most active catalyst in our study shows for 10 mA cm^{-2} a difference of 150 mV versus Pt/C as the reference catalyst.

An interpretation of the achieved activity trends can be attempted from the comparison of the structural compositions as derived from XPS and HER activities.

Comparing the composition of PANI precursors with the one of the catalysts (even after HT1) it becomes clear, that most of the oxygen and sulfur atoms are released during HT1. Regarding the nitrogen content, an increase is observed to almost 20 at%. The N–C_{evap} catalyst has slightly less nitrogen, but higher sulfur content compared to Co_2–N–C_{evap} (HT2). Here, more sulfur remained in the carbon matrix whereas the change in S-content as a function of preparation steps for Co_2–N–C indicate that cobalt sulfide species seem to have been formed during HT1 that are partially acid soluble leading to the same relative decrease for cobalt and sulfur contents going from HT1 to HT1 + AL. Regarding the nitrogen content, it was found that the complexation by metal centers helps during pyrolysis to keep the nitrogen in the system for N_4 metallomacrocycles as compared to metal-free H_2N_4-centers.[27] Hence, a similar effect might apply for the precursors within this study.

Figure 1c shows the S 2p fine-scans from XPS. It indicates the transition from the sulfate state initially found for $PANI_{evap}$ to C–S–C bonds and metal sulfide species in our catalysts.

In our previous work, on the catalysis of the ORR, it was shown that the increase in surface area going from HT1 to HT2 is one very important aspect for catalyst optimization.[14] Also here, the BET specific surface area is 30% larger after HT2 in comparison to HT1 (341 m^2 g^{-1} vs. 261 m^2 g^{-1}). A decrease of the BET surface area was found for increasing cobalt contents (Figure 2a). Here, it has to be noted that the sample Co_2–N–C_{ref} prepared with $PANI_{ref}$ reaches a larger surface area, composed to about 75% of micropores, in comparison to the exclusively mesoporous Co_2–N–C_{evap} catalyst, which can also have an impact on the performance (see later in this article).

In Figure 2b Raman measurements are displayed in the low wavenumber range from 400 cm^{-1} to 800 cm^{-1} to study the possible presence of sulfide and oxide species. Only the A_{1g} band of cobalt oxides (CoO, Co_3O_4) is visible at 670 cm^{-1} for Co contents up to 6 wt%. For high cobalt contents, other bands are visible at 467 cm^{-1} (E_g), 509 cm^{-1} (F_{3g}), 603 cm^{-1} (F_{3g}), which enables an assignment to CoO. This phase is mainly of amorphous nature, as evidenced by X-ray diffraction

Table 1. Elemental composition [at%] of PANI precursors used in the synthesis as well as for Co_2–N–C after different steps of preparation, the metal-free catalyst and the Co_2–N–C_{ref}.

Sample	N	C	O	S	Co
$PANI_{ref}$	5.0	42.2	51.3	1.5	–
$PANI_{evap}$	11.6	32.4	42.1	13.9	–
Co_2–N–C_{evap}-HT1	19.0	67.6	7.7	2.0	3.6
Co_2–N–C_{evap}-HT1-AL	21.3	68.2	7.0	1.4	2.1
Co_2–N–C_{evap}-HT2	16.3	73.0	7.0	1.0	2.7
Co_2–N–C_{ref}-HT2	17.0	75.5	5.1	0.6	1.8
$(Co,Mn)_2$–N–C_{evap}-HT2	15.1	72.3	7.5	1.9	1.5 (Mn:1.6)
N–C_{evap}-HT2	14.7	78.9	4.9	1.5	–

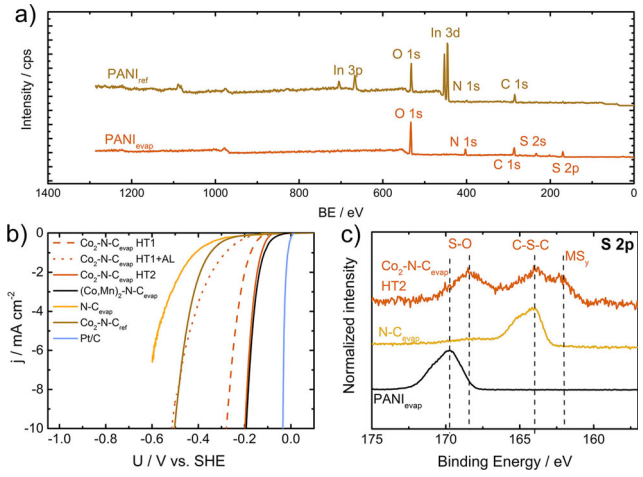

Figure 1. a) XP survey spectra for both PANI, b) HER linear sweeps of Co_2–N–C_{evap} with HT1, HT1-AL, HT2. In addition, reference catalysts (N–C_{evap}, Co_2–N–C_{ref}, (Co,Mn)–N–C_{evap}) subjected to HT1-AL-HT2 and Pt/C are shown. c) XP 2p spectra Co_2–N–C_{evap}-HT2, N–C_{evap} and $PANI_{evap}$.

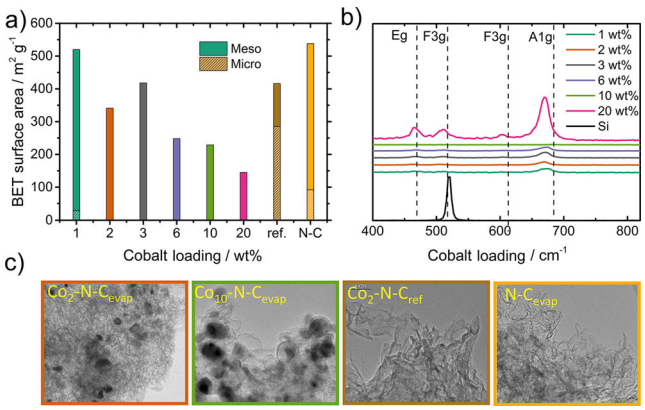

Figure 2. a) BET surface area (with micropore area indicated by dashed area) for all Co–N–C_{evap} catalysts and reference samples. b) Raman spectra from 400 to 800 cm^{-1}, c) high-resolution TEM images (bottom line) for Co_2–N–C_{evap}, Co_{10}–N–C_{evap}, Co_2–N–C_{ref} and N–C_{evap}.

studies (see Figure S1 in the Supporting Information), for which broad amorphous bumps in addition to small amounts of metallic cobalt (particle size of ≈15 nm) are found. For some samples, additional presence of Co–S impurities cannot be ruled out. Therefore, it is possible that basically cobalt particles are formed with thin oxide layers and/ or carbon shells at their surfaces. In addition to this, even though the cobalt content determined by XPS is similar for both Co_2–N–C_{evap} and Co_2–N–C_{ref}, the TEM images show no nanoparticles in the reference sample, whereas Co_2–N–C_{evap} and samples prepared with higher cobalt contents contain nanoparticles (see also Supporting Information, Figure S4 for more images with lower resolution). Again, as in XPS no indication of the metallic state is found, one can conclude that the nanoparticles must be surrounded by a protective layer in Co_2–N–C_{evap}, which makes them undetectable.

Raman spectra for the larger wavenumber range (800 cm^{-1} to 2000 cm^{-1}) were used to get more insights of carbon morphology (Figure S2). Our catalysts display the typical spectrum of amorphous carbon which is dominated by broad bands. It should be noted that in the second-order range no distinct bands are visible which points to the amorphous behavior of the carbon formed within the synthesis. The typical bands are the G- (1585 cm^{-1}) and the D-bands (1335 cm^{-1}), which are characteristic for plane and edge plane vibrations of graphene layers and the D3 band assigned to defects or heteroatoms in the graphene layers.[28] In our previous publication we discussed that a decrease of the I_{D3}/I_G ratio (I = intensity of the Raman band) correlated with a decrease in the catalytic activity of the ORR.[29] Furthermore, the ratio I_G/I_D is directly related to the graphene layer extension.[30] Therefore, I_D/I_G and I_{D3}/I_G are plotted as a function of cobalt content in Figure 3. It seems that Co_{20}–N–C_{evap} should be considered as an outlier within both correlations. Nevertheless, a trend is more pronounced for the I_{D3}/I_G ratio. Moreover, the I_{D3}/I_G ratio correlates with the obtained BET surface area indicating that more hetero-structures are integrated in the surface of the catalyst (Figure S3).

Figure 4 gives fine scans of the Co 2p, N 1s, S 2p and O 1s regions as well as exemplary fits for the N 1s and S 2p regions.

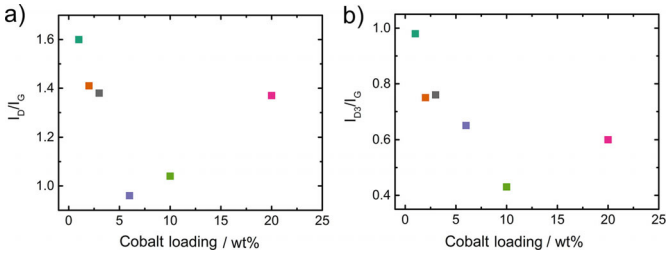

Figure 3. Effect of cobalt content in the precursor on Raman parameters a) I_D/I_G and b) I_{D3}/I_G.

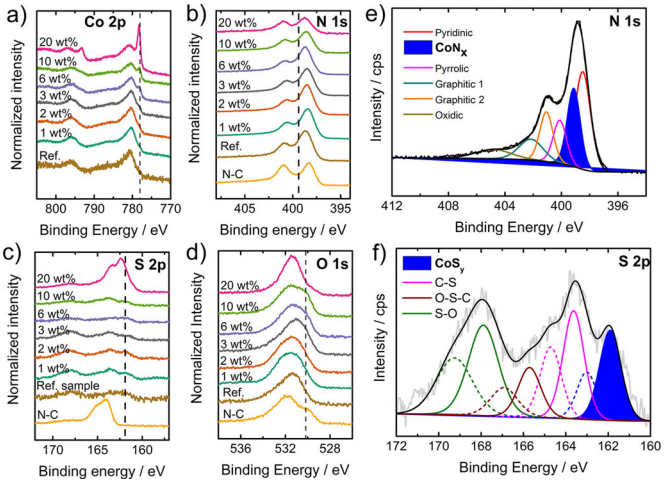

Figure 4. a) Co 2p, b) N 1s, c) S 2p and d) O 1s fine-scan regions of all Co–N–C_{evap} samples and comparison samples (reference compound = Co_2–N–C_{ref}). Exemplary fits of e) N 1s and f) S 2p region for the Co_2–N–C_{evap} catalyst.

The elemental composition as derived from XPS is given in Table S1 for a range of different cobalt contents. It is interesting to note that the nitrogen content and, in particular, the content related to M–N coordination decreases with increasing cobalt content. This could be related to the well-known effect of nanoparticle formation that leads to a disintegration of MN_4 sites.[31]

To sum up, our structural characterization showed that the catalysts contain CoN_x, CoS_y species as well as cobalt nanoparticles. All structures were previously found to be active for the HER. Therefore, to gain a deeper understanding of the reasons for the HER activity of our multiheteroatom-doped catalysts, the elaboration of structure–activity relations is required.

The HER activity was evaluated in acidic medium. The polarization curves, shown in Figure 5a, prove that all samples with a range of different cobalt contents perform significantly better in comparison to the two reference samples (N–C_{evap} and Co_2–N–C_{ref}). The performance at low pH is also significantly improved in comparison to samples from our old MOF-based preparation approach (a comparison of both preparation approaches with respect to the HER activity is given in the Supporting Information Figure S5a). Here, the best performance is obtained for a cobalt content of 2–3 wt% in the precursor. The effect of metal loading is better visualized in Figure 5b, which gives the absolute value of the current density for an overvolt-

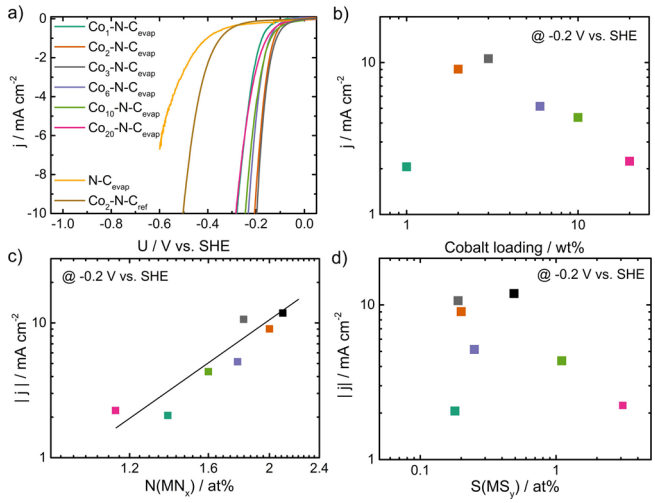

Figure 5. a) HER polarization curve of Co–N–C_{evap} samples prepared with different cobalt contents in the precursor (all with HT2). Correlation between HER activity and b) cobalt content c) N in MN_x and d) S in MS_y. The correlation graphs also include the $(Co,Mn)_2$–N–C_{evap} sample (■).

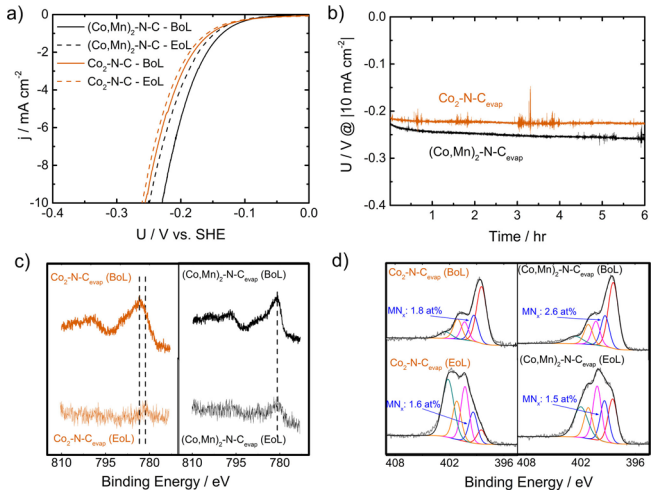

Figure 6. a) Linear sweep voltammetry of Co_2–N–C_{evap} and $(Co,Mn)_2$–N–C_{evap} at "beginning of life" (BoL) and "end of life" (EoL) of the galvanostatic test for 6 h at $-10\ mA\,cm^{-2}$ in 0.1 M H_2SO_4 at 1500 rpm. The galvanostatic tests are shown in b). In c) and d) the Co 2p and N 1 s spectra of the catalyst layers at BoL and EoL are shown.

age of 200 mV as a function of cobalt content. For structure–activity relationships, the nitrogen content in MN_x and sulfur content in MS_y (at %) were determined from the related areas in the fine scans and the overall nitrogen; respectively, sulfur contents of the catalysts. The corresponding plots in dependence of cobalt content are given in the Supporting Information Figure S6. As visible from Figure S6, the trends for N in CoN_x and for S in CoS_y as a function of cobalt content are almost opposite to each other. Cobalt sulfide formation becomes more favorable at higher cobalt contents, while CoN_x sites are preferentially formed at low cobalt contents. As shown in Figures 5 c and d, attempts were made to correlate the N in CoN_x and S in CoS_y, respectively, with the observed HER activity. Interestingly, a correlation between the HER activity and the amount of nitrogen in CoN_x was found, whereas no correlation was indicated between HER activity and content of sulfur assigned to CoS_x. Therefore, the findings shown here indicate that CoN_x sites are the origin of activity for the HER in acidic environment, while CoS_y species might contribute only minor to the HER activity.

To achieve better insight into the applicability of Co–N–C_{evap} catalysts, stability measurements were performed for the Co_2–N–C_{evap} and bimetallic $(Co,Mn)_2$–N–C_{evap} catalysts. The linear sweep voltammograms at the "beginning of life" (BoL) and "end of life" (EoL) are given in Figure 6 a and the change in potential at galvanostatic conditions of $-10\ mA\,cm^{-2}$ are shown in Figure 6 b and indicate an excellent maintenance of potential. Changes of the catalyst composition were further investigated by comparing XPS measurements before and after the galvanostatic test. From analyzing the Co 2p and N 1s regions (Figure 6c and d), it becomes clear that nearly all XPS detectable Co species disappear at the EoL. From the fact that the performance of Co_2–N–C_{evap} is almost constant in the investigated regime, we conclude that the Co species present at the BoL do not contribute significantly to the HER activity. Therefore, the nanoparticles, which were initially present in Co_2–N–C_{evap}, can be ruled out to contribute significantly to the HER activity. For the N 1s region the well-known effect of the formation of protonated nitrogen species is also found for our catalysts.[32] Besides, it has to be noted that while the overall spectrum is changing, the amount of nitrogen assigned to MN_x species decreases by only 12% for Co_2–N–C_{evap} and by 42% for $(Co,Mn)_2$–N–C_{evap}. The stronger decrease for the bimetallic catalyst is consistent with its increased fading of performance.

In conclusion, a group of Co–N–C_{evap} catalysts was synthesized from $PANI_{evap}$, DCDA, and cobalt acetate with changing quantities of cobalt in the precursor. It is shown that the presence of sulfur in the precursor can help to maintain more HER active CoN_x moieties within the catalyst. These CoN_x moieties seem to be more active and significantly more stable in comparison to CoS_y and embedded Co nanoparticles that were found in this catalyst as well. Clearly, this increased knowledge on the detailed nature of the active sites of these catalysts, which dominate the HER activity, will help to develop more knowledge-based preparation approaches for HER catalysis, but especially also for the development of M–N–C catalysts for several other energy relevant applications.

Experimental Section

Experimental Details on catalyst preparation and characterization are given in the Supporting Information.

Acknowledgements

We would like to thank W. Jaegermann's group for the possibility to perform XPS measurements at their system. Financial support by the graduate school of excellence energy science and engineering (GSC1070) the BMBF young research group

(03XP0092) and by the DFG project (KR 3980/4-1) is acknowledged by U.I.K., A.S., I.M., N.W., M.K., and W.D.Z.W.

Conflict of interest

The authors declare no conflict of interest.

Keywords: carbon · cobalt · energy conversion · heterogeneous catalysis · hydrogen evolution reaction · non-precious metal catalysts

[1] G. Gahleitner, *Int. J. Hydrogen Energy* **2013**, *38*, 2039 – 2061.
[2] S.-Y. Huang, D. Sodano, T. Leonard, S. Luiso, P. S. Fedkiw, *J. Electrochem. Soc.* **2017**, *164*, F276 – 282.
[3] X. Zou, X. Huang, A. Goswami, R. Silva, B. R. Sathe, E. Mikmekova, T. Asefa, *Angew. Chem. Int. Ed.* **2014**, *53*, 4372 – 4376; *Angew. Chem.* **2014**, *126*, 4461 – 4465.
[4] a) Y. Wang, Y. Nie, W. Ding, S. G. Chen, K. Xiong, X. Q. Qi, Y. Zhang, J. Wang, Z. D. Wei, *Chem. Commun.* **2015**, *51*, 8942 – 8945; b) S. Dou, L. Tao, J. Huo, S. Wang, L. Dai, *Energy Environ. Sci.* **2016**, *9*, 1320 – 1326.
[5] K. E. Ayers, E. B. Anderson, C. Capuano, B. Carter, L. Dalton, G. Hanlon, J. Manco, M. Niedzwiecki, *ECS Trans.* **2010**, *33*, 3 – 15.
[6] a) E. R. Gonzalez, L. A. Avaca, G. Tremiliosi-Filho, S. A. S. Machado, M. Ferriera, *Int. J. Hydrogen Energy* **1994**, *19*, 17 – 21; b) J. Kibsgaard, T. F. Jaramillo, *Angew. Chem. Int. Ed.* **2014**, *53*, 14433 – 14437; *Angew. Chem.* **2014**, *126*, 14661 – 14665; c) Y.-F. Xu, M.-R. Gao, Y.-R. Zheng, J. Jiang, S.-H. Yu, *Angew. Chem. Int. Ed.* **2013**, *52*, 8546 – 8550; *Angew. Chem.* **2013**, *125*, 8708 – 8712; d) P. Chen, T. Zhou, M. Chen, Y. Tong, N. Zhang, X. Peng, W. Chu, X. Wu, C. Wu, Y. Xie, *ACS Catal.* **2017**, *7*, 7405 – 7411; e) P. Chen, K. Xu, S. Tao, T. Zhou, Y. Tong, H. Ding, L. Zhang, W. Chu, C. Wu, Y. Xie, *Adv. Mater.* **2016**, *28*, 7527 – 7532.
[7] J. Staszak-Jirkovský, C. D. Malliakas, P. P. Lopes, N. Danilovic, S. S. Kota, K.-C. Chang, B. Genorio, D. Strmcnik, V. R. Stamenkovic, M. G. Kanatzidis, N. M. Markovic, *Nat. Mater.* **2015**, *15*, 197 – 203.
[8] H.-W. Liang, S. Brüller, R. Dong, J. Zhang, X. Feng, K. Müllen, *Nat. Commun.* **2015**, *6*, 7992.
[9] Z. Zhang, S. Yang, M. Dou, J. Ji, F. Wang, *Int. J. Hydrogen Energy* **2017**, *42*, 4193 – 4201.
[10] a) U. I. Kramm, I. Abs-Wurmbach, I. Herrmann-Geppert, J. Radnik, S. Fiechter, P. Bogdanoff, *J. Electrochem. Soc.* **2011**, *158*, B69 – B78; b) U. I. Kramm, J. Herranz, N. Larouche, T. M. Arruda, M. Lefevre, F. Jaouen, P. Bogdanoff, S. Fiechter, I. Abs-Wurmbach, S. Mukerjee, J.-P. Dodelet, *Phys. Chem. Chem. Phys.* **2012**, *14*, 11673 – 11688; c) Q. Lai, L. Zheng, Y. Liang, J. He, J. Zhao, J. Chen, *ACS Catal.* **2017**, *7*, 1655 – 1663; d) A. Zitolo, V. Goellner, V. Armel, M.-T. Sougrati, T. Mineva, L. Stievano, E. Fonda, F. Jaouen, *Nat. Mater.* **2015**, *14*, 937 – 942.
[11] M. Ferrandon, X. Wang, A. J. Kropf, D. J. Myers, G. Wu, C. M. Johnston, P. Zelenay, *Electrochim. Acta* **2013**, *110*, 282 – 291.
[12] a) P. Du, R. Eisenberg, *Energy Environ. Sci.* **2012**, *5*, 6012 – 6021; b) A. Morozan, V. Goellner, Y. Nedellec, J. Hannauer, *J. Electrochem. Soc.* **2015**, *162*, H719 – H726; c) Y. Feng, N. Alonso-Vante, *Phys. Status Solidi B* **2008**, *245*, 1792 – 1806.
[13] J. Deng, P. Ren, D. Deng, L. Yu, F. Yang, X. Bao, *Energy Environ. Sci.* **2014**, *7*, 1919.
[14] U. I. Koslowski, I. Herrmann, P. Bogdanoff, C. Barkschat, S. Fiechter, N. Iwata, H. Takahashi, H. Nishikoro, *ECS Trans.* **2008**, *13*, 125 – 141.
[15] U. I. Kramm, I. Herrmann-Geppert, P. Bogdanoff, S. Fiechter, *J. Phys. Chem. C* **2011**, *115*, 23417 – 23427.
[16] N. R. Sahraie, U. I. Kramm, J. Steinberg, Y. Zhang, A. Thomas, *Nat. Commun.* **2015**, *6*, 8618.
[17] I. Martinaiou, T. Wolker, A. Shahraei, G.-R. Zhang, A. Janßen, S. Wagner, N. Weidler, R. W. Stark, B. J. Etzold, U. I. Kramm, *J. Power Sources* **2018**, *375*, 222 – 232.
[18] S. Gupta, S. Zhao, O. Ogoke, Y. Lin, H. Xu, G. Wu, *ChemSusChem* **2017**, *10*, 774 – 785.
[19] W. Deng, H. Jiang, C. Chen, L. Yang, Y. Zhang, S. Peng, S. Wang, Y. Tan, M. Ma, Q. Xie, *ACS Appl. Mater. Interfaces* **2016**, *8*, 13341 – 13347.
[20] a) L. Fu, Y. Chen, S. Zhao, Z. Liu, R. Zhu, *RSC Adv.* **2016**, *6*, 19482 – 19491; b) A. Janßen, I. Martinaiou, S. Wagner, N. Weidler, A. Shahraei, U. I. Kramm, *Hyperfine Interact.* **2018**, *239*, 7; c) I. Herrmann, U. I. Kramm, J. Radnik, S. Fiechter, P. Bogdanoff, *J. Electrochem. Soc.* **2009**, *156*, B1283 – B1292.
[21] U. I. Kramm, I. Herrmann-Geppert, S. Fiechter, G. Zehl, I. Zizak, I. Dorbandt, D. Schmeißer, P. Bogdanoff, *J. Mater. Chem. A* **2014**, *2*, 2663 – 2670.
[22] A. Grimaud, W. T. Hong, Y. Shao-Horn, J.-M. Tarascon, *Nat. Mater.* **2016**, *15*, 121 – 126.
[23] a) P. Zhang, X. Hou, L. Liu, J. Mi, M. Dong, *J. Phys. Chem. C* **2015**, *119*, 28028 – 28037; b) A. J. Clough, J. W. Yoo, M. H. Mecklenburg, S. C. Marinescu, *J. Am. Chem. Soc.* **2015**, *137*, 118 – 121.
[24] a) U. I. Kramm, I. Herrmann-Geppert, J. Behrends, K. Lips, S. Fiechter, P. Bogdanoff, *J. Am. Chem. Soc.* **2016**, *138*, 635 – 640; b) U. I. Koslowski, I. Abs-Wurmbach, S. Fiechter, P. Bogdanoff, *J. Phys. Chem. C* **2008**, *112*, 15356 – 15366.
[25] H. Tributsch, U. I. Koslowski, I. Dorbandt, *Electrochim. Acta* **2008**, *53*, 2198 – 2209.
[26] A. Shahraei, A. Moradabadi, I. Martinaiou, S. Lauterbach, S. Klemenz, S. Dolique, H.-J. Kleebe, P. Kaghazchi, U. I. Kramm, *ACS Appl. Mater. Interfaces* **2017**, *9*, 25184 – 25193.
[27] D. Scherson, A. A. Tanaka, S. L. Gupta, D. Tryk, C. Fierro, R. Holze, E. B. Yeager, *Electrochim. Acta* **1986**, *31*, 1247 – 1258.
[28] J. Robertson, *J. Mater. Sci. Eng. R* **2002**, *37*, 129 – 281.
[29] I. Martinaiou, A. Shahraei, F. Grimm, H. Zhang, C. Wittich, S. Klemenz, S. J. Dolique, H.-J. Kleebe, R. W. Stark, U. I. Kramm, *Electrochim. Acta* **2017**, *243*, 183 – 196.
[30] F. Tuinstra, J. L. Koeing, *J. Chem. Phys.* **1970**, *53*, 1126 – 1130.
[31] J. Blomquist, H. Lang, R. Larsson, A. Widelöv, *J. Chem. Soc. Faraday Trans.* **1992**, *88*, 2007 – 2011.
[32] a) G. Wu, M. A. Nelson, N. H. Mack, S. Ma, P. Sekhar, F. H. Garzon, P. Zelenay, *Chem. Commun.* **2010**, *46*, 7489 – 7491; b) G. Liu, X. Li, P. Ganesan, B. N. Popov, *Electrochim. Acta* **2010**, *55*, 2853 – 2858.

Manuscript received: May 25, 2018
Accepted manuscript online: June 4, 2018
Version of record online: ■■ ■■, 0000

COMMUNICATION

Hydrogen Evolution

*A. Shahraei, I. Martinaiou, K. A. Creutz, M. Kübler, N. Weidler, S. T. Ranecky, W. D. Z. Wallace, M. A. Nowroozi, O. Clemens, R. W. Stark, U. I. Kramm**

■■ – ■■

Exploring Active Sites in Multi-Heteroatom-Doped Co-Based Catalysts for Hydrogen Evolution Reactions

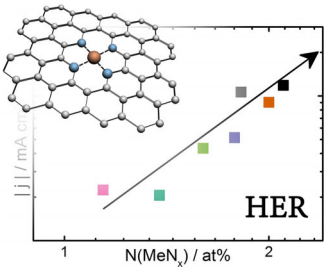

The use of PANI$_{evap}$ as nitrogen, carbon, sulfur and oxygen precursor enables a simple route for the preparation of multi-heteroatom-doped Co-based catalysts. The presence of sulfur enables the formation of larger quantities of CoN$_x$ moieties. Based on structure activity correlation it is shown that these CoN$_x$ moieties dominate the hydrogen evolution reaction active while cobalt sulfides or cobalt nanoparticles contribute only minor.

CHEMISTRY
A European Journal

Supporting Information

Missing "at"

Exploring Active Sites in Multi-Heteroatom-Doped Co-Based Catalysts for Hydrogen Evolution Reactions

Ali Shahraei,[a, b] Ioanna Martinaiou,[a, c] K. Alexander Creutz,[c] Markus Kübler,[b] Natascha Weidler,[c] Simon T. Ranecky,[c] W. David Z. Wallace,[b] Mohammad Ali Nowroozi,[c] Oliver Clemens,[c] Robert W. Stark,[c] and Ulrike I. Kramm*[a, b, c]

chem_201802684_sm_miscellaneous_information.pdf

Experimental

The Co-N-C catalysts were prepared from cobalt acetate, polyaniline (labeled as either $PANI_{evap}$ or $PANI_{ref}$) and dicyandiamide (DCDA). The different steps of preparation are described in the following:

$PANI_{evap}$ synthesis: 20 mmol aniline was polymerized using 60 mmol ammonium peroxidisulfate (APS) as the oxidation agent in 0.5M HCl, while it was kept in an ice bucket to control the temperature. The mixture was stirred during polymerization that took place for 24 hours. The residual solvent was evaporated by heating the mixture to 100 °C. Induced by this treatment, this PANI(+S) has a hygroscopic behavior and is highly acidic.

$PANI_{ref}$ synthesis: 20 mmol aniline was polymerized using 20 mmol ammonium peroxidisulfate (APS) as the oxidation agent in 0.5M HCl, while it was kept in an ice bucket to control the temperature. The mixture was stirred for 24 hours of polymerization. Afterwards the suspension was filtered and washed with water to get rid of APS residues. The recipe with 1:1 ratio aniline to APS is described in literature[1] and therefore labelled as $PANI_{ref}$.

For a complete polymerization of 20 mmol aniline to polyaniline a theoretical mass yield of m_{th} = 1.84 g is expected, the mass yield of $PANI_{evap}$ was m_{PANI_evap} yield= 90% and m_{PANI_ref} yield = 45%

For studying the effect of preparation parameters, Co-N-C catalysts were prepared with 2 wt% Co in the precursor for both PANI. In addition, a variation of cobalt content was made for catalysts that were all prepared with $PANI_{evap}$. The cobalt content was varied between 0.0 wt% to 20 wt% Co in the precursor.

Co-N-C synthesis: For the synthesis of Co_2-N-C (2 wt% Co in precursor), first 62.8 mg cobalt acetate tetrahydrate were mixed with 680 mg $PANI_{evap}$ and 2267 mg DCDA in a mortar until a homogeneous mixture was obtained. Similarly, the amount of cobalt acetate was adapted to prepare catalysts with 0 to 20 wt% cobalt in the precursor. The mixtures were filled in quartz boats and subjected to a preparation protocol that includes HT1-AL-HT2. The first heat treatment (HT1) was run with a ramp of 300 °C h^{-1} from RT to 800 °C. The temperature was held at 300 °C for 30 min, 500 °C for 30 min and 800 °C for 60 min in order to keep all the system for stabilization. After cooling down, the sample was transferred to the acid leaching (AL) in 2 M HCl. The suspension was kept in an ultrasonic bath for 3 hours and then kept overnight. Afterwards the catalyst was filtered, washed with water and dried. The 2nd heat treatment (HT2) included a first ramp of approx. 38 °C min^{-1} to 600 °C where then the ramp was reduced to 300 °C h^{-1} to reach the final temperature of 800 °C. During this HT2 the dwell time at 800 °C was 3 hours. After cooling down the final catalyst was removed from the oven.

In addition to the aforementioned catalysts, a bimetallic (Co,Mn) catalyst was prepared with a nominal metal loading of 2 wt% and an atomic Co to Mn ratio of 2:1. In addition a Co_2-N-C_{ref} was prepared with the same quantities as given above but using $PANI_{ref}$ instead of $PANI_{evap}$. The HER activity of Pt/C 20wt% (0.12 µg/cm^{-2}) is reported for reasons of comparison.

Due to the high amount of precursors that go into the gas phase, the yield for the catalyst preparation, as defined as $m_{catalyst}$ / m_{prec}, is about 2.5 %.

Characterization:

Electrochemistry: The electrochemical performance was studied using a standard three electrode configuration. Glassy carbon disc and Ag/AgCl electrode have been applied as counter and reference electrode, respectively. A catalyst ink containing 5 mg catalyst, 142 µl ethanol, 83.2 µl water and 25 µl Nafion (5 wt%) was drop-casted on the working electrode, which was an RDE electrode with a glassy carbon disc (A = 0.1963 cm^2 → catalyst loading = 1 mg cm^{-2}). In order to compensate for capacity effects the anodic and cathodic sweep were averaged and the average scans are prepared. All electrochemical tests were performed in 0.1M H_2SO_4 from CVs with 5 mV s^{-1} at 1500 rpm in a potential range of U = 0.6 to -0.72 (vs SHE) after 90 cycles of activation (short cycles between U = -0.28 and -0.72 V with 300 mV s^{-1}), all results are iR corrected. For the stability test the catalyst was kept at -10 mA cm^{-2} for six hours. Before and after the HER activity was measured by a CV and structural changes were followed by XPS. Such stability tests were made for Co_2-N-C_{evap} and $(Co,Mn)_2$-N-C_{evap}.

X-Ray Diffraction (XRD): X-ray diffraction measurements were performed using a Bruker D8 Advance in Bragg−Brentano geometry with Cu K_α radiation and a VANTEC detector. Data were recorded in an angular range between 5° and 50° (2θ) for a total measurement time of 1 h using a step size of ∼0.007°, a step time of 0.5 step s^{-1} and a fixed divergence slit of 0.3°.

X-ray induced Photoelectron Spectroscopy (XPS): X-ray photoelectron spectra (XPS) were measured with a Specs Phoibos 150 hemispherical analyzer and a Specs XR50M Al K_α X-ray source (E = 1486.7 eV). Before the measurements, the catalyst powder was pressed on an indium foil and sealed on the sample holder. For the survey scans, an energy step of 1 eV has been applied and two scans were overlaid. For these fine scans an energy step of 0.05 eV has been used. For the stability measurement, a catalyst with the loading of 1 mg cm^{-2} has been drop-casted on a glassy carbon (GC) electrode that was mounted on the XPS sample holder. The same measurement parameters have been set as earlier. Then, the GC electrode was unmounted and the electrochemical stability test was performed, followed by a final XPS measurement of the conditioned catalyst.

Transmission Electron Microscopy (TEM): Catalyst powder was immersed in ethanol and sonicated for 30 seconds in an ultra-sonic bath. The suspension was kept to be settled to reduce the amount of large particles. Then, a small drop was placed on a copper grid with carbon film (Baltec MED010) and kept for drying at room temperature.

Raman Spectroscopy: A drop of catalyst was placed on a silica disc and kept for drying at room temperature. The measurements were done with an alpha 300R confocal Raman microscope from WiTec (Ulm, Germany) with a grid of 600 lines mm^{-1} using an excitation laser (532.2 nm) with a power of 1 mW. Each spectrum was obtained by overlaying data obtained at three different positions (of ten scans each), with an integration of ten seconds at each point.

N_2 sorption measurements: In order to determine the BET specific surface area and an estimate of the micropore surface area N_2 sorption measurements were performed with an Autosorb test station from Quantachrome. Previous to the sorption experiment the sample was degassed at 200 °C for 16 hours. The exact mass was determined afterwards and used for final determination of the surface areas.

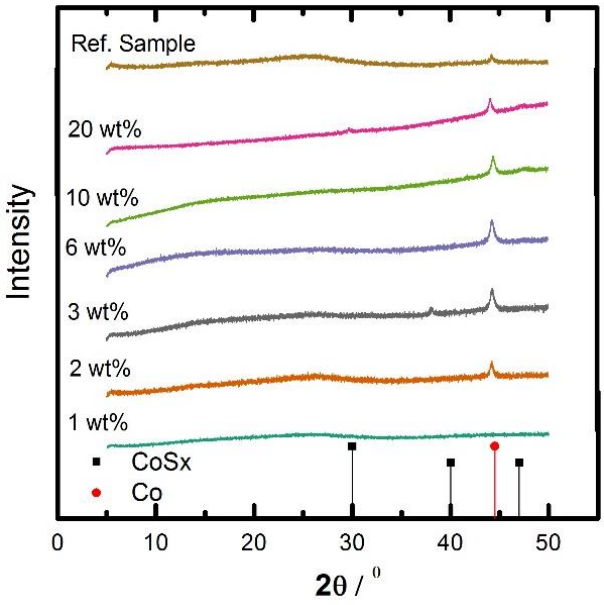

Figure S1. XRD patterns of Co_x-N-C_{evap} catalysts. The metal content in the precursor is given for each of the catalyst. For reasons of comparison XRD of the reference sample Co_2-N-$C_{ref.}$ is shown.

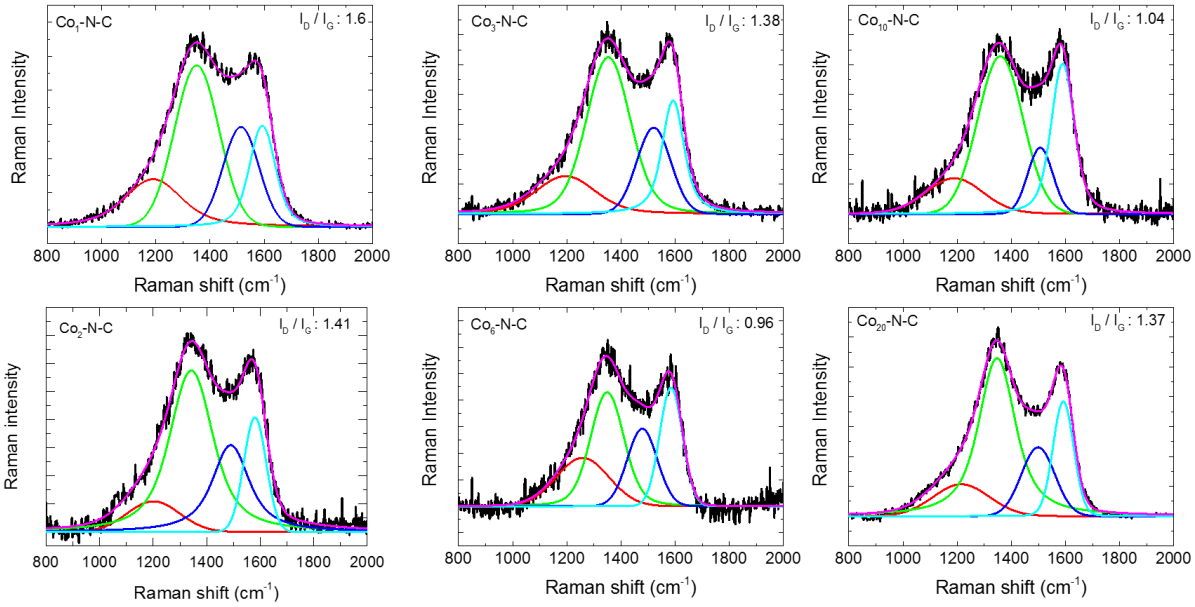

Figure S2. Raman spectra of Co_x-N-C_{evap} in the 1st order region of carbon blacks.

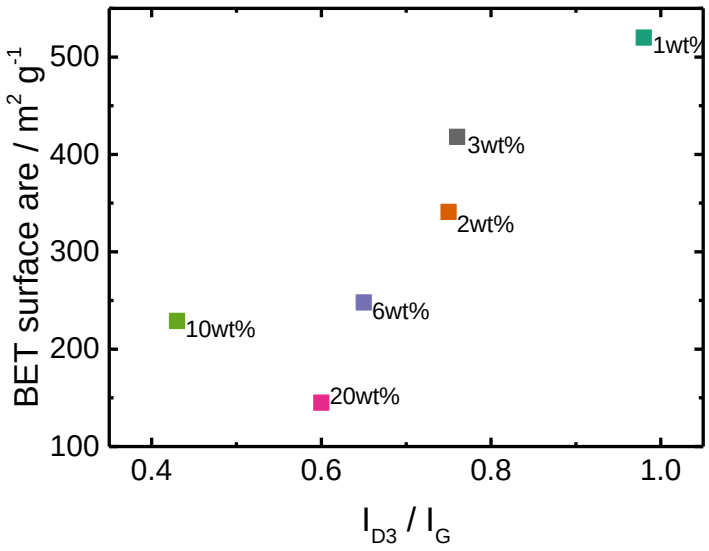

Figure S3. Correlation between BET surface area and the intensity ratio of the D_3 to G band for all Co_x-N-C_{evap} samples.

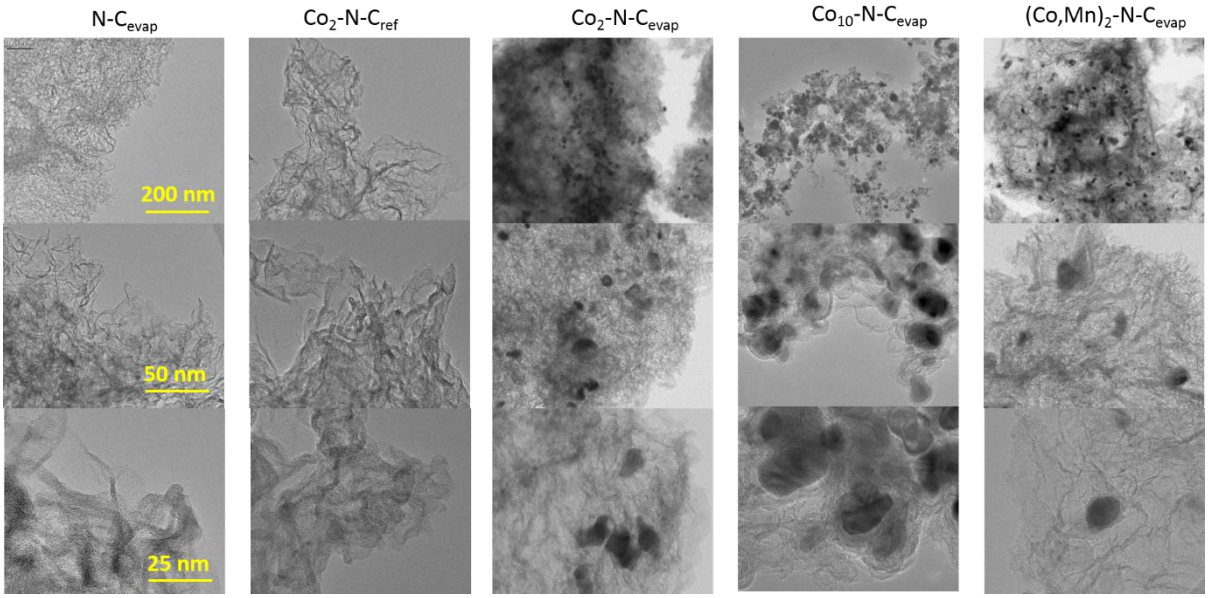

Figure S4. TEM images at different resolutions of Co_x-N-C_{evap} (2 wt% and 10 wt%) catalysts and reference samples.

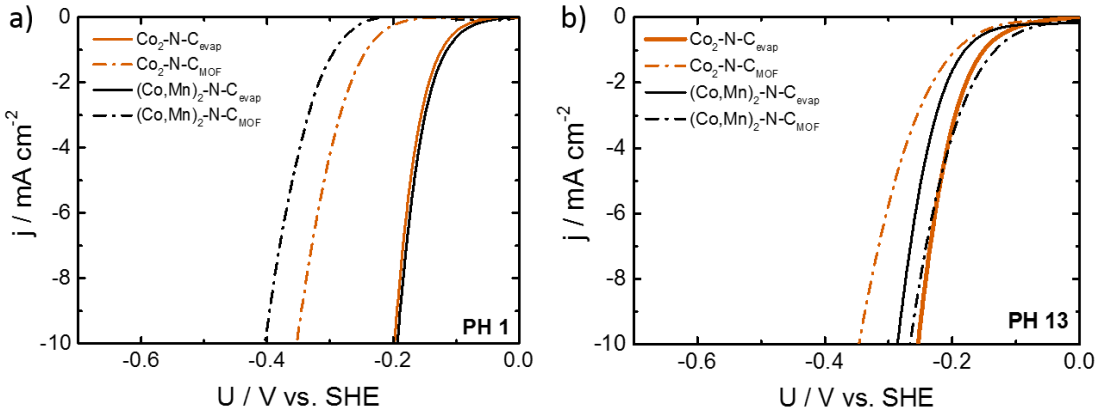

Figure S5: a) HER activity of Co_2-N-C_{MOF} and $(Co,Mn)_2$-N-C_{MOF} catalysts in 0.1M H_2SO_4 and 0.1M KOH in comparison to Co_2-N-C_{evap} and $(Co,Mn)_2$-N-C_{evap} (all 1 mg cm^{-2}, 1500 rpm). Details on the preparation of MOF-based catalysts can be found in Shahraei et al.[2]

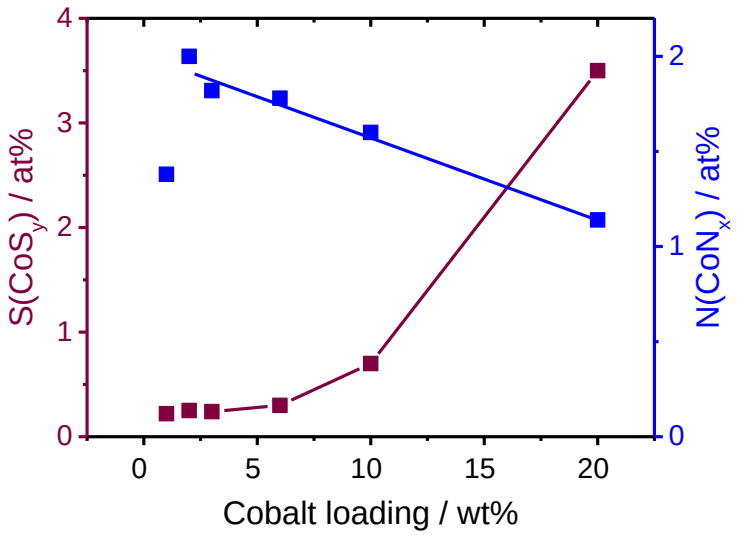

Figure S6. Change of sulfur content related to CoS_y species and change of nitrogen content related to CoN_x moieties as a function of cobalt loading in the precursor.

Table S1. Elemental composition (at%) analysed by XPS for all catalysts prepared by two heat-treatments (HT1-AL-HT2).

at%	N	C	O	Co	S	$S(MS_y)$	$N(MN_x)$
Co_1-N-C_{evap}	16.6	72.5	7.6	2.3	0.96	0.22	1.38
Co_2-N-C_{evap}	16.3	73	7	2.7	0.96	0.25	2
Co_3-N-C_{evap}	13.5	76	7.2	2.3	1	0.24	1.82
Co_6-N-C_{evap}	13.2	13.17	7.8	2.7	0.85	0.3	1.78
Co_{10}-N-C_{evap}	10.4	71.6	8.6	2.6	6.7	0.7	1.6
Co_{20}-N-C_{evap}	6.5	6.5	6.7	4.3	6.5	3.5	1.14
Co_2-N-C_{ref}	17	75.5	5.1	1.8	0.57	0.06	1.2
$(Co.Mn)_2$-N-C_{evap}	15.1	72.3	7.5	1.5 (Mn: 1.6)	1.9	0.49	**2.1**
N-C_{evap}	14.7	78.9	4.9	-	1.5	-	-

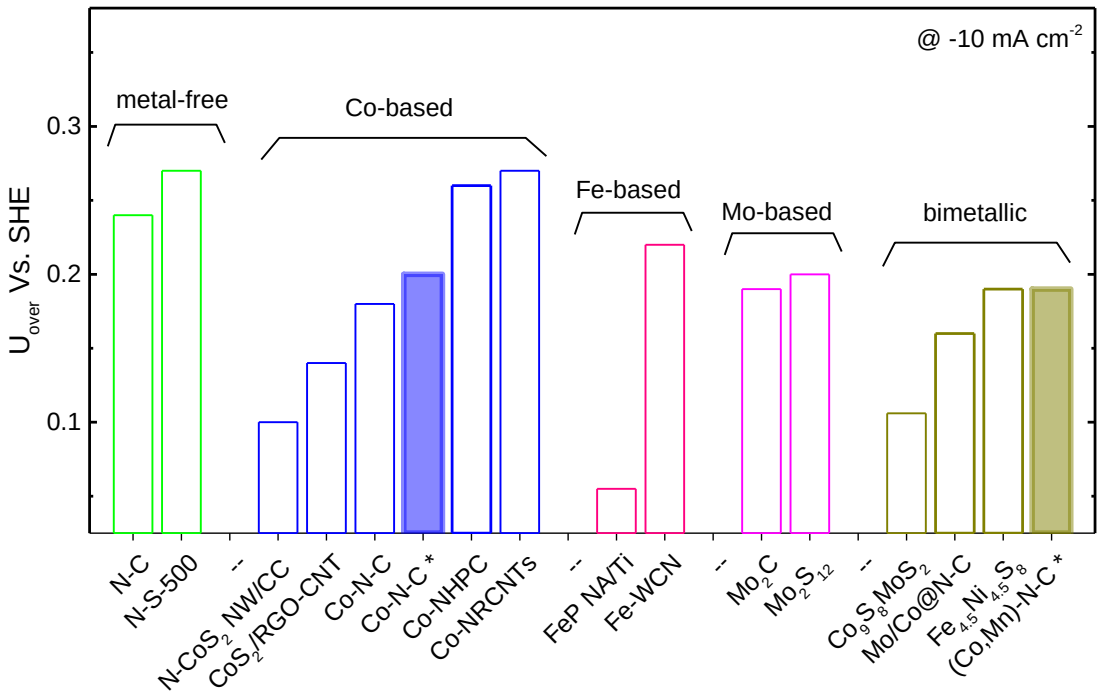

Figure S7. HER comparison of the non-precious metal catalysts in acidic medium

Table S2. Detailed comparison of the most active non-precious catalysts for HER in acidic medium

Catalyst	Loading (mg cm^{-2})	electrolyte	U_{over} (V)	stability	ref
N-C	0.2	0.5 M H_2SO_4	0.24	Stable	[3]
N-S-500	No info	0.5 M H_2SO_4	0.27	55% loss after 1000 cycles	[4]
CoS_2/RGO-CNT	1.15	0.5 M H_2SO_4	0.14	Stable	[5]
N-CoS_2 NW/CC	No info	0.5 M H_2SO_4	0.10	9% loss after 10 h @ 50 mA cm^{-2}	[6]
Co-NRCNTs	0.28	0.5 M H_2SO_4	0.26	Stable	[7]
Co-NHPC	0.285	0.5 M H_2SO_4	0.24	stable	[8]
Co-N-C	0.8	0.1 M H_2SO_4	0.18	No info	[9]
FeP NA/Ti	3.2	0.5 M H_2SO_4	0.055	75% loss after 3000 cycles	[10]
Fe-WCN	0.4	0.5 M H_2SO_4	0.22	No info	[11]
Mo_2C	1.4	1 M H_2SO_4	0.19	Stable	[12]
Mo_2S_{12}	50 nmol cm^{-2} (0.03 mg cm^{-2})	0.5 M H_2SO_4	0.18	30% loss after 1000 cycles	[13]
$Co_9S_8MoS_2$	0.21	0.5 M H_2SO_4	0.106	25% loss after 4 h GS (> 6 %/h)	[14]
Mo/Co@N-C	0.7	0.5 M H_2SO_4	0.157	15% loss after 10 h PS (1.5 %/h)	[[15]
$Fe_{4.5}Ni_{4.5}S_8$	0.025	0.5 M H_2SO_4	0.280 0.190 (after 96 h electrolysis)	Stable	[16]
Co-N-C	**1**	**0.1 M H_2SO_4**	**0.2**	**30% loss after 6 hr GS**	**This work**
(Co,Mn)-N-C	**1**	**0.1 M H_2SO_4**	**0.19**	**13% loss after 6 hr GS**	**This work**

References

[1] a) P. N. Adams, P. J. Laughlin, A. P. Monkman, *Synth. Met.* **1996**, *76*, 157-160; b) Akheel A. Syed, Maravattical K. Dinesan, *Talanta* **1991**, *38*, 815-837.

[2] A. Shahraei, A. Moradabadi, I. Martinaiou, S. Lauterbach, S. Klemenz, S. Dolique, H.-J. Kleebe, P. Kaghazchi, U. I. Kramm, *ACS Appl. Mater. Interfaces* **2017**, *9*, 25184.

[3] R. Zhang, X. Li, L. Zhang, S. Lin, H. Zhu, *Adv. Sci.* **2016**, *3*, 1600208.

[4] Y. Ito, W. Cong, T. Fujita, Z. Tang, M. Chen, *Angew. Chem.* **2015***, 127,* 2159-2164*, Angew. Chem.Int. Ed. Engl.* **2015**, *54*, 2131-2136.

[5] S. Peng, L. Li, X. Han, W. Sun, M. Srinivasan, S. G. Mhaisalkar, F. Cheng, Q. Yan, J. Chen, S. Ramakrishna, *Angew. Chem.* **2014***, 126,* 12802-12807, *Angew. Chem., Int. Ed. Engl.* **2014**, *53*, 12594-12599.

[6] P. Chen, T. Zhou, M. Chen, Y. Tong, N. Zhang, X. Peng, W. Chu, X. Wu, C. Wu, Y. Xie, *ACS Catal.* **2017**, *7*, 7405-7411.

[7] X. Zou, X. Huang, A. Goswami, R. Silva, B. R. Sathe, E. Mikmekova, T. Asefa, *Angew. Chem.* **2014***, 126,* 4461-4465, *Angew. Chem., Int. Ed. Engl.* **2014**, *53*, 4372-4376.

[8] Z. Zhang, S. Yang, M. Dou, J. Ji, F. Wang, *Int. J. Hydrogen Energy* **2017**, *42*, 4193-4201.

[9] A. Morozan, V. Goellner, Y. Nedellec, Hannauer J., *J. Electrochem. Soc.* **2015**, *162*, 719-726.

[10] P. Jiang, Q. Liu, Y. Liang, J. Tian, A. M. Asiri, X. Sun, *Angew. Chem.* **2014**, *126*, 13069-13073, *Angew. Chem., Int. Ed. Engl.* **2014**, *53*, 12855-12859.

[11] Y. Zhao, K. Kamiya, K. Hashimoto, S. Nakanishi, *Angew. Chem.* **2013**, *125*, 13883-13886, *Angew. Chem., Int. Ed. Engl.* **2013**, *52*, 13638-13641.

[12] H. Vrubel, X. Hu, *Angew. Chem.* **2012***, 124,* 12875-12878, *Angew. Chem., Int. Ed. Engl.* **2012**, *51*, 1270312706.

[13] Z. Huang, W. Luo, L. Ma, M. Yu, X. Ren, M. He, S. Polen, K. Click, B. Garrett, J. Lu et al., *Angew. Chem.* **2015***, 127,* 15396-15400, *Angew. Chem., Int. Ed. Engl.* **2015**, *54*, 15181-15185.

[14] V. Ganesan, S. Lim, J. Kim, *Chem.Asian J.* **2018**, *13*, 413-420.

[15] C. Wu, D. Liu, H. Li, J. Li, *Small (Weinheim an der Bergstrasse, Germany)* **2018**, *14*, e1704227.

[16] B. Konkena, K. Junge Puring, I. Sinev, S. Piontek, O. Khavryuchenko, J. P. Dürholt, R. Schmid, H. Tüysüz, M. Muhler, W. Schuhmann et al., *Nat. Commun.* **2016**, *7*, 12269.

4.2 Investigation of OER on Non-PGM catalysts

4.2.1 Variation of sulfur content of Co-N-C for OER in alkaline

To further improve the OER activity of Me-N-C catalysts, ultra-high sulfur doping was probed by introducing elemental sulfur to the synthesis route within the scope of $PANI_{evap}$ approach. The effect of sulfur doping on the structure and activity of the catalyst was investigated by variation of the S/Co ratio in the precursors. Moreover, the role of inorganic species on the reaction mechanism was explored.

Contribution to the project: Catalysts preparation, XPS characterization, Electrochemical characterization, Data analysis and writing

Journal of Materials Chemistry A

PAPER

View Article Online
View Journal

Cite this: DOI: 10.1039/c8ta05769a

On the role of hydroxide species in sulphur- and nitrogen-doped cobalt-based carbon catalysts for the oxygen evolution reaction†

Ali Shahraei,[ab] Markus Kuebler,[a] Ioanna Martinaiou,[ab] K. Alexander Creutz,[a] W. David Z. Wallace,[a] Mohammad A. Nowroozi,[c] Stephen Paul,[ab] Natascha Weidler,[a] Robert W. Stark,[d] Oliver Clemens[c] and Ulrike I. Kramm*[ab]

The influence of high S/Co ratios on the structural composition and oxygen evolution reaction (OER) activity of a group of cobalt-based carbon catalysts was investigated. Catalysts were prepared from polyaniline, cobalt acetate and dicyandiamide as precursors for active site formation and as structure forming agents. The sulphur to cobalt ratio was investigated in a range of S/Co = 10 to 32. On the basis of a comprehensive structural characterisation by XRD, Raman, XPS, TEM and N_2 sorption measurements it was possible to show that the S/Co ratio has a significant impact on the carbon morphology. In fact, with increasing S/Co ratio the carbon morphology continuously changes from highly amorphous carbon to carbon-nanotubes, with increasing diameter. Besides the anticipated CoN_4 sites and cobalt sulphite species, the catalysts also contained cobalt nanoparticles as well as cobalt hydroxide species. The most active catalyst required 0.37 ± 0.01 V overpotential to reach 10 mA cm^{-2} and even increased in activity during galvanostatic treatment and cycling-illustrating its very good performance. A faradaic efficiency of >35% was determined. A detailed analysis of the activity and stability in combination with Raman and XPS provides two explanations for observed Tafel slope changes, that might also be coupled to each other, namely a change in the carbon oxidation rate depending on preparation and potential or a variation in the coverage by hydroxide and oxidic species of the metal, whereas hydroxide species seem to enable a higher OER activity.

Received 16th June 2018
Accepted 3rd October 2018

DOI: 10.1039/c8ta05769a

rsc.li/materials-a

Introduction

Water electrolysis to produce hydrogen is among the most promising technologies considering the need for appropriate storage technologies for renewable energies.[1] This is rather important as for future society we have to move from energy provided by fossil fuels (and the harmful effect of greenhouse gases) to renewable energies. Since renewable energy sources are not available on a continuous basis, appropriate storage technologies have to be developed.

In water electrolyzers, the state-of-the art materials are often precious metals. These systems achieve high conversion rates at relatively low loadings. However, precious metals such as platinum, ruthenium and iridium (all typical catalysts for water splitting reactions) were classified as critical raw materials by the European Commission[2] due to their low availability and high costs. Non-precious metal catalysts therefore play a crucial role in future energy supply.[3] Especially, the group of Me–N–C catalysts with catalytically active MeN_4 sites have received much attention as they are active for the oxygen reduction reaction (ORR),[4–9] CO_2 reduction,[10–13] and the hydrogen evolution reaction (HER)[14–18] as well as the oxygen evolution reaction (OER).[19–24] Me–N–C catalysts that are highly active for the ORR and OER are also promising candidates as bifunctional catalysts for metal air batteries.[25,26] Regarding their synthesis, Me–N–C catalysts can be prepared by pyrolysing a precursor mixture consisting of carbon, nitrogen and metal sources. Most of the preparation routes that result in highly active electrocatalysts also contain inorganic species like carbides, nitrides or metallic nanoparticles that can contribute to the overall performance of the resulting catalyst in various electrocatalytic reactions.

In terms of structural composition and activity, sulphur addition was found beneficial for Me–N–C catalysts.[14,27–29] However, if the sulphur content (or sulphur to metal ratio)

[a]Catalysts and Electrocatalysts Group, Department of Materials- and Earth Sciences, Department of Chemistry, Otto-Berndt-Str. 3, 64287 Darmstadt, Germany. E-mail: kramm@ese.tu-darmstadt.de

[b]Graduate School of Excellence Energy Science and Engineering, Otto-Berndt-Str. 3, 64287 Darmstadt, Germany

[c]Materialdesign durch Synthese Group, Department of Materials- and Earth Sciences, Alarich-Weiss-Str. 2, 64287 Darmstadt, Germany

[d]Physics of Surfaces Group, Department of Materials- and Earth Sciences, Alarich-Weiss-Str. 16, 64287 Darmstadt, Germany

† Electronic supplementary information (ESI) available. See DOI: 10.1039/c8ta05769a

becomes too large, metal sulphides are formed.[14,30–32] Recently, Qiao and his/her team prepared a bifunctional catalyst of cobalt sulphide nanoparticles embedded in nitrogen and sulphur co-doped graphene activating both the ORR and OER.[25] Also others attributed catalytic activity towards the OER to transition metal sulphides.[25,33–37]

Therefore, in the context of this work, sulphur addition might result in OER active metal sulphides and/or enable a variation of the CoN_4 contribution.

Nevertheless, during the last few decades, oxidic surfaces, as found in transition metal oxides/hydroxides such as perovskites,[38] cobalt oxides[39–41] and nickel-based hydroxides,[42–45] have been known as the most promising OER catalysts. Weidler *et al.* studied various cobalt oxides under OER conditions and reported a transition of an oxide surface to oxide-hydroxide sites as active species that were formed on the surface of the catalysts.[41] During the first twelve minutes of operation, a continuous improvement of the OER activity was observed. Afterwards no further change in activity was found. Step-by-step investigation of the as-prepared and "aged" thin film electrodes by X-ray photoelectron spectroscopy (XPS) showed that induced by operation, the contribution of cobalt oxide-hydroxide $CoO_x(OH)_2$ increased.[41] Indeed, the potential induced formation of oxyhydroxides could not only be shown for oxides and sulphides but also for CoN_4 centres in non-pyrolyzed cobalt porphyrin that were active for the OER.[22]

In particular, these described effects as observed by Weidler *et al.* and Daniel *et al.* make it questionable to what extent the OER activity in Co–N–C catalysts can be attributed to CoN_4 species (or Co sulphides, in the case of S-addition).

Inspired by the very promising OER activities observed for Co–N–C and cobalt sulphides embedded in carbon we aimed to investigate whether the OER can indeed be assigned to one of the two active sites (CoN_4 and/or Co sulphide) or if also here oxidic species are the true catalytic sites for the OER. Thus, we prepared samples of cobalt-based carbon catalysts with ultra-high amounts of sulphur and nitrogen in the precursors. The catalysts were thoroughly characterized in terms of morphology, chemical composition and OER activity and stability. We found that cobalt hydroxide species improved the OER activity of the catalysts. This result gives an important indication for the development of more active and stable non-precious metal catalysts by a rational design of the synthesis.

Results and discussion

Structural characterisation of the Co–N–C catalysts

In Fig. 1 a scheme of the synthesis is shown. Similar to our previous work,[14] $PANI_{evap}$ was used as the main nitrogen precursor.

$PANI_{evap}$ was prepared by the oxidative polymerisation of aniline in the presence of ammonium peroxidisulphate (APS). The precipitate was dried without the application of washing and filtering procedures, and thus the final product was highly acidic and contained polyaniline as well as the residuals from APS. Therefore, it is labelled $PANI_{evap}$. Following this procedure, $PANI_{evap}$ is a carbon, nitrogen, sulphur and oxygen source within

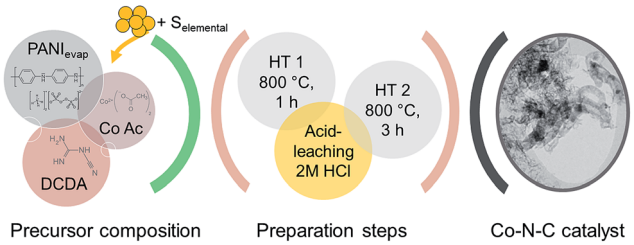

Fig. 1 Schematic of the synthesis of sulphur-doped Co–N–C catalyst.

the synthesis. Catalysts prepared with PANI obtained very good stability in fuel cell operation[46] and the carbon formed during the synthesis might therefore also be of stronger corrosion resistance as required for the OER. With the given cobalt content in the precursor (3 wt%), even without addition of elemental sulphur ($S_{elemental}$), the molar S/Co ratio equaled ten (S/Co = 10).

In order to evaluate the impact of $S_{elemental}$ addition during the synthesis on the structure and morphology of the catalysts, N_2 sorption measurements and transmission electron microscopy (TEM) images were obtained as shown in Fig. 2.

It is evident from the N_2 sorption measurements that the addition of $S_{elemental}$ leads to a decrease in BET surface area (SA)

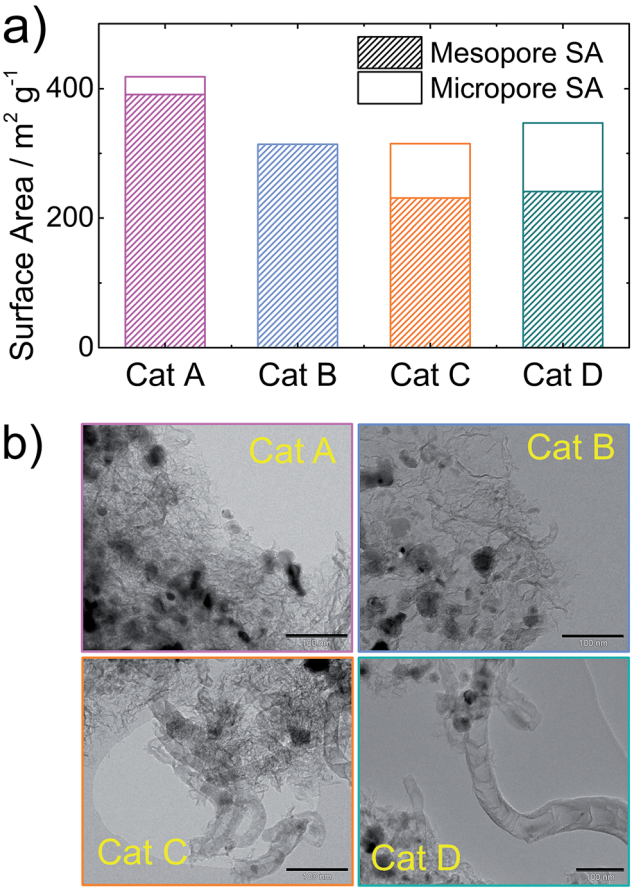

Fig. 2 (a) Results of BET and meso- and micropore surface area (SA) obtained from N_2 sorption measurements. In (b) exemplary TEM images of the catalysts are shown, the scale bar is 100 nm.

while on the other hand, the micropore SA tended to increase. In ESI Fig. S1,† the cyclic voltammograms of the catalysts are shown as well as a correlation of the double layer capacity (taken from the CVs at 0.5 V) and the overall BET surface area.

The change in specific surface area was associated with a change in the carbon morphology from amorphous carbon to more defined carbon as visible from TEM images in Fig. 2b and in ESI Fig. S2.†

In fact, for the catalysts with S/Co ratios of 15, 24 and 32 the formation of carbon nanotubes was identified. It seems that higher S/Co ratios led to more and larger nanostructures. This is in agreement with previous reports on a positive effect of sulphur-addition on the growth of carbon nanofibers.[47,48]

Also visible in the TEM images (see Fig. 2b) is the presence of nanoparticles, which seem to be surrounded by multiple layers of carbon, as also distinctly visible in Fig. S2.† Most likely, these shells also acted as the protectant of the metal during the acid-leaching step after the first heat-treatment. The presence of these nanoparticles was also confirmed by X-ray diffraction (XRD), shown in Fig. 3a. The refinement of the diffraction data

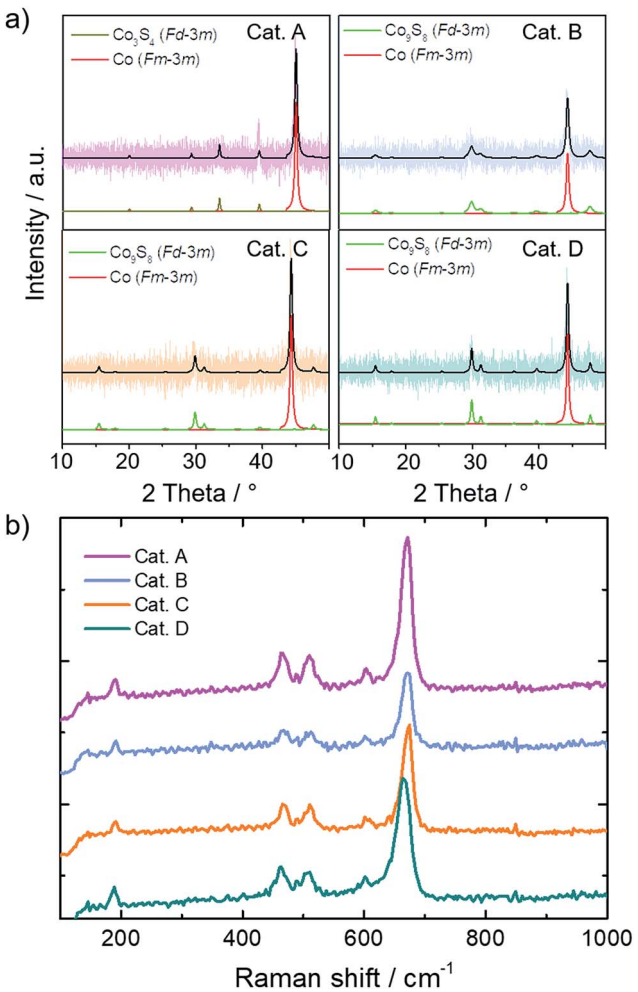

Fig. 3 (a) X-ray diffraction data including refinement of the four investigated catalysts. In (b) Raman spectra are shown in the range <1000 cm^{-1}. As the inset, the 1st order region assigned to carbon is shown.

identified cobalt nanoparticles in all of our catalysts together with smaller amounts of cobalt sulphide species.

However, in the case of cat A Co_3S_4 was formed, all other catalysts contained Co_9S_8. This is interesting, as from the S/Co ratio in the precursor, a higher sulphur content would have been expected for cat B to D.

As described in the Introduction, both Co_3S_4 and Co_9S_8 have been reported as catalysts for the oxygen evolution reaction (OER) and hydrogen evolution reaction (HER).[33,36,49]

The Raman spectra for the range <1000 cm^{-1} of the catalysts are displayed in Fig. 3b. There are four well-pronounced bands at 463 cm^{-1}, 507 cm^{-1}, 601 cm^{-1} and 664 cm^{-1} and a weakly pronounced band at about 200 cm^{-1} that were assigned to metallic cobalt and/or cobalt oxide particles.[14,50] A comparison of the observed bands with model systems reported in the literature suggests the presence of CoO_x and Co_3O_4 species.[51,52] However, the small intensity of the band at 200 cm^{-1} and the results concluded from X-ray photoelectron spectroscopy (XPS) (see below) indicate that the presence of CoO_x is more likely, while it seems that Co_3O_4 can be excluded.

As TEM indicated some protective carbon layers around the nanoparticles and also the absence of reflections which could be assigned to cobalt oxides/hydroxides in XRD, we assume that these were small particles with a lower degree of order and thus X-ray amorphous. Indication of partial oxidation of the cobalt on the surface was also given by X-ray photoelectron spectroscopy (XPS, see later in this section).

In ESI Fig. S3,† the first order region related to carbon blacks is deconvoluted into four bands, namely, the G band (*ca.* 1585 cm^{-1}), D band (1355 cm^{-1}), D_3 band (*ca.* 1500 cm^{-1}) and the D_4 band (*ca.* 1200 cm^{-1}). Following the same order, they are assigned to vibrations within the graphene plane, vibrations at the edges or at curvations, vibrations induced by heteroatoms and vibrations of lower hydrocarbons.[53–55] The ratio of I_D/I_G is inversely proportional to the graphene layer extension L_a,[53] while in our previous publications we found indications that MeN_4 centres as well as pyridinic nitrogen contributed to the D_3 band intensity.[56] A tendency for higher I_{D3}/I_G ratios is found for catalysts with mir N_{MeN} and N_{pyrid}, as is shown in ESI Fig. S4.†

Influence of sulphur modification on the composition

In order to get additional insights into the near-surface structure and composition of the catalysts, XPS was performed (Fig. 4). In Fig. 4a the survey scan of cat D is shown. Similar to all other catalysts, cobalt, oxygen, nitrogen, carbon and sulphur were detected. The respective peaks are indicated in the survey spectrum. For further analysis, the fine scans of the different regions were analysed. In Fig. 4b–e the Co 2p 3/2, O 1s, N 1s and S 2p regions are shown for all four catalysts. The shape of the curves in the Co 2p, N 1s and O 1s region seemed very similar for all catalysts. In ESI Fig. S5† the overall Co 2p energy range is shown as well as measurements of reference samples. Furthermore, in Fig. S6† the fit of the Co 2p 3/2 region of the most active catalyst of this study (cat D) is exemplarily shown. A good fit was obtained assuming the presence of metallic cobalt/Co_9S_8, CoN_4, CoO and $Co(OH)_2$. Due to the similarities of the Co

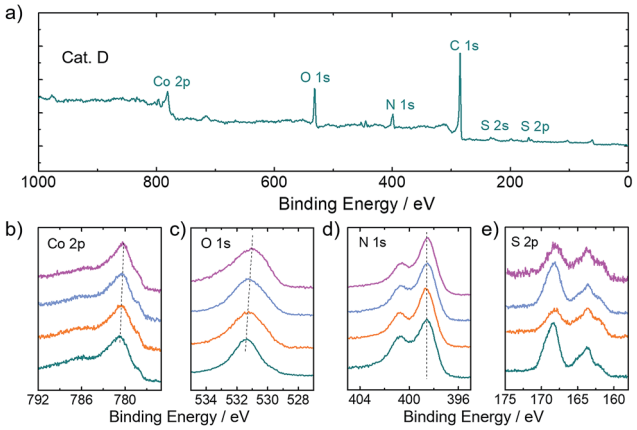

Fig. 4 XPS results giving an exemplary survey scan of cat D (a) and finescan regions related to Co 2p 3/2 (b), O 1s (c), N 1s (d) and S 2p (e) for cat A to D (from top to bottom).

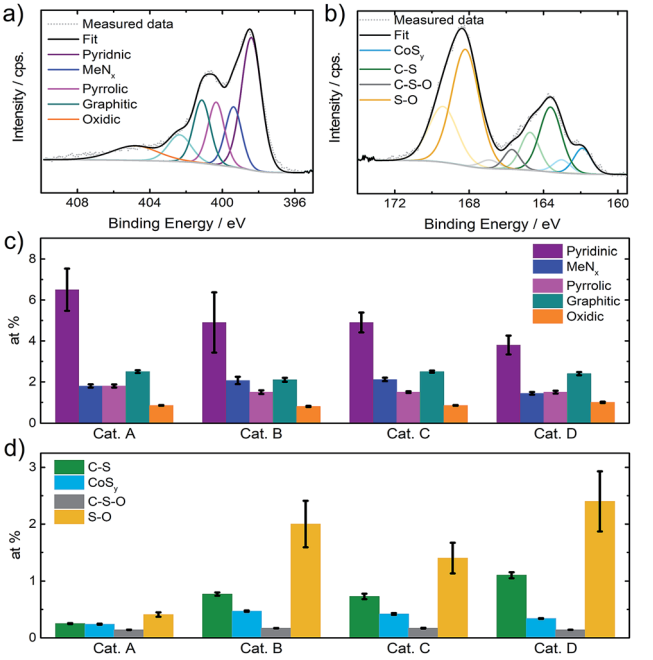

Fig. 5 Deconvoluted N 1s (a) and S 2p (b) spectra of cat D. In addition, the contents assigned to each N 1s and S 2p species were determined and are plotted in (c) and (d), respectively.

spectra, qualitatively the same species were attributed to the other three catalysts. Note: it was visible by XRD that the catalysts contained crystalline cobalt sulphides. However, as a reference measurement is missing to implement it in our fit, a Co 2p spectrum from the literature was considered as a reference. Alstrup *et al.*[57i] showed in their work that the Co 2p spectra of Co_9S_8 and cobalt single crystal are almost identical; hence in the fit in Fig. S6† it can only give a minor contribution in agreement with the calculated value for S in CoS_y in Table 1.

The quantitative analysis of cat D is in relatively good agreement with contributions in the N 1s and O 1s spectra. However, due to the need to integrate several species in this fitting, the error might be rather large. Instead of integrate, the difference spectra of the catalysts were analysed and will be discussed in relation to Fig. 8, below.

Considerable changes were visible in the S 2p region. Here, the relative intensity of the peak located at about 168 eV was significantly higher for cat B and cat D compared to cat A and cat C. The opposite trend was observed for a shoulder at *ca.* 166 eV.

The deconvoluted N 1s and S 2p spectra are shown in Fig. 5a and b. The peaks at 168 eV and 166 eV, respectively, were assigned to sulphate and C–S–O bonds (integrated in carbon). We will refer to this again, later. In addition to these two species, cobalt sulphide (CoS_y, *ca.* 161.8 eV) and sulphur integrated in carbon (C–S, 163.7 eV) were identified in the S 2p spectra. Within the N 1s region (Fig. 5a) oxidic (404–406 eV), graphitic (*ca.* 402 eV), pyrrolic (*ca.* 400.5 eV), pyridinic (*ca.* 398.5 eV) and Me–N interactions (*ca.* 399.5 eV) were found.[58] From the relative areas and the nitrogen and sulphur contents, the fraction of atoms bound to nitrogen and sulphur could be determined for each species.

These values are given in Fig. 5c and d, respectively, for the N 1s and S 2p regions. Already here, the decrease of pyridinic nitrogen and pronounced increase of sulphur heteroatoms in carbon are visible. The trends get even better pronounced in ESI† Fig. S7† where these values are plotted as a function of the S/Co ratio in the precursor.

Thus, the higher initial S/Co ratio caused the release of nitrogen and favoured the integration of sulphur as a dopant into the carbon network.

The overall elemental composition of the catalysts is summarised in Table 1; also here the estimated amounts of nitrogen in CoN_4 and sulphur in cobalt sulphide are added. This indicates that all catalysts contained large fractions of nitrogen and oxygen, while the sulphur content – considering its large amounts in the precursor – was relatively small, but increased when $S_{elemental}$ was added during the synthesis.

Table 1 Summary of the elemental composition (at%) derived from XPS measurements of the investigated samples. Besides the overall composition, the contents assigned to sulphur, respectively, nitrogen in CoS_y and CoN_x are given as well

At%	N	C	O	Co	S	CoS_{yx}	CoN_{xx}
Cat A	13.5 ± 0.3	76.0 ± 0.5	7.2 ± 0.3	2.3 ± 0.3	1.0 ± 0.1	0.24 ± 0.02	1.8 ± 0.1
Cat B	11.4 ± 0.4	72.5 ± 0.6	10.0 ± 0.3	2.7 ± 0.4	3.4 ± 0.1	0.47 ± 0.02	2.1 ± 0.2
Cat C	11.8 ± 0.4	74.9 ± 0.6	8.0 ± 0.4	2.6 ± 0.4	2.7 ± 0.2	0.42 ± 0.03	2.1 ± 0.1
Cat D	10.2 ± 0.3	71.2 ± 0.5	11.4 ± 0.3	3.1 ± 0.3	4.0 ± 0.1	0.34 ± 0.01	1.4 ± 0.1

Impact of the composition on oxygen evolution reaction (OER) activity and stability

Being aware of the chemical composition and local structural environments, the electrocatalytic applicability of the catalysts was investigated. Therefore, in Fig. 6 the linear scan voltammograms (LSVs) for evaluating the OER activity in 0.1 M KOH as well as the corresponding Tafel plots are shown for a loading of 1 mg cm^{-2} (Fig. S8† shows the OER activity trend for a smaller loading of 0.5 mg cm^{-2} (0.1 M KOH) and Fig. S9† the comparison of two measurements of each catalyst for high loading). Considering the low onset potentials, it is evident that the catalysts displayed a good catalytic activity for oxygen evolution in agreement with previous findings.[33,36,49]

In Fig. S10† measurements with a RRDE electrode were performed for the catalysts to distinguish between contributions of the desired oxygen evolution reaction and the undesired carbon oxidation reaction. In contrast to Li *et al.*[59] the applied potential at the ring was 0.45 V (SHE) rather than −0.6 V in their work. This potential of 0.45 V was chosen to avoid contributions of the HER or CO_2 reduction. Our selected potential is similar to the recommendations for using the RRDE for efficiency determination by Diaz-Molares *et al.*[45] and McCrory *et al.*[60] It should be pointed out that these data were measured on aged samples (stored in air) and were not *iR* corrected as the related bipotentiostat does not offer *iR* correction. In addition, efficiency determination by the RRDE on a porous catalyst might underestimate the real OER contribution as part of the formed O_2 might be trapped in the pores.

Nevertheless, there are some important observations to be made:

(1) Due to the storage in air the activity of the samples became less, consequently the onset for the OER was shifted to higher potential values (see Fig. S11† for the time-dependent change of the most active cat D).

(2) The faradaic efficiency $\varepsilon_{Faraday}$ towards the OER (Fig. S12†), for the recommended value[60] of $j = 1$ mA cm^{-2}, was in the case of the anodic scan about 20–25% (>50% for cat C) and in the cathodic scan about 50% (cat A, cat D) or 70% (cat B, cat C).

The OER activity was found to be highest for cat D followed by cat A > cat B ≈ cat C. Also the Tafel slope (determined in a current density range 1–10 mA cm^{-2}) varied for the catalysts. A value of 95 ± 5 mV dec^{-1} was observed for cat D, 125 ± 2 mV dec^{-1} for cat B, about 128 ± 1 mV dec^{-1} for cat C and 190 ± 5 mV dec^{-1} for cat A. The error was determined by considering variation in the current density range between 0.9 and 20 mA cm^{-2}.

Note, as the faradaic efficiency was obtained only for the aged samples and without *iR* correction, the absolute values of the Tafel slopes would change, whereas we assume that the relative trend between the four samples would remain. It is interesting to note that while the capacity correlated with the overall BET SA, the OER activity correlates with the micropore SA, as indicated in Fig. S1c.† The error bars from double measurements of the OER activity are included in this graph.

In Fig. 7 both the durability (in terms of activity changes induced by potential cycling) and the stability (in terms of galvanostatic treatment) of the best performing catalyst (cat D)

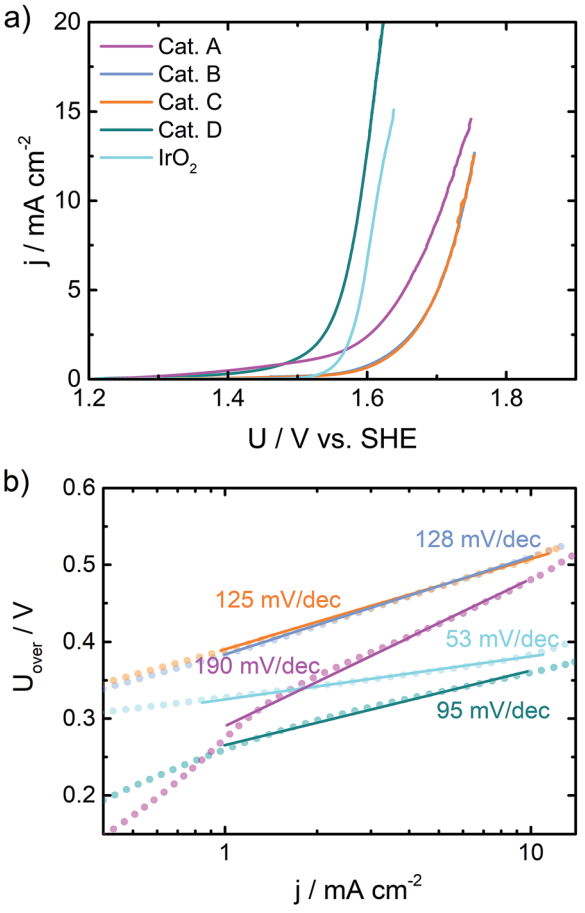

Fig. 6 (a) Linear scan voltammetry (LSV) of the catalysts in 0.1 M KOH at 1500 rpm (catalyst loading 1 mg cm^{-2}). The potential was corrected for *iR* drop. In (b) the Tafel plots related to these measurements are given. For reasons of comparison a commercial IrO_2 catalyst was measured (loading 250 μg cm^{-2} at 10 mV s^{-1}).

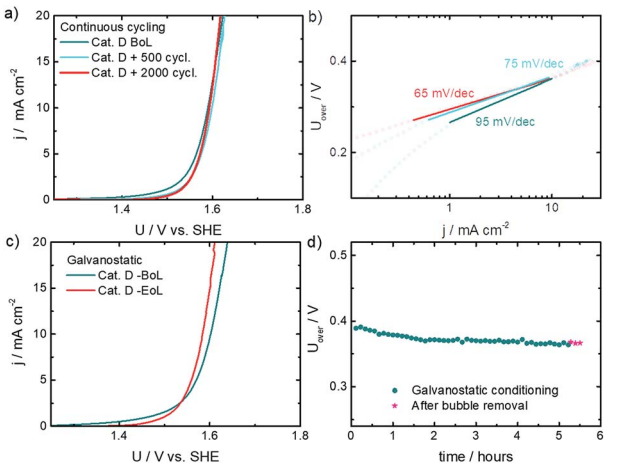

Fig. 7 (a) LSVs of cat D in 0.1 M KOH at 1500 rpm (catalyst loading 1 mg cm^{-2}) at the beginning of life (B.o.L.) and after 500 and 2000 potential cycles. In (b) the Tafel plots related to these measurements are shown. In (c) the LSVs at the B.o.L. and End of Life (E.o.L.) of the galvanostatic treatment at 10 mA cm^{-2} (d) are given.

were evaluated. The former was performed in order to check for performance changes induced by carbon oxidation, the latter to confirm stable performance during constant current operation. It is evident that the current density was stable or even slightly increased during these treatments. In addition to this, a decrease of the Tafel slope from 95 ± 5 mV dec^{-1} to 65 ± 2 mV dec^{-1} was observed.

In Fig. S13† the change in the CVs during this durability cycling is shown with only minor effects on the capacity induced by cycling.

Discussion of possible origins of Tafel slope changes

Here we propose and discuss two different explanations for the observed trends that might even be coupled. More work is required to enable final conclusions.

Explanation 1. The obtained value of the Tafel slope could depend on the degree of overlap between the OER and carbon oxidation. Under this assumption, the contribution of carbon oxidation is different for the different catalysts, causing the variation in current density and Tafel slopes. In this case, it could be expected that the Tafel slopes were related to the properties of the carbon, *e.g.* the degree of graphitization (as expressed by the I_D/I_G ratio) or edge-exposed heteroatoms. (In the work of Charreteur *et al.*[61] it was shown for other Me–N–C that the full width at half maximum (fwhm) increased as more heteroatoms were integrated at the edges of graphene layers.)

The degree of graphitization is inversely proportional to the I_D/I_G ratio. Thus if I_D/I_G increases, a larger contribution of carbon oxidation to the current density is expected. Consequently, Tafel slopes might increase with increasing I_D/I_G ratio. To check this statement, the related graph is shown in Fig. S14a.† Indeed, related changes in the Raman spectra were observed by Zana *et al.*[62] for carbon black, that was continuously cycled between 1.0 and 1.5 V. However, for the catalysts in this work Raman spectra were not measured after conditioning.

Similarly, it can be expected that heteroatoms at the edges of graphene layers get oxidized more easily; to evaluate this the Tafel slope is correlated with the fwhm of the D band, in Fig. S14b.† Also here, catalysts that could be assumed to exhibit a stronger carbon oxidation current show larger Tafel slope values. Following this explanation, the trends observed within the stability tests in Fig. 7 could be explained, for example by a decreasing ratio of I_D/I_G (as expected in relation to Zana's work[62]).

Explanation 2. There is a strong relationship between the rate determining step (RDS) as well as surface coverage and the observed Tafel slopes for multi-electron transfer reactions.[63–65]

For the OER in alkaline electrolyte on single metal sites, the following mechanism is proposed:[63,64,66]

$$M + OH^- \rightleftharpoons M\text{–}OH_{ads} + e^- \quad (1)$$

$$M\text{–}OH_{ads} + OH^- \rightleftharpoons M\text{–}O_{ads} + H_2O + e^- \quad (2)$$

$$M\text{–}O_{ads} + OH^- \rightleftharpoons M\text{–}OOH_{ads} + e^- \quad (3)$$

$$M\text{–}OOH_{ads} + OH^- \rightleftharpoons M + H_2O + O_2\uparrow + e^- \quad (4)$$

In these equations M indicates the metal of the catalytically active species. In terms of the catalysis relevant surface coverage, the equations indicate that empty sites, Co–OH, Co–O and Co–OOH, will be formed during the oxidation cycle. There are two extreme cases in terms of the dimension of theoretically expected Tafel slopes. In general, a Tafel slope of 120 mV dec^{-1} is expected when the species that is formed before the RDS is dominating the surface coverage, *e.g.* if the fourth step is the RDS a surface coverage dominated by OOH_{ads} would be expected.

However, smaller values are observed, if the surface coverage is shifted to species formed at an earlier stage in the oxidation cycle. For example, if the third step would be rate determining, it is expected that the surface of the cobalt-based catalytic sites is mainly determined by O_{ads}. A decrease of the Tafel slope could then also indicate that the surface coverage with O_{ads} becomes less, but more OH_{ads} is found. Depending on which species are mainly found on the surface of catalytic sites, the value might even go down to about 20 mV dec^{-1} when for instance empty sites remain the dominating surface sites (M without adsorbate). This has been nicely illustrated by Shinagawa[64] (see Fig. 4b–f shown in their work).

How does the second explanation relate to the results obtained in this work?

From Fig. 6 and 7 it was possible to draw the following conclusion with respect to the activity trend: the Tafel slope of the best performing catalyst was 95 mV dec^{-1} and became larger for the catalysts with the lowest performance. In accordance to this, during the stability and durability measurements the Tafel slope decreased from 95 ± 4 mV dec^{-1} to 75 ± 4 mV dec^{-1} and further down to 65 ± 2 mV dec^{-1} while the activity got enhanced. Thus, in this work more active catalysts displayed smaller Tafel slopes.

As described above, in terms of surface occupation, a decrease of the Tafel slope could be indicative of a dominance of species formed prior to the RDS within the overall oxidation cycle.

To get further conclusions on the mechanism, the O 1s spectra were deconvoluted into their different components. The spectra were fitted with Co–O, Co–OH (assigned to hydroxide and defective oxide), H_2O_{ads} and organic species (C–O, C=O). Fig. 8 shows the deconvoluted O 1s spectrum of the most active catalyst and correlates the concentration of $Co\text{–}OH_{ads}$ (from O 1s) with the amount of cobalt in the catalysts. Furthermore, it shows that the amount of $Co\text{–}OH_x$ increases and the amount of Co–O decreases, when the Tafel slope decreases.

Even though these data were obtained *ex situ*, the relationship between Tafel slopes and both Co–O and Co–OH seems to indicate that the surface occupations of both species was of importance for the OER on our catalysts. Indeed also the Co 2p difference spectra (in relation to the most active cat D) in Fig. S15† point in the same direction: while the contribution of CoO decreased in the order cat A > cat B ≈ cat C > cat D, the contribution for the binding energy associated with $Co(OH)_2$ was largest for cat D while it was approx. similar for cat B, cat A and cat C.

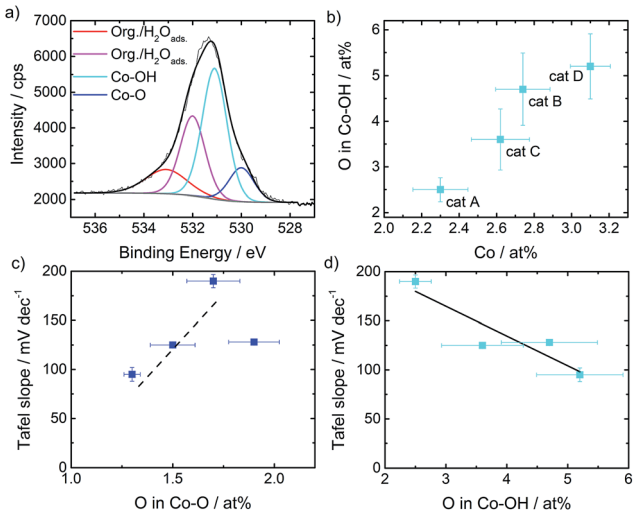

Fig. 8 Deconvoluted O 1s spectrum of the most active catalyst (cat D) of this work (a). In (b) the oxygen content assigned to Co–OH is given as a function of the as-measured cobalt content in the catalysts. Illustration of the changes in Tafel slope as a function of O in Co–O (c) and in Co–OH (d).

Usually a Tafel slope of 120 mV dec^{-1} is assigned to the first electron transfer step as the RDS. However, it seems that on this group of catalysts, the surface occupation might be more important for changes of the Tafel slope instead of a change of the RDS. Comparing our trends in Fig. 8c and d to the relationship of Tafel slope and surface occupation proposed by Shingagawa *et al.*,[64] the fourth electron transfer step could be assigned as the RDS.

These results are further supported by the fact that during OER stability and durability testing (Fig. 7) a decrease of the Tafel slope could be observed.

Therefore, also for this group of sulphur- and nitrogen-doped cobalt-based carbon catalysts the concentration dependence of surface hydroxide on the OER[41] was strongly indicated.

To what extent the CoN_4 and CoS_y species remain intact during the OER or whether they transform to hydroxides is an important question that needs to be addressed in more detail in future work. It is also important to mention that carbon oxidation and the formation/presence of hydroxide species at the surface of the catalyst might be related to each other. For example, the formation of hydroxide species might be initiated by carbon oxidation and exposure of cobalt species to the surface of the catalyst.

Conclusions

A group of multi-heteroatom doped carbon-based catalysts were synthesised from $PANI_{evap.}$, DCDA, $S_{elemental}$ and cobalt acetate by a pyrolysis process. The catalysts revealed a heterogeneous composition of cobalt nanoparticles, cobalt sulphide, CoN_4 sites, and oxidised cobalt. Regarding the carbon morphology, it was found that with a molar ratio of S/Co > 15 nanotube formation took place, whereas at the same time the overall BET surface area decreased. More importantly, the diameter and relative contribution of the carbon nanotubes to the overall carbon became larger. The catalysts obtained high catalytic activity towards the oxygen evolution reaction and even improved performance with time. The faradaic efficiency is minimum 35% at 1 mA cm^{-2} for the investigated catalysts. The remaining current contribution is most probably given by carbon oxidation.

The analysis of Tafel plots in relation to the 1st order region of carbon in Raman spectroscopy and the near-surface composition obtained by XPS let us conclude that either carbon oxidation or a beneficial formation of cobalt hydroxide species at the surface dominated the observed Tafel slope trends. Also a combined mechanism is possible. In future work, emphasis should be given to a more detailed study of structural changes induced by the OER for this group of carbon-based catalysts by post mortem analysis.

Experimental

Synthesis procedures

Synthesis of $PANI_{evap}$. The synthesis of $PANI_{evap}$ was already described in our previous article.[14] Briefly, $PANI_{evap}$ was synthesised by oxidative polymerisation of aniline with ammonium peroxidisulfate (APS) in hydrochloric acid. The molar ratio was 1 : 3. After synthesis, the solution was evaporated so that the product contains polyaniline, the residuals of APS and HCl. The quantities of $PANI_{evap}$ and the other precursors are given in Table 2.

Procedure for synthesis of Co–N–C catalysts. In order to prepare the sulphur- and nitrogen-doped cobalt-based carbon catalysts (CoAc), 99 mg cobalt acetate tetrahydrate and 680 mg $PANI_{evap}$ were mixed and ground with a mortar and pestle. In the next step, 2268 mg dicyandiamide (DCDA) is added as a structure forming agent (SFA). The elemental sulphur ($S_{elemental}$) was added to the mixture after pre-grinding and the overall mixture was ground further until a homogeneous mixture was obtained. Without considering the mass of the SFA and $S_{elemental}$, the precursor contains 3 wt% cobalt.

The mixed powder was filled into quartz boats and subjected to the pyrolysis in a furnace under constant flow of nitrogen. The synthesis procedure includes two heat treatment steps with an acid leaching step in between. The first heat treatment involves heating from room temperature (RT) to 800 °C at 5 °C min^{-1}, with intermediate temperature equilibrations at 300 °C for 30 min, at 500 °C for 30 min and finally at 800 °C for 60 min. Subsequently, the mixture was cooled down to RT and then

Table 2 Mass quantities for the preparation of N- and S-doped cobalt-based carbon catalysts

[mg]	$S_{elemental}$	$CoAc \cdot 4H_2O$	$PANI_{evap}$	DCDA	S/Co (molar)
Cat A	0	98.7	680	2280	10
Cat B	98	98.7	680	2280	15
Cat C	180	98.7	680	2280	25
Cat D	362	98.7	680	2280	32

transferred to 2 M HCl for the acid leaching step (60 min in an ultrasonic bath, followed by stirring over-night). The suspension was washed with water, dried and transferred again to the furnace for the second heat treatment. Also here, the catalysts were continuously heated in a nitrogen atmosphere but with a significantly larger ramp of 38 °C min^{-1} up to 600 °C. The heating ramp was then slowed down to 5 °C min^{-1} up to 800 °C with a dwell time of three hours. After cooling down, the catalyst powder was ground and stored for further characterisation.

Electrochemical evaluation

Preparation of the working electrode. In order to prepare the working electrodes, a catalyst suspension was prepared and then drop-cast on a glassy carbon disc. For the ink preparation, 5 mg of catalyst powder was mixed with 25 μl Nafion (5 wt%), 142 μl of ethanol, and 83.2 μl of water. The suspension was placed for 30 min in an ultrasonic bath. Before use, the ink was homogenised with an ultrasonic homogenisator. Then, 10 μl of the ink was drop-cast on the glassy carbon disc to obtain a loading of 1 mg cm^{-2}. It should be noted that the OER activity was also evaluated with a smaller loading (0.5 mg cm^{-2}), therefore 5 μl of the same ink were used in the working electrode preparation.

Evaluating OER activity. The measurements were accomplished by using a standard three electrode configuration. The setup contains the RDE electrode with a glassy carbon disc equipped with the catalyst, a glassy carbon rod (counter electrode), and a Hg|HgO|1 M NaOH reference electrode. First, for activation of the electrodes, cyclic voltammetry (CV) was carried out in 0.1 M KOH from 0.0 V to 1.2 V with a sweep rate of 100 mV s^{-1} with 10 cycles and afterwards in the range 1.2–1.8 V for 30 cycles with a sweep rate of 300 mV s^{-1}. To evaluate the OER activity, linear sweep voltammograms were measured from 1.2 V to 1.9 V with a sweep rate of 5 mV s^{-1} at a rotation speed of 1500 rpm. The reported potentials refer to the standard hydrogen electrode and are corrected for *iR* drop.

Evaluation of the faradaic efficiency $\varepsilon_{Faraday}$. The faradaic efficiency was determined by rotating ring disc electrode (RRDE) experiments with a glassy carbon disc ($A = 0.238$ cm^2) with the deposited catalysts (5 μl ink) and a platinum ring. Potential control of the disc and ring was made with a Versastat 3/3F bipotentiostat with the same counter and reference electrodes as given above. After activation of the catalysts, RRDE experiments for selectivity evaluation were performed. The faradaic efficiency for oxygen formation during the OER was determined using the following equation:

$$\varepsilon_{Faraday} = I_{Ring} {I_{disc}}^{-1} N^{-1} \quad (5)$$

where I_{Ring} is the measured ring current, I_{disc} is the as-measured disc current and N the collection efficiency. For the given electrode design N equals 0.38.

The selectivity measurements were made in a potential range of 1.9 V to 1.2 V for the disc electrode with a sweep rate of 10 mV s^{-1} at a rotation speed of 1500 rpm. The ring potential was fixed to $U = 0.45$ V (SHE).

The internal resistivity (ohmic) was determined using a Nordic electrochemistry potentiostat in the corresponding OER potential window at a constant frequency (5 kHz), obtained values are depicted in Fig. S16.† Fig. S17† shows the comparison of the non- and *iR*-corrected OER polarization curve for cat D. Compensation for ohmic losses was made according to eqn (6):

$$U_{iR\text{-corr.}} = U_{exp} - iR \quad (6)$$

Fig. S17† also gives the non-corrected OER data of the four catalysts.

All potentials in this work were converted to the standard hydrogen electrode (SHE) by measuring the potential shift between the reference electrode in 0.1 M KOH towards a commercial SHE (giving a potential difference of 0.9 V).

This value fits nicely to the theoretically assumed value of 0.907 V.

$$E_{SHE} = E_{measured} + E^0_{Hg|HgO|1\ M\ NaOH} + 0.059\ V\ pH \quad (7)$$

$$E_{SHE} = E_{measured} + 0.140\ V + 0.767\ V = E_{measured} + 0.907\ V \quad (8)$$

Evaluating OER stability and durability. The durability test was performed with cycling between 1.1 and 1.8 V *vs.* SHE and a sweep rate of 0.3 V s^{-1}, and the stability test was carried out galvanostatically at 10 mA cm^{-2} at a rotation speed of 1500 rpm.

Structural characterisation

X-ray diffraction. The measurements were performed at RT using a Bruker D8 Advance diffractometer in Bragg–Brentano geometry employing a monochromatised Cu K_α radiation source and a VANTEC detector. Data were recorded in an angular range between 5° and 50° (2θ) for a total measurement time of one hour using a step size of ~0.007°, a step time of 0.5 step per s and a fixed divergence slit of 0.3°. Due to the low signal to noise ratio, assignment of the reflections was made using a logarithmic plot of the data and the presence of the phases could be confirmed by Rietveld analysis.

TEM imaging. TEM characterisation was performed with a FEI CM20 STEM (Eindhoven, the Netherlands) microscope equipped with a LaB6 cathode and a Gatan double tilt holder at a nominal acceleration voltage of 200 kV. The catalyst powder was dissolved in ethanol and ultrasonicated for 30 seconds. Large agglomerates and particles were allowed to settle down, before a small quantity was dropped on a cupper grid with a carbon film (Baltec MED010).

Raman spectroscopy. The measurements were performed using an alpha 300R confocal Raman microscope from WiTec (Ulm, Germany) with a grid of 600 lines mm^{-1} and an excitation laser of $\lambda = 532.2$ nm with a power of 1 mW. The catalyst was suspended and then dropped on a silica disc and left to dry. The data were obtained for three different spots in a wavenumber range of 0 to 2000 cm^{-1}. An integration time of 10 s was used for each data point. The as-given spectra are the sum-spectra of the three measurements obtained for each catalyst. The main paragraph text follows directly on here.

N_2 sorption measurements. N_2 sorption measurements were performed with an Autosorb test station from Quantachrome. Prior to the measurements, the samples were degassed at 200 °C for 16 h. From N_2 sorption data the BET specific surface area as well as the micropore surface area from *V*–*t*-plots were determined. Micropores are pores with a diameter < 20 nm. The given data of the mesopore surface area are calculated by subtracting the micropore surface area from the overall BET SA.

X-ray photoelectron spectroscopy. XPS measurements were performed using a Specs Phoibos 150 hemispherical analyzer and a Specs XR50M Al K_α X-ray source ($E = 1486.7$ eV). For the survey scans, an energy step of 1 eV has been applied and two scans were overlaid. In addition, fine scans were obtained for the Co 2p, O 1s, N 1s, C 1s and S 2p regions. For the fine scans an energy step of 0.05 eV has been used. For the fitting of the spectra, the software Casa XPS was used. The standard deviation corresponding to each species was determined by using Monte Carlo simulation and error propagation.

Statement of contributions

Concept of the work A. S. and U. I. K., preparation of catalysts A. S. and K. A. C., electrochemical characterization A. S., W. D. Z. W., and N. W., physicochemical characterization and data analysis M. K., I. M., M. A. N., S. P., and O. C., and all authors contributed to the writing process.

Conflicts of interest

There are no conflicts to declare.

Acknowledgements

Financial support by the German Research Foundation within the Graduate School of Excellence Energy Science and Engineering (GSC1070) is gratefully acknowledged by A. S., I. M., S. P. and U. I. K., U. I. K. and W. D. Z. W also acknowledges financial support *via* the grant KR3980/4-1. We would also like to thank W. Jaegermann and his group for the possibility to use the XPS system DAISY-FUN for characterisation of our catalysts.

References

1 P. Larscheid, L. Lück and A. Moser, *Renewable Energy*, 2018, **125**, 599–608.
2 European Commission, *Report on critical Raw Materials for the EU*, 2014.
3 P. Du and R. Eisenberg, *Energy Environ. Sci.*, 2012, **5**, 6012–6021.
4 M. Shao, Q. Chang, J.-P. Dodelet and R. Chenitz, *Chem. Rev.*, 2016, **116**, 3594–3657.
5 U. I. Kramm, M. Lefèvre, N. Larouche, D. Schmeisser and J.-P. Dodelet, *J. Am. Chem. Soc.*, 2014, **136**, 978–985.
6 E. Proietti, F. Jaouen, M. Lefévre, N. Larouche, J. Tian, J. Herranz and J.-P. Dodelet, *Nat. Commun.*, 2011, **2**, 416.
7 J. Y. Cheon, T. Kim, Y. Choi, H. Y. Jeong, M. G. Kim, Y. J. Sa, J. Kim, Z. Lee, T.-H. Yang, K. Kwon, O. Terasaki, G.-G. Park, R. R. Adzic and S. H. Joo, *Sci. Rep.*, 2013, **3**.
8 J. Shui, C. Chen, L. Grabstanowicz, D. Zhao and D.-J. Liu, *Proc. Natl. Acad. Sci. U. S. A.*, 2015, **112**, 10629–10634.
9 G. Wu and P. Zelenay, *Acc. Chem. Res.*, 2013, **46**, 1878–1889.
10 A. S. Varela, N. Ranjbar Sahraie, J. Steinberg, W. Ju, H.-S. Oh and P. Strasser, *Angew. Chem., Int. Ed.*, 2015, **54**, 10758–10762.
11 T. N. Huan, N. Ranjbar, G. Rousse, M. Sougrati, A. Zitolo, V. Mougel, F. Jaouen and M. Fontecave, *ACS Catal.*, 2017, **7**, 1520–1525.
12 O. Hitoshi, M. Tomomi, O. Yuji and Y. Ichiro, *ChemistrySelect*, 2016, **1**, 5533–5537.
13 F. Pan, W. Deng, C. Justiniano and Y. Li, *Appl. Catal., B*, 2018, **226**, 463–472.
14 A. Shahraei, I. Martinaiou, K. A. Creutz, M. Kübler, N. Weidler, S. T. Ranecky, W. D. Z. Wallace, M. A. Nowroozi, O. Clemens, R. W. Stark and U. I. Kramm, *Chem.–Eur. J.*, 2018, **24**, 122480–12484.
15 A. Shahraei, A. Moradabadi, I. Martinaiou, S. Lauterbach, S. Klemenz, S. J. Dolique, H.-J. Kleebe, P. Kaghazchi and U. I. Kramm, *ACS Appl. Mater. Interfaces*, 2017, **9**, 25184–25193.
16 W. Deng, H. Jiang, C. Chen, L. Yang, Y. Zhang, S. Peng, S. Wang, Y. Tan, M. Ma and Q. Xie, *ACS Appl. Mater. Interfaces*, 2016, **8**, 13341–13347.
17 A. Morozan, V. Goellner, Y. Nedellec, J. Hannauer and F. Jaouen, *J. Electrochem. Soc.*, 2015, **162**, H719–H726.
18 Q. Lu, G. S. Hutchings, W. Yu, Y. Zhou, R. V. Forest, R. Tao, J. Rosen, B. T. Yonemoto, Z. Cao, H. Zheng, J. Q. Xiao, F. Jiao and J. G. Chen, *Nat. Commun.*, 2015, **6**, 6567.
19 L. Zhang, J. Xiao, H. Wang and M. Shao, *ACS Catal.*, 2017, **7**, 7855–7865.
20 P. Chen, T. Zhou, L. Xing, K. Xu, Y. Tong, H. Xie, L. Zhang, W. Yan, W. Chu, C. Wu and Y. Xie, *Angew. Chem., Int. Ed.*, 2017, **56**, 610–614.
21 A. Abbaspour and E. Mirahmadi, *Electrochim. Acta*, 2013, **105**, 92–98.
22 Q. Daniel, R. B. Ambre, B. Zhang, B. Philippe, H. Chen, F. Li, K. Fan, S. Ahmadi, H. Rensmo and L. Sun, *ACS Catal.*, 2017, **7**, 1143–1149.
23 F. Dai, W. Fan, J. Bi, P. Jiang, D. Liu, X. Zhang, H. Lin, C. Gong, R. Wang, L. Zhang and D. Sun, *Dalton Trans.*, 2016, **45**, 61–65.
24 Y. Gorlin and T. F. Jaramillo, *J. Am. Chem. Soc.*, 2010, **132**, 13612–13614.
25 X. Qiao, J. Jin, H. Fan, Y. Li and S. Liao, *J. Mater. Chem. A*, 2017, **5**, 12354–12360.
26 S. Dresp, F. Luo, R. Schmack, S. Kühl, M. Gliech and P. Strasser, *Energy Environ. Sci.*, 2016, **9**, 2020–2024.
27 U. I. Kramm, I. Herrmann-Geppert, S. Fiechter, G. Zehl, I. Zizak, I. Dorbandt, D. Schmeißer and P. Bogdanoff, *J. Mater. Chem. A*, 2014, **2**, 2663–2670.
28 I. Herrmann, U. I. Kramm, J. Radnik, P. Bogdanoff and S. Fiechter, *J. Electrochem. Soc.*, 2009, **156**, B1283–B1292.

29 W. Kiciński, B. Dembinska, M. Norek, B. Budner, M. Polański, P. J. Kulesza and S. Dyjak, *Carbon*, 2017, **116**, 655–669.
30 M. Ferrandon, A. J. Kropf, D. J. Myers, K. Artyushkova, U. Kramm, P. Bogdanoff, G. Wu, C. M. Johnston and P. Zelenay, *J. Phys. Chem. C*, 2012, **116**, 16001–16013.
31 A. Janßen, I. Martinaiou, S. Wagner, N. Weidler, A. Shahraei and U. I. Kramm, *Hyperfine Interact.*, 2018, **239**, 7.
32 N. R. Sahraie, U. I. Kramm, J. Steinberg, Y. Zhang, A. Thomas, T. Reier, J. P. Paraknowitsch and P. Strasser, *Nat. Commun.*, 2015, **6**, 8618.
33 H. Qian, J. Tang, Z. Wang, J. Kim, J. H. Kim, S. M. Alshehri, E. Yanmaz, X. Wang and Y. Yamauchi, *Chem.–Eur. J.*, 2016, **22**, 18259–18264.
34 P. Cai, J. Huang, J. Chen and Z. Wen, *Angew. Chem., Int. Ed.*, 2017, **56**, 4858–4861.
35 K. Jayaramulu, J. Masa, O. Tomanec, D. Peeters, V. Ranc, A. Schneemann, R. Zboril, W. Schuhmann and R. A. Fischer, *Adv. Funct. Mater.*, 2017, **27**, 1700451.
36 M. Zhu, Z. Zhang, H. Zhang, H. Zhang, X. Zhang, L. Zhang and S. Wang, *J. Colloid Interface Sci.*, 2018, **509**, 522–528.
37 M. Chauhan, K. P. Reddy, C. S. Gopinath and S. Deka, *ACS Catal.*, 2017, 5871–5879.
38 J. Suntivich, K. J. May, H. A. Gasteiger, J. B. Goodenough and Y. Shao-Horn, *Science*, 2011, **334**, 1383–1385.
39 H. Wang, Z. Li, G. Li, F. Peng and H. Yu, *Catal. Today*, 2015, **245**, 74–78.
40 W. T. Hong, M. Risch, K. A. Stoerzinger, A. Grimaud, J. Suntivich and Y. Shao-Horn, *Energy Environ. Sci.*, 2015, **8**, 1404–1427.
41 N. Weidler, S. Paulus, J. Schuch, J. Klett, S. Hoch, P. Stenner, A. Maljusch, J. Brotz, C. Wittich, B. Kaiser and W. Jaegermann, *Phys. Chem. Chem. Phys.*, 2016, **18**, 10708–10718.
42 D. Friebel, M. W. Louie, M. Bajdich, K. E. Sanwald, Y. Cai, A. M. Wise, M.-J. Cheng, D. Sokaras, T.-C. Weng, R. Alonso-Mori, R. C. Davis, J. R. Bargar, J. K. Nørskov, A. Nilsson and A. T. Bell, *J. Am. Chem. Soc.*, 2015, **137**, 1305–1313.
43 M. W. Louie and A. T. Bell, *J. Am. Chem. Soc.*, 2013, **135**, 12329–12337.
44 K. Fominykh, P. Chernev, I. Zaharieva, J. Sicklinger, G. Stefanic, M. Döblinger, A. Müller, A. Pokharel, S. Böcklein, C. Scheu, T. Bein and D. Fattakhova-Rohlfing, *ACS Nano*, 2015, **9**, 5180–5188.
45 O. Diaz-Morales, I. Ledezma-Yanez, M. T. M. Koper and F. Calle-Vallejo, *ACS Catal.*, 2015, **5**, 5380–5387.
46 G. Wu, K. L. More, C. M. Johnston and P. Zelenay, *Science*, 2011, **332**, 443–447.
47 P. Ghosh, T. Soga, K. Ghosh, T. Jimbo, R. Katoh, K. Sumiyama and Y. Ando, *Nanoscale Res. Lett.*, 2008, **3**, 242.
48 L. Ci, Y. Li, B. Wei, J. Liang, C. Xu and D. Wu, *Carbon*, 2000, **38**, 1933–1937.
49 H. Wang, Z. Li, G. Li, F. Peng and H. Yu, *Catal. Today*, 2015, **245**, 74–78.
50 P.-G. Yin, L. Jiang, T.-T. You, W. Zhou, L. Li, L. Guo and S. Yang, *Phys. Chem. Chem. Phys.*, 2010, **12**, 10781–10785.
51 B. Rivas-Murias and V. Salgueiriño, *J. Raman Spectrosc.*, 2017, **48**, 837–841.
52 J. Zhu, L. Huang, Y. Xiao, L. Shen, Q. Chen and W. Shi, *Nanoscale*, 2014, **6**, 6772–6781.
53 F. Tuinstra and J. L. König, *J. Chem. Phys.*, 1970, **53**, 1126–1130.
54 N. Larouche and B. L. Stansfield, *Carbon*, 2010, **48**, 620–629.
55 A. Sadezky, H. Muckenhuber, H. Grothe, R. Niessner and U. Pöschl, *Carbon*, 2005, **43**, 1731–1742.
56 I. Martinaiou, A. Shahraei, F. Grimm, H. Zhang, C. Wittich, S. Klemenz, S. J. Dolique, H.-J. Kleebe, R. W. Stark and U. I. Kramm, *Electrochim. Acta*, 2017, **243**, 183–196.
57 I. Alstrup, I. Chorkendorff, R. Candia, B. S. Clausen and H. Topsøe, *J. Catal.*, 1982, **77**, 397–409.
58 F. Jaouen, J. Herranz, M. Lefèvre, J.-P. Dodelet, U. I. Kramm, I. Herrmann, P. Bogdanoff, J. Maruyama, T. Nagaoka, A. Garsuch, J. R. Dahn, T. S. Olson, S. Pylypenko, P. Atanassov and E. A. Ustinov, *ACS Appl. Mater. Interfaces.*, 2009, **1**, 1623–1639.
59 L. Li, H. Yang, J. Miao, L. Zhang, H.-Y. Wang, Z. Zeng, W. Huang, X. Dong and B. Liu, *ACS Energy Lett.*, 2017, **2**, 294–300.
60 C. C. L. McCrory, S. Jung, J. C. Peters and T. F. Jaramillo, *J. Am. Chem. Soc.*, 2013, **135**, 16977–16987.
61 F. Charreteur, F. Jaouen, S. Ruggeri and J.-P. Dodelet, *Electrochim. Acta*, 2008, **53**, 2925–2938.
62 A. Zana, J. Speder, N. E. A. Reeler, T. Vosch and M. Arenz, *Electrochim. Acta*, 2013, **114**, 455–461.
63 M. T. M. Koper, *J. Electroanal. Chem.*, 2011, **660**, 254–260.
64 T. Shinagawa, A. T. Garcia-Esparza and K. Takanabe, *Sci. Rep.*, 2015, **5**, 13801.
65 R. L. Doyle and M. E. G. Lyons, in *Photoelectrochemical Solar Fuel Production*, ed. S. Giménez and J. Bisquert, Springer, 2016, DOI: 10.1007/978-3-319-29641-8_2.
66 F. Calle-Vallejo, J. I. Martinez and J. Rossmeisl, *Phys. Chem. Chem. Phys.*, 2011, **13**, 15639–15643.

Electronic Supplementary Material (ESI) for Journal of Materials Chemistry A.

Supplementary information

On the role of hydroxide species in sulphur- and nitrogen-doped cobalt-based carbon catalysts for the oxygen evolution reaction

Ali Sharaei, Markus Kuebler, Ioanna Martinaiou, K. Alexander Creutz, W. David Z. Wallace, Mohammad A. Nowroozi, Stephen Paul, Natascha Weidler, Robert W. Stark, Oliver Clemens, and Ulrike I. Kramm

Figure S1. Cyclic voltammetry in N_2 saturated 0.1M KOH at 100 mV s^{-1} (a) and correlation attempts of the double layer capacity with the BET surface area (b) and of the current density at 1.6 V versus micropore surface area.

Figure S2. TEM images of the catalysts at different magnifications, on top the related scaling of the scale bar is given.

Figure S3. Deconvoluted Raman spectra of the 1st order region assigned to carbon blacks for all four catalysts.

Figure S4. Correlation between I_{D3}/I_G ratio and the sum of $N_{Me\text{-}N}$ plus $N_{pyrid.}$ and correlation between I_D/I_G ratio and the relative fraction of C-S-O (increase).

Figure S5: Co 2p full spectra range for all investigated catalysts as well as reference systems.

Figure S6: Exemplary fit of Co 2p 3/2 region of cat D with different components. The spectrum of Co_9S_8 was digitalized from data provided in Alstrup et al., J. Catalysis 1982, see reference 57 of the main manuscript.

Figure S7. Correlation of the atomic concentrations of $N_{pyridinic.}$, and C-S as a function of the S/Co ratio in the precursors.

Figure S8. The linear scan voltammograms (LSVs) and Tafel plots for evaluating the OER activity with lower catalyst loading (0.5 mg cm^{-2}) in 0.1M KOH (rpm1500).

Figure S9. Repetition of the OER activity measurements of the catalysts and standard deviation of the overpotential

Figure S10: RRDE data of the four aged catalysts measured at 10 mV s^{-1} with 5 µl ink (corresponding loading on disc: 0.412 mg cm^{-2}), the ring potential was kept at 0.45 V (SHE). Darker colors refer to the anodic (initial) scan, lighter colors to the related cathodic scan that was performed after.

Figure S11. LSVs of the most active catalyst measured at different time intervals after preparation (as indicated in the label) and plot of the overpotential versus time after preparation. It becomes visible that there is a strong decay of the catalyst with storage time.

Figure S12. Trends in faradaic efficiency as a function of applied potential for the aged catalysts A to D. See Table S1 for summary of average values at 1 mA cm^{-2}.

Figure S13. CVs during durability cycling (compare Figure 7a), shown are every 100th cycle, whereas the initial cycle, cycle No. 500 and cycle No. 2000 are highlighted in the respective color. All other cycles displayed in black. Cycling in 0.1M KOH at 1500 rpm with a sweep rate of 300 mV s^{-1}.

Figure S14. Correlation attempts of the I_D/I_G ratio (a) and the full-width at half maximum (fwhm) of the D-band (b) versus the Tafel slopes.

Figure S15. Co 2p difference spectra of catalysts A-C in relation to the most active cat D. The arrow at ca. 778 eV might be attributed to Co-O species, whereas the arrow at ca. 782 eV is indicative of hydroxide species.

Figure S16. As-measured resistivity data (related to Figure 6 of the main manuscript) versus applied potential for the four catalysts A-D.

Figure S17: Comparison of the original activity scan of cat D and after iR correction (top graph) and comparison of the original data of all four catalysts (bottom graph). All measurements for a loading of 1 mg cm^{-2}.

Table S1: Summary of the faradaic efficiencies of catalysts A-D at a current density of 1 mA cm^{-2} in the anodic and cathodic scan.

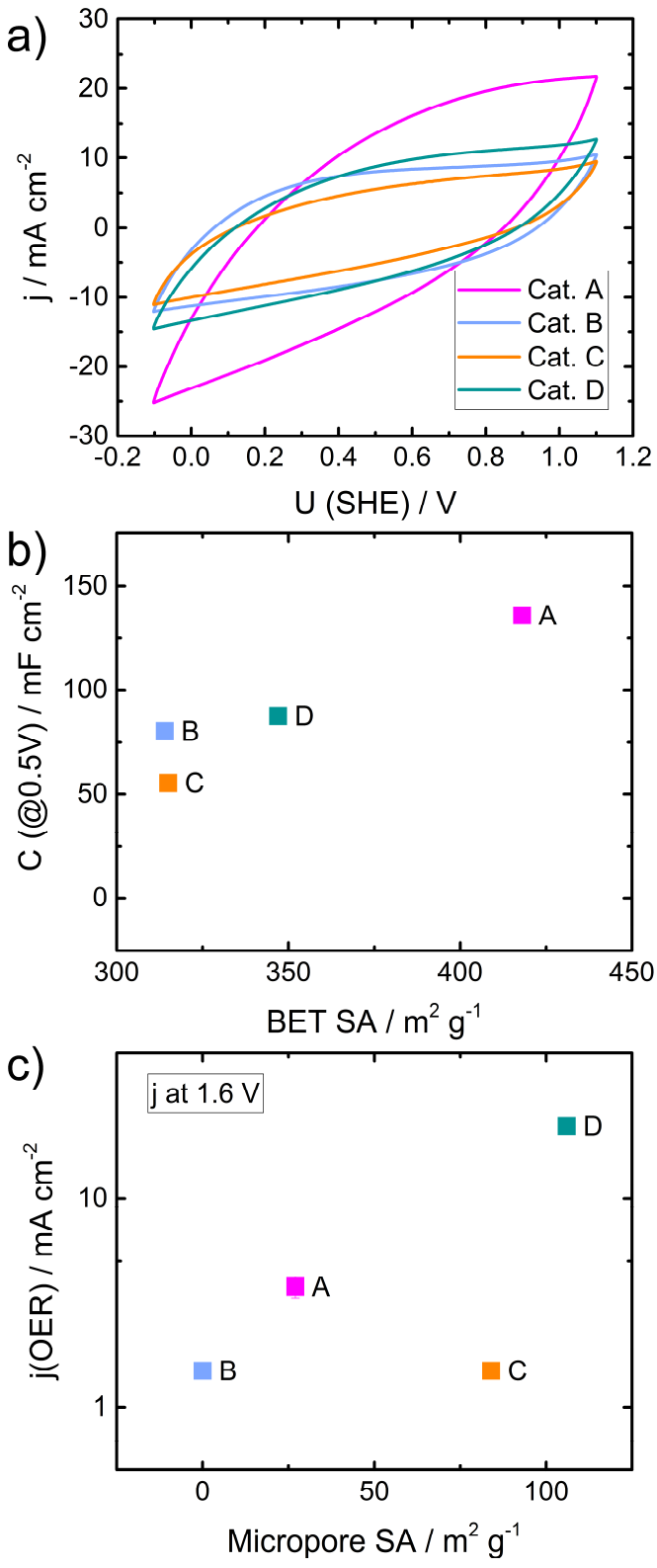

Figure S1. Cyclic voltammetry in N_2 saturated 0.1M KOH at 100 mV s^{-1} (a) and correlation attempts of the double layer capacity with the BET surface area (b) and of the current density at 1.6 V versus micropore surface area.

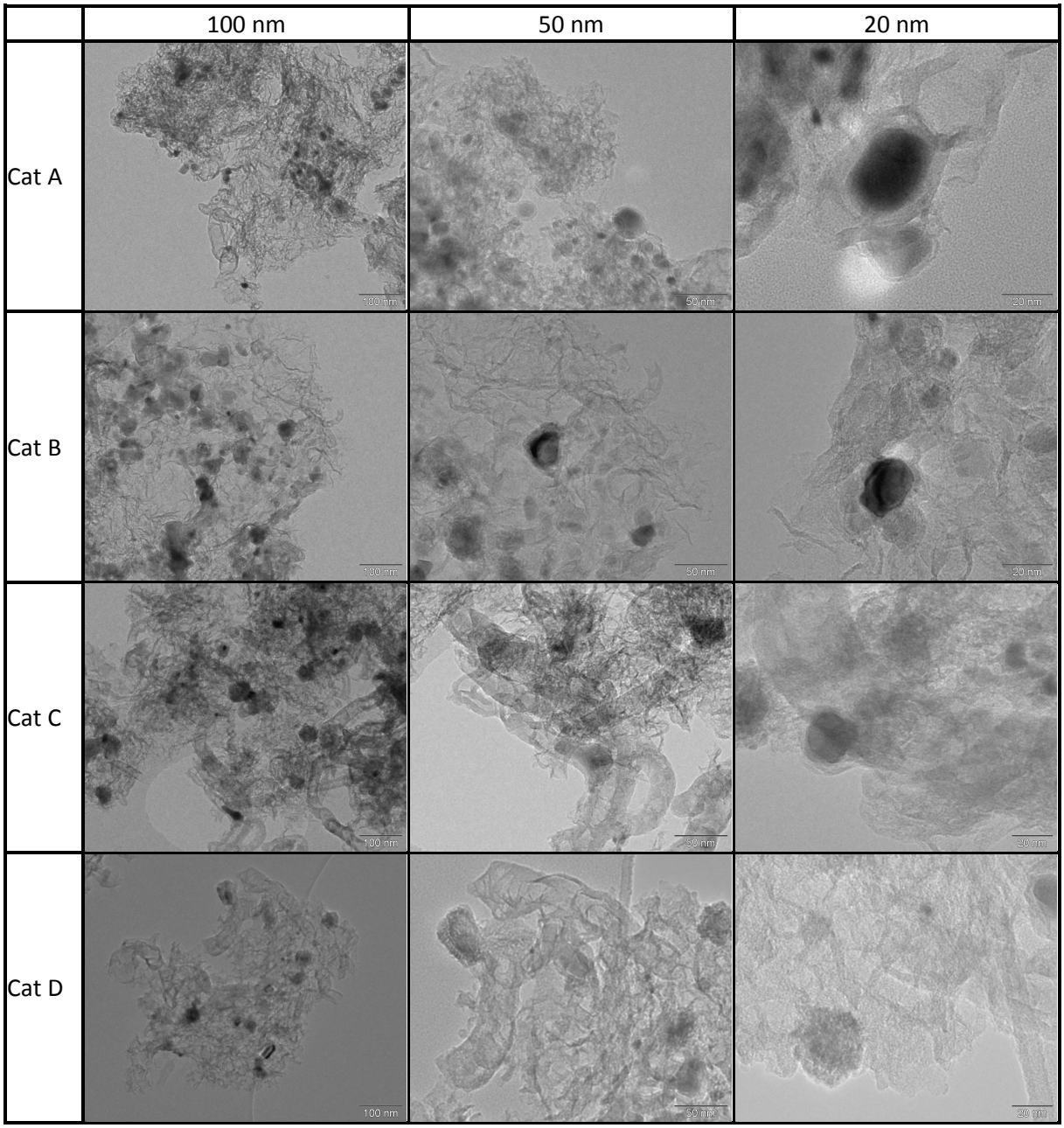

Figure S2. TEM images of the catalysts at different magnifications, on top the related scaling of the scale bar is given.

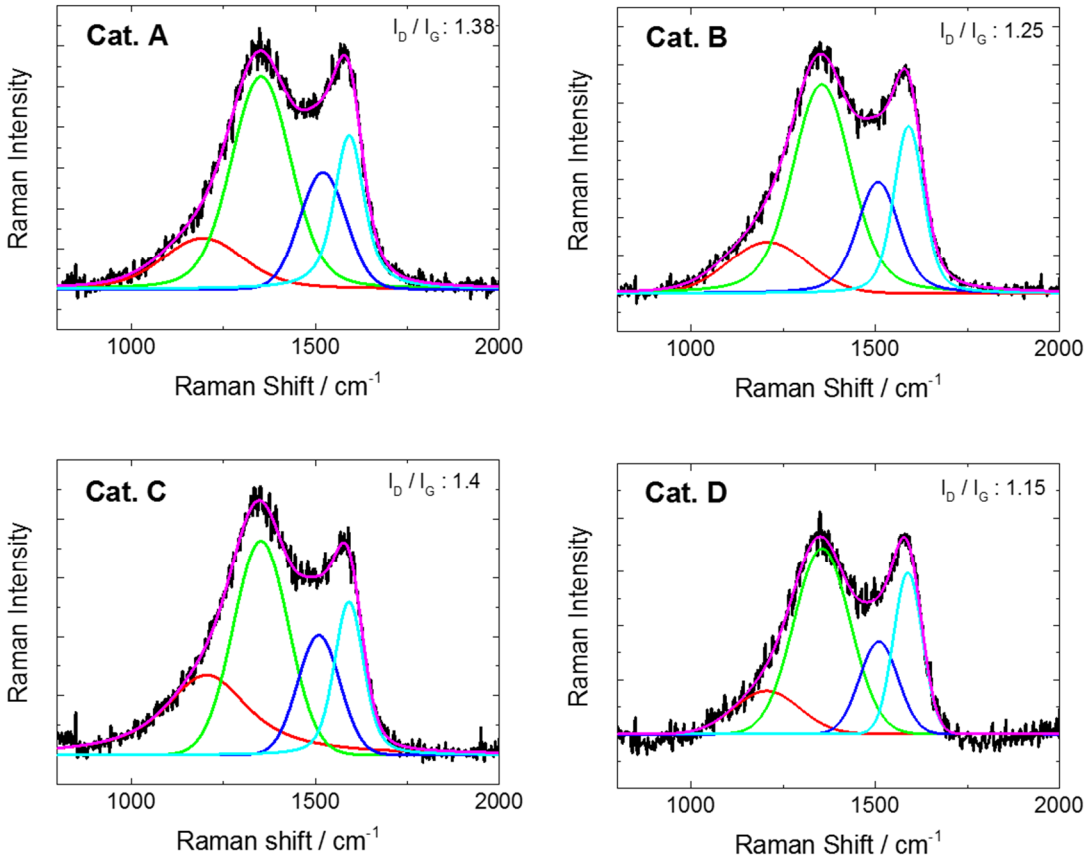

Figure S3. Deconvoluted Raman spectra of the 1st order region assigned to carbon blacks for all four catalysts.

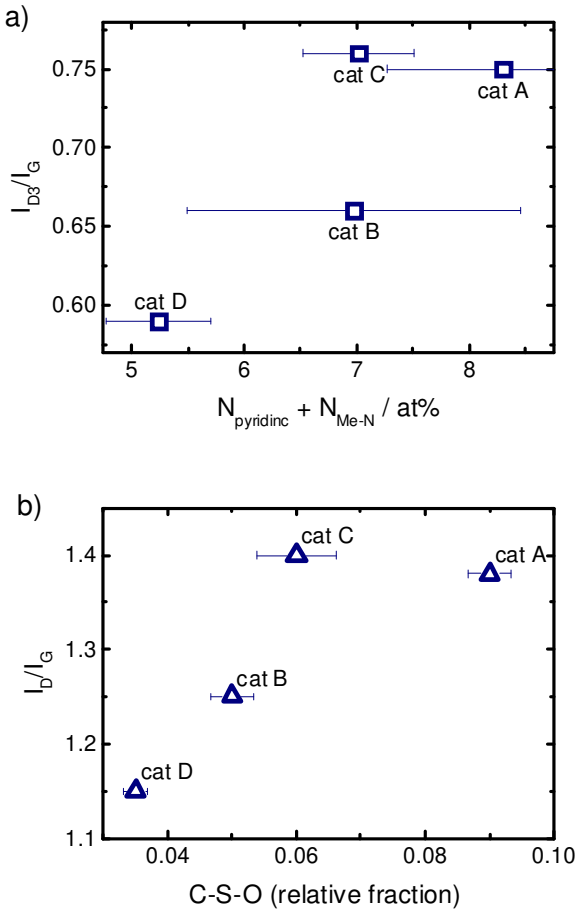

Figure S4. Correlation between I_{D3}/I_G ratio and the sum of N_{Me-N} plus $N_{pyrid.}$ and correlation between I_D/I_G ratio and the relative fraction of C-S-O (increase).

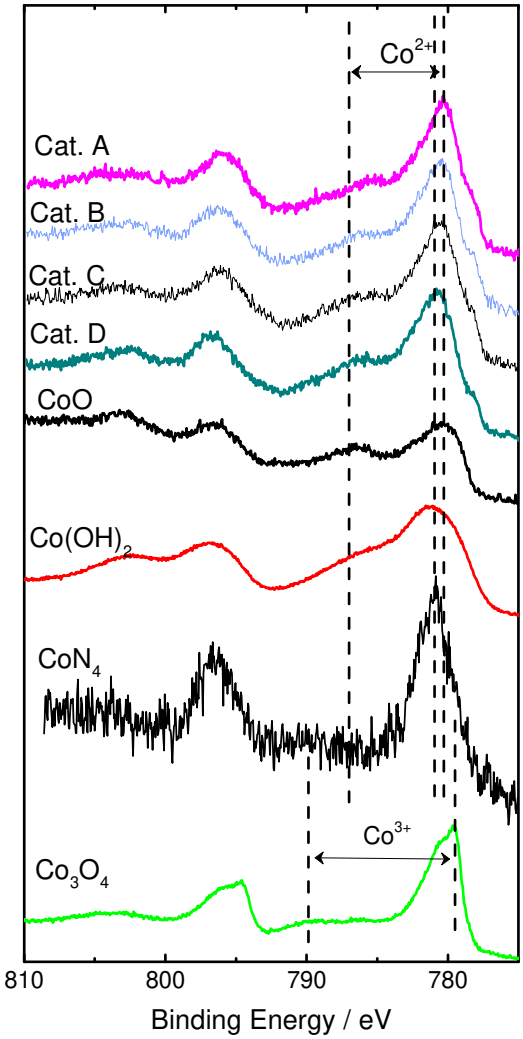

Figure S5: Co 2p full spectra range for all investigated catalysts as well as reference systems.

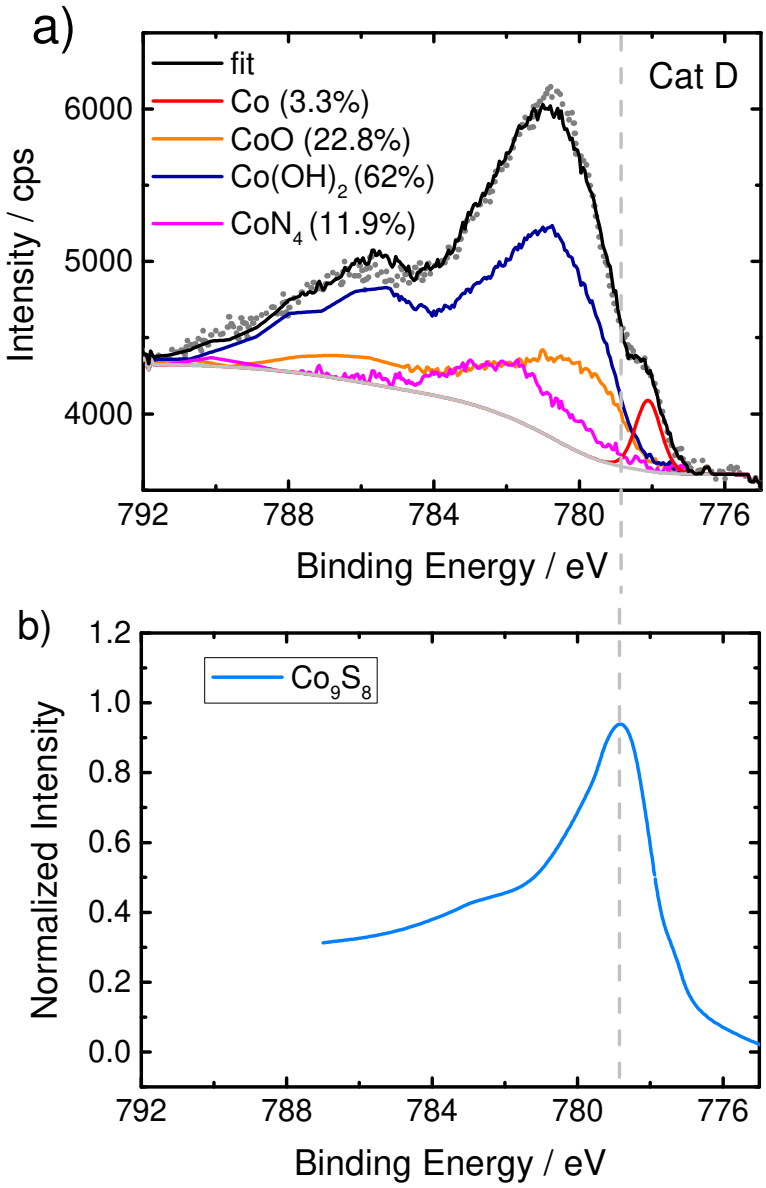

Figure S6: Exemplary fit of Co 2p 3/2 region of cat D with different components. The spectrum of Co_9S_8 was digitalized from data provided in Alstrup et al., J. Catalysis 1982, see reference 57 of the main manuscript.

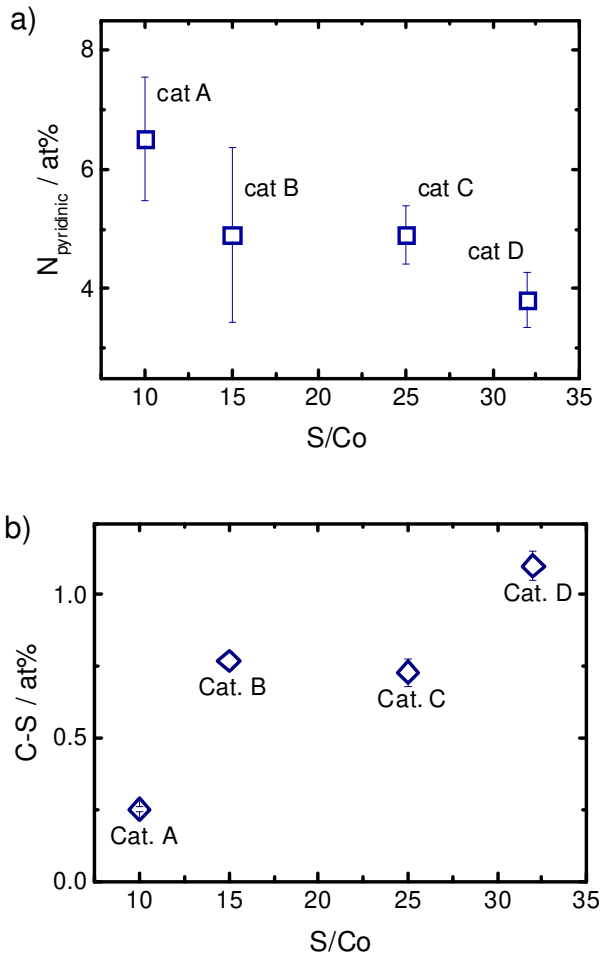

Figure S7. Correlation of the atomic concentrations of $N_{pyridinic.}$, and C-S as a function of the S/Co ratio in the precursors.

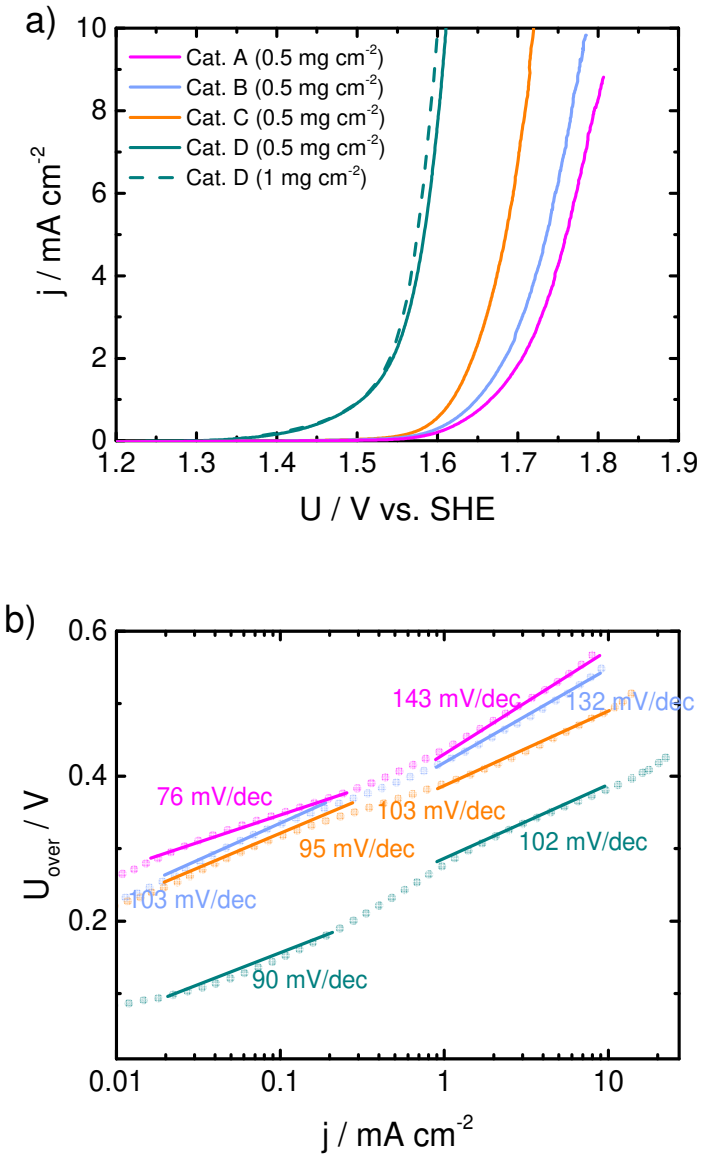

Figure S8. The linear scan voltammograms (LSVs) and Tafel plots for evaluating the OER activity with lower catalyst loading (0.5 mg cm^{-2}) in 0.1M KOH (rpm1500).

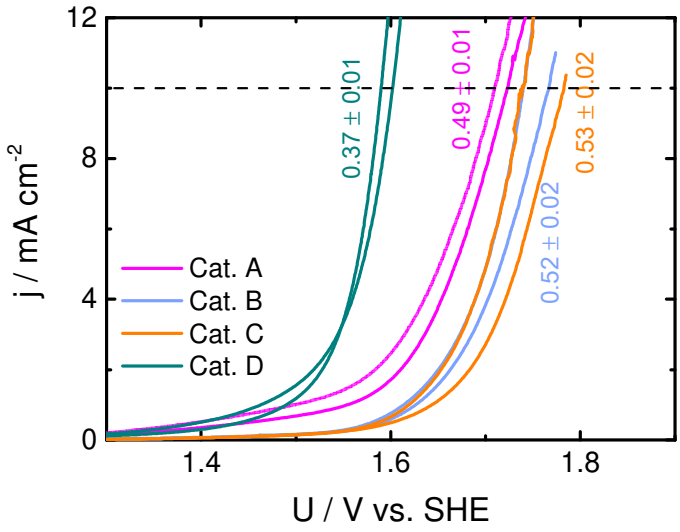

Figure S9. Repetition of the OER activity measurements of the catalysts and standard deviation of the overpotential

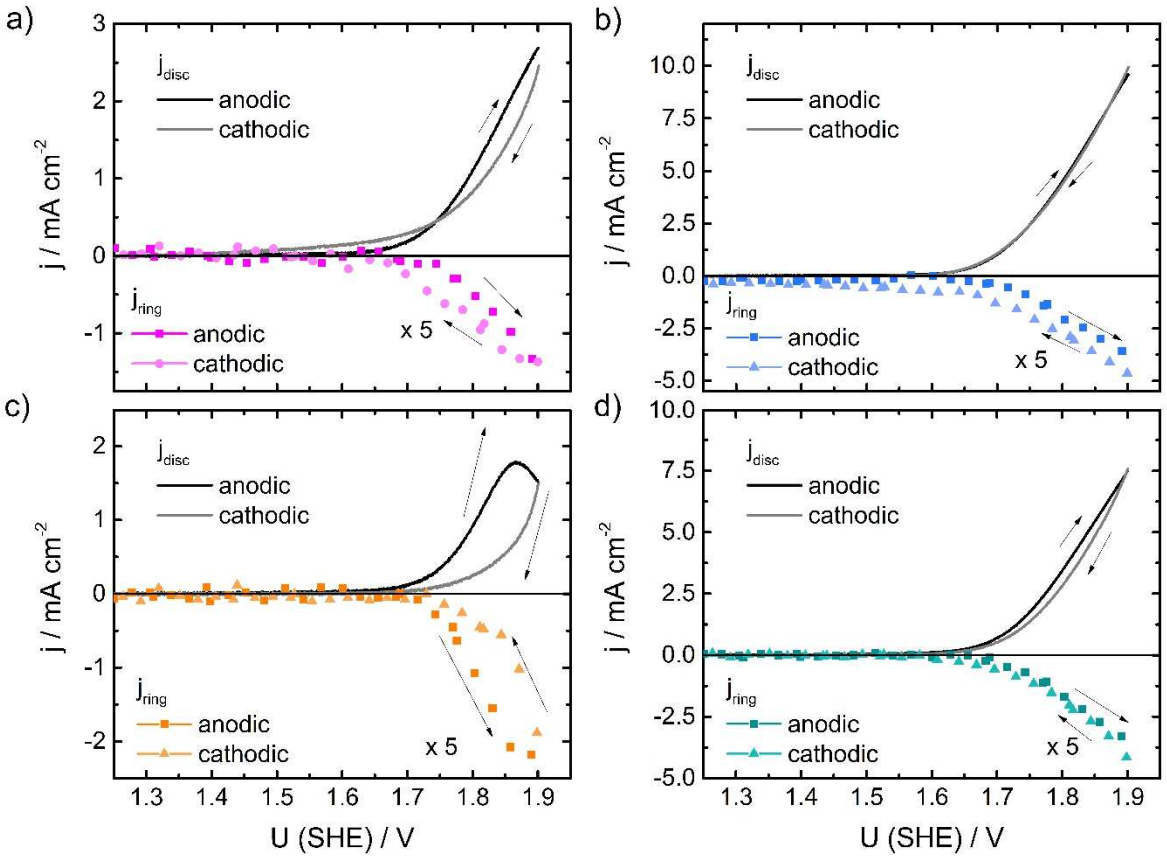

Figure S10: RRDE data of the four aged catalysts measured at 10 mV s^{-1} with 5 µl ink (corresponding loading on disc: 0.412 mg cm^{-2}), the ring potential was kept at 0.45 V (SHE). Darker colors refer to the anodic (initial) scan, lighter colors to the related cathodic scan that was performed after.

The increase of efficiency from anodic to cathodic sweep might have been caused by the decrease in the carbon oxidation contribution as it was shown for some carbon blacks that carbon oxidation decreases with number of cycles.

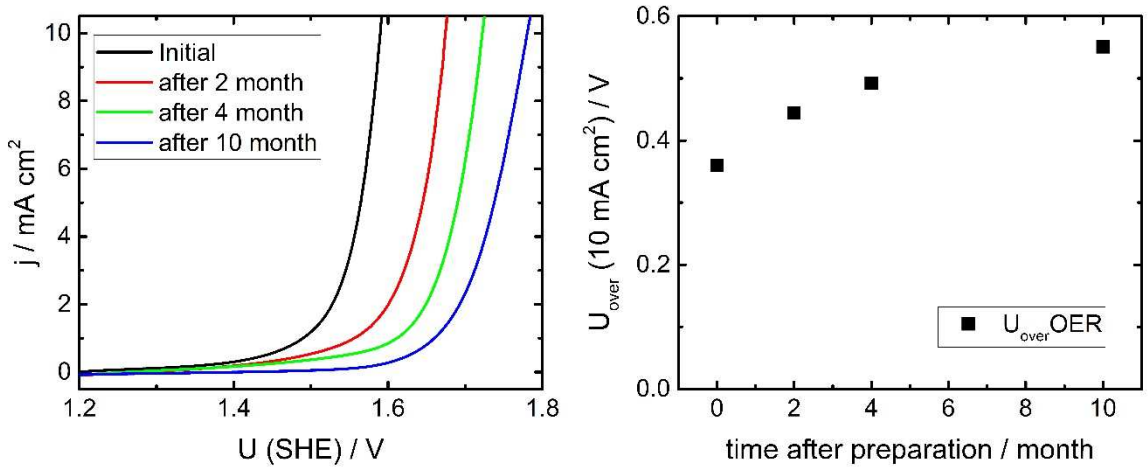

Figure S11. LSVs of the most active catalyst measured at different time intervals after preparation (as indicated in the label) and plot of the overpotential versus time after preparation. It becomes visible that there is a strong decay of the catalyst with storage time.

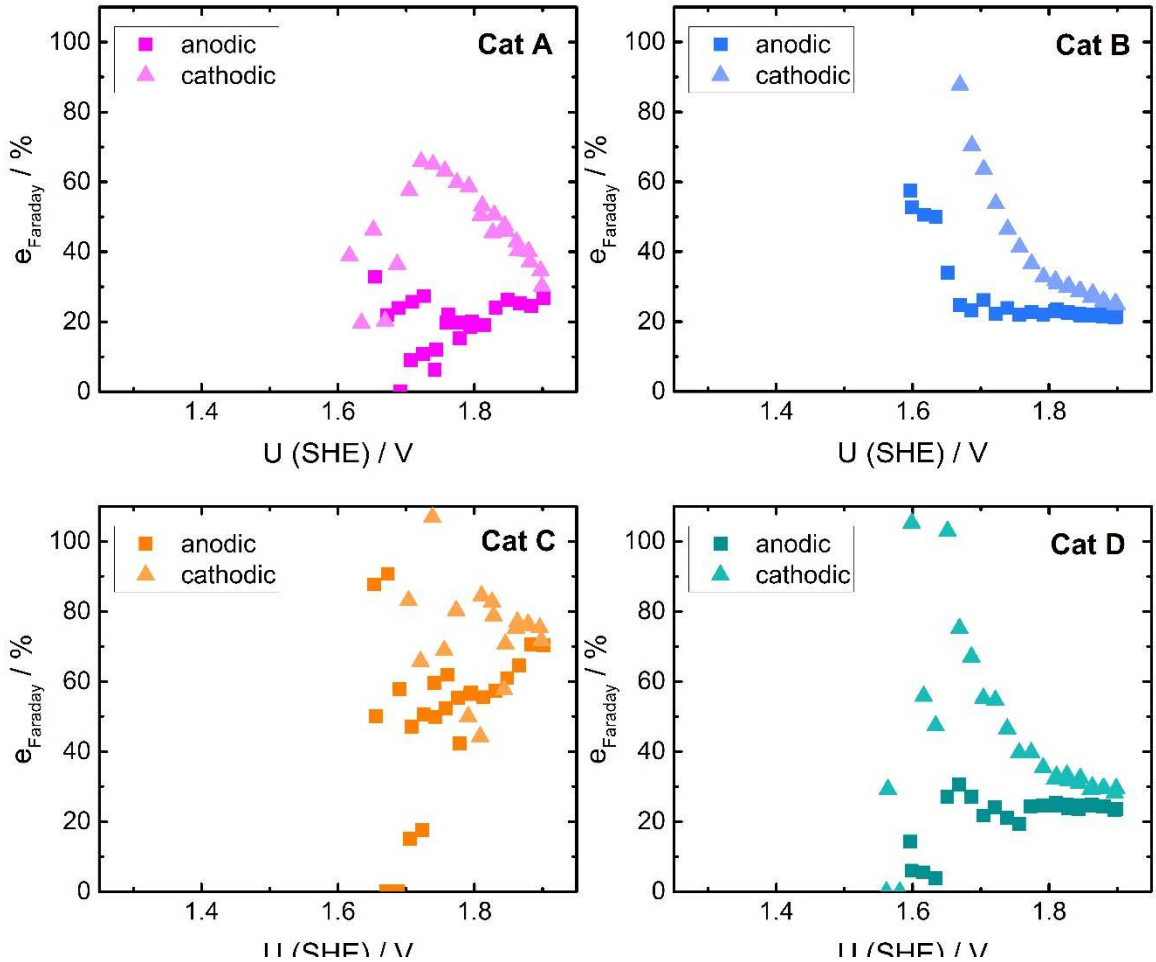

Figure S12. Trends in faradaic efficiency as a function of applied potential for the aged catalysts A to D. See Table S1 for summary of average values at 1 mA cm^{-2}.

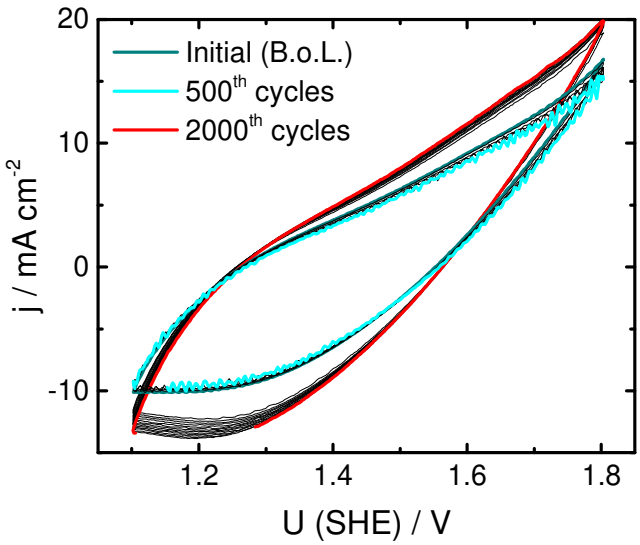

Figure S13. CVs during durability cycling (compare Figure 7a), shown are every 100th cycle, whereas the initial cycle, cycle No. 500 and cycle No. 2000 are highlighted in the respective color. All other cycles displayed in black. Cycling in 0.1M KOH at 1500 rpm with a sweep rate of 300 mV s^{-1}.

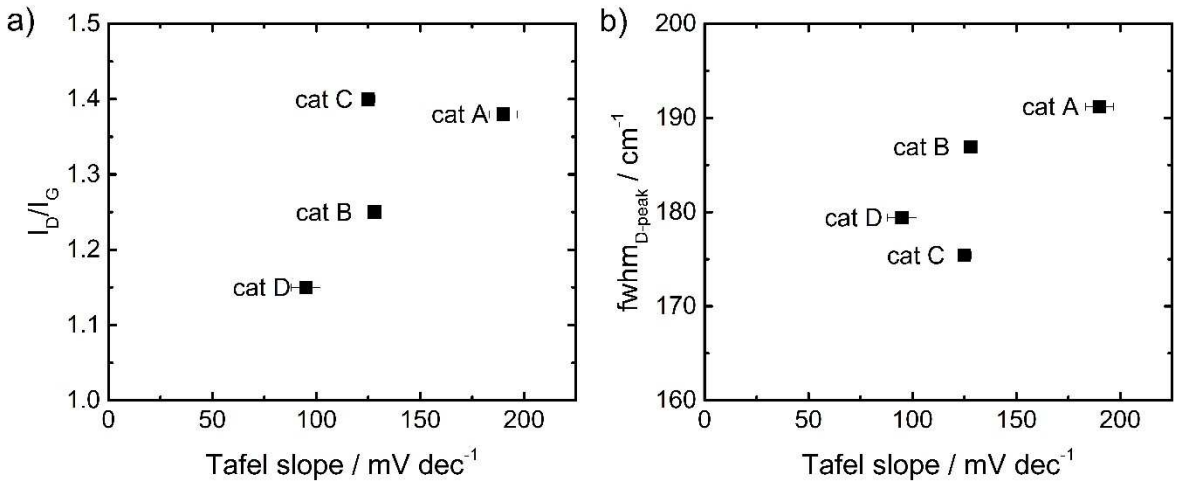

Figure S14. Correlation attempts of the I_D/I_G ratio (a) and the full-width at half maximum (fwhm) of the D-band (b) versus the Tafel slopes.

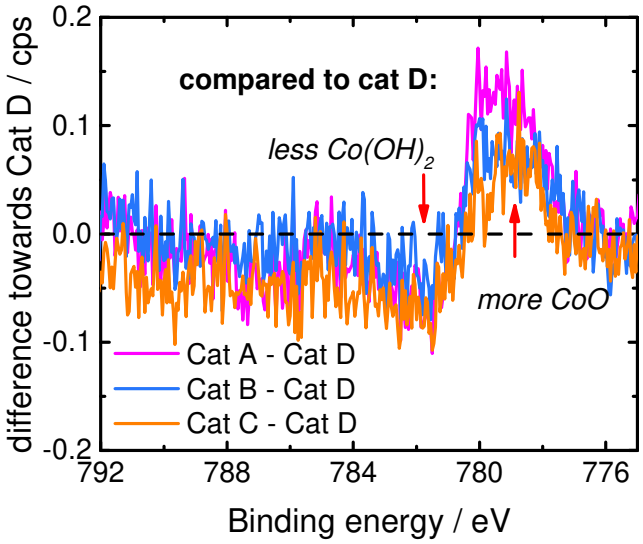

Figure S15. Co 2p difference spectra of catalysts A-C in relation to the most active cat D. The arrow at ca. 778 eV might be attributed to Co-O species, whereas the arrow at ca. 782 eV is indicative of hydroxide species.

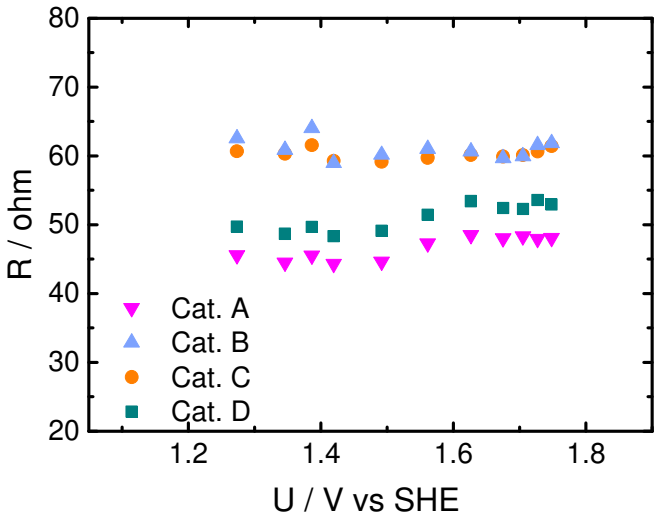

Figure S16. As-measured resistivity data (related to Figure 6 of the main manuscript) versus applied potential for the four catalysts A-D.

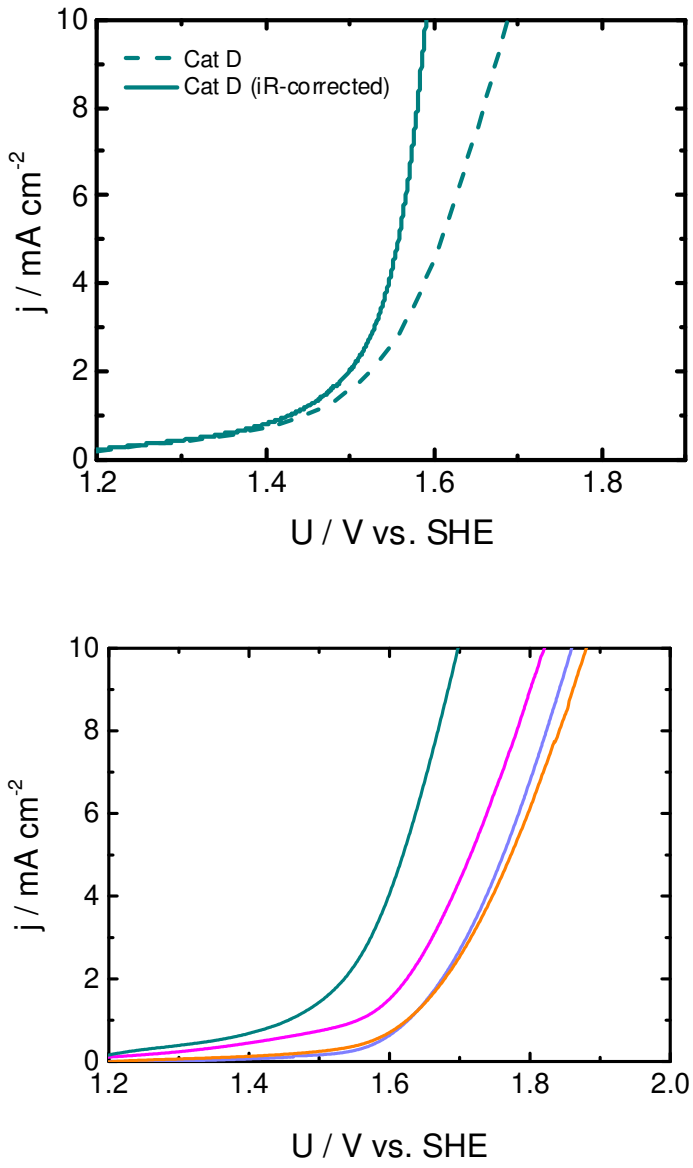

Figure S17: Comparison of the original activity scan of cat D and after iR correction (top graph) and comparison of the original data of all four catalysts (bottom graph). All measurements for a loading of 1 mg cm^{-2}.

Table S1: Summary of the faradaic efficiencies of catalysts A-D at a current density of 1 mA cm^{-2} in the anodic and cathodic scan.

$\varepsilon_{Faraday}$ / %	Cat A	Cat B	Cat C	Cat D
Anodic	20 ± 1	21 ± 2	55 ± 3	24 ± 1
Cathodic	49 ± 4	68 ± 2	77 ± 1	49 ± 3
Average	35	44	66	36

For the efficiency determination all values in the range 0.9 – 1.1 mA cm^{-2} were considered to determine the average and standard deviation.

4.2.2 Comparative study of structural changes of Co-based catalysts for the OER

In this project, a manganese-doped and a sulfur-doped catalyst within the PANI approach were prepared and characterized under oxygen evolution reaction in alkaline media. XPS and Identical Location TEM (IL-TEM) were performed to establish the post mortem analysis of the catalysts. Therefore, near-surface and bulk properties of the catalysts were investigated before and after electrochemical conditioning in order to identify the origin of the excellent OER activity.

Contribution to the project: Catalysts preparation, XPS characterization, Electrochemical characterization, Post mortem analysis (XPS), Data analysis and writing

Post mortem evaluation of sulfur- and manganese-doped cobalt-based catalyst under water oxidation

Ali Shahraei, Natascha Weidler, Markus Kübler, Lingmei Ni, Ioanna Martinaiou, Bernhard Kaiser, Robert W. Stark, Wolfram Jaegermann, Ulrike I. Kramm

Abstract

In order to develop non-precious catalysts for the water oxidation reaction, a fundamental understanding of the nature of active center is required. Herein, we present a comprehensive study performing X-ray Photoelectron Spectroscopy (XPS) and Identical Location Transmission Electron Microscopy (IL-TEM) before and after electrochemical conditioning within multiple steps to investigate potential-induced changes to the structure and morphology of S- and Mn-doped PANI-based cobalt catalysts. We were able to identify that the change in structure does strongly depend on the type of doping and the type of active sites present in the catalysts. Based on the post mortem analysis of the here presented Co-N-C catalysts and the comparison with thin film cobalt based model systems, we could even show that both, metal oxyhydroxides and MeN_4 species,can activate the oxygen evolution reaction in alkaline medium. Moreover, the combination of IL-TEM with XPS as characterization methods applied to carbon based materials presents an highly innovative approach to address the effect of doping on the unavoidable carbon oxidation.

Introduction

Electrochemical energy conversion plays a tremendous role in the transition from fossil fuels to renewable energies. In particular, zero-emission electrolysis is a promising technology to produce hydrogen by water splitting, which is regarded as a future energy carrier. This process includes a cathodic half-cell reaction, hydrogen evolution reaction (HER) and an anodic half-cell reaction, oxygen evolution reaction (OER). Unlike the HER, the OER is considered as a sluggish complex reaction with four sequential electron transfer steps, which requires a large overpotential to overcome the thermodynamic barriers.[1] In order to decrease the overpotential, numerous studies have focused on developing stable catalysts activating oxygen evolution reaction based on noble metal oxides (Ir and Ru)[2–4], complex composites of transition metal oxides[5–7], sulfides[8–10]and proviskites[11]. More recently, metal- and nitrogen-doped carbon-based materials, known as Me-N-C, have gained increased attention due to their astonishing activity toward oxygen reduction reaction (ORR)[12–15]. Despite the accelerating progress in the development and optimization of these catalysts for ORR, the progress in the field of OER is much more dawdling. The main reason for this is the lack of detailed systematic studies

exploring the nature of active sites, the reaction mechanism and atomic-scale catalytic properties in the case of OER.[16] During the last decade, several authors investigated model catalysts to gain a fundamental understanding of OER mechanism for transition metal complexes.[7,16,17,18] There is still a strong debate whether the non-oxide metal complexes (Me-N, Me-S) are participating directly in the electrochemical reaction or if the improved activity is originating from their decomposition to metal oxides.[19,20] Daniel et al. reported the decomposition of cobalt porphyrin deposited on FTO substrate (as a model catalyst) into CoOx species during water oxidation. In this work, the newly formed film was considered as the main active catalyst for OER.[17] In contrast to this report, Wang et al demonstrated the formation of Co^{4+}-porphyrin cation radical as the reactive oxidant which is responsible for oxygen evolution. Indeed, the authors claimed that the catalyst was stable during electrochemical conditioning with no evidence of cobalt oxide film formation.[21] Despite the great knowledge regarding model catalysts, it is required to study the real complex catalyst systems and compare them with the models to acquire a reliable explanation of the nature of the active sites. In our recent publication, we reported an active sulfur modified Co-N-C catalyst active toward OER in alkaline medium. It was found that the hydroxide formation during pyrolysis plays an important role for the OER mechanism and the rate determining step. Besides, numerous studies have been made to develop OER catalysts on the basis of manganese inspired by the tetranuclear manganese cluster in the photosystem II.[22,23]In order to get a comprehensive insight into the role of oxide species and MeN_x complexes on Me-N-C catalysts, we performed post mortem analysis of S- and Mn-doped Co-N-C as catalyst for water oxidation. Based on the the structural changes observed for differently doped Co-N-C catalysts in comparison to thin film cobalt oxide model catalysts, we were able to elucidate the origin of OER activity in dependence on the dopant.

Experimental

- **Catalyst preparation**

To synthesize Co-N-C catalysts, $PANI_{evap}$ (previously reported in our publications,[24] elemental sulfur, dicyandiamide (DCDA) and metal acetates (manganese and cobalt) were used. For non-dopant Co-N-C, 99 mg cobalt acetate tetrahydrate and 680 mg $PANI_{evap}$ were mixed and grounded using a mortar. In a next step, 2268 mg dicyandiamide (DCDA)) was added to the mixture. In case of the S-doped sample, 362 mg of elemental sulfur (S_8) was added to the precursor mixture that was described before for the non-dopant catalyst. For Mn-doped sample, 68 mg cobalt acetate tetrahydrate, 31 mg manganese acetate and 680 mg $PANI_{evap}$ were mixed and grounded with a mortar. Then, 2268 mg dicyandiamide (DCDA) was added to the mixture.

All three catalysts were subjected to the heat treatment step at 800° C with a ramp of 300° C/h. This step was including 300° C (dwelling 30 min), 500° C (dwelling 30 min) and 800° C (dwelling 60 min). Then, the cooled down powder was transferred to 2M HCL for acid leaching followed by 2 hours sonication and remained overnight. After washing with distilled water, the remaining powder was subjected to the second heat treatment including a fast ramp of 38° C/min to 600° C and a heating to 800° C with the ramp of 300° C/min (dwelling 3 hours).
Cobalt oxide model catalysts were prepared by plasma-enhanced chemical vapor deposition as described elsewhere.[7]

- **X-ray photoelectron spectroscopy (XPS)**

The XPS characterization of the as prepared S-, and Mn-doped Co-N-C catalysts were performed using Indium-foil as a substrate. For the post mortem analysis of the S-, and Mn-doped Co-N-C catalysts a custom-made sample holder was developed to perform XPS directly from the catalyst ink coated on the working electrode.
The measurements were carried out with A Specs Phoibos 150 hemispherical analyzer and a Specs XR50M Al X-ray source (E = 1486.7 eV). The energy steps of 1 eV and 0.05 eV were applied for survey scnas and high resolution scans. The spectra were analyzed with CasaXPS software using a shirely background and the Gaussian to Lorentzian ratio GL30.

- **Identical Location Transmission Electron Spectroscopy (IL-TEM)**

Before each measurement, the catalyst powder was dispersed in ethanol and sonicated of 30 sec in ultrasonic bath. After settlement of the large particles in the suspension, a drop was placed on a gold mesh (perforated carbon layer on gold finder grid F1/200) suitable for identical location TEM measurement. The FEI CM20STEM (Eindhoven, The Netherlands) microscope equipped with a LaB_6 cathode and a Gatan double tilt holder at a nominal acceleration voltage of 200 kV were used to perform he measurement.

- **Raman Spectroscopy**

Raman spectra were conducted using an alpha 300R confical Raman microscope from WiTec with a grid of 600 lines mm^{-1}. To obtain Raman spectra, a laser with the power of 1 mW with excitation of 532.2 nm was applied. The average reported spectra is obtained with overlapping 10 scans (integration of 10 seconds per scan) in four different positions.

- **Electrochemical characterization**

Catalyst ink: The catalyst ink was prepared by mixing 5 mg of catalyst powder with 25 μl Nafion (5 wt%), 142 μl of ethanol, and 83.2 μl of water. In order to prepare the working electrode, 10 μl of the ink was drop-casted on glassy carbon resulting in a catalyst loading of 1 mg cm^{-2}.

Cyclic voltammetry (CV): The CVs were obtained using a RDE setup in standard three electrode configuration. The setup was including a glassy carbon coated with the catalyst as working electrode, glassy carbon rod as the counter electrode and Hg/HgO as a reference electrode. First, a CV was carried out in 0.1M KOH from 0.0 V to 1.2 V with a sweep rate of 100 mV s^{-1} as an activation step. To evaluate the OER activity, linear sweep voltammograms were measured from 1.2 V to 1.9 V with a sweep rate of 5 mV s^{-1} at a rotation of 1500 rpm. The reported potentials refer to the standard hydrogen electrode and are corrected for iR drop.

Electrochemical activity: The polarization curve was reported after 30 cycles with a sweep rate of 300 mV s^{-1} between 1.2 to 1.8 V.

Electrochemical conditioning: The durability test was performed with cycling (2000 cycles) between 1.2 and 1.9 V versus standard hydrogen electrode and the sweep rate of 300 mV s^{-1}. The stability test was carried out galvano-statically at 10 mA cm^{-2} and potentio-statically at 1.85 V (versus hydrogen electrode). All the measurements were performed at the rotation speed of 1500 rpm.

- **Post-mortem**

suitable Sample hwolders were specifically designed for each technique. For XPS, a male screw thread was constructed on a standard XPS sample holder for mounting the electrode. To maintain the electronic conduction, a gold pin was installed in order to connect the glassy carbon to the sample holder. The height of the electrode was optimized to maintain the beam radiation. To perform electrochemical conditioning, the working electrode was unscrewed and mounted on a RDE shaft.

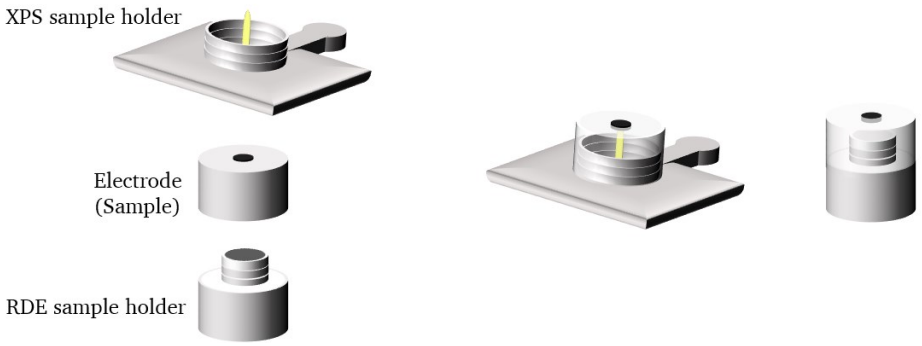

Figure E1. Designed apparatus for Post mortem XPS experiments

For electrochemical condition related to IL-TEM, the gold mesh was placed on the glassy carbon and mounted on the RDE shaft for the electrical connection. A cap was designed to be mounted on the electrode to fix the position of gold mesh in contact between the glassy carbon and electrolyte. This method was adapted from Meier et al.[25]

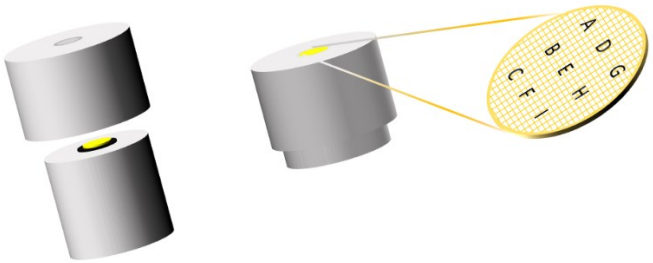

Figure E2. Designed apparatus for Post mortem IL-TEM experiments

First of all, each catalyst was drop-cast on a glassy carbon (GC) disc or gold mesh and characterized without any conditioning. Then, three steps electrochemical conditioning (EC) with different timing (increasing consecutively) were performed followed by the characterization within each step. The EC steps might be Galvanostatic (GS), Potantiostatic (PS) or cycling. Table E1 shows the post mortem analysis performed for different conditions.

Table E1. Post-mortem analysis performed in this work

	GS	**PS**	**Cycling**
Reference cat.	XPS		
S-doped	XPS	XPS, IL-TEM	XPS
Mn-doped	XPS	IL-TEM	

Results

Part I: Effect of doping on catalyst properties

Previously we reported the positive effect of multi-heteroatom doping on the electrochemical activity of the unique PANI-based Co-N-C catalyst system.[24] Based on the experimental post-mortem approach, the effect of doping on the potential induced changes in structure and morphology occurring under OER conditions. And hence their influence on the electrochemical OER activity and stability of the PANI-based Co-N-C catalyst were investigated.

In this study, a PANI-based dopant free, a sulfur doped and a manganese doped Co-N-C catalyst were prepared and characterized with respect to their surface and bulk properties. First, the electronic structure and elemental composition of the as prepared catalysts were investigated with XPS. As reported in Table1, doping elemental sulfur or manganese decreased the nitrogen content in the final Co-N-C catalysts. These findings agreed with the results reported in our recent works.[24,26] Besides, the overall decrease in nitrogen content, a change in oxygen concentration was identified, that depends on the type of dopant. It was observed that sulfur doping increases the oxygen content, while doping with manganese causes a drop in the oxygen content.

Table 1. Summary of the elemental composition derived from XPS

At% / Co-N-C	**C**	**N**	**O**	**Co**	**S**	**N_{MeN}**	**S_{MeS}**	**O_{MeO}**	**O_{MeOH}**
Not-doped	76	13,5	7,2	2,3	1	1,8	0,24	1,7	2,5
S-doped	71,2	10,2	11,5	3,1	4	1,4	0,34	1,36	5,2
Mn-doped	91	4,9	1,6	0,39+1,17	0,85	0,43	0,22	0,51	0,51

The high resolution XP spectra of the Co $2p_{3/2}$ and O 1s, presented in Figure 1, revealed that the type of dopant strongly determines the type of inorganic species that is finally formed in the catalysts after the pyrolysis. The Co $2p_{3/2}$ line of the dopant-free Co-N-C consisted of a main

peak at a binding energy of 780 eV and a satellite at a distance of 6 eV as it was typically found for Co(II) in CoO and CoN_4.[7,27,28]

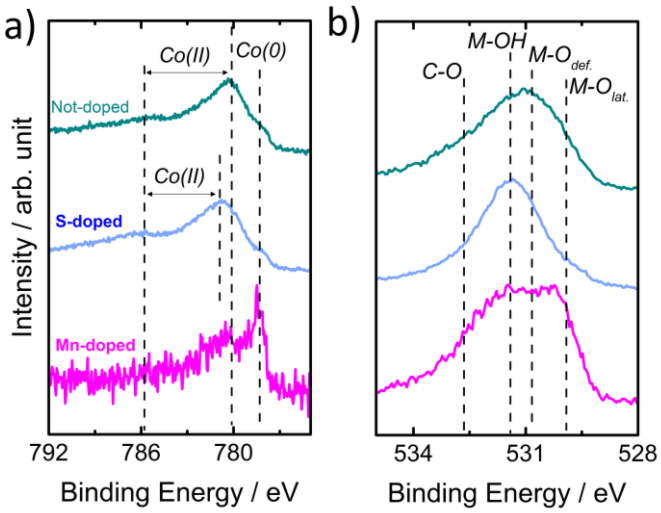

Figure 1. The high resolution XPS spectra of the Co 2p, Mn 2p and O 1s of the as prepared catalysts.

The small shoulder at a binding of 778 eV referred to the presence of metallic Co nanoparticles. It should be noted that this peak overlaps with the one attributed to Co_9S_8.[29] In comparison, the low binding energy feature attributed to lattice oxygen in CoO appears at a binding energy of 529.8 eV.[30] With sulfur doping, the main peak was shifted to higher binding energy (~780.5 eV) compared with non-doped catalyst, as it was typically found for Co(II) in $Co(OH)_2$.[28] In addition, the O 1s line identified $Co(OH)_2$ being present as inorganic species supported on the Co-N-C by the high binding energy feature at 531.4 eV. Therefore, one can conclude that the increase in oxygen content was related to an increased formation of $Co(OH)_2$.[28] In contrast to the sulfur-doped catalysts, the Co $2p_{3/2}$ peak of the manganese doped sample did not show a shift in binding energy. The Co 2p line identified the presence of metallic Co by the Co $2p_{3/2}$ peak at a binding energy of 778 eV and of Co(II) by the Co $2p_{3/2}$ peak at a binding energy of 780 eV. Indeed, according to literature reports and the reference spectrum of CoTMPP that is shown in Figure S1, the Co 2p peak at 780 eV can be assigned to Co(II) in CoN_4 or CoO. But especially the low oxygen content of only 1.6 % indicated Co(II) predominantly being present as CoN_4 sites. The Mn $2p_{3/2}$ signature of the Mn- doped catalyst (Figure S2) showed a peak at 641.1 eV and a satellite at 647.1 eV which was attributed to Mn(II).[31] The main peak at 642 eV is suggested as Mn(III) in MnN_4 coordination in agreement with MnTMPyP XP spectrum reported in literature.[32]

One can conclude that the addition of Mn as a dopant seems to suppress the formation of CoO and $Co(OH)_2$ during the preparation and hence reduces the amount of inorganic impurities.

The latter conclusion was confirmed by analyzing Raman spectra of the Co-N-C catalysts in the lower wavelength range, which is shown in Figure S3. The peaks can be assigned to oxide species, such as CoO_x and Co_3O_4 observed for dopant-free and S-doped catalysts.[33] The absence of Co_3O_4 can be confirmed as the XP spectra show no presence of any Co^{3+} species. In contrast, no peaks in this region were observed in the case of Mn-doped catalyst, which underlines the effect of manganese in suppressing formation of metal oxide species.

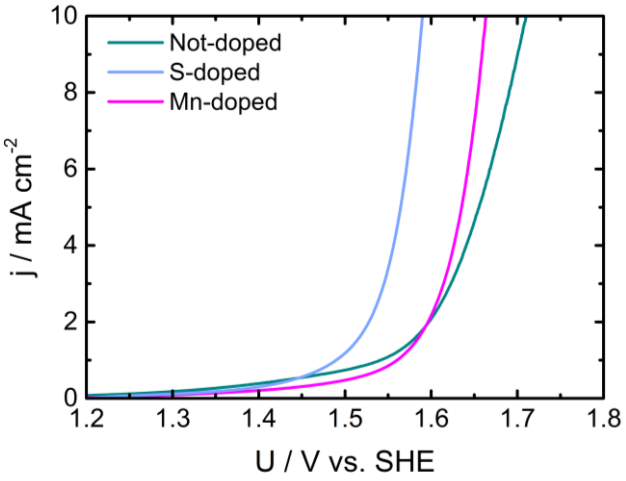

Figure 2. OER polarization curves of the as prepared catalysts

Figure 2 shows the OER polarization curves of the as prepared catalysts recorded in 0.1 M KOH before the galvanostatic conditioning was performed. It was observed that both, manganese and sulfur doping enhance the OER activity. At a current density of 10 mA cm^{-2}, the overpotential decreased by 50 mV for the Mn-doped and by 120 mV for the S-doped catalyst. So far, it was shown that heteroatom doping determines the formation of oxide species, which affects the electrochemical activity. Here the question arises if the improved electrochemical activity is attributed to the metal oxides/hydroxide species or MeN_4 sites.

Exploring the origin of activity for S-doped catalyst

To get further insight into the single contributions of different species (inorganic, CoN_4 and cobalt nanoparticles) to the OER activity, the electronic structure and morphology of sulfur doped Co-N-C catalyst was investigated post mortem with XPS and IL-TEM. The analysis was made after performing a stepwise galvanostatic polarization at 10 mA cm^{-2} for 5, 10 and 60 minutes as it is described in experimental part.

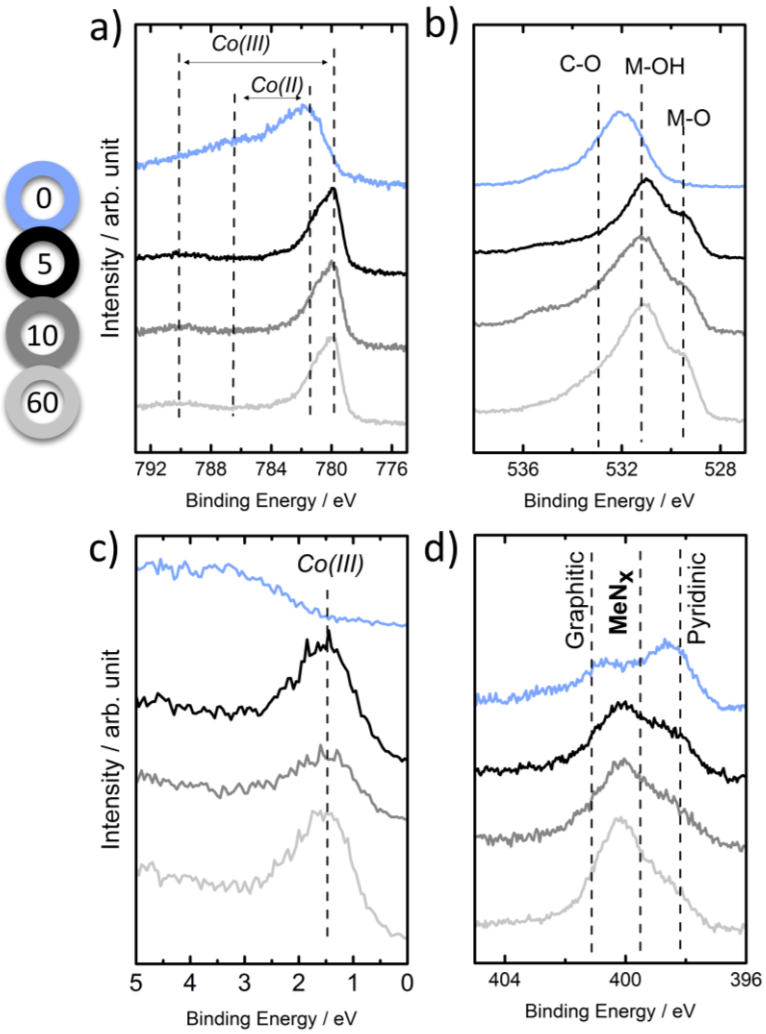

Figure 3. High resolution XP spectra of the a) Co 2p, b) O 1s, c) VB, d) N1s regions of the S-doped catalyst after electrochemical conditioning (GS)

Figure3 shows the high resolution XP spectra of the Co 2p, the O 1s, N1s, and VB regions of the not-conditioned S-doped catalyst in comparison to the spectra that were subsequently carried out after the respective galvanostatic polarization. The Co 2p signature of the not-conditioned sample showed a broad peak at 781.4 eV and a satellite at 786.4 eV (5 eV difference), which was ascribed to Co(II) in $Co(OH)_2$. After five minutes of electrochemical conditioning the Co $2p_{3/2}$ peak was shifted to a lower binding energy of 779.7 eV. Associated to this binding energy shift, the intensity of the Co(II) satellite at 786.4 eV decreased and a satellite attributed to Co(III) appeared at a binding energy of 790.1 eV. In addition, the valence band region showed the $3d(t_{2g})^6$ feature at 1.5 eV that was assigned to the Co(III) oxidation state.[7,18] Interestingly, the cobalt phase was not changed while continuing the galvanostatic polarization for prolonged time (10 and 60 minutes).

The change in binding energy of the Co 2p peak as well as the change in satellite structure clearly pointed to the oxidation of $Co(OH)_2$ to CoOOH. In agreement with the change in Co 2p

line, the O 1s line showed an increased intensity for the low binding energy peak at 529.5 eV after the galvanostatic conditioning which is related to M-O in CoOOH.

Recently, Weidler et al. reported a correlation between the presence of hydroxide moieties and the OER activity studying thin film Co- and Ni-oxides as model catalysts. They found that the overpotential decreases with increasing hydroxide moieties.[7,34] By characterizing the catalysts as prepared surface and post mortem after the electrochemical characterization, they found that the presence of hydroxide moieties support the formation of the active cobalt oxyhydroxide phase during OER in which the Co(III) oxidation sate is stabilized the best.[7]

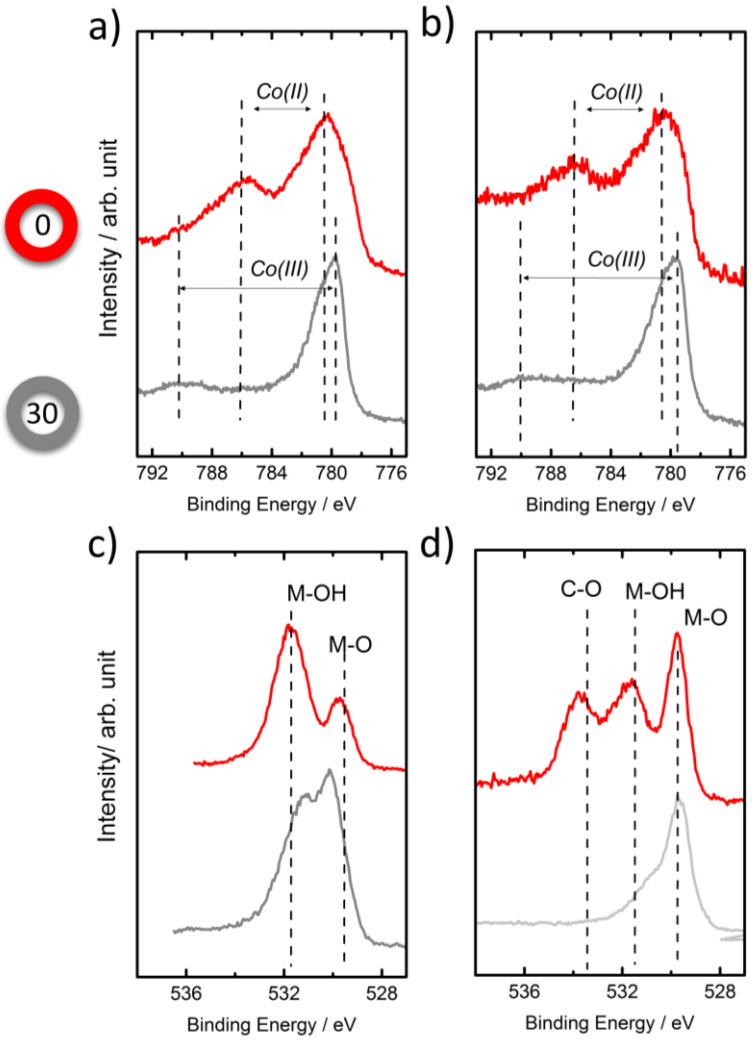

Figure 4. High resolution XP spectra of the Co 2p an O 1s region recorderd for the initial hydroxylated CoO(OH)2 and after the galvanostatic conditioning (a and c) and for the initial and galvanostatically conditioned CoO (b and d).

To discuss the single contribution of $Co(OH)_2$ in more detail, the post mortem analysis was conducted in addition for support-free hydroxylated thin film cobalt oxide (CoO_x) as model catalyst prepared by PECVD. The hydroxylated CoO was further denoted as $CoO_x(OH)_2$. Figure

4a and 4c show the high resolution XP spectra of the Co 2p, the O 1s regions of the as prepared $CoO_x(OH)_2$ film and post mortem after the galvanostatic polarization.

In agreement with the changes in Co 2p spectrum observed for the sulfur-doped Co-N-C (+S) catalyst, the Co $2p_{3/2}$ peak of $CoO_x(OH)_2$ shifted towards lower binding energies from 780.6 eV to 780.1 eV. Furthermore, the satellite structure changed while the Co(II) satellite at a distance of 5.5 eV to the main peak vanished, the Co(III) satellite at a distance of 10 eV appeared. The oxidation of the hydroxylated CoO to CoOOH was also confirmed by the appearance of the valence band feature at 1.4 eV identifying Co(III) as the dominant oxidation state. (Figure S4) For the model catalyst, the change in the O 1s line after the galvanostatic test was more pronounced compared to the highly complex S-doped catalyst system: The decrease in intensity of the high binding energy O 1s peak of to Co-OH is associated with the increase in the low binding energy feature of Co-O. In addition, the binding energy difference between the M-OH and M-O peak was found to be decreased as it was typically observed for Co-OOH.[7,18] The XP spectra of the model catalyst provides the advantage to carry out component fits, whereby one can determine the content of Co(III) as well as the content of Co-OH. All in all, it can be proven that the Co(III) content increased from below 1% to 91 % after the galvanostatic polarization.

In contrast to the hydroxylated CoO model catalyst, the hydroxide-free CoO was not able to oxidize from CoO to CoOOH during galvanostatic polarization. The presence of both satellites, (790 eV for Co(III) and 786 eV for Co(II)) as well as the double peak feature of the Co $2p_{3/2}$ peak at a binding energy of 779.9 eV identified the presence of Co(II) and Co(III) as it was reported for spinel type Co_3O_4. The presence of Co(III) was further confirmed by the Co(III) feature at 1.4 eV in the valence band (Figure S4). Furthermore, the O 1s spectrum clearly shows the predominant presence of cobalt oxide by the O 1s peak at 529.7 eV that was assigned to lattice oxygen.

The cyclic voltammograms recorded in 0.1 M KOH for the hydroxide-free and the hydroxylated CoO model catalysts (Supporting Information) clearly showed that the presence of hydroxide moieties in the as-prepared catalyst promoted the potential-induced formation of the highly active CoOOH under operating conditions. (Figure S5) Based on the results derived for the model catalysts, one can suggest that the increase in activity due to sulfur doping is most probable related to the increased content of hydroxide moieties.

In the N 1s region, a constant decrease in pyridinic nitrogen groups can be identified with conditioning. Besides, the increase in intensity at a binding energy of 402 eV can be observed. Therefore, the peak related to the graphitic species is increased while pyridine was reduced stepwise. Also, for carbon-based systems, the contribution of carbon oxidation to OER cannot

be neglected. In our previous work, the S-doped catalyst revealed a Faradic efficiency of 50% in the cathodic sweep based on RRDE measurements.[24] Therefore, it is crucial to explore C 1s spectra after water oxidation in order to evaluate the carbon oxidation effects on the structure. As typical for carbon based materials, carbon corrosion can be identified by the shift of the C 1s from 284.3 eV for the as prepared catalyst to 284.7 eV after galvanostatic conditioning (Figure S6). [35]

To study the effect of conditioning on morphology of the catalyst, Identical location TEM experiments (IL-TEM) were carried out. The potentiastatic method was chosen since other methods easily tear down the fine gold mesh specifically designed for IL-TEM. It was shown in Figure S7, and S8 that the main conclusion for GS, PS and cycling were similar for S-doped catalyst). Therefore, low and high magnification TEM images recorded after 5, 10 and 60 minutes of potentiostatic polarization are reported in Figure 5 in comparison to the initial S-doped Co-N-C. The carbon morphology of the initial S-doped Co-N-C was characterized by so-called bamboo-type carbon tubes that encapsulate cobalt particles. The fine bamboo tubes have a diameter between 40-70 nm. It was observed that after conditioning of the catalyst, the cobalt particles were protected within the bamboo tubes and they were kept intact. This drops to the conclusion that the potential induced carbon corrosion was mainly occurring on the edges/walls of the bamboo tubes.

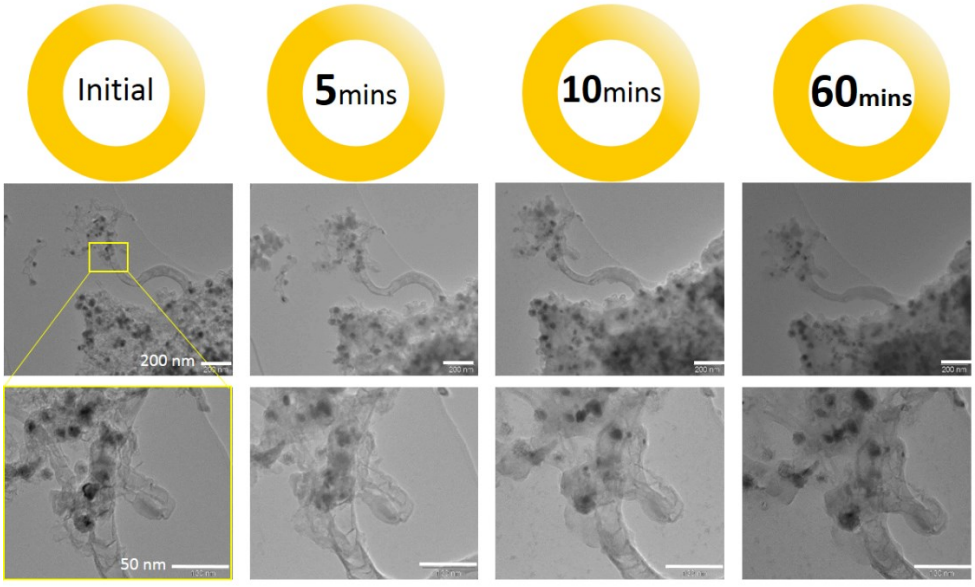

Figure 5. Low and high magnification TEM images of S-doped catalyst recorded after electrochemical conditioning (PS)

Exploring the origin of activity for Mn-doped catalyst

The comparison of XP spectra of the as-prepared catalysts revealed that in contrast to the S-doped Co-N-C, the Mn-doped Co-N-C catalyst exhibits Co(II), Mn(III) predominantly present as MeN_4. To explore the activity and stability of MeN_4 as the active sites post-mortem analysis were performed analog to that of the S-doped catalyst. Figure 6 presents the Co $2p_{3/2}$ spectra of the initial Mn-doped Co-N-C and after 5, 10 and 60 minutes of galvanostatic conditioning at a current density of 10 mA cm^{-2}. Interestingly, no potential-dependent change in structure was observed for the Mn-doped catalyst. The Co $2p_{3/2}$ peak associated to CoN_4 is positioned at a binding energy of 780.4 eV for the initial Mn-doped Co-N-C and after the galvanostatic conditioning. In agreement with this observation, the valence band spectra confirmed the absence of Co (III) species after the galvanostatic conditioning. It should be noted that the broad and narrow Co 2p peak at 783.3 eV was most probably related to cobalt impurities in the initial catalysts.

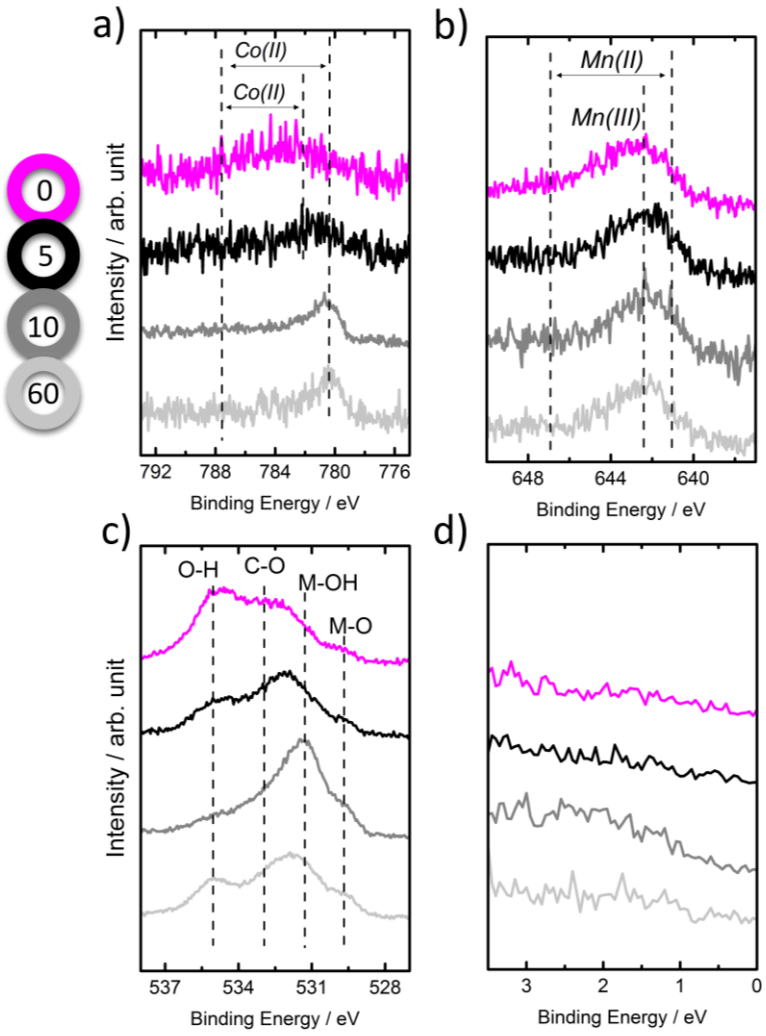

Figure 6. High resolution XP spectra of the a) Co 2p, b) Mn 2p, c) O 1s, and d) VB regions of the Mn-doped catalyst after electrochemical conditioning (GS).

Nevertheless, since the Co 2p spectra after conditioning did not exhibit this peak, one can exclude that these impurities immediately dissolved and did not contribute to the activity. Similarly, in Mn 2p spectra, the peaks at 641.1 and 642 eV related to Mn(II) and Mn(III) remained at the same position after galvanostatic conditioning. A broad peak at 644 eV related to higher Mn oxidation states vanished after conditioning which was considered as impurities. Similar to the S-doped catalyst, the N 1s spectrum revealed the increase of graphitic nitrogen by an increased intensity at above 400 eV. The C 1s spectra of the Mn- doped Co-N-C catalyst shows identical shift of the C 1s peak towards higher values indicating the oxidation of the carbon. (Figure S9) The identical location TEM measurements carried out for the Mn-doped catalyst confirmed the low corrosion resistivity of the carbon structure. The initial structure was characterized by fine graphene layers in which cobalt and manganese particles were wrapped by graphene layers. After conditioning, it was observed that carbon layers were mostly covered with KOH from the electrolyte and corroded on the surface, and consequently the particles were partially removed or replaced.

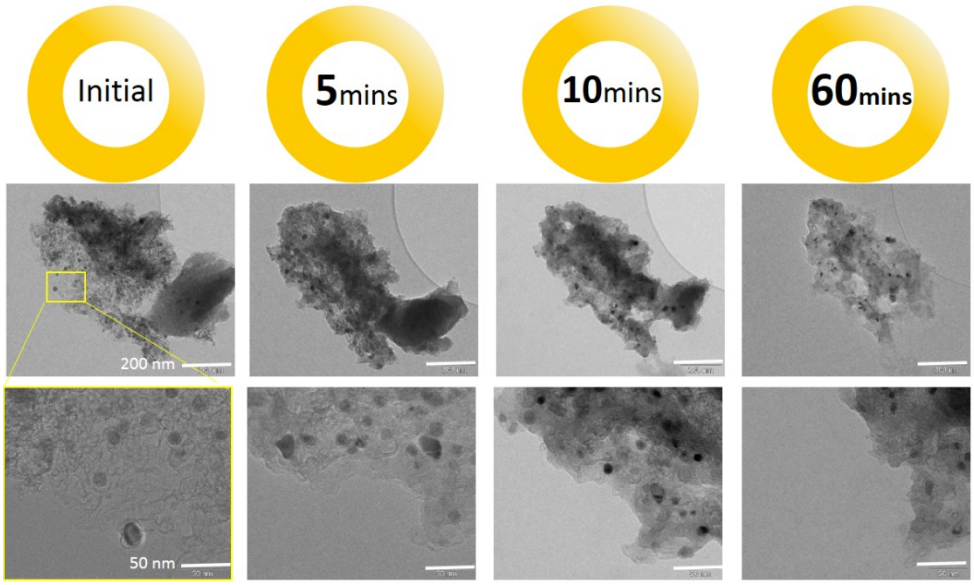

Figure 7. Low and high magnification TEM images of S-doped catalyst recorded after electrochemical conditioning after electrochemical conditioning (PS)

Discussion

In order to investigate subtle changes on the structure of S- and Mn-doped Co-N-C in more detail, we calculated difference spectra between the initial spectrum and from the spectrum recorded after the galvanostatic conditioning (Figure 8). Positive (negative) area is assigned to the increase (decrease) of the corresponded component. Regarding carbon region, steep

changes at the energy of 284.3, 285.7, 286.3 and 288.7 eV were spotted, shown in Figure 8. In the case of S-doped sample a negative peak at 284.3 eV and positive peak at 285.7 eV, revealed the formation of surface group C-OH with oxidization of carbon in C=C. In contrast to S-doped catalyst, no negative peak at C=C region was observed while the formation of C=O and COOH was detectable in the case of Mn-doped catalyst.[36] Therefore, the conclusion can be drawn that both catalysts suffer from carbon corrosion, though the carbon oxidation mechanism might be different.[36] Regarding cobalt region, a systematic uprising of the positive peak at 779.7 eV and negative peak at 783 eV, confirmed the transition of Co(II) to stable Co (III) species. Comparison of O 1s region difference spectra showed two identical positive peaks at 529.5 eV and 530.7 eV confirming the formation of CoOOH species similar as it was observed in case of the model catalysts. In fact, it was reported that the unique O 1s line of CoOOH typically consisted of two O 1s peaks with the same intensity: A low binding energy peak at 529.9 eV assigned to Co-O and a high energy peak at 531.2 eV attributed to Co-OH, which was in agreement with our results.[30]

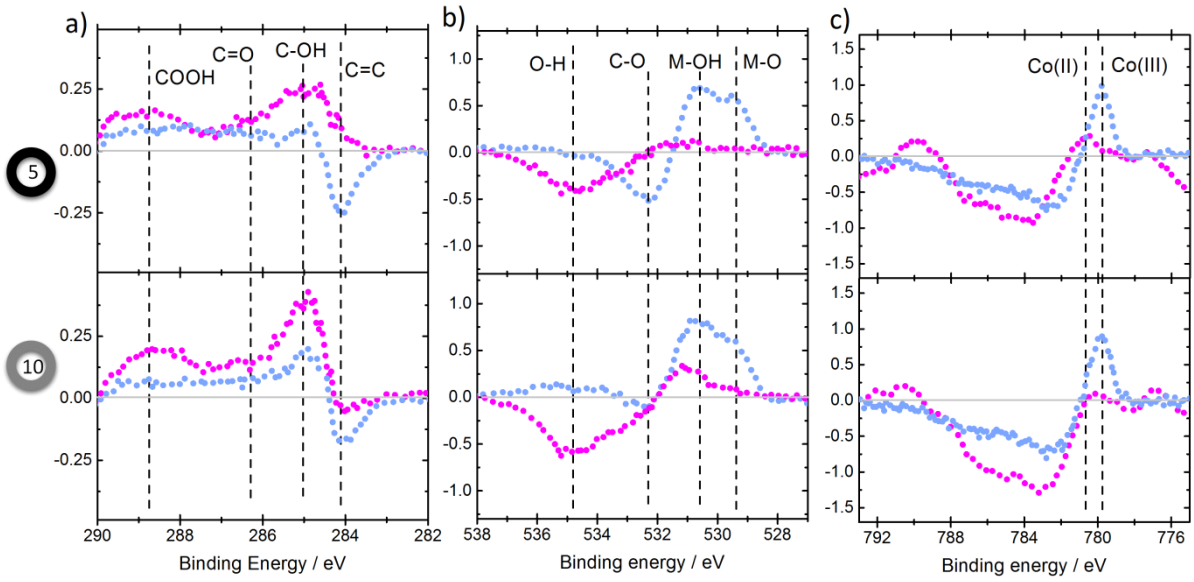

Figure 8. Comparison of difference spectra of S- and Mn-doped catalyst after 5 and 10 minutes galvanostatic conditioning

The equivalent Mn-doped difference of Co 2p spectra showed a negative peak at 778 eV corresponded to cobalt nanoparticles. This observation implied that the cobalt nanoparticles were removed during water oxidation and they were not participating in OER activity. Indeed, it can be shown that CoN_4 sites were stable during the conditioning since no peak changes was observed at 780.1 eV. It should be noted that the difference spectra of Mn 2p region showed negative peaks at 642 eV and 644 eV attributed to MnN_4 and manganese oxide impurities,

respectively (Figure S10). Thus, it could be concluded that MnN_4 species are not stable during water oxidation and destructed after electrochemical conditioning.

Therefore, the dominant active sites participating in OER for Me-N-C catalyst is strongly depending on the surface structure controlled by dopant. However, it is crucial to study this influence of inorganic species on the reaction kinetic. The OER mechanism in alkaline medium (for a single metal atom) is described below,

$$\mathrm{M} + OH^- \rightleftharpoons M - OH_{ads} + e^- \quad (1)$$

$$M - OH_{ads} + OH^- \rightleftharpoons M - O_{ads} + H_2O + e^- \quad (2)$$

$$M - O_{ads} + OH^- \rightleftharpoons M - OOH_{ads} + e^- \quad (3)$$

$$M - OOH_{ads} + OH^- \rightleftharpoons \mathrm{M} + H_2O + O_2 \uparrow + e^- \quad (4)$$

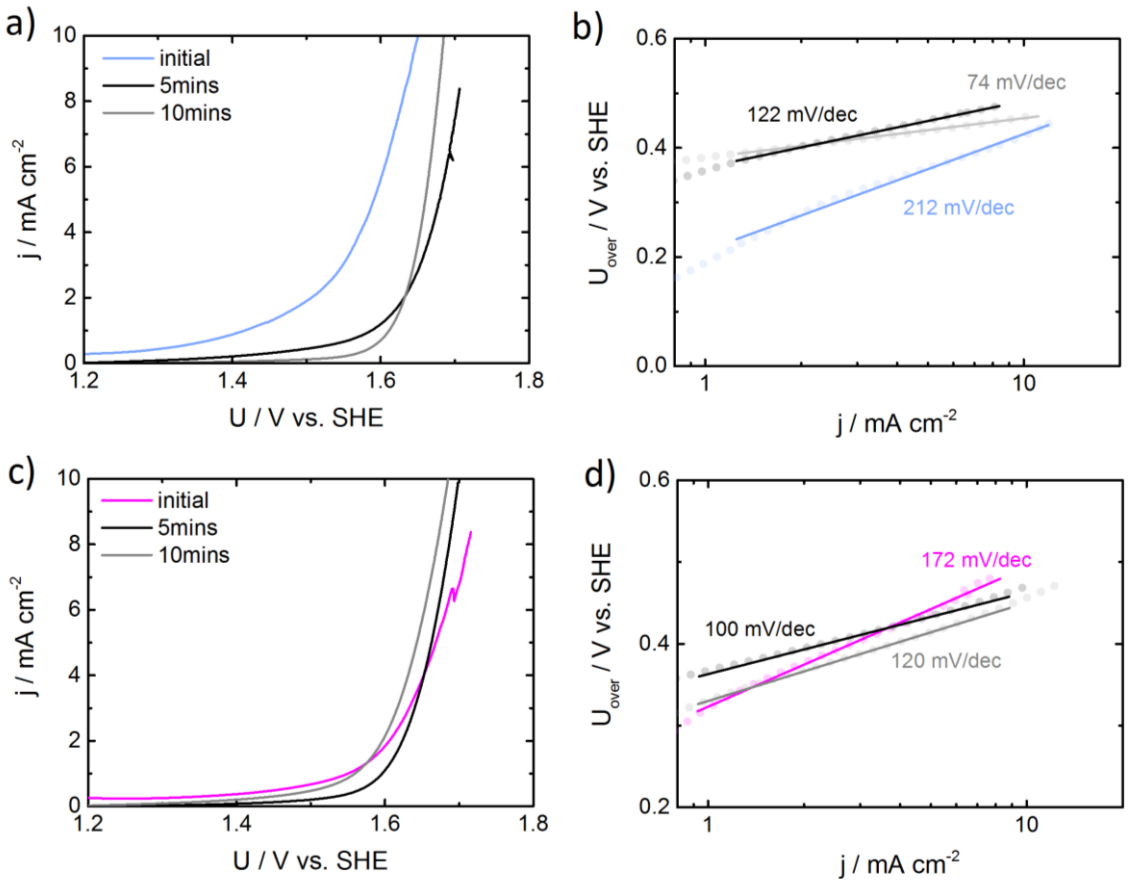

Figure 9. Comparison of stability measurement of S- and Mn-doped catalyst (a and c) and Tafel plots for initial (b and d), 5 and 10 minutes galvanostatic conditioning

Therefore, Tafel slopes were derived for initial, 5 and 10 minutes conditioning depicted in Figure 9. S-doped catalyst showed systematic decrease in Tafel slope, unlike the ones for Mn-

doped catalyst. This decrease to 65 mV/dec corresponded to the formation of oxy/hydroxide (high hydroxide coverage) and transition of Co(II) to Co (III) as it was reported in the recent studies confirming XPS results.[7,24] As a conclusion, primary discharge step would not be the rate determining step (RDS) after 10 minutes conditioning. [37] However, Mn-doped catalyst showed a 120 mV/dec slope corresponded to the first discharge step as RDS. The comparable behavior was observed for long-term stability test shown in Figure S11. It might be concluded that the presence of inorganic species on the surface define the rate determining step and reaction mechanism.

Conclusion

In this work, sulfur- and manganese doped Co-N-C catalysts were presented as promising electrocatalysts for OER in alkaline medium. The catalysts were evaluated by XPS and IL-TEM with respect to structural and morphological changes induced by water oxidation. It was shown that the formation of metal oxide and the carbon morphology can be controlled during the synthesis with heteroatom doping (sulfur or manganese). In the case of the sulfur-doped catalyst with predominant cobalt hydroxide species, the transformation of Co(II) to Co(III) (cobalt oxyhydroxide) similar to model film catalyst was observed. In contrast to S-doped, the Mn-doped catalyst with predominant MeN_4 sites did not show the abovementioned transformation with stable MeN_4 sites during water oxidation. Besides, both catalysts suffered from carbon oxidation as side-reaction of water oxidation observed by XPS and IL-TEM measurements. However, doping with sulfur or manganese can control the carbon morphology and affecting the carbon oxidation mechanism.

References

(1) Dau, H.; Limberg, C.; Reier, T.; Risch, M.; Roggan, S.; Strasser, P. *ChemCatChem* **2010**, *2*, 724–761.

(2) Lee, Y.; Suntivich, J.; May, K. J.; Perry, E. E.; Shao-Horn, Y. *J. Phys. Chem.Lett.* **2012**, *3*, 399–404.

(3) Li, G.; Li, S.; Ge, J.; Liu, C.; Xing, W. *J. Mater. Chem. A* **2017**, *5*, 17221–17229.

(4) Reier, T.; Oezaslan, M.; Strasser, P. *ACS Catal.* **2012**, *2*, 1765–1772.

(5) Diaz-Morales, O.; Ledezma-Yanez, I.; Koper, M. T. M.; Calle-Vallejo, F. *ACS Catal.* **2015**, *5*, 5380–5387.

(6) Fominykh, K.; Chernev, P.; Zaharieva, I.; Sicklinger, J.; Stefanic, G.; Döblinger, M.; Müller, A.; Pokharel, A.; Böcklein, S.; Scheu, C.; Bein, T.; Fattakhova-Rohlfing, D. *ACS nano* **2015**, *9*, 5180–5188.

(7) Weidler, N.; Paulus, S.; Schuch, J.; Klett, J.; Hoch, S.; Stenner, P.; Maljusch, A.; Brötz, J.; Wittich, C.; Kaiser, B.; Jaegermann, W. *Phys. Chem. Chem. Phys.* **2016**, *18*, 10708–10718.

(8) Chauhan, M.; Reddy, K. P.; Gopinath, C. S.; Deka, S. *ACS Catal. [Online]* **2017**, 5871–5879.

(9) Qiao, X.; Jin, J.; Fan, H.; Li, Y.; Liao, S. *J. Mater. Chem. A* **2017**, *5*, 12354–12360.

(10) Ganesan, P.; Prabu, M.; Sanetuntikul, J.; Shanmugam, S. *ACS Catal.* **2015**, *5*, 3625–3637.

(11) Jin Suntivich, Kevin J. May, Hubert A. Gasteiger, John B. Goodenough, Yang Shao-Horn. *Science (New York, N.Y.)* **2011**, *334*, 1380–1383.

(12) Kramm, U. I.; Herrmann-Geppert, I.; Behrends, J.; Lips, K.; Fiechter, S.; Bogdanoff, P. *J. Am. Chem. Soc.* **2016**, *138*, 635–640.

(13) Kramm, U. I.; Bogdanoff, P.; Fiechter, S. *Encyclopedia of Sustainability Science and Technology.*; pp 8265–8307.

(14) Ranjbar Sahraie, N.; Paraknowitsch, J. P.; Göbel, C.; Thomas, A.; Strasser, P. *J. Am. Chem. Soc.* **2014**, *136*, 14486–14497.

(15) Liu, Y.; Jiang, H.; Zhu, Y.; Yang, X.; Li, C. *J. Mater. Chem. A* **2016**, *4*, 1694–1701.

(16) Subbaraman, R.; Tripkovic, D.; Chang, K.-C.; Strmcnik, D.; Paulikas, A. P.; Hirunsit, P.; Chan, M.; Greeley, J.; Stamenkovic, V.; Markovic, N. M. *Nat. Mater.* **2012**, *11*, 550–557.

(17) Daniel, Q.; Ambre, R. B.; Zhang, B.; Philippe, B.; Chen, H.; Li, F.; Fan, K.; Ahmadi, S.; Rensmo, H.; Sun, L. *ACS Catal.* **2017**, *7*, 1143–1149.

(18) Favaro, M.; Yang, J.; Nappini, S.; Magnano, E.; Toma, F. M.; Crumlin, E. J.; Yano, J.; Sharp, I. D. *J. Am. Chem. Soc.* **2017**, *139*, 8960–8970.

(19) Stracke, J. J.; Finke, R. G. *ACS Catal.* **2013**, *3*, 1209–1219.

(20) Martin, D. J.; McCarthy, B. D.; Donley, C. L.; Dempsey, J. L. *Chem. Commun.* **2015**, *51*, 5290–5293.
(21) Wang, D.; Groves, J. T. *Proc. Natl. Acad. Sci. U. S. A.* **2013**, *110*, 15579–15584.
(22) Yamaguchi, A.; Inuzuka, R.; Takashima, T.; Hayashi, T.; Hashimoto, K.; Nakamura, R. *Nat. Commun.* **2014**, *5*, 4256.
(23) Yoshinori Naruta. MASA-aki Sasayama, Takao Sasaki. *Angew. Chem., Int. Ed. Engl.* **1994**, *33*, 1839–1841.
(24) Shahraei, A.; Martinaiou, I.; Creutz, K. A.; Kübler, M.; Weidler, N.; Ranecky, S. T.; Wallace, W. D. Z.; Nowroozi, M. A.; Clemens, O.; Stark, R. W.; Kramm, U. I. *Chem. - Eur. J.* **2018**, 24, 12480-12484 .
(25) Meier, J. C.; Katsounaros, I.; Galeano, C.; Bongard, H. J.; Topalov, A. A.; Kostka, A.; Karschin, A.; Schüth, F.; Mayrhofer, K. J. J. *Energy Environ. Sci.* **2012**, *5*, 9319.
(26) Shahraei, A.; Moradabadi, A.; Martinaiou, I.; Lauterbach, S.; Klemenz, S.; Dolique, S.; Kleebe, H.-J.; Kaghazchi, P.; Kramm, U. I. *ACS Appl. Mater. Interfaces* **2017**, *9*, 25184–25193.
(27) Biesinger, M. C.; Lau, L. W.; Gerson, A. R.; Smart, R. S. *Appl. Surf. Sci.* **2010**, *257*, 887–898.
(28) N. S. McIntyre and M. G. Cook. *Anal. Chem.* **1975**, *47*, 2208–2213.
(29) IB Alstrup, IB Chorkendorff, Robberto Candia, Bierne S. Clausen, Henrik Topsoe. *Journal of Catalysis* **1982**, *77*, 397–409.
(30) T. J. Chuang, C. R. Brundle, D.W. Rice. *Surf. Sci.* **1976**, *59*, 413–429.
(31) H.W. Nesbitt AND D. Banerjee. *Am. Mineral.* **1998**, *83*, 305–315.
(32) Kaplan, A.; Korin, E.; Bettelheim, A. *Eur. J. Inorg. Chem.* **2014**, *2014*, 2288–2295.
(33) Zhu, J.; Huang, L.; Xiao, Y.; Shen, L.; Chen, Q.; Shi, W. *Nanoscale* **2014**, *6*, 6772–6781.
(34) Weidler, N.; Schuch, J.; Knaus, F.; Stenner, P.; Hoch, S.; Maljusch, A.; Schäfer, R.; Kaiser, B.; Jaegermann, W. *J. Phys. Chem. C* **2017**, *121*, 6455–6463.
(35) Takabayashi, S.; Takahagi, T. *Surf. Interface Anal.* **2015**, *47*, 345–349.
(36) Wang, W.; Luo, J.; Chen, S. *Chem. Commun.* **2017**, *53*, 11556–11559.
(37) Shinagawa, T.; Garcia-Esparza, A. T.; Takanabe, K. *Sci. Rep.* **2015**, *5*, 13801.

Supporting information

Post mortem evaluation of sulfur- and manganese-doped cobalt-based catalyst under water oxidation

Ali Shahraei, Natascha Weidler, Markus Kübler, Lingmei Ni, Ioanna Martinaiou, Bernhard Kaiser, Robert W. Stark, Wolfram Jaegermann, Ulrike I. Kramm

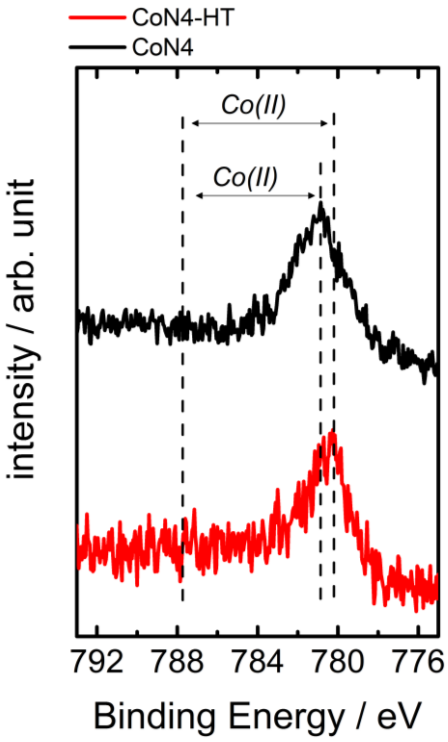

Figure S1. Co 2p Xp spectra of the reference sample CoTMPP, before and after heat treatment (@800 °C for 4 hour at N_2 atmosphere)

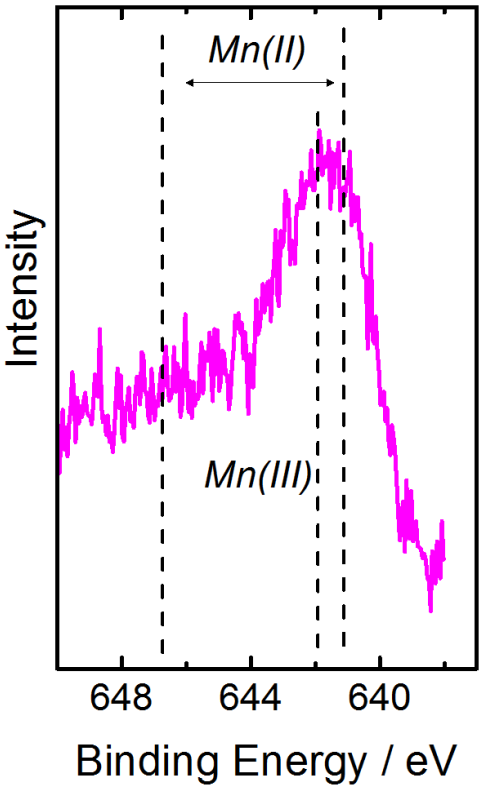

Figure S2. Mn 2p XP spectrum of the as-prepared Mn-doped catalyst

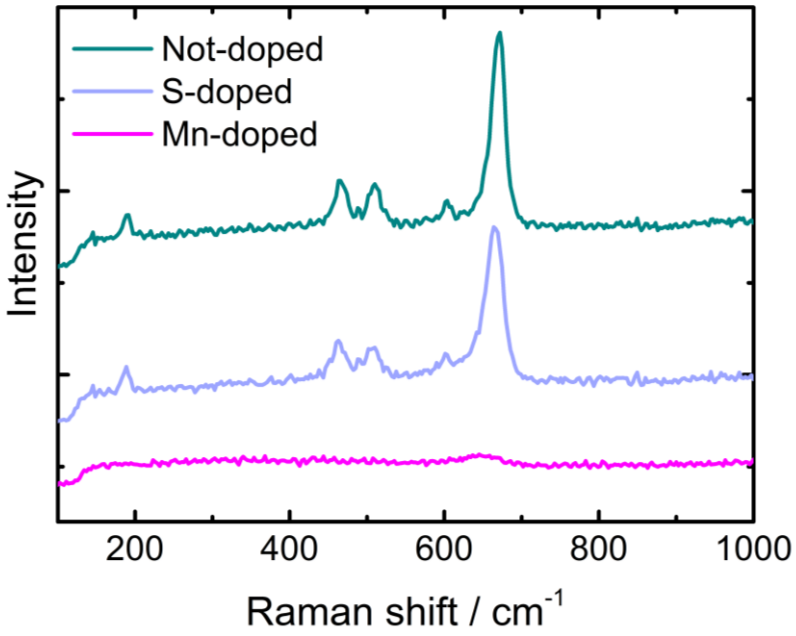

Figure S3. Low wavenumber range of the Raman spectra of the as-prepared catalysts.

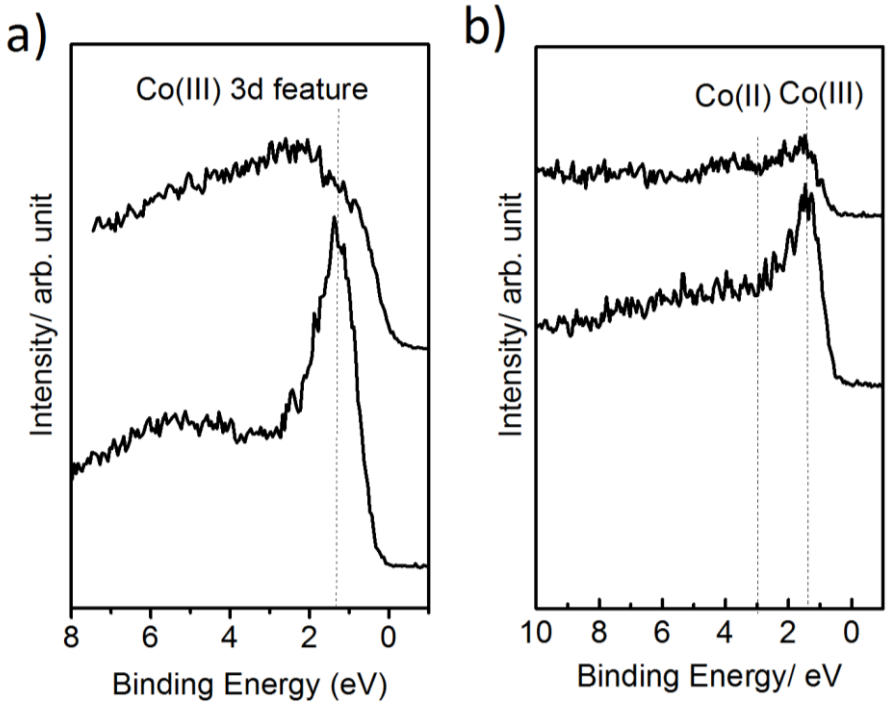

Figure S4. The VB feature of the model catalysts a) $CoO(OH)_2$, b) CoO_x

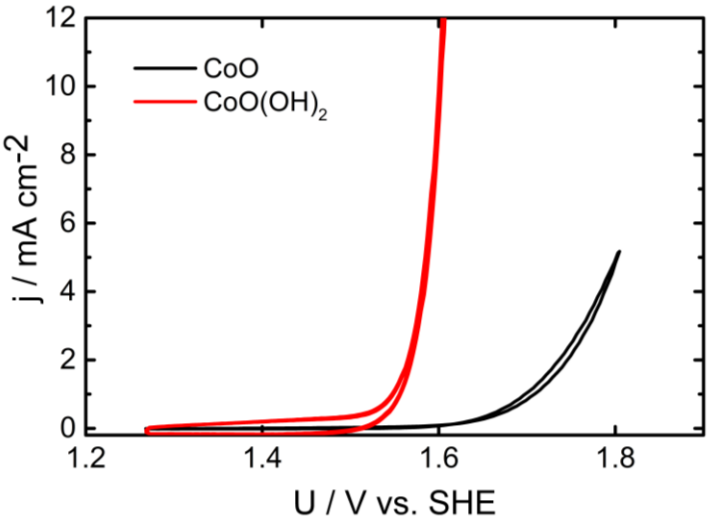

Figure S5. The cyclic voltammograms of the hydroxide-free and the hydroxylated CoO model catalysts in 0.1M KOH

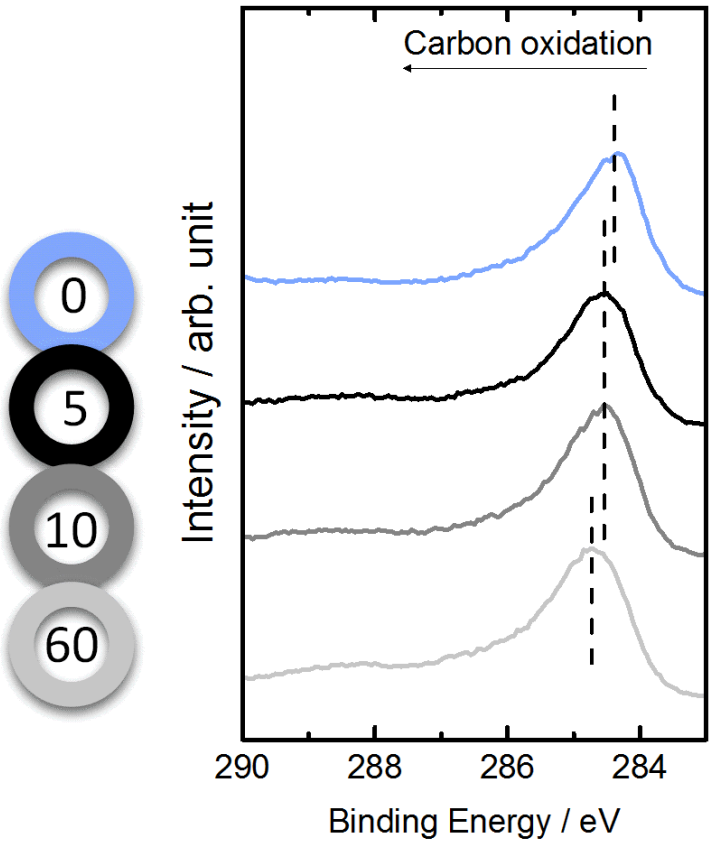

Figure S6. High resolution XP spectra of the C 1s of the S-doped catalyst after electrochemical conditioning (GS)

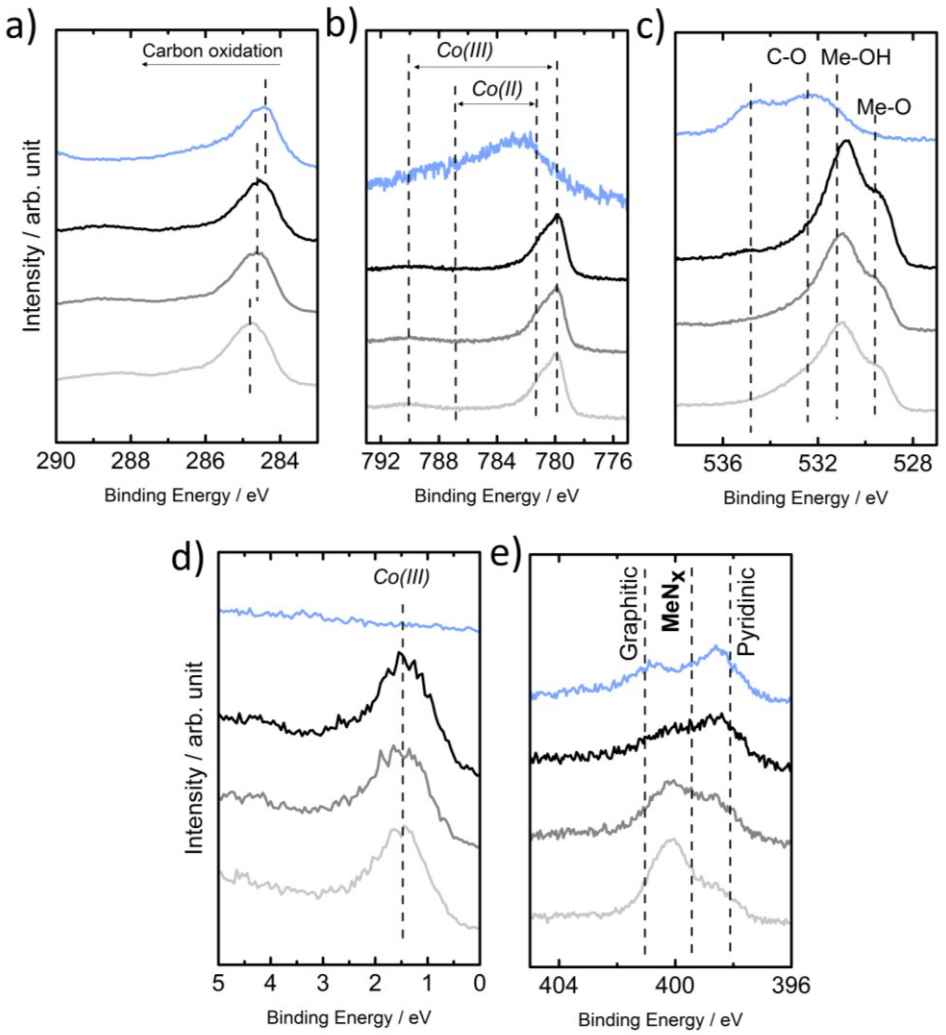

Figure S7. High resolution XP spectra of the a) C 1s, b) Co 2p, c) O 1s, d) VB and e) N1s regions of the S-doped catalyst after electrochemical conditioning (PS)

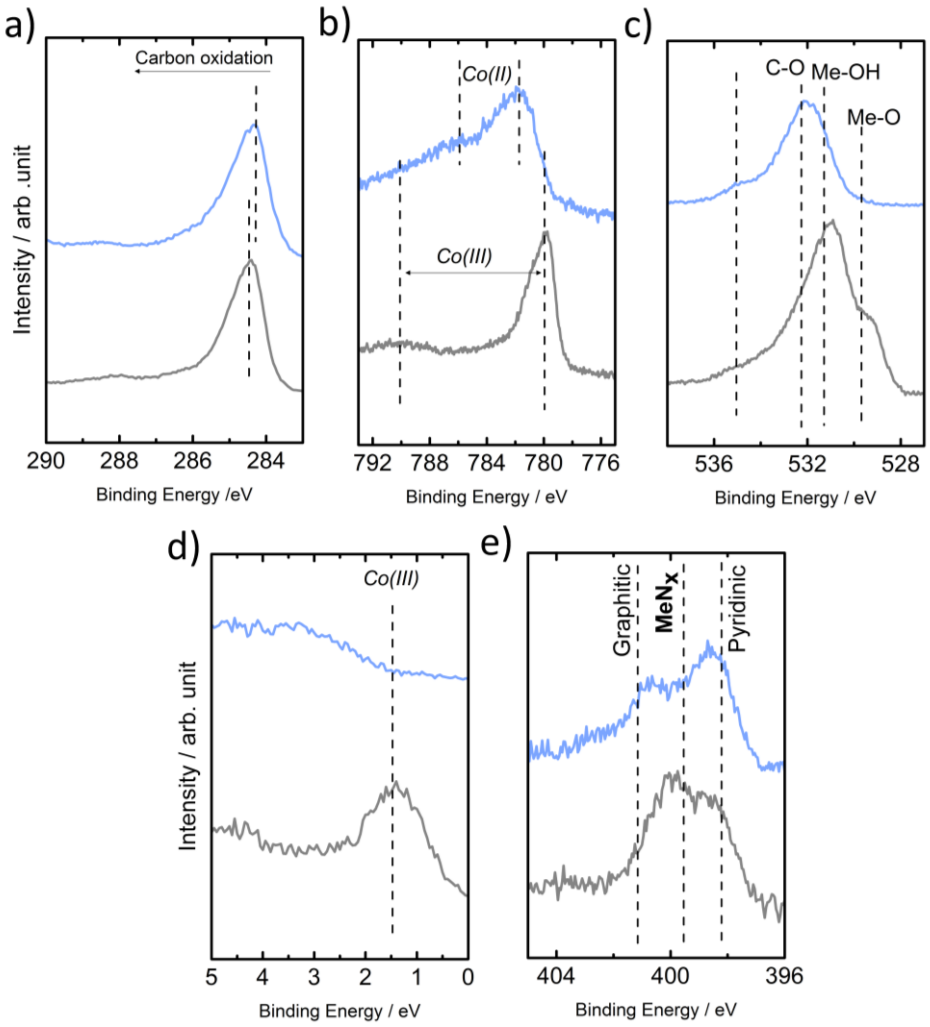

Figure S8. High resolution XP spectra of the a) C 1s, b) Co 2p, c) O 1s, d) VB and e) N1s regions of the S-doped catalyst after electrochemical conditioning (Cycling)

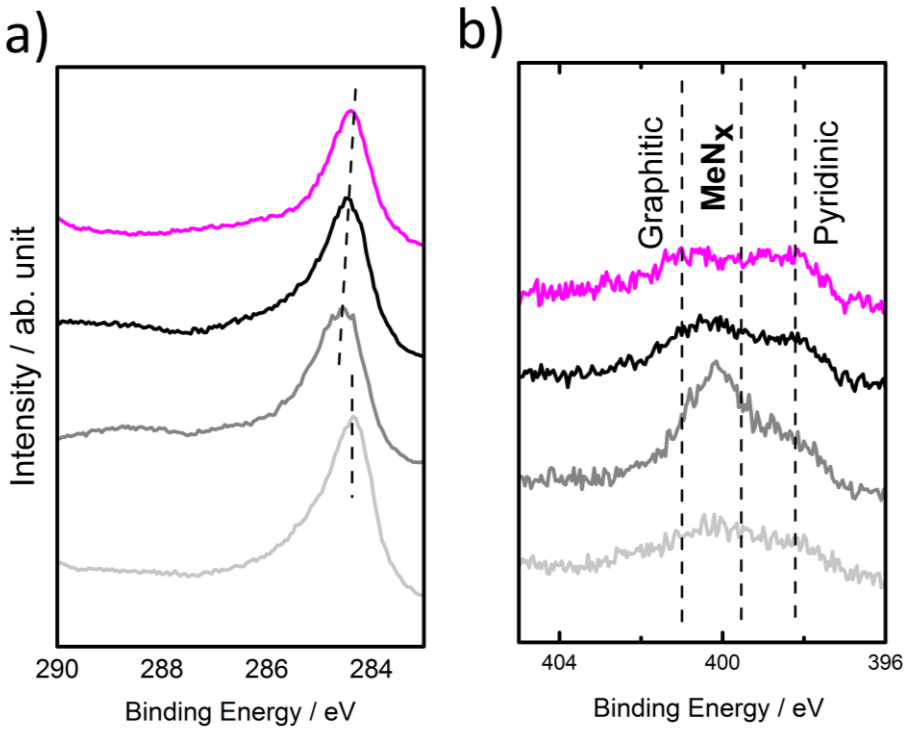

Figure S9. High resolution XP spectra of the a) C 1s and b) N 1s of the Mn-doped catalyst after electrochemical conditioning (GS)

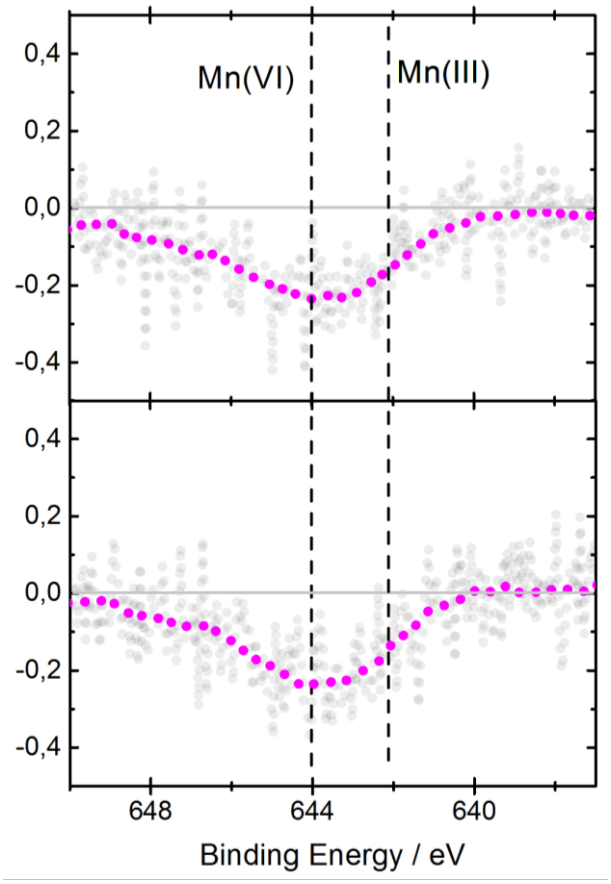

Figure S9.

Figure S10. Comparison of difference XP spectra of Mn 2p XP spectra of the Mn-doped catalyst after 5 and 10 minutes galvanostatic conditioning

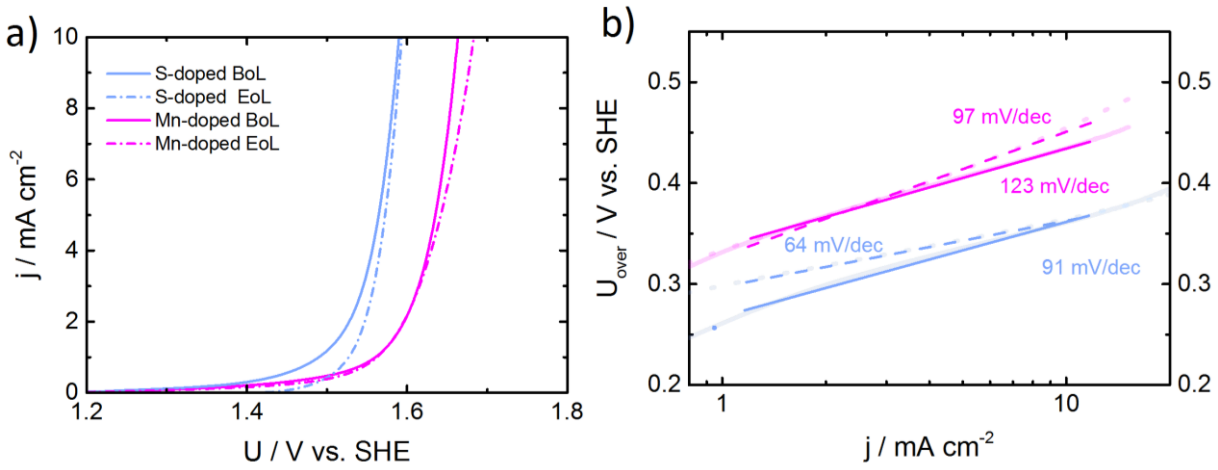

Figure S11. a) Long term stability and b) Tafel plot of S- and Mn-doped catalyst after 2000 cycles,

4.3 Comparison of the different catalyst types for HER and OER

Carbon-based catalysts are recently reported as promising electrocatalysts for water splitting reactions, particularly in alkaline media.[41] In order to improve the activity and stability of the carbon-based materials, heteroatom (non-metal and metal) doping was suggested.[37, 77, 139] Besides, it has been shown that the choice of the precursors, specifically the choice of carbon source, affects the material structure and catalytic activity. However, the majority of the optimization techniques have been adapted from those in oxygen reduction reaction (ORR) since 1960s.[41] Despite the focus of active site identification in Me-N-C for ORR, a few reports were published considering the origin of the activity of those for hydrogen evolution reaction (HER) and oxygen evolution reaction (OER). In this work, two main approaches were introduced to synthesize Me-N-C catalysts for water splitting reactions, namely MOF and PANI. Within the MOF approach, Z1200, phenanthroline and metal acetate used as the precursors and the catalysts prepared at the temperature of 950° C. Within the PANI approach, $PANI_{ref}$, $PANI_{evap}$ and $PANI_{evap}$+S as the nitrogen and sulfur sources (multi-heteroatom doping), dicyandiamide as the structure forming agent and metal acetate are used to prepare Me-N-C catalysts at the temperature of 800° C (Figure 4.1). The metal loading in the precursors are set to 2 wt% (Co-$PANI_{evap}$+S is an exception because of the high sulfur loading). It should be noted that the sulfur content in the precursors is changing in the order of zero = MOF< $PANI_{ref}$ < $PANI_{evap}$ < $PANI_{evap}$+S. In this section, the aforementioned samples are compared with respect to the structural properties and their catalytic activity for HER and OER. Besides, the effect of a second metal (Mn) is discussed for the first three approaches in this summary. This comparison is limited to alkaline media for a straight forward discussion.

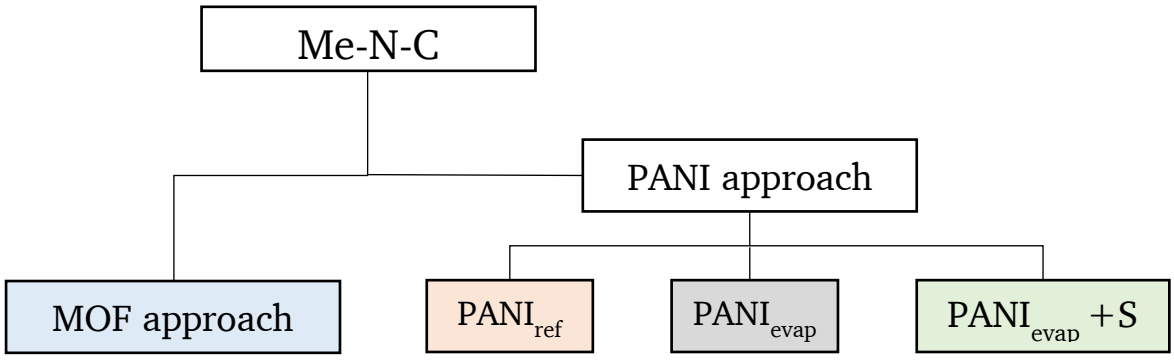

Figure 4.1 Schematic of the reported approaches for synthesizing Me-N-Cs in this thesis

Structure characterization

X-ray photo electron spectroscopy (XPS) was performed to study the elemental compositions and electronic structure of catalysts obtained by different approaches. Table 14 shows that the catalysts mostly contain carbon (70-80%), nitrogen (7-16%) and oxygen (5-11%) in at%. It should be noted that MOF-based catalysts contain a fraction of zinc due to incomplete evaporation of zinc included in MOF (Z1200). The most notable change considering elemental compositions is related to the resulting nitrogen content comparing the different approaches. It becomes clear that the PANI catalysts contain more nitrogen doped into carbon than the ones prepared by the MOF approach. This is most probably related to the use of different nitrogen sources and/or the different pyrolysis temperature. Nevertheless, for PANI synthesis routes, increasing sulfur reduces the nitrogen content from 17 to 10 wt%.

Table 14 elemental composition of the reported catalysts, derived by XPS

At%	N	C	O	Co + Mn	S or (Zn)	Me N	MeS	MeO	MeOH
Co-MOF	7.5	79	12.4	0.5	(0.6)	1.2	0	0.38	4
Co,Mn-MOF	7.4	83.35	7.3	0.9 0.23	(1.1)	0.8	0	0.69	1.7
Co-PANI$_{ref}$	17	72.5	5.1	1.8	0.57	1.2	0.06	1.02	1.9
Co,Mn-PANI$_{ref}$	17	73.8	5.6	1.7 0.9	0.77	2.7	0.07	0.63	1.96
Co-PANI$_{evap}$	16.3	73	7	2.7	0.96	2	0.25	1.11	2.5
Co,Mn-PANI$_{evap}$	15.1	72.3	7.5	1.5 1.6	1.9	2.1	0.49	1.17	3.37
Co- PANI$_{evap}$ +S	10.2	71.2	11.4	3.1	4	1.4	0.34	1.36	5.2

An increase of sulfur leads to an increase in the metal content as a sign of the formation of metal nanoparticles/composites (carbides, oxides), as well. Interestingly, no significant changes in elemental compositions are observed after introducing manganese as the second metal to the synthesis route for all three approaches. As it was described before, the Me-N-C catalysts have a complex hybrid structure containing various composites or inorganic species. Therefore, XPS fine scans of N 1s, S 2p and O1s were analyzed and reported above.

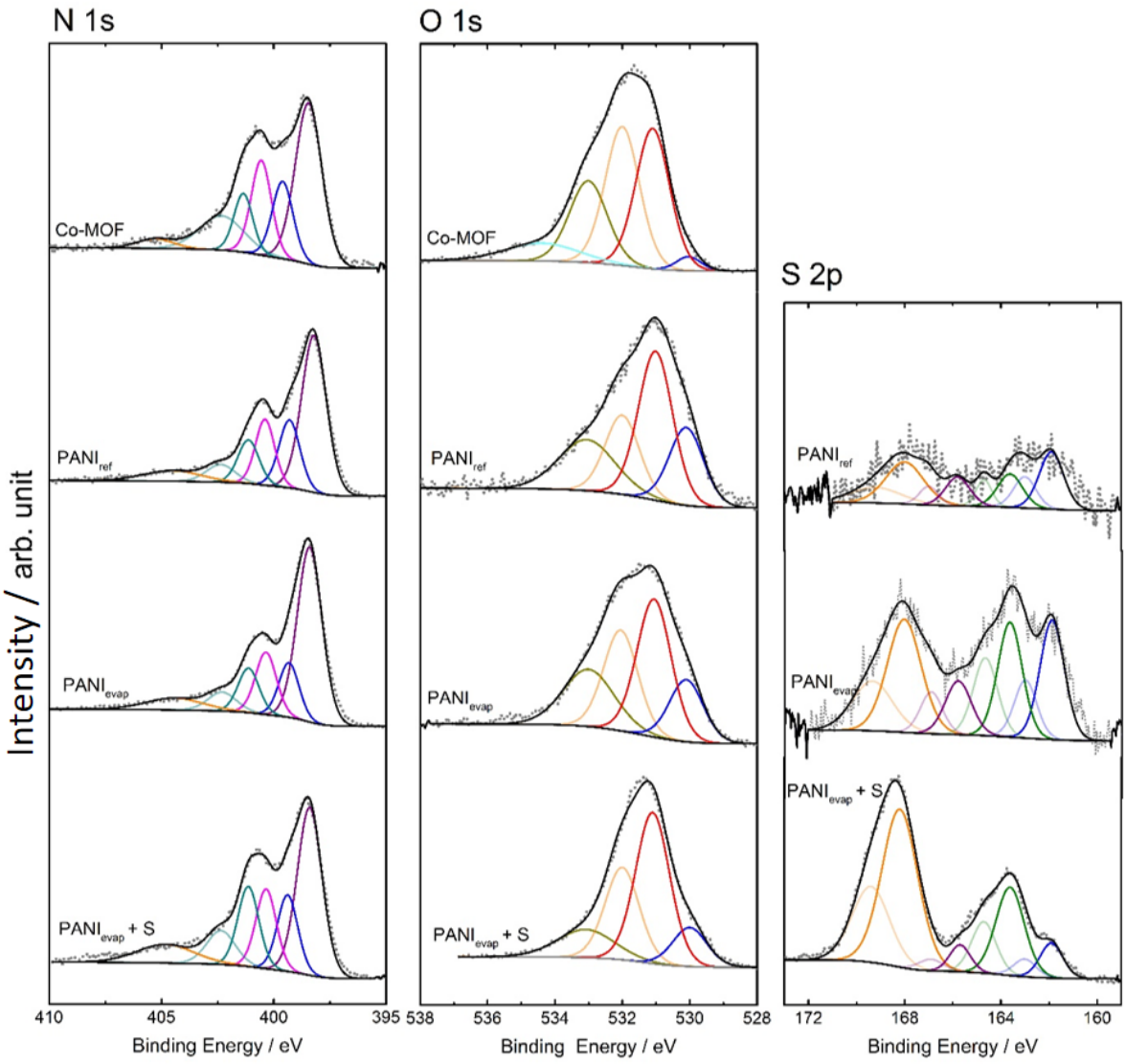

Figure 4.2 Deconvolution of N 1s, S 2p and O 1s spectra of Co-based catalysts

Analysis of the spectra suggests that the content of MeS_y and oxide/hydroxide species are increased with increasing sulfur content in the precursors. Although the content of MeN_x moieties is increased with exchange of the MOF to the $PANI_{ref/evap}$, addition of the ulta-high amount of elemental sulfur in $PANI_{evap}$ sample seems not beneficial for MeN_x formation. In order to investigate the effect of the precursors on the morphology of the catalyst, transmission

electron microscopy (TEM) was performed. It is observed that all samples (independent of the type of doping and precursors) contain metallic nanoparticles/composites. In the case of the MOF-based sample, cobalt particles are dispersed in turbostratic carbon. In contrast to MOF, PANI-based samples contain metallic particles embedded in bamboo-shaped/nanotube carbon structure where the thickness of the tubes increases with the addition of sulfur.

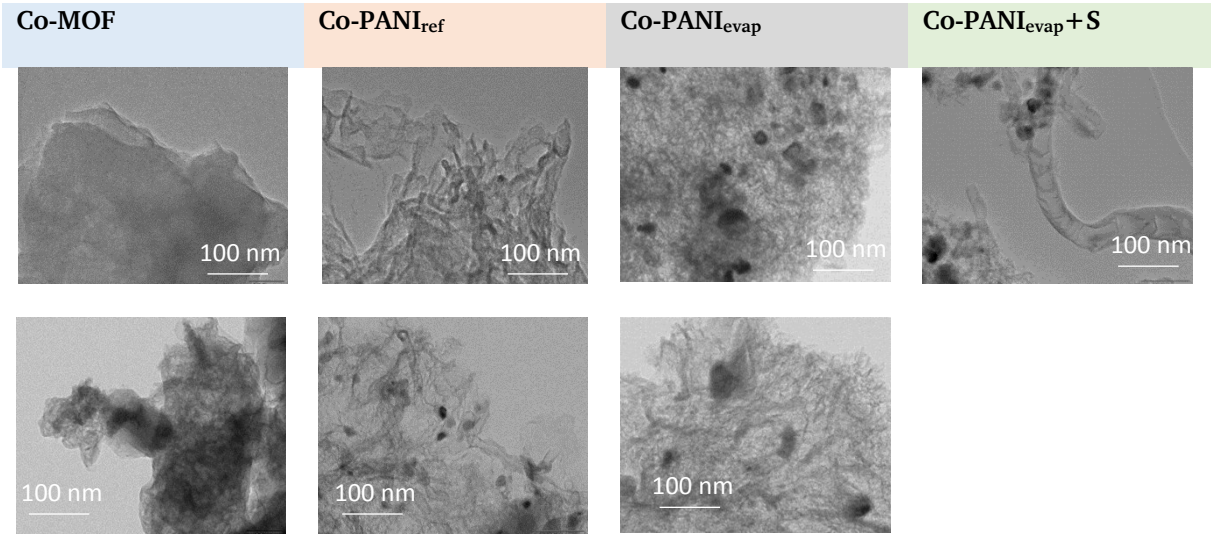

Figure 4.3 TEM images (100 nm) of different approaches, monometallic top and bimetallic below images

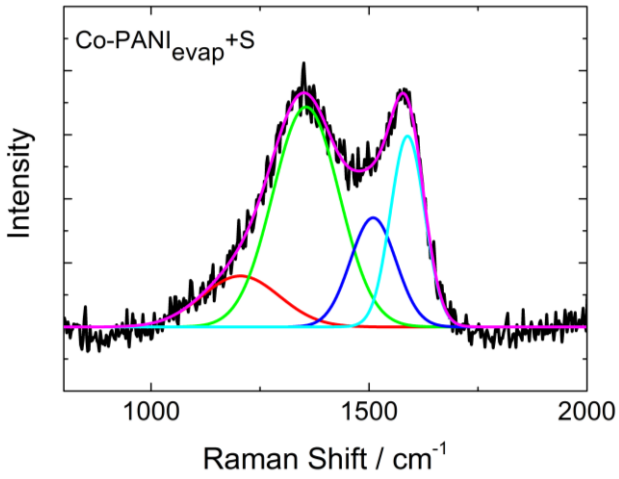

Figure 4.4 Raman spectra of a Co-PANI$_{evap}$+S sample in the first order region

Raman spectroscopy was performed to evaluate the carbon morphology obtained with different approaches. Figure 4.4 shows the Raman spectra for the Co-PANI$_{evap}$+S sample as an example. The D band at 1355 cm^{-1} related to the C-atoms at the edges of graphene layer and G band at 1586 cm^{-1} is related to the C-atoms (in plane) bond stretching vibrations.[140, 141] The deconvolution of Raman spectra was performed for all the catalysts and the respective ratio of

I_D/I_G and I_{D3}/I_G are reported in Table 15. I_D/I_G demonstrates the degree of graphitization and I_{D3}/I_G is suggested as an indicator MeN_x integration in graphene layers.[142]

MOF- and $PANI_{ref}$-based samples obtained higher degree of graphitization (lower I_D/I_G) related to the turbostatic carbon structure as shown in TEM images. However, lower degree of graphitization is corresponded to the $PANI_{evap}$ samples with higher sulfur doping. These results are in agreement with the literature claiming sulfur as a hindering component for the graphitization process.[143]

Table 15 Degree of graphitization and defect ratio

	I_D/I_G	I_{D3}/I_G
Co-MOF	1.07	0.65
Co,Mn-MOF	1.05	0.61
Co-$PANI_{ref}$	1.07	0.52
Co,Mn-$PANI_{ref}$	1	0.98
Co-$PANI_{evap}$	1.41	0.75
Co,Mn-$PANI_{evap}$	1.36	0.65
Co-$PANI_{evap}$ +S	1.15	0.57

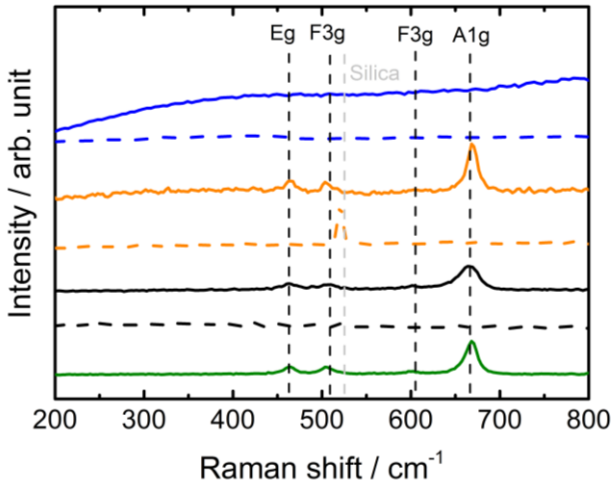

Figure 4.5 low wavenumber range (< 1000 cm^{-1}) of Raman spectra and the peak assignments of the different preparation, solid line: Co-based and dashed like: (Co,Mn)-based

Moreover, the Raman spectra in low wavenumber range from 400 cm^{-1} to 800 cm^{-1} can be used to identify the possible presence of metal composites close to the surface of carbon, where XRD is not an applicable technique. The low wavenumber range of Raman spectra and corresponding assignment is shown in Figure 4.5. No feature related to metal composites is found in the case

of MOF-based samples which is in agreement with XPS data and in disagreement with TEM images in which metallic particles are detectable. PANI-based monometallic samples demonstrates peaks at 670, 467 and 603 cm^{-1} corresponding to cobalt oxides species based on literature.[144] However, these features vanished when the catalysts were co-doped with manganese. Therefore, one can conclude that the addition of manganese prohibits the formation of cobalt oxide during the synthesis and stabilized CoN_4 formation.

Electrochemical characterization

- **Hydrogen Evolution Reaction (HER)**

The HER activity of the catalysts was evaluated in alkaline media (0.1M KOH). The polarization curves are reported in Figure 4.6. The order in the HER activity for monometallic catalysts is Co-$PANI_{evap}$ > Co-$PANI_{evap}$+S > Co-MOF > Co-$PANI_{ref}$. Accordingly, the highest activity among catalysts with different preparation methods is related to the $PANI_{evap}$-based catalysts with the overpotential of 250 mV at 10 mA cm^{-2} . It is observed that the excessive amount of elemental sulfur negatively affects HER activity, in the case of PANI-based samples for this condition. Interestingly, addition of Mn as the second metal improves the HER activity for MOF- and $PANI_{ref}$ – based samples, unlike the actvity for Co-$PANI_{evap}$

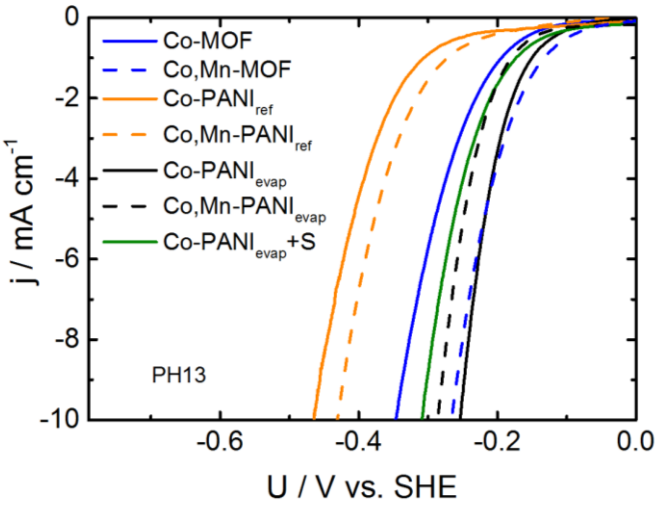

Figure 4.6 HER polarization curves of Me-N-Cs prepared with different approaches

It was shown before in chapter 2.14.1 that the HER activity is correlated with MeN_4 content determined by XPS in the $PANI_{evap}$ catalysts. Interestingly the same correlation, in the case of monometallic samples, is found for the different preparation routes, this is shown in

Figure 4.7. This important finding confirms that the MeN_4 sites are the main contributor to the HER activity independent of the preparation method. However, the bimetallic samples do not fit to the correlation in this case. This lack in correlation might be caused by the fact that CoN_4 and MnN_4 sites present in the bimetallic catalyst cannot be distinguished by XPS. Therefore, the total amount of MeN_4 corresponds to both CoN_4 and MnN_4 species. It was reported in chapter 4.1 that the MnN_4 sites are less active and less stable than CoN_4 sites in the potential range of hydrogen and cobalt coordinated with nitrogen promoting HER activity, though manganese is not participating in the reaction directly. Nevertheless, this idea needs to be assessed further with in-situ characterization techniques in order to draw a comprehensive conclusion.

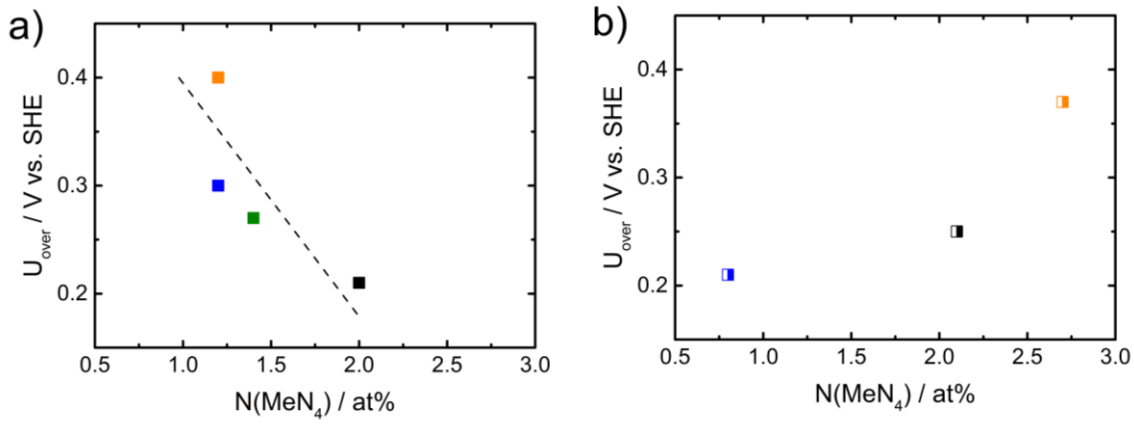

Figure 4.7 Correlation of the HER activity of a) monometallic b) bimetallic with $N(MeN_4)$ content from XPS for different preparation

Oxygen Evolution Reaction (OER)

The OER activity of Me-N-C catalysts was investigated in alkaline media (0.1M KOH). Co-MOF shows the lowest OER activity among differently prepared catalysts and the PANI-based samples follow the order of Co-$PANI_{ref}$ < Co-$PANI_{evap}$ < Co-$PANI_{evap}$+S. The main reason for the poor performance of the MOF-based catalysts might be the unstable turobstratic carbon under corrosive conditions. In contrast to MOF, PANI provides high-surface area nanocarbons with proper structure, more applicable for OER in harsh condition.[124] Indeed, it is observed that using the approach with more sulfur involved in the synthesis is more likely to establish an active and stable OER catalyst.

It was shown in the chapter 4.2.1 that more hydroxide species were formed in the preparation when more sulfur was introduced through the synthesis of Co-$PANI_{evap}$ catalysts. In this summary, it is observed that the oxide/hydroxide and sulfide contents in the samples increase

in the order of $PANI_{ref}$ < $PANI_{evap}$ < $PANI_{evap}$+S which correlates with the OER activity improvement. Therefore, the origin of activity improvement can be explained by formation of the inorganic species which can possibly participate in the reaction.

Figure 4.8 shows the progress of the catalyst optimization for OER with multi-heteroatom doping method in this work. It is observed that introducing manganese as the second metal enhances the OER activity for each preparation route.

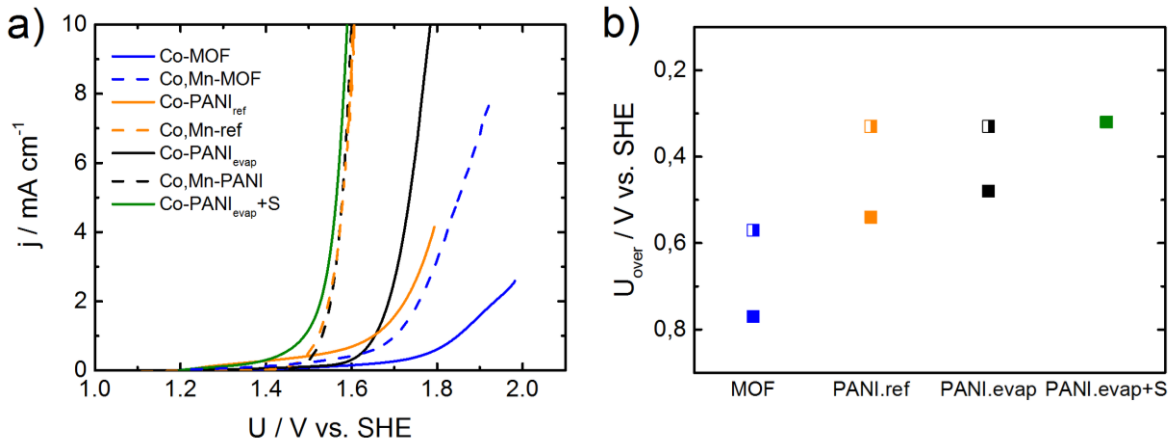

Figure 4.8 a) OER polarization curves of the catalysts with different preparation, b) catalytic activity improvement of the catalyst by multi-heteroatom doping

It was reported in the previous chapter that manganese complexes stabilize CoN_4 sites in the potential region of the oxygen evolution reaction for $PANI_{evap}$ –based sample. This conclusion might be expanded to different preparation techniques, although more fundamental characterization is required to make a concrete conclusion.

From comparison of different preparation methods in this work, it can be concluded that:

1) MeN_4 sites are the dominant species attributed to the HER activity in alkaline and acidic media
2) Heteroatom doping is an effective way to control the formation or blockage of oxidic species in the synthesis process
3) Combination of cobalt and manganese is an effective way to improve OER activity of Me-N-C catalysts

5 Conclusions and outlook

In this work, two different approaches (MOF and PANI) were used to synthesize Me-N-C catalysts for HER (acid and alkaline media)and OER (alkaline media). The catalysts were intensively investigated regarding their electrochemical and physico-chemical properties. Within different projects, the role of transition metals, synergetic effects in bimetallic catalysts, the influence of heteroatom doping and co-doping and the nature of active sites were explored. This broad knowledge can be employed to the rational design of the carbon-based catalysts applicable for water splitting reactions in the future.

Variation of metal species on HER (in alkaline). In this project, it was aimed to elucidate the role of transition metals on catalytic activity, structure and morphology of the mono- and bimetallic catalysts. Owing to DFT calculations, indications were found that the most favorable configuration for different transition metals is MeN_4 sites embedded in the edge of graphene layer among other proposed configuration (Me3CN, Me….). The structure-activity correlations derived from XPS, DFT calculations and electrochemical characterization gave indication of the importance of the nature of the metal in Me-N-C catalysts. It was concluded that the type of metal can affect the active site density, the charge distributing within the complex and the hydrogen binding energy (HBE). Moreover, it was shown that doping with a second metal (manganese or molybdenum) significantly enhances the HER activity . The synergetic effect related to tuned HBE was suggested as the origin of activity improvement.

Variation of Co-content for HER (in acid). A method for co-doping of nitrogen and sulfur using PANI was reported to prepare Co-N-C catalysts. The project was defined to explore the effect of co-doping and the nature of active sites considering the hybrid structure of the catalysts. Therefore, beside CoN_x moieties, the catalyst contained cobalt sulfide (CoS_y) and metal nanoparticles/nanocomposites (oxides). It was found that co-doping of nitrogen and sulfur is an effective way to promote CoN_x formation. Based on the established correlation between CoN_x content and HER activity as well as post mortem analysis, the high catalytic activity for HER was attributed to CoN_x sites.

Variation of sulfur content of Co-N-C for OER (in alkaline). This project focused on multi heteroatom doping, in which the effect of introducing elemental sulfur to the preparation route for PANI-based catalysts was studied. It was found that the addition of sulfur might change the

carbon morphology of the catalysts as well as formation of inorganic species (hydroxide). Moreover, the important role of hydroxide species on the reaction kinetic was discussed using the Tafel analysis.

Comparative study of structural changes of Co-based catalysts for OER. A manganese doped and a sulfur doped Co-based catalyst were evaluated considering structural and morphological changes induced by oxygen evolution reaction in order to elucidate the origin of catalytic activity. It was shown that the S-doped catalyst with predominant cobalt hydroxide species (Co(II)) transforms to cobalt oxyhydroxide (Co(III)) as the real active site. In case of the Mn-doped catalyst with predominant MeN_4 species and cobalt nanoparticle, the main activity was attributed to stable MeN_4 sites. Due to different carbon morphology, it was found that the contribution of carbon oxidation to OER current is unalike for the case of S- and Mn-doped catalyst, which was observed by XPS and IL-TEM analysis.

Finally, within the choice of precursors and the use of multi-heteroatom doping method, it was possible to tune the structure of the catalysts for the requirement assigned to a particular reaction. Overall, it was possible to address the effect of co-doping (S and N), effect of metallic-heteroatom doping (manganese) and the nature of active sites for HER and OER in the scope of this thesis.

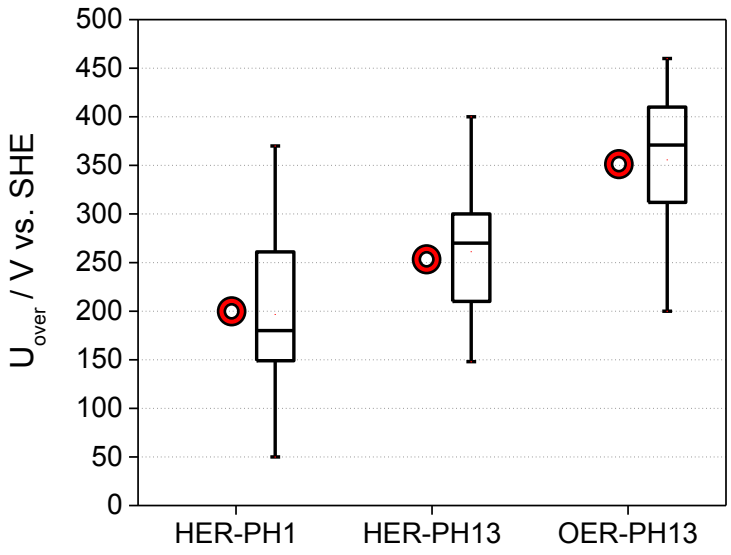

Figure 5.1 The activity comparison of cobalt- and nitrogen-doped carbon-based materials for HER (acid and alkaline) and OER (alkaline) with best-off catalysts in this work (spheres)

Even though great progress in developing of Me-N-C catalysts for water splitting reactions has been made in this work (Figure 5.1), there are still open issues that need to be addressed in the future:

1) Validation of the active site identification for different catalytic systems

2) Stabilization of the active sites under different operation conditions

3) Synthesis of a pure catalyst including only one specific active site activating the reaction

4) Optimization for a scale-up synthesis of Me-N-Cs for the real electrolyzer operation.

In order to address the aforementioned concerns, it is required to provide more controlled doping/co-doping methods to study the structural changes systematically and compare them with model studies. Furthermore, in-situ synthesis is a valuable technique to construct one specific active moiety in the favor of the reaction. Therefore, owing to the controlled preparation methods combined with in-situ characterization, it is possible to address the reliability of active site identification and to discuss the density of active sites. It is also necessary to investigate more novel preparation techniques with a variety of the precursors, particularly the carbon source. A great effort is required to study carbon corrosion and possible active site destruction under different conditions. Indeed, it is necessary to optimize and tune the catalyst composition via adapting the new methods used for other catalytic systems in order to improve the catalytic activity. For instance, surface modification via Ionic Liquids (IL) and modifying the surface functional groups via plasma treatment could be possible improving strategies. It is strongly recommended to test the suggested carbon-based catalysts under the real performance condition in electrolyzers or photo-electrochemical devices. Hence, the obtained results and information can be applied to optimize the synthesis for a large-scale application.

6 References

(1) Edenhofer, O.; Pichs-Madruga, R.; Sokona, Y.; Minx, J.; Farahani, E.; Kadner, S.; Seyboth, K.; Eickemeier, P.; Kriemann, B.; Savolainen, J.; Schlömer, S.; Stechow, C.; Zwickel T. *Climate change 2014;* Cambridge University Press: New York, NY, 2014.

(2) Larscheid, P.; Lück, L.; Moser, A. *J. Renewable Energy* **2018**, *125*, 599–608.

(3) Dincer, I.; Acar, C. *Int. J. Hydrogen Energy* **2015**, *40*, 11094–11111.

(4) Fischedick, M.; Nitsch, J.; Ramesohl, S. *J. Sol. Energy* **2005**, *78*, 678–686.

(5) Ursua, A.; Gandia, L. M.; Sanchis, P. *Proc. IEEE* **2012**, *100*, 410–426.

(6) Bertuccioli, L.; Chan, A.; Hart, D.; Lehner, F.; Madden, B.; Standen, E. *Study on development of water electrolysis in the EU*, 2014.

(7) Levie, R. de. *J. Electroanal. Chem.* **1999**, *476*, 92–93.

(8) Safizadeh, F.; Ghali, E.; Houlachi, G. *Int. J. of Hydrogen Energy* **2015**, *40*, 256–274.

(9) *ELECTROCHEMICAL METHOD: Fundamentals and Applications.;* Bard, A. J., Faulkner, L. R., Eds.; John Wiley & Sons, Inc., 2010.

(10) Trasatti, S. *J. Electrochem. Soc.* **1972**, *39*, 162–183.

(11) Dau, H.; Limberg, C.; Reier, T.; Risch, M.; Roggan, S.; Strasser, P. *ChemCatChem* **2010**, *2*, 724–761.

(12) Behret, H.; Binder, H.; Clauberg, W.; Sandstedf G. *Electrochim. Acta* **1978**, *23*, 1023–1029.

(13) Zou, X.; Zhang, Y. *Chem. Soc. Rev.* **2015**, *44*, 5148–5180.

(14) Conway, B. E.; Tilak, B. V. *Electrochim. Acta* **2002**, *47*, 3571–3594.

(15) Tymoczko, J.; Calle-Vallejo, F.; Schuhmann, W.; Bandarenka, A. S. *Nat. Commun.* **2016**, *7*, 10990.

(16) Durst, J.; Siebel, A.; Simon, C.; Hasché, F.; Herranz, J.; Gasteiger, H. A. *Energy Environ. Sci.* **2014**, *7*, 2255–2260.

(17) Kramm, U. I.; Bogdanoff, P.; Fiechter, S. *Encyclopedia of Sustainability Science and Technology*; pp 8265–8307.

(18) Byon, H. R.; Suntivich, J.; Crumlin, E. J.; Shao-Horn, Y. *Phys. Chem. Chem. Phys.* **2011**, *13*, 21437–21445.

(19) Jasinski, R. *Nature* **1964**, *201*, 1212–1213.

(20) Jahnke, H.; Schönborn, M.; Zimmermann G. *Top. Curr. Chem* **1976**, *61*, 133–138.

(21) Rajat K. Sen; Jose. Zagal; and Ernest. Yeager. *Inorg. Chem.* **1977**, *16*, 3379–3380.

(22) Gupta, S.; Tryk, D.; Bae, I.; Aldred, W.; Yeager, E. *J. Appl. Electrochem.* **1989**, *19*, 19–27.

(23) Kramm, U. I.; Herranz, J.; Larouche, N.; Arruda, T. M.; Lefevre, M.; Jaouen, F.; Bogdanoff, P.; Fiechter, S.; Abs-Wurmbach, I.; Mukerjee, S.; Dodelet, J.-P. *Phys. Chem. Chem. Phys.* **2012**, *14*, 11673–11688.

(24) Kramm, U. I.; Lefèvre, M.; Larouche, N.; Schmeisser, D.; Dodelet, J.-P. *J. Am. Chem. Soc.* **2014**, *136*, 978–985.

(25) Jaouen, F.; Proietti, E.; Lefèvre, M.; Chenitz, R.; Dodelet, J.-P.; Wu, G.; Chung, H. T.; Johnston, C. M.; Zelenay, P. *Energy Environ. Sci.* **2011**, *4*, 114–130.

(26) Dodelet, J.-P. Oxygen Reduction in PEM Fuel Cell Conditions: Heat-treated Non-precious Metal-N4 Macrocycles and Beyond. In *N4-Macrocyclic Metal Complexes*; Zagal, J. H., Bedioui, F., Dodelet, J.-P., Eds.; Springer New York: New York, NY, 2006; pp 83–147.

(27) Kramm, U. I.; Zana, A.; Vosch, T.; Fiechter, S.; Arenz, M.; Schmeißer, D. *J. Solid State Electrochem.* **2016**, *20*, 969–981.

(28) Kramm, U. I.; Herrmann-Geppert, I.; Bogdanoff, P.; Fiechter, S. *J. Phys. Chem. C* **2011**, *115*, 23417–23427.

(29) Koslowski, U. I.; Abs-Wurmbach, I.; Fiechter, S.; Bogdanoff, P. *J. Phys. Chem. C* **2008**, *112*, 15356–15366.

(30) Zitolo, A.; Goellner, V.; Armel, V.; Sougrati, M.-T.; Mineva, T.; Stievano, L.; Fonda, E.; Jaouen, F. *Nat. Mater.* **2015**, *14*, 937–942.

(31) Ranjbar Sahraie N.; Kramm, U. I.; Steinberg, J.; Zhang, Y.; Thomas, A; Reier, T.; Paraknowitsch, J.; Strasser, P. *Nat. Commun.* **2015**, *6*, 8618.

(32) Jose H. Zagal. *Coord. Chem. Rev.* **1992**, *119*, 89–136.

(33) J. Zagal; M. Paez. *J. Electroanal. Chem.* **1992**, *339*, 13–30.

(34) Zagal, J.; Gulppi, M.; Isaacs, M.; Cardenas-Jiron, G.; Jesus Aguirre, M. *Electrochim. Acta* **1998**, *44*, 1349–1357.

(35) Gasteiger, H. A.; Kocha, S. S.; Sompalli, B.; Wagner, F. T. *Appl. Catal., B* **2005**, *56*, 9–35.

(36) Jaouen, F.; Dodelet, J.-P. *Electrochim. Acta* **2007**, *52*, 5975–5984.

(37) Tang, C.; Zhang, Q. *J. Mater. Chem. A* **2016**, *4*, 4998–5001.

(38) Karweik, D. H.; Winograd, N. *Inorg. Chem.* **1976**, *15*, 2336–2342.

(39) Jaouen, F.; Herranz, J.; Lefevre, M.; Dodelet, J.; Kramm, U. I. .; Herrmann, I.; Bogdanoff, P.; Maruyama, J.; Nagaoka, T.; Garsuch, A.; Dahn, J. R.; Olson, T.; Pylypenko, S.; Atanassov, P.; Ustinov, E. *ACS Appl. Mater. Interfaces* **2009**, *1*, 1623–1639.

(40) Kramm, U. I.; Abs-Wurmbach, I.; Herrmann-Geppert, I.; Radnik, J.; Fiechter, S.; and Bogdanoff, P. *J. Electrochem. Soc.* **2011**, *158*, 69–78.

(41) Zhang, L.; Xiao, J.; Wang, H.; Shao, M. *ACS Catal.* **2017**, *7*, 7855–7865.

(42) Wang, J.; Gao, D.; Wang, G.; Miao, S.; Wu, H.; Li, J.; Bao, X. *J. Mater. Chem. A* **2014**, *2*, 20067–20074.

(43) Zhou, W.; Zhou, J.; Zhou, Y.; Lu, J.; Zhou, K.; Yang, L.; Tang, Z.; Li, L.; Chen, S. *Chem. Mater.* **2015**, *27*, 2026–2032.

(44) Tavakkoli, M.; Kallio, T.; Reynaud, O.; Nasibulin, A. G.; Johans, C.; Sainio, J.; Jiang, H.; Kauppinen, E. I.; Laasonen, K. *Angew. Chem. Int. Ed.* **2015**, *54*, 4535-4538.

(45) Wang, Z.-L.; Hao, X.-F.; Jiang, Z.; Sun, X.-P.; Xu, D.; Wang, J.; Zhong, H.-X.; Meng, F.-L.; Zhang, X.-B. *J. Am. Chem. Soc.* **2015**, *137*, 15070–15073.

(46) Huang, S.-Y.; Sodano, D.; Leonard, T.; Luiso, S.; Fedkiw, P. S. *J. Electrochem. Soc.* **2017**, *164*, 276–282.

(47) Maruyama, J.; Ioroi, T.; Hasegawa, T.; Mori, T.; Orikasa, Y.; Uchimoto, Y. *ChemCatChem* **2014**, *6*, 2197–2200.

(48) Liang, H.-W.; Brüller, S.; Dong, R.; Zhang, J.; Feng, X.; Müllen, K. *Nat. Commun.* **2015**, *6*, 7992.

(49) Fei, H.; Dong, J.; Arellano-Jiménez, M. J.; Ye, G.; Dong Kim, N.; Samuel, E. L. G.; Peng, Z.; Zhu, Z.; Qin, F.; Bao, J.; Yacaman, M. J.; Ajayan, P. M.; Chen, D.; Tour, J. M. *Nat. Commun.* **2015**, *6*, 8668.

(50) Deng, J.; Ren, P.; Deng, D.; Yu, L.; Yang, F.; Bao, X. *Energy Environ. Sci.* **2014**, *7*, 1919–1923.

(51) Li, Y.; Niu, S.; Rakov, D.; Wang, Y.; Cabán-Acevedo, M.; Zheng, S.; Song, B.; Xu, P. *Nanoscale* **2018**, *10*, 7291–7297.

(52) Zou, X.; Huang, X.; Goswami, A.; Silva, R.; Sathe, B. R.; Mikmekova, E.; Asefa, T. *Angew. Chem., Int. Ed.* **2014**, *53*, 4372–4376.

(53) Wang, Y.; Nie, Y.; Ding, W.; Chen, S. G.; Xiong, K.; Qi, X. Q.; Zhang, Y.; Wang, J.; Wei, Z. D. *Chem. Commun.* **2015**, *51*, 8942–8945.

(54) Morozan, A.; Goellner, V.; Nedellec, Y.; Hannauer J. *J. Electrochem. Soc.* **2015**, *162*, 719–726.

(55) Zhang, L.; Liu, W.; Dou, Y.; Du, Z.; Shao, M. *J. Phys. Chem. C* **2016**, *120*, 29047–29053.

(56) Yang, Y.; Lun, Z.; Xia, G.; Zheng, F.; He, M.; Chen, Q. *Energy Environ. Sci.* **2015**, *8*, 3563–3571.

(57) Li, X.; Niu, Z.; Jiang, J.; Ai, L. *J. Mater. Chem. A* **2016**, *4*, 3204–3209.

(58) Zhang, K.; Zhao, Y.; Fu, D.; Chen, Y. *J. Mater. Chem. A* **2015**, *3*, 5783–5788.

(59) Wu, H. B.; Xia, B. Y.; Le Yu; Yu, X.-Y.; Lou, X. W. D. *Nat. Commun.* **2015**, *6*, 6512.

(60) Deng, W.; Jiang, H.; Chen, C.; Yang, L.; Zhang, Y.; Peng, S.; Wang, S.; Tan, Y.; Ma, M.; Xie, Q. *ACS Appl. Mater. Interfaces* **2016**, *8*, 13341–13347.
(61) Li, D. J.; Maiti, U. N.; Lim, J.; Choi, D. S.; Lee, W. J.; Oh, Y.; Lee, G. Y.; Kim, S. O. *Nano Lett.* **2014**, *14*, 1228–1233.
(62) Zhou, W.; Jia, J.; Lu, J.; Yang, L.; Hou, D.; Li, G.; Chen, S. *Nano Energy* **2016**, *28*, 29–43.
(63) Chen, J.; Xia, G.; Jiang, P.; Yang, Y.; Li, R.; Shi, R.; Su, J.; Chen, Q. *ACS Appl. Mater. Interfaces* **2016**, *8*, 13378–13383.
(64) Jin, H.; Wang, J.; Su, D.; Wei, Z.; Pang, Z.; Wang, Y. *J. Am. Chem. Soc.* **2015**, *137*, 2688–2694.
(65) Jing, S.; Zhang, L.; Luo, L.; Lu, J.; Yin, S.; Shen, P. K.; Tsiakaras, P. *Appl. Catal., B* **2018**, *224*, 533–540.
(66) Shima, S.; Pilak, O.; Vogt, S.; Schick, M.; Stagni, M.; Meyer-Klaucke, W.; Warkentin, E.; Thauer, R.; Ermler, U. *Science* **2008**, *321*, 569–572.
(67) Gonzalez, E. R.; Avaca, L. A.; Tremiliosi-Filho, G.; Machado, S. A. S. and Ferriera, M. *Int. J. Hydrogen Energy* **1994**, *19*, 17–21.
(68) Staszak-Jirkovský, J.; Malliakas, C. D.; Lopes, P. P.; Danilovic, N.; Kota, S. S.; Chang, K.-C.; Genorio, B.; Strmcnik, D.; Stamenkovic, V. R.; Kanatzidis, M. G.; Markovic, N. M. *Nat. Mater.* **2015**, *15*, 197–203.
(69) Faber, M. S.; Lukowski, M. A.; Ding, Q.; Kaiser, N. S.; Jin, S. *J. Phys. Chem. C* **2014**, *118*, 21347–21356.
(70) Shinde, S. S.; Sami, A.; Kim, D.-H.; Lee, J.-H. *Chem. Commun.* **2015**, *51*, 15716–15719.
(71) Raybaud, P.; Hafner, J.; Kresse, G.; Kasztelan, S.; Toulhoat, H. *J. Catal.* **2000**, *189*, 129–146.
(72) Hinnemann, B.; Moses, P. G.; Bonde, J.; Jørgensen, K. P.; Nielsen, J. H.; Horch, S.; Chorkendorff, I.; Nørskov, J. K. *J. Am. Chem. Soc.* **2005**, *127*, 5308–5309.
(73) Gupta, S.; Zhao, S.; Ogoke, O.; Lin, Y.; Xu, H.; Wu, G. *ChemSusChem* **2017**, *10*, 774–785.
(74) Jaksic, M. M. *Electrochim. Acta* **1984**, *29*, 1539–1550.
(75) Lu, Q.; Hutchings, G. S.; Yu, W.; Zhou, Y.; Forest, R. V.; Tao, R.; Rosen, J.; Yonemoto, B. T.; Cao, Z.; Zheng, H.; Xiao, J. Q.; Jiao, F.; Chen, J. G. *Nat. Commun.* **2015**, *6*, 6567.
(76) Chen, W.-F.; Sasaki, K.; Ma, C.; Frenkel, A. I.; Marinkovic, N.; Muckerman, J. T.; Zhu, Y.; Adzic, R. R. *Angew. Chem., Int. Ed. Engl.* **2012**, *51*, 6131–6135.
(77) Hieringer, W.; Flechtner, K.; Kretschmann, A.; Seufert, K.; Auwärter, W.; Barth, J. V.; Görling, A.; Steinrück, H.-P.; Gottfried, J. M. *J. Am. Chem. Soc.* **2011**, *133*, 6206–6222.

(78) Ito, Y.; Cong, W.; Fujita, T.; Tang, Z.; Chen, M. *Angew. Chem. Int. Ed.* **2015**, *54*, 2131–2136.

(79) Kiciński, W.; Dembinska, B.; Norek, M.; Budner, B.; Polański, M.; Kulesza, P. J.; Dyjak, S. *Carbon* **2017**, *116*, 655–669.

(80) Herrmann, I.; Kramm, U. I.; Radnik, J.; Fiechter, S.; Bogdanoff, P. *J. Electrochem. Soc.* **2009**, *156*, 1283–1292.

(81) Li, Y.; Niu, S.; Rakov, D.; Wang, Y.; Cabán-Acevedo, M.; Zheng, S.; Song, B.; Xu, P. *Nanoscale* **2018**, *10*, 7291–7297.

(82) Downes, C. A.; Marinescu, S. C. *Dalton Trans.* **2016**, *45*, 19311–19321.

(83) Gu, W.; Hu, L.; Hong, W.; Jia, X.; Li, J.; Wang, E. *Chem. Sci.* **2016**, *7*, 4167–4173.

(84) Lee, Y.; Suntivich, J.; May, K. J.; Perry, E. E.; Shao-Horn, Y. *J. Phys. Chem.Lett.* **2012**, *3*, 399–404.

(85) Reier, T.; Oezaslan, M.; Strasser, P. *ACS Catal.* **2012**, *2*, 1765–1772.

(86) Diaz-Morales, O.; Ledezma-Yanez, I.; Koper, M. T. M.; Calle-Vallejo, F. *ACS Catal.* **2015**, *5*, 5380–5387.

(87) Fominykh, K.; Chernev, P.; Zaharieva, I.; Sicklinger, J.; Stefanic, G.; Döblinger, M.; Müller, A.; Pokharel, A.; Böcklein, S.; Scheu, C.; Bein, T.; Fattakhova-Rohlfing, D. *ACS nano* **2015**, *9*, 5180–5188.

(88) Suntivich, J.; May, K.; Gasteiger, H.; Goodenough, J.; Shao-Horn, Y. *Science* **2011**, *334*, 1380–1383.

(89) Rossmeisl, J.; Dimitrievski, K.; Siegbahn, P.; Nørskov, J. K. *J. Phys. Chem. C* **2007**, *111*, 18821–18823.

(90) Rossmeisl, J.; Logadottir, A.; Nørskov, J. K. *Chem. Phys.* **2005**, *319*, 178–184.

(91) Nørskov, J. K.; Bligaard, T.; Rossmeisl, J.; Christensen, C. H. *Nat. Chem.* **2009**, *1*, 37–46.

(92) Man, I. C.; Su, H.-Y.; Calle-Vallejo, F.; Hansen, H. A.; Martínez, J. I.; Inoglu, N. G.; Kitchin, J.; Jaramillo, T. F.; Nørskov, J. K.; Rossmeisl, J. *ChemCatChem* **2011**, *3*, 1159–1165.

(93) Calle-Vallejo, F.; Martinez, J. I.; Rossmeisl, J. *Phys. Chem. Chem. Phys.* **2011**, *13*, 15639–15643.

(94) Busch, M.; Halck, N. B.; Kramm, U. I.; Siahrostami, S.; Krtil, P.; Rossmeisl, J. *Nano Energy* **2016**, *29*, 126–135.

(95) Zhao, Y.; Kamiya, K.; Hashimoto, K.; Nakanishi, S. *J. Phys. Chem. C* **2015**, *119*, 2583–2588.

(96) Ranjbar Sahraie, N.; Paraknowitsch, J. P.; Göbel, C.; Thomas, A.; Strasser, P. *J. Am. Chem. Soc.* **2014**, *136*, 14486–14497.

(97) He, D.; Xiong, Y.; Yang, J.; Chen, X.; Deng, Z.; Pan, M.; Li, Y.; Mu, S. *J. Mater. Chem. A* **2017**, *5*, 1930–1934.
(98) Qiao, X.; Liao, S.; Zheng, R.; Deng, Y.; Song, H.; Du, L. *ACS Sustainable Chem. Eng.* **2016**, *4*, 4131–4136.
(99) Chen, P.; Zhou, T.; Xing, L.; Xu, K.; Tong, Y.; Xie, H.; Zhang, L.; Yan, W.; Chu, W.; Wu, C.; Xie, Y. *Angew. Chem., Int. Ed. Engl.* **2017**, *56*, 610–614.
(100) Wang, Z.; Xiao, S.; Zhu, Z.; Long, X.; Zheng, X.; Lu, X.; Yang, S. *ACS Appl. Mater. Interfaces* **2015**, *7*, 4048–4055.
(101) Liu, Y.; Jiang, H.; Zhu, Y.; Yang, X.; Li, C. *J. Mater. Chem. A* **2016**, *4*, 1694–1701.
(102) Zhao, J.; Quan, X.; Chen, S.; Liu, Y.; Yu, H. *ACS Appl. Mater. Interfaces* **2017**, *9*, 28685–28694.
(103) Liu, T.; Guo, Y.-F.; Yan, Y.-M.; Wang, F.; Deng, C.; Rooney, D.; Sun, K.-N. *Carbon* **2016**, *106*, 84–92.
(104) Ganesan, P.; Ramakrishnan, P.; Prabu, M.; Shanmugam, S. *Electrochim. Acta* **2015**, *183*, 63–69.
(105) Tang, Y.; Jing, F.; Xu, Z.; Zhang, F.; Mai, Y.; Wu, D. *ACS Appl. Mater. Interfaces* **2017**, *9*, 12340–12347.
(106) Qiao, X.; Jin, J.; Fan, H.; Li, Y.; Liao, S. *J. Mater. Chem. A* **2017**, *5*, 12354–12360.
(107) Aijaz, A.; Masa, J.; Rösler, C.; Xia, W.; Weide, P.; Botz, A. J. R.; Fischer, R. A.; Schuhmann, W.; Muhler, M. *Angew. Chem., Int. Ed.* **2016**, *55*, 4087–4091.
(108) Stracke, J. J.; Finke, R. G. *ACS Catal.* **2013**, *3*, 1209–1219.
(109) Daniel, Q.; Ambre, R. B.; Zhang, B.; Philippe, B.; Chen, H.; Li, F.; Fan, K.; Ahmadi, S.; Rensmo, H.; Sun, L. *ACS Catal.* **2017**, *7*, 1143–1149.
(110) Wang, D.; Groves, J. T. *Proc. Natl. Acad. Sci. U. S. A.* **2013**, *110*, 15579–15584.
(111) Wurster, B.; Grumelli, D.; Hotger, D.; Gutzler, R.; Kern, K. *J. Am. Chem. Soc.* **2016**, *138*, 3623–3626.
(112) Zhang, J.; Zhao, Z.; Xia, Z.; Dai, L. *Nat. Nanotechnol.* **2015**, *10*, 444–452.
(113) Weidler, N.; Paulus, S.; Schuch, J.; Klett, J.; Hoch, S.; Stenner, P.; Maljusch, A.; Brötz, J.; Wittich, C.; Kaiser, B.; Jaegermann, W. *Phys. Chem. Chem. Phys.* **2016**, *18*, 10708–10718.
(114) Weidler, N.; Schuch, J.; Knaus, F.; Stenner, P.; Hoch, S.; Maljusch, A.; Schäfer, R.; Kaiser, B.; Jaegermann, W. *J. Phys. Chem. C* **2017**, *121*, 6455–6463.
(115) Ren, J.; Antonietti, M.; Fellinger, T.-P. *Adv. Energy Mater.* **2015**, *5*, 1401660.
(116) Chen, S.; Duan, J.; Jaroniec, M.; Qiao, S. Z. *Angew. Chem., Int. Ed.* **2013**, *52*, 13567–13570.

(117) Chauhan, M.; Reddy, K. P.; Gopinath, C. S.; Deka, S. *ACS Catal.* **2017**, *7*, 5871–5879.
(118) Ganesan, V.; Lim, S.; Kim, J. *Chem.Asian J.* **2018**, *13*, 413–420.
(119) Wang, H.; Liang, Y.; Li, Y.; Dai, H. *Angew. Chem., Int. Ed. Engl.* **2011**, *50*, 10969–10972.
(120) Ganesan, P.; Prabu, M.; Sanetuntikul, J.; Shanmugam, S. *ACS Catal.* **2015**, *5*, 3625–3637.
(121) Wang, H.; Li, Z.; Li, G.; Peng, F.; Yu, H. *Catal. Today* **2015**, *245*, 74–78.
(122) Choi, C. H.; Baldizzone, C.; Grote, J.-P.; Schuppert, A. K.; Jaouen, F.; Mayrhofer, K. J. J. *Angew. Chem., Int. Ed.* **2015**, *54*, 12753–12757.
(123) Wang, W.; Luo, J.; Chen, S. *Chem. Commun.* **2017**, *53*, 11556–11559.
(124) Wu, G.; Santandreu, A.; Kellogg, W.; Gupta, S.; Ogoke, O.; Zhang, H.; Wang, H.-L.; Dai, L. *Nano Energy* **2016**, *29*, 83–110.
(125) Wang, H.; Lin, J.; Shen, Z. X. *Adv. Mater. Devices* **2016**, *1*, 225–255.
(126) Wu, G.; Johnston, C. M.; Mack, N. H.; Artyushkova, K.; Ferrandon, M.; Nelson, M.; Lezama-Pacheco, J. S.; Conradson, S. D.; More, K. L.; Myers, D. J.; Zelenay, P. *J. Mater. Chem.* **2011**, *21*, 11392–11404.
(127) Byon, H. R.; Suntivich, J.; Shao-Horn, Y. *Chem. Mater.* **2011**, *23*, 3421–3428.
(128) Corrigan, D. A. *J. Electrochem. Soc.* **1987**, *134*, 377–384.
(129) Gong, M.; Dai, H. *Nano Res.* **2015**, *8*, 23–39.
(130) Zhao, D.; Li, L.; Xie, L.; Zhou, N.; Chen, S. *J. Alloys Compd.* **2018**, *741*, 368–376.
(131) Proietti, E.; Jaouen, F.; Lefevre, M.; Larouche, N.; Tian, J.; Herranz, J.; Dodelet, J.-P. *Nat. Commun.* **2011**, *2*, 416.
(132) Adams, P. N.; Laughlin, P. J.; Monkman, A. P. *Synth. Met.* **1996**, *76*, 157–160.
(133) Bokobza, L.; Bruneel, J.-L.; Couzi, M. *Vib. Spectrosc.* **2014**, *74*, 57–63.
(134) B. J. Lindberg, K. Hamrin, G. Johansson, U. Gelius, A. Fahlman, C. Nordling and K. Siegbahn. *Phys. Scr.* **1970**, *1*, 286–298.
(135) Biesinger, M. C.; Lau, L. W.; Gerson, A. R.; Smart, R. S. *Appl. Surf. Sci.* **2010**, *257*, 887–898.
(136) Alstrup, I. B.; Chorkendorff, I.; Candia, R.; Clausen, B.; Topsoe, H. *J. Catal.* **1982**, *77*, 397–409.
(137) Nørskov, J. K.; Bligaard, T.; Logadottir, A.; Kitchin, J. R.; Chen, J. G.; Pandelov, S.; Stimming, U. *J. Electrochem. Soc.* **2005**, *152*, J23.
(138) Meier, J. C.; Katsounaros, I.; Galeano, C.; Bongard, H. J.; Topalov, A. A.; Kostka, A.; Karschin, A.; Schüth, F.; Mayrhofer, K. J. J. *Energy Environ. Sci.* **2012**, *5*, 9319–9330.

(139) Deng, W.; Jiang, H.; Chen, C.; Yang, L.; Zhang, Y.; Peng, S.; Wang, S.; Tan, Y.; Ma, M.; Xie, Q. *ACS Appl. Mater. Interfaces* **2016**, *8*, 13341–13347.

(140) J. Robertson. *J. Mater. Sci. Eng., R* **2002**, *37*, 129–281.

(141) Yan Wang; Daniel C. Alsmeyer; and Richard L. McCreery. *Chem. Mater.* **1990**, *2*, 557–563.

(142) Martinaiou, I.; Shahraei, A.; Grimm, F.; Zhang, H.; Wittich, C.; Klemenz, S.; Dolique, S. J.; Kleebe, H.-J.; Stark, R. W.; Kramm, U. I. *Electrochim. Acta* **2017**, *243*, 183–196.

(143) Grabke, H. J.; Moszynski, D.; Müller-Lorenz, E. M.; Schneider, A. *Surf. Interface Anal.* **2002**, *34*, 369–374.

(144) Zhu, J.; Huang, L.; Xiao, Y.; Shen, L.; Chen, Q.; Shi, W. *Nanoscale* **2014**, *6*, 6772–6781.

Erklärung zur Begutachtung der Veröffentlichungen

Datum: 27.08.2018

Weder Referent (Prof. Dr. Ulrike I. Kramm) noch Korreferent (Prof. Dr. Jin Suntivich) der vorliegenden kumulativen Doktorarbeit waren an der Begutachtung nachstehender Veröffentlichen beteiligt:

[1] On the role of oxidic species in sulphur- and nitrogen-doped cobalt-based carbon catalysts for the oxygen evolution reaction
A. Shahraei, M. Kübler, I. Martinaiou, K. A. Creutz, D. Z. Wallace, M. A. Nowroozi, S. Paul, N. Weidler, R. W. Starck, O. Klemenz, U. I. Kramm
2018-Journal of Material Chemistry A, under the second round of revision. First submission: Jun 2018

[2] Adding a New Member to the MXene Family: Synthesis, Structure, and Electrocatalytic Activity for the Hydrogen Evolution Reaction of V4C3T*x*
M. H. Tran, T. Schäfer, A. Shahraei, M. Dürrschnabel, L. Molina-Luna, U. I. Kramm, C. Birkel, ACS Applied Energy Materials, 2018

[3] Exploring Active Sites in Multi-heteroatom Doped Co-based Catalysts for Hydrogen Evolution Reaction
A Shahraei, I. Martinaiou, K. A. Creutz, M. Kübler, N. Weidler, S. T. Ranecky, W.D.Z. Wallace, M. A. Nowroozi, O. Clemens, R. W. Stark, U. I. Kramm, *Chemistry- A European Journal, 2018*

[4] Influence of sulfur in the precursor mixture on the structural composition of Fe-N-C catalysts
A. Janßen, I. Martinaiou, S. Wagner, N. Weidler, A. Shahraei, U. I. Kramm, *Hyperfine Interactions*, 2018

[5] On the effect of sulfite ions on the structural composition and ORR activity of Fe-N-C catalysts
S. Wagner, I. Martinaiou , A. Shahraei, N. Weidler, U. I. Kramm, *Hyperfine Interactions*, 2018

[6] Elucidating the Origin of Hydrogen Evolution Reaction Activity in Mono-and Bimetallic Metal-and Nitrogen-Doped Carbon Catalysts (Me–N–C)
A. Shahraei, A. Moradabadi, I. Martinaiou, S. Lauterbach, S. Klemenz, S. Dolique, H. Kleebe, P. Kaghazchi, U. I. Kramm, *ACS applied materials & interfaces*, 2017

[7] Effect of metal species on the stability of Me-NC catalysts during accelerated stress tests mimicking the start-up and shut-down conditions
I. Martinaiou, A. Shahraei, F. Grimm, H. Zhang, C. Wittich, S. Klemenz, S. J Dolique, H. Kleebe, R. W Stark, u. I. Kramm, *Electrochimica Acta*, 2017

[8] Metall-N-C-Katalysatoren in der Elektrokatalyse
U. I. Kramm, A. Shahraei, I. Martinaiou, *Nachrichten aus der Chemie*, 2017

[9] Improved electrochemical performance of Fe-N-C catalysts through ionic liquid modification in alkaline media
I. Martinaiou, T. Wolker, A. Shahraei, G. R. Zhang, A. Janßen, S. Wagner, N. Weidler, R. W. Stark, B. J. M. Etzold, U. I. Kramm*, *Journal of Power Sources*, 2017

[10] Effect of rf-Plasma Treatment on the Activity and Selectivity of Me-NC Electrocatalysts for the Oxygen Reduction Reaction
N. Weidler, D. J Babu, I. Martinaiou, S. Paul, S. Wagner, A.Shahraei, A. Janßen, R.W Stark, J. J Schneider, U. I. Kramm, *ECS Transactions*, 2017

Referent

(Prof. Dr. Ulrike I. Kramm)

Korreferent

(Prof. Dr. Jin Suntivich)

Ali Shahraei
Otto-Berndt-Straße 3
64287 Darmstadt
Tel: 017675986891
Email: Shahraei@ese.tu-darmstadt.de

28.08.2018

Erklärung

Ich erkläre hiermit, dass ich meine Dissertation selbstständig und nur mit den angegeben Hilfsmitteln angefertigt und noch keinen Promotionsversuch unternommen habe.

Ali Shahraei

Curriculum Vitae

Ali Shahraei- PhD researcher

Personal Details

Contact	Ali Shahraei Havel straße 18 64295 Darmstadt Shahraei@ese.tu-darmstadt.de
Date of Birth	14.02.1989
Place of Birth	Ferdos, Iran
Nationality	Iran
Marital status	Single

Work Experience

08/2015-10/2018

PhD researcher
TU Darmstadt, Catalysis and Electrocatalysis, Prof. Kramm

Dissertation: Investigation of the water splitting reactions on multi-heteroatom doped cobalt-based carbon catalysts
Grade: Very good

- Synthesis of Me-N-C catalysts
- Characterization expertise (XPS, Ap-XPS, In-operando XAS, TEM SEM, FTIR, RAMAN)
- Electrochemical methods (RRDE, RDE, CV, GS)

8/2015-07/2018

Teacher assistant
TU Darmstadt, Chemistry Department, Prof. Kramm
Courses: Chemistry for Energy sciences and Engineering, Electrochemistry

02/2014- 02/2015

Student research assistant
Zentrum für Sonnenenergie- und Wasserstoff-Forschung (ZSW)

- Fuel cell systems and test stands
- Fuel cell vehicle simulation project
- Fuel cell degradation mathematical (impact project) in cooperation with DLR

Education

10/2012- 07/2015

Master of Science (Energy Science and Technology), Ulm University
Research-oriented and focused on electrochemical conversion, renewable energy
Thesis: Further improvement, Thermal management and pressure controls of the fuel cell vehicle model with Matlab/Simulink (Grade: 1.3)

10/2007- 10/2011

Bachelor of Science (Chemical engineering)
University of Tehran-Iran
Thesis: performance studies of Mixed Matrix Membranes permeability models including impermeable particles (Grade: 90%)

Curriculum Vitae

Ali Shahraei- PhD researcher

Publications

[1] On the role of hydroxide species in sulphur- and nitrogen-doped cobalt-based carbon catalysts for the oxygen evolution reaction

A. Shahraei, M. Kübler, I. Martinaiou, K. A. Creutz, D. Z. Wallace, M. A. Nowroozi, S. Paul, N. Weidler, R. W. Starck, O. Klemenz, U. I. Kramm, *Journal of Material Chemistry A, 2018*

[2] Adding a New Member to the MXene Family: Synthesis, Structure, and Electrocatalytic Activity for the Hydrogen Evolution Reaction of V4C3T*x*

M. H. Tran, T. Schäfer, A. Shahraei, M. Dürrschnabel, L. Molina-Luna, U. I. Kramm, C. Birkel, *ACS Applied Energy Materials, 2018*

[3] Exploring Active Sites in Multi-heteroatom Doped Co-based Catalysts for Hydrogen Evolution Reaction

A Shahraei, I. Martinaiou, K. A. Creutz, M. Kübler, N. Weidler, S. T. Ranecky, W.D.Z. Wallace, M. A. Nowroozi, O. Clemens, R. W. Stark, U. I. Kramm, *Chemistry- A European Journal, 2018*

[4] Influence of sulfur in the precursor mixture on the structural composition of Fe-N-C catalysts

A. Janßen, I. Martinaiou, S. Wagner, N. Weidler, A. Shahraei, U. I. Kramm, *Hyperfine Interactions,* 2018

[5] On the effect of sulfite ions on the structural composition and ORR activity of Fe-N-C catalysts

S. Wagner, I. Martinaiou , A. Shahraei, N. Weidler, U. I. Kramm, *Hyperfine Interactions,* 2018

[6] Elucidating the Origin of Hydrogen Evolution Reaction Activity in Mono-and Bimetallic Metal-and Nitrogen-Doped Carbon Catalysts (Me–N–C)

A. Shahraei, A. Moradabadi, I. Martinaiou, S. Lauterbach, S. Klemenz, S. Dolique, H. Kleebe, P. Kaghazchi, U. I. Kramm, *ACS applied materials & interfaces*, 2017

[7] Effect of metal species on the stability of Me-NC catalysts during accelerated stress tests mimicking the start-up and shut-down conditions

I. Martinaiou, A. Shahraei, F. Grimm, H. Zhang, C. Wittich, S. Klemenz, S. J Dolique, H. Kleebe, R. W Stark, u. I. Kramm, *Electrochimica Acta*, 2017

[8] Metall-N-C-Katalysatoren in der Elektrokatalyse

U. I. Kramm, A. Shahraei, I. Martinaiou, *Nachrichten aus der Chemie,* 2017

[9] Improved electrochemical performance of Fe-N-C catalysts through ionic liquid modification in alkaline media

I. Martinaiou, T. Wolker, A. Shahraei, G. R. Zhang, A. Janßen, S. Wagner, N. Weidler, R. W. Stark, B. J. M. Etzold, U. I. Kramm, *Journal of Power Sources*, 2017

Curriculum Vitae

Ali Shahraei- PhD researcher

[10] Effect of rf-Plasma Treatment on the Activity and Selectivity of Me-NC Electrocatalysts for the Oxygen Reduction Reaction

N. Weidler, D. J Babu, I. Martinaiou, S. Paul, S. Wagner, A.Shahraei, A. Janßen, R.W Stark, J. J

Schneider, U. I. Kramm, *ECS Transactions*, 2017